



Improved post-processing in searches for continuous gravitational waves

and

**a model for transient continuous gravitational wave emission from
neutron star glitches**

Von der Fakultät für Mathematik und Physik
der Gottfried Wilhelm Leibniz Universität Hannover
zur Erlangung des Grades

*Doctor der Naturwissenschaften
Dr. rer. nat.*

genehmigte Dissertation
von

M.Sc. Avneet Singh^{1,2,3,†}

geboren am 12. January 1991 in *Ambala Cantt*

2017

Referent: Dr. Maria Alessandra Papa^{1,2,4}

Korreferenten: Prof. Tobias Osborne³, Prof. Alicia Sintes⁵, Prof. Pia Astone⁶
und Prof. Andrew Melatos⁷

Tag der Promotion: 10. November 2017

[†]avneet.singh@ligo.org, avneet.singh@aei.mpg.de

¹ Max-Planck-Institut für Gravitationsphysik, am Mühlenberg 1, 14476, Potsdam-Golm

² Max-Planck-Institut für Gravitationsphysik, Callinstraße 38, 30167, Hannover

³ Leibniz Universität Hannover, Welfengarten 1, 30167, Hannover

⁴ University of Wisconsin-Milwaukee, Milwaukee, Wisconsin 53201, USA

⁵ Universitat de les Illes Balears, IAC3-IEEC, E-07122 Palma de Mallorca, Spain

⁶ Istituto Nazionale di Fisica Nucleare (INFN), Sezione di Roma, I-00185 Roma, Italy

⁷ University of Melbourne, Parkville VIC 3010, Sydney, Australia

Abstract

Gravitational waves (GW) are tiny oscillations in the fabric of space-time, first hypothesised within the framework of Einstein's General theory of Relativity (GR) a little more than 100 years ago. The first direct detection of gravitational waves (GW150914) was made on Sept. 14, 2015 by the two LIGO detectors in Hanford and Livingston [27]. In this path-breaking discovery, the first GW observation revealed a coalescence of two black holes in a binary orbit.

Besides compact binary systems, isolated rotating neutron stars with physical asymmetries are also expected to emit GW; in this case, the emission is in the form of long lasting nearly monochromatic continuous gravitational waves (CW). In addition to these standard CW, transient-continuous gravitational waves (tCW) are another subset within the category of CW, characterised by their relatively shorter duration timescales. CW and tCW are considered to bear an important and direct association with the internal dynamics of neutron stars, such as their elusive equations of state. Unfortunately, no direct detections of CW have yet been made despite their enormous importance to astrophysics and astronomy [45].

This thesis encompasses several aspects of the science surrounding CW and tCW, such as the source-modeling and the emission mechanisms for tCW, searches for CW, and improvements to the post-processing methods in the deepest searches for CW.

In source-modeling, we address the dynamics during the post-glitch relaxation phase of a neutron star and estimate the extent of tCW emission expected to occur via the process of Ekman pumping. We explore multiple GW emission channels, and compare the physical expectation with the current and future detection capabilities of the LIGO detectors [65].

This thesis details the first high-frequency search in LIGO's fifth science run data, which is one of the very few CW searches targeting the high-frequency bandwidth of the LIGO spectrum. We report no detection and quote the strictest upper-limits from the fifth science run [68].

We also present a new clustering algorithm aimed at reducing the computational cost of hierarchical multi-stage follow-up search schemes. This new procedure adaptively analyses the topology of the data and offers a novel way to cluster contrasting densities of candidates from broad parameter space grid-based searches. This allows us to lower the threshold and gain sensitivity when operating at a fixed computing budget [66].

Lastly, we describe the procedure for setting the upper-limits on the continuous gravitational wave amplitudes in the latest CW searches on the *Einstein@Home* volunteer distributed computing project. This procedure is robust in its implementation and details the uncertainty measurement in the final upper-limit statements quoted by the respective searches [67].

Keywords: gravitational waves, continuous gravitational waves, neutron stars, fluid dynamics, equation of state, einstein@home, ligo, data analysis, algorithms, topology.

Kurzfassung

Gravitationswellen (GW) sind winzige Schwingungen in der Struktur der Raumzeit und wurden erstmals vor etwas mehr als 100 Jahren im Rahmen der Einstein'schen Allgemeinen Relativitätstheorie vorhergesagt. Der erste direkte Nachweis von Gravitationswellen (GW150914) gelang am 14. September 2015 durch die zwei LIGO-Detektoren in Hanford und Livingston [27]. In dieser bahnbrechenden Entdeckung enthüllte die erste Beobachtung von Gravitationswellen eine Verschmelzung zweier einander umkreisender schwarzer Löcher.

Abgesehen von kompakten Binärsystemen wird auch von isoliert rotierenden Neutronensternen mit physischer Asymmetrie erwartet, dass diese GW emittieren. In diesem Fall wird die Emission in Form lang anhaltender, fast monochromatischer und kontinuierlicher Gravitationswellen (CW) vorhergesagt. Zusätzlich zu diesen Standard-CW sind flüchtig-kontinuierliche Gravitationswellen (tCW) eine weitere Unterklasse der Klasse der CW und werden charakterisiert durch ihre vergleichsweise kürzere Lebensdauer. CW und tCW werden als wichtige und direkte Verbindung zur internen Dynamik der Neutronensterne wie der schwer fassbaren Zustandsgleichung angesehen. Unglücklicherweise ist bisher trotz der enormen Bedeutung für die Astrophysik und Astronomie noch keine direkte Entdeckung einer CW gelungen [45].

Diese Arbeit umfasst mehrere Aspekte der Wissenschaft um CW and tCW wie die Modellbildung von Quellen und die Emissionsmechanismen von tCW, sowie Suchen nach CW und Verbesserungen der Nachbereitungsmethoden in den empfindlichsten Suchen nach CW.

Bei der Modellbildung von Quellen befassen wir uns mit der Dynamik während der Post-Glitch-Erholungsphase eines Neutronensterns und schätzen den Umfang der zu erwartenden tCW-Emission ab, die im Verlauf des Ekman-Pumpens auftritt. Wir untersuchen zahlreiche GW-Emissionskanäle und vergleichen die physikalischen Erwartungen mit dem gegenwärtigen und zukünftigen Nachweisvermögen der LIGO-Detektoren [65].

Diese Arbeit beschreibt detailliert die erste Hochfrequenz-Suche in den Daten von LIGOs fünftem Beobachtungslauf, welche eine unter sehr wenigen CW-Suchen ist, die auf das Hochfrequenz-Band des LIGO-Spektrums ausgerichtet ist. Wir haben keinen Nachweis erzielt und geben die strengsten Obergrenzen für den fünften Beobachtungslauf an [68].

Außerdem präsentieren wir einen neuen Gruppierungsalgorithmus, der darauf abzielt Rechenkosten der hierarchischen, mehrstufigen Methoden der Nachbearbeitung zu reduzieren. Dieses neue Verfahren analysiert die Topologie der Daten adaptiv und ermöglicht es sich abhebende Dichten von Kandidaten zu gruppieren, die aus Gitter-basierten Suchen über weite Parameterräume resultieren. Dies erlaubt es uns bei vorgegebenen Rechenkosten die Obergrenzen zu senken und empfindlicher zu werden [66].

Schließlich beschreiben wir das Verfahren zur Festlegung von Höchstgrenzen für die Amplituden der CW in den aktuellsten CW-Suchen auf dem verteilten freiwilligen Rechenprojekt *Einstein@Home*. Das Verfahren ist stabil implementiert und beschreibt die Unsicherheitsmessung in den abschließenden Angaben von Höchstgrenzen, die von den jeweiligen Suchen zitiert werden [67].

Schlüsselworte: Gravitationswellen, kontinuierliche Gravitationswellen, Neutronensterne, Fluidynamik, Zustandsgleichung, Einstein@Home, LIGO, Datenanalyse, Algorithmen, Topologie.

Contents

<i>Abstract</i>	2
<i>Kurzfassung</i>	4
<i>Contents</i>	5
I Introduction	7
1 A transient continuous gravitational wave emission model	8
2 A search for high-frequency continuous gravitational waves	8
3 A new clustering procedure	8
4 A method for setting upper limits on continuous gravitational wave amplitudes	9
5 Implementation to continuous gravitational wave searches	9
II Gravitational Wave transient signal emission via Ekman Pumping in Neutron Stars during post-glitch relaxation phase	10
1 Introduction	10
2 Hydrodynamics of the system	11
2.1 Governing equations	11
2.2 Orders of magnitude	12
3 Solution	12
3.1 Equilibrium solution	12
3.2 Induced perturbations	13
3.3 Method of multiple scales	13
3.4 $O(E^0)$ solutions	14
3.5 $O(E^{1/2})$ solutions	14
3.6 More on the scale-based solutions	14
3.7 The characteristic equation	15
3.8 Temporal evolution	15
3.9 Initial and final conditions	16
3.10 Final solutions	16
4 Gravitational wave emission	17
4.1 Gravitational wave emission via mass-quadrupole	17
4.2 Gravitational wave emission via current-quadrupole	18
4.3 A verdict on parameter space	19
5 Time-scales of emitted signals and corresponding amplitudes	20
5.1 Growing modes	20
6 Discussion	22
6.1 Detectability of emitted signals	23
6.2 Energetics of the system	24
6.3 Choice of equation of state	25
Appendix	26
III Results of an all-sky high-frequency Einstein@Home search for continuous gravitational waves in LIGO's fifth Science Run	32
1 Introduction	32
2 The data	32

3	The search	33
4	Identification of undisturbed bands	34
5	Upper-limits	36
6	Conclusions	37
	<i>Appendix</i>	39
IV	Adaptive clustering algorithm for continuous gravitational wave searches	43
1	Introduction	43
2	Clustering of candidates	43
3	The cluster size	45
3.1	A measure of distance in frequency and spin-down space (F-space)	45
3.2	Distribution of distances in F-space	45
3.3	Cluster size in F-space	46
3.4	Hill parameters in F-space and further constraints	47
3.5	A measure of distance in the sky (S-space)	47
3.6	Distribution of distances in S-space	47
3.7	Cluster in S-space	48
4	Performance	49
4.1	Clustering parameters	49
4.2	Safety	49
4.3	Noise Rejection	50
4.4	Results	50
5	Conclusions	51
	<i>Appendix</i>	52
V	The upper-limit procedure for the most recent Einstein@Home searches	54
1	Introduction	54
1.1	A typical Einstein@Home search	54
2	The upper-limit procedure	54
2.1	Monte-Carlo simulations	54
2.2	Detection criteria	55
2.3	Confidence level	55
2.4	Sensitivity-depth	56
2.5	Uncertainty in the upper-limits	56
3	Conclusions	57
VI	Implementation to CW searches	59
1	<i>First low-frequency Einstein@Home all-sky search for continuous gravitational waves in Advanced LIGO data</i>	59
2	<i>Results of the deepest all-sky survey for continuous gravitational waves on LIGO S6 data running on the Einstein@Home volunteer distributed computing project</i>	85
3	<i>Hierarchical follow-up of subthreshold candidates of an all-sky Einstein@Home search for continuous gravitational waves on LIGO sixth science run data</i>	119
	Conclusions	133
	References	135
	Acknowledgments	138
	Curriculum Vitae	139
	List of Publications	140

I Introduction

The world of astrophysics and astronomy was excited by the first direct detection of gravitational waves (GW150914) made by the two LIGO detectors in Hanford and Livingston on Sept. 14, 2015 [27]. In its groundbreaking glory, the first GW observation revealed a pair of black holes nearing the end of their life in a binary orbit and coalescing to form a larger black hole, emitting a short pulse of GW in the process. Since then, more detections have followed (GW151226 [31], GW170104 [32] and LVT151012 [31]) revealing a universe inhabited by binary black holes with individual masses as high as 20–40 M_{\odot} . These detections serve as the first probe into the extremely energetic dynamics of black holes [29], the fundamental laws of nature through the predictions of General Relativity as well as countless other astrophysical implications [28, 30].

Compact binary coalescence (CBC) events such as GW150914 are not the only astronomical sources of gravitational waves. For example, isolated rotating neutron stars with physical asymmetries are also hypothesized to emit long lasting [$O(\text{years})$] nearly monochromatic gravitational waves called the continuous gravitational waves (CW) [24, 40]. Within this broad category of CW, a family of relatively short-duration [$O(\text{days-months})$] continuous gravitational waves is also predicted, known as the *transient continuous gravitational waves* (tCW) [65, 60, 41].

The emission of CW or tCW from neutron stars is fundamentally enabled by mass asymmetries or mass-current asymmetries associated with the object [70]. Typically, these progenitor asymmetries may arise from a rigid aspherical non-axisymmetry in the crust of the neutron star [24, 39, 40, 7], or due to the non-axisymmetric flow of the internal (super)fluid, e.g. in form of r -modes, Ekman flow following glitches, or

other quasinormal instabilities [65, 62, 24]. The former case is typically associated with the emission of long-lasting CW while the latter case may be responsible for long-duration as well as short emission time-scales. This is generally because the dissipative effects (e.g. due to sheer and bulk viscosity, crust-core interaction, superfluid friction, stratification of flow, exotic matter interactions etc) tend to dampen the asymmetries in an astatic superfluid quicker than in the rigid outer crust. The nature of these asymmetries naturally depends on the overall composition of the neutron star, the nature of the constituent matter in the bulk and in the crust, exotic nuclear matter interactions, and most importantly, the equation of state¹.

While more than 2,000 pulsating neutron stars have been found with electromagnetic observations, there still remains a large amount of uncertainty in their structure [24, 43], primarily because such observations are incapable of resolving the different internal physical phenomenon (described above) in interplay. Electromagnetic observations of known pulsars² and terrestrial experiments³ have yielded some information about the neutron stars structure, but the outcome of such studies have barely scratched the surface of the extreme physics that might be at play inside the neutron stars. Since the properties of the CW or tCW emission are non-trivially dependent on the physical properties of the neutron stars, CW or tCW detections may prove to be a vital element in constraining the structure of the neutron stars. This makes CW searches a task of great significance.

A significant amount of effort has been made in the past decade to search for the elusive CW signals in the data from many science and observation runs of LIGO [8, 10, 5, 7, 81, 11, 68, 45, 55, 13]. However, no detections have yet been made for CW or tCW despite the consistent improvements in detector sensitivities and in search pipelines [77]. At the same time, very strin-

¹The nature and the properties of the thin outer crust are weakly coupled to the equation of state in comparison to the bulk superfluid due to the rigidity and the thinness of the crust.

²The electromagnetic observations of pulsars have simplified the problem to some extent by constraining the strength of the magnetic field, the thickness and rigidity of the crust, and by providing a crude estimate on the distribution of neutron star population in space and frequency etc.

³Heavy element collision experiments have attempted to understand the flow and the interaction of nuclear matter under high pressure and temperature [19, 20].

gent upper-limits have been placed on the amplitudes of the CW across a wide range of frequencies. The most sensitive searches on LIGO O1 data for CW (i.e. Einstein@Home searches [45, 55, 11, 68, 81]) are able to “dig” into the data roughly 50 times below the intrinsic detector noise [15, 45]. This is an impressive improvement and the future holds promise for further improvements [66, 80].

This thesis attempts to improve upon many of the aspects of our understanding of CW/tCW mentioned above, such as the source-modeling, searches in LIGO data, and new novel post-processing algorithms. This thesis is a collection of several scientific articles and internal LIGO documents written and published during my work at the Albert Einstein Institute (11/2014 – 08/2017). During the course of this, I have been a part of the data-analysis team for Einstein@Home searches for continuous gravitational waves, and a member of the LIGO Scientific Collaboration (LSC). Consequently, a significant part of this work is implemented in LSC publications (see section 1, 2 in chapter VI). In sections 1–5 below, I provide short introductions to the chapters contained in this thesis and I detail my specific contributions.

1 A transient continuous gravitational wave emission model

In chapter II, we study a mechanism which allows for the emission of tCW in a large range of time-scales and frequencies following a glitch in the neutron star’s rotational frequency. Glitches in neutron stars’ rotation have long been observed and the evolution of the fluid flow in the relaxation phase following the glitch has been a subject of high interest for astronomers in the past few decades. In this work, we elaborate upon the most recent work done on the subject and relax the assumptions on physical parameters in order to arrive at a more general model of *Ekman transport* in the post-glitch relaxation phase. We explore the mass-quadrupole and current-quadrupole GW emission channels and find that it is possible for a neutron star to emit relatively loud tCW in the post-glitch relaxation phase in certain ranges of the physical parameters, which also characterise the internal equation of state. We determine the nature of the dependence of the time-scales and of the amplitudes on the physical parameters and their spatial variations. We conclude by estimating the detectability of these type of tCW signals in the most sensitive advanced LIGO data available at that time, and hope that this study will provide a motivation for searches exclusively targeting tCW. The content of this chapter has been published in *Physical Review D* as [65]. This work was carried out independently in two fragments over the long Hanoverian winter of 2014–2015 and then another long winter of 2015–2016.

2 A search for high-frequency continuous gravitational waves

In chapter III, we report the results from a CW search for isolated neutron stars in LIGO’s fifth science run (S5) data in the high-frequency region between 1.25–1.5 kHz. This chapter details a typical Einstein@Home search in a rarely explored frequency region in the LIGO band as far as the CW searches are concerned. This search covered nearly 10^{17} templates in frequency, spin-down and sky spread across more than 6 million work units clocking close to 40 million CPU hours. This search ran on the Einstein@Home volunteer distributed computing project (powered by BOINC) for nearly 6 months involving over 10,000 volunteers. The Einstein@Home network has since grown five-folds to > 50,000 active users. This search dealt with fairly quiet S5 data compared to the more sensitive but rather disturbed O1 data. In the end, no interesting candidates were found and upper-limits are placed on the amplitudes of CW. The data preparation and setting up of this search on the Einstein@Home framework was led by Holger Pletsch before my time at AEI. The post-processing and the analysis presented in this article was performed in entirety by me with valuable contributions from the post-processing and data-analysis team (Maria Alessandra Papa, Heinz-Bernd Eggenstein, Sylvia Zhu). The material in this chapter has been published in *Physical Review D* as [68].

3 A new clustering procedure

In chapter IV, we present a novel procedure that helps to ease the computational cost of hierarchical follow-up CW searches, especially in context of the Einstein@Home searches. This new adaptive algorithm analyses the topological properties of the distribution of candidates across the parameter space and uses them as a veto to accept clusters of candidates that bear some resemblance to a signal. In doing so, we greatly reduce the number of candidates to be followed up in the hierarchical stages of the search by discarding a lot of noise candidates. In case of limited computational resources, this allows for a deeper search. This method is adopted in the most recent Einstein@Home low-frequency all-sky search [45], and it will certainly remain an integral part of the Einstein@Home pipeline. The procedure discussed in this chapter may find utility in many other fields besides the CW searches since the principle behind it is rather simple – it proposes a way to estimate the topographical properties of a distribution of values assigned to grid-points in a multidimensional parameter space. The development and implementation of the algorithm presented in this article was carried out in entirety by me with valuable discussions and inputs from Maria Alessandra Papa. In order to characterise the algorithm, a signal population was required for the Monte-Carlo simulations, and this population of signals

was provided by Sinéad Walsh. The analysis comparing the new method against the previously accepted procedure in its various aspects was assisted by Heinz-Bernd Eggenstein. The content of this chapter has been published in *Physical Review D* as [66]. This work took more or less two years in development across several Einstein@Home searches.

4 A method for setting upper limits on continuous gravitational wave amplitudes

In chapter V, we briefly present the upper-limit procedure implemented in all of the most recent Einstein@Home CW searches [45, 68, 11, 55]. This method presents several improvements upon the previous version used to estimate the upper-limits on the amplitudes. It uses Monte-Carlo simulations to estimate the sensitivity-depth of a search with respect to the noise floor, and compares these sensitivity-depths across several Einstein@Home searches. We also detail the calculations behind the quoted uncertainties on the upper-limit values in the associated observational papers. The basic principle behind this procedure was preexisting and developed by Maria Alessandra Papa. The adaptation to recent Einstein@Home searches were discussed by the data analysis team (myself, Maria Alessandra Papa, Sylvia Zhu, Heinz-Bernd Eggenstein), and I was responsible for the implementation, development and review of the procedure. The characterisation of this procedure also required a signal population which was provided by Sinéad Walsh. This chapter is part of the LIGO Document Database (DCC) as [67]. This work was developed in fragments over the winter of 2016 and 2017.

5 Implementation to continuous gravitational wave searches

In chapter VI, I include other co-authored publications which implement the methods and procedures

developed in the previous chapters III–V. The articles included in the subsections of this chapter are self-contained original manuscripts as published by the American Physical Society, unlike chapters I–IV. The bibliography for each article is given at the end of each subsection⁴.

In subsection 1 [45], we present the most recent Einstein@Home all-sky search for CW in the low-frequency regime in advanced LIGO’s first observation run (O1) data. This search implemented the new clustering procedure (item IV.A) [66] as well as the upper-limit procedure (item V, VI) [67]. With the help of the new clustering procedure, we were able to reduce the number of follow-up candidates in the first stage of the search from 15.5 million to a mere 35,963. This is a significant improvement over the previous clustering procedure, as shown in chapter IV. In this search, no CW signal was confirmed and thus, upper limits are placed on the CW amplitude using the upper-limit procedure detailed in chapter VI.

In subsections 2 and 3 [11, 55], we present the recent Einstein@Home searches for CW in the mid-frequency regime in LIGO’s sixth science run (S6) data. This search did not recover any CW signal and it implemented the upper-limit procedure to quote the sensitivity of the search in LIGO1 data (before LIGO’s upgrade to advanced LIGO) [67]. Note that the subsection 2 contains the primary search [11] while the subsection 3 is a sub-threshold search on the same data. These articles (especially [11]) were developed in parallel with [68] and they share many common characteristics. For example, the estimation of disturbed regions in search frequency and the calculation of the expected loudest candidate in noise (item III.B in [11]), estimation of the average power spectral density and the exclusion of frequency disturbances from it (item IV in [11]), and the final upper-limit statements (item V and IV, V in [11] and [55] respectively) are a product of the collaborative work done by me, Sylvia Zhu, Maria Alessandra Papa and Heinz-Bernd Eggenstein in the year 2016.

⁴Note that the internal referencing within each subsection is independent of the cross-referencing of this thesis.

II Gravitational Wave transient signal emission via Ekman Pumping in Neutron Stars during post-glitch relaxation phase

Avneet Singh^{1,2,3,†,‡}

¹ Max-Planck-Institut für Gravitationsphysik, am Mühlenberg 1, 14476, Potsdam-Golm

² Max-Planck-Institut für Gravitationsphysik, Callinstraße 38, 30167, Hannover

³ Leibniz Universität Hannover, Welfengarten 1, 30167, Hannover

Abstract

Glitches in the rotational frequency of a spinning neutron star could be promising sources of gravitational wave signals lasting between a few μs to a few weeks. The emitted signals and their properties depend upon the internal properties of the neutron star. In neutron stars, the most important physical properties of the fluid core are the viscosity of the fluid, the stratification of flow in the equilibrium state and the adiabatic sound speed. Such models were previously studied by van Eysden and Melatos [73] and Bennett et al. [26] following simple assumptions on all contributing factors, in which the post-glitch relaxation phase could be driven by the well-known process of *Ekman pumping* [76, 17]. We explore the hydrodynamic properties of the flow of fluid during this phase following more relaxed assumptions on the stratification of flow and the pressure-density gradients within the neutron star than previously studied. We calculate the time-scales of duration as well as the amplitudes of the resulting gravitational wave signals, and we detail their dependence on the physical properties of the fluid core. We find that it is possible for the neutron star to emit gravitational wave signals in a wide range of decay time-scales and within the detection sensitivity of aLIGO for selected domains of physical parameters.

1 Introduction

Pulsar glitches are sudden fractional increases in the rotational velocity of a neutron star. Several pulsars, observed in radio, X-ray and γ -ray bands of the electromagnetic spectrum, have been repeatedly observed to glitch [35, 79, 46]. The fractional spin-up $\delta\Omega$ of the rotational velocity Ω of the neutron star lies in the range of $\frac{\delta\Omega}{\Omega} \in [O(10^{-11}), O(10^{-4})]$ [73, 46, 52].

Gravitational wave emission is typically associated with a non-zero derivative of the quadrupole moment stemming from accelerated flow of non-axisymmetrically distributed bulk of matter. It is possible that such non-axisymmetric motions are excited following a glitch; possible mechanisms for producing such non-axisymmetric motions, besides Ekman pumping, include bulk two-stream instabilities [21], surface two-stream instabilities [47], crust deformation and precession [40], meridional circulation and super-fluid turbulence driven by crust-core differential rotation [56], crust-core coupling via magnetic field [36], excitation of pulsation modes [62, 63, 64], and mutual friction in two-fluid model for superfluid core [23]. These mechanisms have been briefly reviewed by van Eysden and Melatos [73] and Bennett et al. [26]. In this paper, we solely consider the hydrodynamic properties of the fluid core following a glitch and concentrate on the mechanism of Ekman pumping.

In this work, we consider the hydrodynamic evolution the post-glitch relaxation phase via the mechanism of Ekman pumping, pioneered by Walin [76] and Abney and Epstein [17]. We extend the previous works on this by van Eysden and Melatos [73] and Bennett et al.

[26], where an initial non-axisymmetric perturbation introduced by the glitch induces *Ekman pumping* in the core of the star. Ekman pumping is briefly described as the induced flow of the bulk matter in the core when it is acted upon by a tangential force (in this case, Coriolis force) at its boundary i.e. the crust-core interface. In our case, the Coriolis force results from the differential rotation of the crust with respect to the bulk fluid, resulting from the glitch in the star's rotational velocity. This induced flow of the bulk matter could then have a time-varying quadrupole moment and lead to emission of gravitational waves. In this context, a glitch can lead to gravitational wave emission in two phases. Initially, a burst-type emission occurs during the fast spin-up of crust at time-scales of at most a few seconds [49]. Secondly, a decaying continuous-wave signal during the post-glitch relaxation phase is emitted on much longer time-scales. The initial non-axisymmetric motion of the bulk with respect to the crust in the second case is excited by the glitch. The resulting damped continuous-wave-like signal arises as the internal fluid dynamics evolve to set the bulk in co-rotation or a steady differential rotation with the crust, erasing the non-axisymmetric motions in the bulk [73, 26].

In this paper, we relax certain assumptions in more recent works [73, 26] on the stratification length and the adiabatic sound speed; we explore a regime of Ekman pumping where these quantities are allowed to vary across the star and study their effect on the emitted gravitational wave signal. This extends the parameter space and introduces more generality to the analysis.

We will keep other simplifying assumptions made in [17, 73], and analyze the system in a pure hydrodynamical sense, ignoring the two-stream dynamics, sidestep-

[†]avneet.singh@aei.mpg.de; [‡]avneet.singh@ligo.org

ping the crust-core interface, neglecting the effects of pinning and unpinning of quantum vortices, and disallowing the crust to precess, and ignoring the affects of magnetic field. In particular, the inclusion of magnetic field in the current model would make it analytically intractable. In the spirit of first tackling these two aspects separately i.e. magnetic field and Ekman pumping, this paper concentrates on the latter process only; such an approach has been extensively considered in the past [17, 73, 26]. Moreover, for analytic simplicity, we approximate our spherical neutron star to a fluid-filled rigid cylinder [26], as opposed to the choice of semi-rigidity [73]. The correctness of this choice will be explained in the next section. In nutshell, as a result of all these simplifications, a toy-model for a neutron star is studied for the possibility of emission of gravitational waves.

2 Hydrodynamics of the system

Let us consider a rotating neutron star of radius of order $O(L)$ with a solid crust around a compressible and viscous fluid with viscosity ν , pressure p and density ρ . We now approximate this spherical system with a rigid cylindrical container of height $2L$ and radius L rotating at an angular frequency of Ω along the z -axis (figure 1). We represent the glitch as a sudden perturbation in the angular velocity of magnitude $\delta\Omega$ along the z -axis. This geometric simplification doesn't lead to an order-of-magnitude change in the amplitude or duration of the emitted gravitational wave signal from Ekman pumping [74], and has extensively been used in majority of literature on neutron star modeling. Moreover, this reformulation to the cylindrical system leads to simpler analytic solutions.

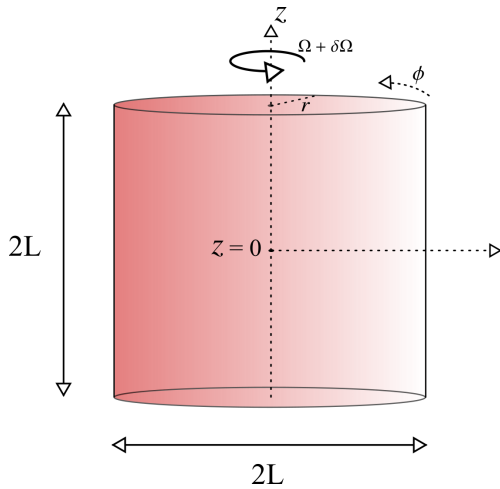


Figure 1: Idealized system

2.1 Governing equations

Our physical system is described by the velocity field \vec{v} , the pressure p and the density ρ of the fluid. The forces acting on fluid elements of the bulk volume are the viscous force, the Coriolis force, the centrifugal force, the compressible strain, pressure gradients and gravitational force. The Navier-Stokes equation, the conservation of mass equation, and the ‘energy equation’ (i.e. equation of state) govern our physical system. The Navier-Stokes equation for a fluid element in the rotating Lagrangian frame of the cylinder for a compressible fluid is given by

$$\frac{\partial \vec{v}}{\partial t} + \vec{v} \cdot \nabla \vec{v} + 2\vec{\Omega} \times \vec{v} = -\frac{1}{\rho} \nabla p + \nu \nabla^2 \vec{v} + \frac{\nu}{3} \nabla(\nabla \cdot \vec{v}) + \nabla[\Omega \times (\Omega \times r)] + \vec{g}, \quad (1)$$

where, \vec{v} is the fluid velocity and \vec{g} is the gravitational acceleration. The Navier-Stokes equation relates the restoring forces on a fluid element (written on the right-hand side: pressure gradients, viscous force, gravitational force, compressible strain, centrifugal force) to the impulsive change in momentum of the fluid element (written on the left-hand side: Coriolis force etc). We have ignored terms from the magnetic field of the neutron star as previously stated, restricting ourselves to a purely hydrodynamic analysis. The gravitational acceleration is taken to be of the following form:

$$\vec{g} = -\frac{z}{|z|} g \hat{z}. \quad (2)$$

This form for \vec{g} is unphysical since it is generated by a singular and planer mass distribution located at $z = 0$. However, such a choice is standard in neutron star literature [17, 73]; it is equivalent to a radial field for a sphere which compares well to numerical simulations comprising of more realistic mass distributions [54]. This assumption leads to symmetric flow across the mid-plane of the cylinder and we can restrict ourselves to $z \geq 0$.

The second governing equation is the ‘Continuity equation’ i.e. the conservation of mass equation

$$\frac{\partial \rho}{\partial t} + \nabla \cdot (\rho \vec{v}) = 0. \quad (3)$$

Lastly, we write the ‘energy equation’, i.e. the equation of state in terms of the adiabatic sound speed v_c (where, the sub-script S represents derivative taken at constant entropy) of the form

$$\left[\frac{\partial p}{\partial \rho} \right]_S = v_c^2, \quad (4)$$

[†]The adiabatic limit for an isolated neutron star allows us to drop the sub-script S in (4); more discussion in section 6.3.

which, in the adiabatic limit¹ and expressed in Lagrangian frame, takes the following form:

$$\left[\frac{\partial}{\partial t} + \vec{v} \cdot \nabla \right] \rho = \left[\frac{\partial}{\partial t} + \vec{v} \cdot \nabla \right] \frac{p}{v_c^2} \quad (5)$$

Note that we do not impose invariance of v_c in either space or time as previously done in [73, 26].

In addition, we scale our variables to dimensionless form by redefining them as, $r \rightarrow Lr$, $z \rightarrow Lz$, $\vec{v} \rightarrow (\delta\Omega)L\vec{v}$, $\rho \rightarrow \rho_0\rho$, $p \rightarrow \rho_0gLp$, $\nabla \rightarrow L^{-1}\nabla$, $t \rightarrow t_e t$; where we define ρ_0 as the equilibrium mass-density at $z = 0$, and t_e and the *Ekman number* E as,

$$t_e = E^{\frac{1}{2}}\Omega^{-1}, \text{ and } E = \frac{\nu}{L^2\Omega}. \quad (6)$$

One can then write the governing equations (1), (3) and (5) in the re-scaled form as

$$\begin{aligned} \epsilon F \left[E^{\frac{1}{2}} \frac{\partial \vec{v}}{\partial t} + \epsilon \vec{v} \cdot \nabla \vec{v} + 2\hat{e}_z \times \vec{v} \right] &= -\frac{1}{\rho} \nabla p - \vec{e}_z + \\ &\epsilon F E \left[\nabla^2 \vec{v} + \frac{1}{3} \nabla \{ \nabla \cdot \vec{v} \} \right] + F \nabla \left[\frac{1}{2} r^2 \right], \end{aligned} \quad (7)$$

$$E^{\frac{1}{2}} \frac{\partial \rho}{\partial t} + \epsilon \nabla \cdot (\rho \vec{v}) = 0, \quad (8)$$

$$E^{\frac{1}{2}} \frac{\partial [\rho \eta]}{\partial t} + \epsilon \vec{v} \cdot \nabla [\rho \eta] = K \left[E^{\frac{1}{2}} \frac{\partial p}{\partial t} + \epsilon \vec{v} \cdot \nabla p \right], \quad (9)$$

where η , the *Froude number* F , the maximum *scaled compressibility* K , and ϵ are defined as

$$\eta = \frac{v_c^2}{c^2}, \quad K = g \frac{L}{c^2}, \quad F = \Omega^2 \frac{L}{g}, \quad \epsilon = \frac{\delta\Omega}{\Omega}. \quad (10)$$

2.2 Orders of magnitude

Here, we list the physical constants and parameters introduced in the previous section, and their order-of-magnitude values in SI units for the interior of a neutron star from estimates on the expected and observed physical properties.

$$\begin{aligned} g &= O(10^{12}), \quad L = O(10^4), \quad \frac{\Omega}{2\pi} = O(1\text{Hz} - 10^2\text{Hz}), \\ E &\in [O(10^{-17}), O(10^{-7})], \quad \frac{v_c}{c} \in [O(10^{-2}), 1]. \end{aligned} \quad (11)$$

The viscosity ν of the fluid for a neutron star is currently unknown and widely debated. The associated value of Ekman number E also remains volatile. Yet, there are estimates on the value of E from results of heavy-ion collision experiments [73, 19, 48, 20, 42] and from theoretical calculations of neutron-neutron scattering in the superfluid limit [33, 50]. The results from such analysis lead to the wide range of possible values for E quoted

above in (11). The parameters listed in (10) then take the following values²

$$\begin{aligned} K &= O(10^{-1}), \quad F \in [O(10^{-9}), O(10^{-3})], \\ \epsilon &\in [O(10^{-11}), O(10^{-4})]. \end{aligned} \quad (12)$$

3 Solution

In this section, we solve to the governing equations given in the section 2.1.

3.1 Equilibrium solution

In equilibrium, due to the symmetry of the system across the $z = 0$ mid-plane, the flow is steady and axisymmetric, and the density and pressure are functions of z and r only. Since ϵ and F are quite small in their absolute magnitude, we can ignore the centrifugal term [17] in the re-scaled equations (7), (8) and (9). With this approximation, (7) reduces to

$$\frac{1}{\rho} \nabla p + \vec{e}_z = 0. \quad (13)$$

In order to solve the above equation, we need to make an assumption for either the mass-density or the pressure. We introduce the dimensionless parameter K_s , following [73], and assume the following:

$$\rho^{-1} (d\rho/dz) = -K_s(z). \quad (14)$$

The stratification length, z_s , is defined in terms of the dimensionless quantity K_s as $z_s = L K_s^{-1}$. The above expression defines a steady-state density profile of the system. The equilibrium pressure and density profiles are then given by solving (13) and (14) respectively, as

$$\rho_e(z) = e^{-\int_0^z K_s(z') dz'}, \quad (15)$$

$$p_e(z) = K_s^{-1}(z) e^{-\int_0^z K_s(z') dz'}. \quad (16)$$

Here, we have not assumed K_s to be a constant, as previously done in [73, 26]. The introduction of the form K_s is not trivial. In fact, the assumption of a certain form of K_s incorporates the nature of entropic or compositional gradients, which in turn incorporate the deviation of equilibrium state from an adiabatic state. We introduce *equilibrium sound speed* accordingly, given by $v_{\text{eq}}^2 = \frac{gL}{K_s(z)}$. We note that in the equilibrium state, gravity acts to vary density and pressure along the axis of the cylinder.

²We will use the values quoted in (11) and (12) when making order-of-magnitude estimates on the emitted gravitational wave signals.

3.2 Induced perturbations

Let us assume that a glitch induces perturbations in pressure, density and velocity fields of the internal bulk fluid of the neutron star and that the resultant bulk fluid flow may be non-axisymmetric. When such non-axisymmetric perturbations are induced, the density $\rho(r, \phi, z, t)$ and pressure $p(r, \phi, z, t)$ are functions of all spatial coordinates and time, as opposed to the case of stable equilibrium. In order to solve for the perturbed fluid motion, we treat the system ‘perturbatively’, given the small magnitude of ϵ . In the perturbative treatment, the density, pressure and the velocity field can be expanded as $\rho \rightarrow \rho + \epsilon \delta\rho$, and $p \rightarrow p + \epsilon \delta p$, where we have let the magnitude of δp and $\delta\rho$ run free and normalized it by ϵ . The velocity field, however, is written simply as $\vec{v} \rightarrow \delta\vec{v}$. We do not perturb η explicitly; the variation in η occurs naturally from variation in v_c . Now, ignoring all terms larger than $O(1)$ in ϵ , the set of three re-scaled governing equations (7), (8) and (9) reduce to

$$\begin{aligned} F \left[E^{\frac{1}{2}} \frac{\partial[\delta\vec{v}]}{\partial t} + 2\hat{e}_z \times [\delta\vec{v}] \right] &= -\frac{1}{\rho} \nabla[\delta p] - \frac{\delta\rho}{\rho} \hat{e}_z + \\ F E \left[\nabla^2[\delta\vec{v}] + \frac{1}{3} \nabla\{\nabla \cdot [\delta\vec{v}]\} \right] &+ F \frac{\delta\rho}{\rho} \nabla \left[\frac{1}{2} r^2 \right], \end{aligned} \quad (17)$$

$$E^{\frac{1}{2}} \frac{\partial[\delta\rho]}{\partial t} + \nabla \cdot (\rho \delta\vec{v}) = 0, \quad (18)$$

$$E^{\frac{1}{2}} \frac{\partial[\eta\delta\rho]}{\partial t} + \delta\vec{v} \cdot \nabla[\rho\eta] = K \left[E^{\frac{1}{2}} \frac{\partial[\delta p]}{\partial t} + \delta\vec{v} \cdot \nabla p \right]. \quad (19)$$

3.3 Method of multiple scales

In the perturbative treatment, we employ the *method of multiple scales* [73, 26, 76, 17]. The perturbations in the density, pressure and velocity field are expanded into scales of order E^0 , $E^{\frac{1}{2}}$ and E^1 , such that for density perturbations,

$$\delta\rho = \delta\rho^{(0)} + E^{\frac{1}{2}} \delta\rho^{(1)} + E^1 \delta\rho^{(2)}, \quad (20)$$

and for pressure perturbations,

$$\delta p = \delta p^{(0)} + E^{\frac{1}{2}} \delta p^{(1)} + E^1 \delta p^{(2)}, \quad (21)$$

and for velocity perturbations,

$$\delta\vec{v} = \delta\vec{v}^{(0)} + E^{\frac{1}{2}} \delta\vec{v}^{(1)} + E^1 \delta\vec{v}^{(2)}. \quad (22)$$

The idea behind the method of multiple scales is to separate sub-process that occur at time-scales in increments of $E^{\frac{1}{2}}$, and solve them individually.

One can now solve (17) for the the velocity field, its

radial, azimuthal and vertical components of $v_r^{(i)}$, $v_\phi^{(i)}$ and $v_z^{(i)}$, up to i th order in $E^{\frac{1}{2}}$,

$$\begin{aligned} F \left[E^{\frac{1}{2}} \frac{\partial\delta v_r}{\partial t} - 2\delta v_\phi \right] &= -\frac{\partial}{\partial r} \left[\frac{\delta p}{\rho} \right] + F E \times \\ &\left[\left\{ \nabla^2 - \frac{1}{r^2} \right\} \delta v_r - \frac{2}{r^2} \frac{\partial[\delta v_\phi]}{\partial\phi} + \frac{1}{3} \frac{\partial}{\partial r} [\nabla \cdot \delta\vec{v}] \right], \end{aligned} \quad (23)$$

$$\begin{aligned} F \left[E^{\frac{1}{2}} \frac{\partial\delta v_\phi}{\partial t} - 2\delta v_r \right] &= -\frac{1}{r} \frac{\partial}{\partial\phi} \left[\frac{\delta p}{\rho} \right] + F E \times \\ &\left[\left\{ \nabla^2 - \frac{1}{r^2} \right\} \delta v_\phi - \frac{2}{r^2} \frac{\partial[\delta v_r]}{\partial\phi} + \frac{1}{3r} \frac{\partial}{\partial\phi} [\nabla \cdot \delta\vec{v}] \right], \end{aligned} \quad (24)$$

$$\begin{aligned} F E^{\frac{1}{2}} \frac{\partial\delta v_z}{\partial t} &= -\frac{1}{\rho} \frac{\partial}{\partial z} \left[\frac{\delta p}{\rho} \right] - \frac{\delta\rho}{\rho} + F E \times \\ &\left[\nabla^2[\delta v_z] - \frac{1}{3} \frac{\partial}{\partial\phi} [\nabla \cdot \delta\vec{v}] \right]. \end{aligned} \quad (25)$$

Two additional relations are derived from the energy equation (19) and the continuity equation (18), and they are given by

$$E^{\frac{1}{2}} \frac{\partial}{\partial t} \left[\frac{\delta\rho}{\rho} \right] + \nabla \cdot \delta\vec{v} = K_s(z) \delta v_z, \quad (26)$$

and,

$$\eta(z) E^{\frac{1}{2}} \frac{\partial}{\partial t} \left[\frac{\delta\rho}{\rho} \right] = K E^{\frac{1}{2}} \frac{\partial}{\partial t} \left[\frac{\delta p}{\rho} \right] + F N^2(z) \delta v_z, \quad (27)$$

where, we have introduced $N(z)$ - the redefined *Brunt-Väisälä frequency*³,

$$N^2(z) = \frac{[\eta K_s - \partial_z \eta] - K}{F} = \frac{K}{F} \left[\frac{v_c^2}{v_{\text{eq}}^2} - 1 \right] - \frac{\partial_z \eta}{F}. \quad (28)$$

We can reformulate (28) by introducing $K'_s(z)$ as

$$K'_s(z) = \eta K_s - \partial_z \eta = K \frac{v_c^2}{v_{\text{eq}}^2} - \partial_z \eta, \quad (29)$$

such that (28) takes the form of

$$N^2(z) = \frac{K'_s(z) - K}{F}. \quad (30)$$

Here, η and K_s are allowed to vary with z only. In the set of equations (23)-(27), the terms on different $O(E^0)$, $O(E^{\frac{1}{2}})$ and $O(E^1)$ scales are reducible at each order. Moreover, we can distinguish and deduce the time-scales at which several processes contribute to the overall perturbed flow of the bulk matter, such as the formation of viscous *Rayleigh shear layer* layer, followed by partial spin-up of the interior fluid via Ekman pumping, followed by complete spin-up of the interior on longer time-scales. These processes have been discussed briefly by van Eysden and Melatos [73] and in

³Note that the Brunt-Väisälä frequency N is a well-known quantity in fluid mechanics and atmospheric sciences. It is a measure of the buoyant force experienced by a fluid element when displaced from equilibrium.

much greater detail by Abney and Epstein [17]. We will also discuss them in the later section(s). These times scales are $E^0\Omega^{-1}$, $E^{-\frac{1}{2}}\Omega^{-1}$ and $E^{-1}\Omega^{-1}$. One can now isolate solutions at these different scales since they are effectively independent due to very small magnitude of the Ekman number E .

3.4 $O(E^0)$ solutions

On the order of E^0 , the expressions (23)-(27) yield

$$\delta v_r^{(0)} = -\frac{1}{2Fr} \frac{\partial}{\partial \phi} \left[\frac{\delta p^{(0)}}{\rho} \right], \quad (31)$$

$$\delta v_\phi^{(0)} = \frac{1}{2F} \frac{\partial}{\partial r} \left[\frac{\delta p^{(0)}}{\rho} \right], \quad (32)$$

$$\delta v_z^{(0)} = 0, \quad (33)$$

$$\delta \rho^{(0)} = -\frac{\partial[\delta p^{(0)}]}{\partial z}, \text{ and} \quad (34)$$

$$\nabla \cdot \delta \vec{v}^{(0)} = 0. \quad (35)$$

Note that the solutions on the order E^0 are exactly the ones previously achieved in [73, 26, 76, 17]. These solutions, given by (31)-(35), correspond to the formation of a viscous boundary layer (also referred to as the Rayleigh shear layer) on the top and bottom faces of the cylinder on a time-scale $O(E^0\Omega^{-1})$. Within this viscous boundary layer, the flow moves radially outward due to the gradient in the azimuthal velocity and the resulting imbalance between centrifugal and pressure gradient forces [76, 17].

3.5 $O(E^{1/2})$ solutions

In solving for the $O(E^{\frac{1}{2}})$ solutions, we assume that

$$\frac{\delta p^{(0)}}{p} \gg \frac{\delta p^{(1)}}{p} \sim 0, \quad \frac{\delta \rho^{(0)}}{\rho} \gg \frac{\delta \rho^{(1)}}{\rho} \sim 0 \quad (36)$$

The $O(E^{\frac{1}{2}})$ terms in (23)-(27) yield

$$\delta v_r^{(1)} = \frac{1}{4F} \frac{\partial \chi}{\partial r}, \quad (37)$$

$$\delta v_\phi^{(1)} = \frac{1}{4Fr} \frac{\partial \chi}{\partial \phi}, \quad (38)$$

$$\delta v_z^{(1)} = \frac{\eta(z)}{FN^2(z)} \frac{\partial \chi}{\partial z} + \left[\frac{-\partial_z \eta}{FN^2(z)} - 1 \right] \chi, \text{ and} \quad (39)$$

$$\frac{\partial}{\partial t} \left[\frac{\delta \rho^{(0)}}{\rho} \right] + \nabla \cdot \delta \vec{v}^{(1)} = \mathcal{K}_s(z) \delta v_z^{(1)}, \quad (40)$$

where, we have defined χ as

$$\chi = -\frac{\partial}{\partial t} \left[\frac{\delta p^{(0)}}{\rho} \right] \sim O(E^0). \quad (41)$$

These set of solutions represent the process of Ekman pumping – the flow in the viscous boundary layer, given by (31)-(35), sets a secondary motion in the interior⁴, by which the fluid is pulled into the viscous boundary layer from the interior to replace the radial outward flow in it [76, 17]. Note that the results on the order $O(E^{\frac{1}{2}})$, given by (37)-(40), are different from those in previous works with respect to the expression for $\delta v_z^{(1)}$ (39) and the continuity equation (40). This affects all future calculations and results.

3.6 More on the scale-based solutions

We will skip the discussion of the $O(E^1)$ solutions since they occur on much larger time-scales of $O(E^{-1}\Omega^{-1})$. These $O(E^{-1}\Omega^{-1})$ solutions correspond to the eventual ‘spin-up’ of the entire interior bulk matter when the interior bulk sets in complete co-rotation or steady differential co-rotation with the crust, as previously mentioned [76, 17]. This sub-process on much larger time-scales is irrelevant to our discussion since it does not contribute to the gravitational wave emission. To recap the scale-based solutions, the sudden spin-up of the rotating cylinder leads to the formation of a viscous boundary layer at the top and bottom faces of the rotating cylinder. This viscous layer forms on a time-scale of $O(E^0\Omega^{-1})$. The velocity field within this layer pushes the fluid radially outward across the layer, given by (31)-(33). This $O(E^0)$ flow excites Ekman pumping in the interior on a time-scale of $O(E^{-\frac{1}{2}}\Omega^{-1})$, pushing the fluid radially inward and vertically into the boundary layer, given by (37)-(39). Note that the vertical velocity of the $O(E^{-\frac{1}{2}})$ flow, given by (39), is non-zero. This vertical velocity is constrained by the continuity law applied to the viscous layer [17, 73, 76, 26], such that

$$\delta v_z|_{z=\pm 1} = \pm \frac{1}{2} E^{\frac{1}{2}} [\nabla \times (\delta \vec{v} - \vec{v}_B)]_z|_{z=\pm 1}. \quad (42)$$

where, \vec{v}_B is the dimensionless velocity of the boundary layer in the frame rotating at Ω . In this rotating frame, $\vec{v}_B = r\vec{e}_\phi$ [26]. Note that we have assumed that the boundary layer is rigidly co-rotating with the cylinder with angular frequency $\Omega + \delta\Omega$ without any slippage. The above expression (42) describes the continuity of the vertical flow across and inside the viscous boundary layer as a function of flow just outside the layer. This process occurs on a time-scale of $O(E^{\frac{1}{2}})$, which is reflected in the magnitude term $E^{\frac{1}{2}}$ in (42). We also find that the process of Ekman pumping continues until the local velocity field $\delta \vec{v}$ becomes equal to the boundary velocity \vec{v}_B . This is followed by spin-up of the entire interior on much larger time-scales of $O(E^{-1}\Omega^{-1})$. Furthermore, the magnitude term of $E^{\frac{1}{2}}$ can be understood

⁴The important development is the excitation of flow in z -direction in the boundary layer, given by (39).

in terms of scaling arguments. The viscous term in the dimensionless Navier-Stokes equation (7) is given by

$$FE\nabla^2 \sim FE \left[\frac{1}{\delta L} \right]^2 \sim O(F), \quad (43)$$

where, δL is the scale of the thickness of the viscous boundary layer. Clearly, from the relation given above, $\delta L = O(E^{\frac{1}{2}})$; also see the detailed discussion by Abney and Epstein [17] on this subject. The characteristic thickness of the boundary layer and the time-scale of Ekman pumping are both attributable to the magnitude term $E^{\frac{1}{2}}$ in (42).

3.7 The characteristic equation

Considering the $O(E^0)$ and $O(E^{\frac{1}{2}})$ solutions obtained in the previous section(s), we combine them to write the following differential equation with terms up to order $O(E^{\frac{1}{2}})$ and $O(F^0)$:

$$\frac{1}{r} \frac{\partial}{\partial r} \left[r \frac{\partial \chi}{\partial r} \right] + \frac{1}{r^2} \frac{\partial^2 \chi}{\partial \phi^2} - \left[\frac{4\eta(z)K_s(z)}{N^2(z)} \right] \frac{\partial \chi}{\partial z} + \frac{4\eta(z)}{N^2(z)} \frac{\partial^2 \chi}{\partial z^2} = \left[\frac{\partial_z \eta - \partial_z^2 \eta}{N^2(z)} \right] \chi. \quad (44)$$

The above characteristic equation can be solved via the standard *method of separation of variables* to yield

$$\chi(r, \phi, z, t) = \sum_{\alpha=0}^{\infty} \sum_{\gamma=1}^{\infty} J_{\alpha}(\lambda_{\alpha\gamma} r) \left[\frac{A_{\alpha\gamma}(t) - iB_{\alpha\gamma}(t)}{2} \times e^{i\alpha\phi} + \frac{A_{\alpha\gamma}(t) + iB_{\alpha\gamma}(t)}{2} e^{-i\alpha\phi} \right] Z_{\alpha\gamma}(z), \quad (45)$$

where, $\lambda_{\alpha\gamma}$ is the γ th zero of the α th Bessel mode (J_{α}), and $A_{\alpha\gamma}(t)$, $B_{\alpha\gamma}(t)$ are the associated *Bessel-Fourier coefficients* which depend upon the assumed steady-state solution, which we will see shortly. The flow is constrained by a trivial boundary condition which requires no penetration through the side walls, i.e. $\delta v_r^{(0)}|_{r=1} = 0$. This simply translates to $\partial_{\phi} \chi|_{r=1} = 0$ for $\forall \phi$, via (31). Moreover, $Z_{\alpha\gamma}(z)$ is the solution to the following differential equation:

$$\frac{4\eta(z)}{N^2(z)} \frac{\partial^2 Z_{\alpha\gamma}(z)}{\partial z^2} - \frac{4\eta(z)K_s(z)}{N^2(z)} \frac{\partial Z_{\alpha\gamma}(z)}{\partial z} - \left[\frac{\partial_z \eta - \partial_z^2 \eta}{N^2(z)} + \lambda_{\alpha\gamma}^2 \right] Z_{\alpha\gamma}(z) = 0, \quad (46)$$

which depends on N^2 , which in turn depends exclusively on K_s and η . When K_s (or, v_{eq}) and η (or, v_c) are constants, $Z_{\alpha\gamma}(z)$ takes the simple form given below,

$$Z_{\alpha\gamma}(z) = \frac{(FN^2 - \mathcal{B}_-)e^{\mathcal{B}_+z} - (FN^2 - \mathcal{B}_+)e^{\mathcal{B}_-z}}{(FN^2 - \mathcal{B}_-)e^{\mathcal{B}_+} - (FN^2 - \mathcal{B}_+)e^{\mathcal{B}_-}}, \quad (47)$$

where,

$$\mathcal{B}_{\pm} = \frac{1}{2} [K_s \pm (K_s^2 + \eta^{-1}N^2\lambda_{\alpha\gamma}^2)^{\frac{1}{2}}]. \quad (48)$$

It must be noted that, following [73], we have temporally and seemingly arbitrarily⁵ assumed $Z_{\alpha\gamma}(1) = 1$. Moreover, we also assume $v_z|_{z=0} \sim v_z^{(1)}|_{z=0} = 0$ to ensure symmetric flow across the $z = 0$ plane⁶, given the relation prescribed in (42). This is precisely the result obtained by van Eysden and Melatos [73] and Bennett et al. [26].

3.8 Temporal evolution

The temporal evolution of Ekman pumping is governed by the boundary condition given in (42) [73, 17]. Taking the first-order derivative of (42) and using the results from the $O(E^0)$ and $O(E^{\frac{1}{2}})$ solutions, we find the exponentially decaying time-dependence⁷ of χ as,

$$\chi(r, \phi, z, t) = \sum_{\alpha=0}^{\infty} \sum_{\gamma=1}^{\infty} J_{\alpha}(\lambda_{\alpha\gamma} r) \left[\frac{A_{\alpha\gamma} - iB_{\alpha\gamma}}{2} \times e^{i\alpha\phi} + \frac{A_{\alpha\gamma} + iB_{\alpha\gamma}}{2} e^{-i\alpha\phi} \right] Z_{\alpha\gamma}(z) e^{-\omega_{\alpha\gamma} t}, \quad (49)$$

where, momentarily assuming $Z_{\alpha\gamma}(1)$ to be an arbitrary value that we will define shortly, we get

$$\omega_{\alpha\gamma} = \frac{1}{4F} \lambda_{\alpha\gamma}^2 Z_{\alpha\gamma}(1) \left[\frac{\eta(1)}{FN^2(1)} \frac{\partial Z_{\alpha\gamma}}{\partial z} \Big|_{z=1} + \left\{ \frac{-\partial_z \eta|_{z=1}}{FN^2(1)} - 1 \right\} Z_{\alpha\gamma}(1) \right]^{-1}. \quad (50)$$

Note that for the simple case of $K_s(z)$, $\eta \sim$ constant and $Z_{\alpha\gamma}(1) = 1$, (50) reduces to

$$\omega_{\alpha\gamma} = \frac{\lambda_{\alpha\gamma}^2 [(FN^2 - \mathcal{B}_-)e^{\mathcal{B}_+} - (FN^2 - \mathcal{B}_+)e^{\mathcal{B}_-}]}{(4FK + \lambda_{\alpha\gamma}^2)(e^{\mathcal{B}_+} - e^{\mathcal{B}_-})}. \quad (51)$$

Further, given the explicit dependence of χ on time, we integrate (49) over $t \in [t, \infty)$ and get

$$\frac{\delta p^{(0)}(r, \phi, z, t)}{\rho(z)} = \frac{\delta p_{t \rightarrow \infty}^{(0)}(r, \phi, z)}{\rho(z)} + \sum_{\alpha=0}^{\infty} \sum_{\gamma=1}^{\infty} \omega_{\alpha\gamma}^{-1} \times J_{\alpha}(\lambda_{\alpha\gamma} r) [A_{\alpha\gamma} \cos(\alpha\phi) + B_{\alpha\gamma} \sin(\alpha\phi)] \times Z_{\alpha\gamma}(z) e^{-\omega_{\alpha\gamma} t}, \quad (52)$$

where, the first term on the right-hand side is the constant of integration evaluated at $t \rightarrow \infty$, i.e. the steady-state pressure profile of the spun-up cylinder. The relation given in (52) encodes the variation of pressure perturbations up to the leading order in magnitude as a function of time.

⁵The function $Z_{\alpha\gamma}(z)$ must be explicitly re-normalised to lie in the range $[0, 1]$, since (41) dictates that χ – as a dimensionless variable – must be at most of the order $O(E^0) \sim 1$. This requires $Z_{\alpha\gamma}(z)$ to be of the same order in magnitude.

⁶The boundary condition on axial flow, i.e. setting $v_z|_{z=0} \sim v_z^{(1)}|_{z=0} = 0$ in (39), is equivalent to specifying $Z_{\alpha\gamma}(z)$ at $z = 0$.

⁷Refer to section A.1 in Appendix for details.

3.9 Initial and final conditions

We are left with one intrinsic degree of freedom in our model in form of initial and final conditions in time, i.e. state of perturbations immediately following the glitch at $t = 0$ and when Ekman pumping stops as $t \rightarrow \infty$, respectively. In principle, we only require one boundary condition in time – once $A_{\alpha\gamma}$, $B_{\alpha\gamma}$ are known – since the state of modes at $t \rightarrow \infty$ is coupled to their state at $t = 0$ by the relation (52), and vice-versa. In this case, however, we require both the initial and final conditions in time to calculate $A_{\alpha\gamma}$, $B_{\alpha\gamma}$ since they are unknown. For example, two of the most general choices are: **a)** one can assume a scenario where the perturbations modes continuously grow from an axisymmetric state in the post-glitch phase at $t = 0$ and reach a steady non-axisymmetric state as $t \rightarrow \infty$, and remain in that state. This leads to emission of gravitational waves even in the steady state at $t \rightarrow \infty$, and is somewhat unphysical. In fact, this equates to the scenario of ‘semi-rigidity’, where the top and bottom faces of the cylinder rotate differentially at $t \rightarrow \infty$, potentially causing the crust to crack [73]. On the contrary, **b)** an alternative scenario is when the perturbation modes are instantaneously excited at $t = 0$ and eventually decay as $t \rightarrow \infty$, which is more physical than the former choice. This choice disallows for any residual non-axisymmetry in the bulk, ensures zero residual steady-state emission, and also incorporates the feature of rigidity between the two faces of the cylinder [26]. Both these possibilities are encoded our choice of assumed boundary conditions at $t = 0$ and $t \rightarrow \infty$. Hence, we assume the more physical set of initial and final conditions where the modes originate arbitrarily and instantaneously at $t = 0$, and decay from some unknown initial value δP_0 to a symmetric steady-state δP_∞ as $t \rightarrow \infty$ according to (52). Note that the steady state solution at $t \rightarrow \infty$ is an axisymmetric state with no angular or z -dependence but only radial dependence, given by $\delta P_\infty = r^2$ in dimensionless form [26]. This axisymmetric state doesn’t lead to any gravitational wave emission, as previously stated.

Finally, in order to calculate $A_{\alpha\gamma}$, $B_{\alpha\gamma}$, we write

$$\delta P_0 = \delta P_\infty + \sum_{\alpha=0}^{\infty} \sum_{\gamma=1}^{\infty} \omega_{\alpha\gamma}^{-1} J_\alpha(\lambda_{\alpha\gamma} r) [A_{\alpha\gamma} \cos(\alpha\phi) + B_{\alpha\gamma} \times \sin(\alpha\phi)] Z_{\alpha\gamma}(z) = \sum_{\alpha=0}^{\infty} C_\alpha r^\alpha (r^2 - 1) \cos(\alpha\phi) Z_{\alpha\gamma}(z), \quad (53)$$

where, wherever suitable from this point onward, we will abbreviate for simplicity,

$$\delta P_{t'} \equiv \frac{\delta p_{t \rightarrow t'}^{(0)}(r, \phi, z)}{\rho(z)}.$$

The assumed form of the initial arbitrary perturbations δP_0 in (53) is a sum of non-axisymmetric modes sat-

isfying the boundary conditions [26]. C_α are the relative weights of modes with respect to the loudest mode, excited at $t = 0$, and they will be set equal to 1 in the calculations in section 4. Note that any assumed form of δP_0 must be constrained by the boundary conditions in space, i.e. no penetration allowed across the side walls, and be a solution to the Navier-Stokes equation by satisfying the relations in (17)-(19). Our assumption of δP_0 guarantees the decay of all modes at $t \rightarrow \infty$, while it also ensures that the flow vanishes at the lateral surface at $r = L$. We have assumed trivial z -dependence and ϕ -dependence in (53) for simplicity [73, 26], without potentially corrupting the generality of the solutions. The associated Bessel-Fourier coefficients $A_{\alpha\gamma}$ and $B_{\alpha\gamma}$ can now be calculated⁸ as an implicit function of z as follows,

$$A_{\alpha\gamma} = \frac{2\omega_{\alpha\gamma}}{\pi J_{\alpha+1}^2(\lambda_{\alpha\gamma})} \int_0^{2\pi} d\phi \int_0^1 dz \int_0^1 r dr \times J_\alpha(\lambda_{\alpha\gamma} r) \cos(\alpha\phi) [\delta P_0 - \delta P_\infty] Z_{\alpha\gamma}^{-1}(z) = \frac{2C_\alpha \omega_{\alpha\gamma}}{J_{\alpha+1}^2(\lambda_{\alpha\gamma})} \int_0^1 dr r^{\alpha+1} (r^2 - 1) J_\alpha(\lambda_{\alpha\gamma} r), \quad (54)$$

and,

$$B_{\alpha\gamma} = \frac{2\omega_{\alpha\gamma}}{\pi J_{\alpha+1}^2(\lambda_{\alpha\gamma})} \int_0^{2\pi} d\phi \int_0^1 dz \int_0^1 r dr \times J_\alpha(\lambda_{\alpha\gamma} r) \sin(\alpha\phi) [\delta P_0 - \delta P_\infty] Z_{\alpha\gamma}^{-1}(z) = 0. \quad (55)$$

In principle, the Bessel-Fourier coefficients may not be constants. In fact, they could be functions of ϕ and z depending on the chosen initial conditions in (53). However, since we chose trivial dependence on ϕ and z in our assumed initial conditions in (53), $A_{\alpha\gamma}$ and $B_{\alpha\gamma}$ remain constant. The first few values of $A_{\alpha\gamma}$ are: $A_{11} = -0.706 \omega_{11}$, $A_{21} = -0.521 \omega_{21}$, $A_{12} = 0.154 \omega_{12}$, and $A_{22} = 0.148 \omega_{22}$.

3.10 Final solutions

We restore the dimensions and calculate the final velocity, density, and pressure fields in the inertial rest frame instead of the rotating frame. The density profile in the inertial frame is given by

$$\rho(r, \phi, z, t) = \rho_0 \rho_e(z/L) + \rho_0 \frac{(\delta\Omega)\Omega L}{g} \times \sum_{\alpha=0}^{\infty} \sum_{\gamma=1}^{\infty} \omega_{\alpha\gamma}^{-1} C_\alpha A_{\alpha\gamma} J_\alpha\left(\frac{\lambda_{\alpha\gamma} r}{L}\right) \cos[\alpha(\phi - \Omega t)] \times \quad (56)$$

$$\partial_z [-L Z_{\alpha\gamma}(z/L) \rho_e(z/L)] e^{-E^{\frac{1}{2}} \omega_{\alpha\gamma} \Omega t},$$

whereas, from (34),

$$\delta p_{t \rightarrow 0}^{(0)}(r, \phi, z) = -\partial_z [\rho(z) \delta P_0] = - \left[\sum_{\alpha=0}^{\infty} C_\alpha r^\alpha (r^2 - 1) \cos(\alpha\phi) \right] \frac{\partial[\rho(z)]}{\partial z}. \quad (57)$$

⁸Refer to section A.2 in Appendix for details

$\delta v_r^{(0)}(r, \phi, z, t \rightarrow 0)$ and $\delta v_\phi^{(0)}(r, \phi, z, t \rightarrow 0)$ can be similarly calculated from (31) and (32) respectively. The pressure profile, and the velocity field up to order $O(E^{\frac{1}{2}})$ are given by,

$$p(r, \phi, z, t) = \rho_0 g L p_e(z/L) + \left[\rho_0 (\delta\Omega) \Omega L^2 \sum_{\alpha=0}^{\infty} \sum_{\gamma=1}^{\infty} \omega_{\alpha\gamma}^{-1} C_\alpha A_{\alpha\gamma} J_\alpha \left(\frac{\lambda_{\alpha\gamma} r}{L} \right) Z_{\alpha\gamma}(z/L) \times \cos[\alpha(\phi - \Omega t)] \rho_e(z/L) e^{-E^{\frac{1}{2}} \omega_{\alpha\gamma} \Omega t} \right], \quad (58)$$

$$\delta v_r \sim \delta v_r^{(0)}(r, \phi, z, t) = \frac{1}{2} (\delta\Omega) L^2 \sum_{\alpha=0}^{\infty} \sum_{\gamma=1}^{\infty} \frac{\alpha}{r} \omega_{\alpha\gamma}^{-1} C_\alpha \times A_{\alpha\gamma} J_\alpha \left(\frac{\lambda_{\alpha\gamma} r}{L} \right) \cos[\alpha(\phi - \Omega t)] Z_{\alpha\gamma}(z/L) e^{-E^{\frac{1}{2}} \omega_{\alpha\gamma} \Omega t}, \quad (59)$$

$$\delta v_\phi \sim \delta v_\phi^{(0)}(r, \phi, z, t) = \Omega r + \frac{1}{2} (\delta\Omega) L \sum_{\alpha=0}^{\infty} \sum_{\gamma=1}^{\infty} \omega_{\alpha\gamma}^{-1} \times C_\alpha A_{\alpha\gamma} \lambda_{\alpha\gamma} \partial_r \left[L J_\alpha \left(\frac{\lambda_{\alpha\gamma} r}{L} \right) \right] \cos[\alpha(\phi - \Omega t)] \times Z_{\alpha\gamma}(z/L) e^{-E^{\frac{1}{2}} \omega_{\alpha\gamma} \Omega t}, \quad (60)$$

and⁹,

$$\delta v_z \sim v_z^{(1)}(r, \phi, z, t) = \frac{1}{\text{FN}^2(z)} \frac{\partial \chi}{\partial z} - \chi = O(E^{\frac{1}{2}}) \quad (\text{in dimensionless units}); \quad (61)$$

4 Gravitational wave emission

In this section, we describe the gravitational wave emission from mass-quadrupole and current-quadrupole moments of the non-axisymmetric flow derived in section 3.

4.1 Gravitational wave emission via mass-quadrupole

The density, pressure and velocity fields calculated in the previous section lead to gravitational wave emission if the mass distribution and fluid flow are non-axisymmetric in nature. Gravitational wave emission is attributable to a non-axisymmetric distribution of mass that has a non-zero mass-quadrupole moment with at least second-order non-vanishing time-derivative. We derive the gravitational wave emission for the leading order quadrupole term ($\alpha = 2$) straightaway¹⁰ for the + and \times polarizations for a *polar observer* – for an observer located at a distance d_s along the axis of rotation

of the neutron star,

$$h_+^{\text{MP}}(t) = h_0^{\text{M}} \sum_{\gamma=1}^{\infty} \kappa_{2\gamma} \left[-4\omega_{2\gamma} E^{\frac{1}{2}} \sin(2\Omega t) + (4 - E\omega_{2\gamma}^2) \cos(2\Omega t) \right] e^{-E^{\frac{1}{2}} \omega_{2\gamma} \Omega t}, \quad (62)$$

$$h_\times^{\text{MP}}(t) = h_0^{\text{M}} \sum_{\gamma=1}^{\infty} \kappa_{2\gamma} \left[-4\omega_{2\gamma} E^{\frac{1}{2}} \cos(2\Omega t) - (4 - E\omega_{2\gamma}^2) \sin(2\Omega t) \right] e^{-E^{\frac{1}{2}} \omega_{2\gamma} \Omega t}, \quad (63)$$

where the full expression of $\kappa_{\alpha\gamma}$ is too lengthy to quote here and is given in section A.5 in Appendix and C_α are set to 1. The characteristic dimensionless strain h_0 , and $t_{\alpha\gamma}$ – the relaxation time-scale for the $\{\alpha, \gamma\}$ th mode – are given by,

$$h_0^{\text{M}} = \pi \rho_0 \Omega^4 L^6 \epsilon \frac{G}{c^4 d_{\text{sg}}} \quad (64)$$

$$t_{\alpha\gamma} = E^{-\frac{1}{2}} \Omega^{-1} \omega_{\alpha\gamma}^{-1} \quad (65)$$

where, $\kappa_{2\gamma}$ and h_0^{M} are both constant quantities. We transform the expressions (62)-(63) for time-series amplitudes to the more useful Fourier space for a polar observer as follows¹¹:

$$|h_+^{\text{MP}}(\omega)|^2 = h_0^{\text{M}2} \sum_{\gamma=1}^{\infty} |\kappa_{2\gamma}|^2 \left\{ \left[t_{2\gamma}^{-2} (4 + t_{2\gamma}^{-2} \Omega^{-2})^2 + \omega^2 (4 - t_{2\gamma}^{-2} \Omega^{-2})^2 \right] \left[(4\Omega^2 + t_{2\gamma}^{-2} - \omega^2)^2 + (2\omega t_{2\gamma}^{-1})^2 \right]^{-1} \right\}, \quad (66)$$

$$|h_\times^{\text{MP}}(\omega)|^2 = h_0^{\text{M}2} \sum_{\gamma=1}^{\infty} |\kappa_{2\gamma}|^2 \left\{ \left[4\Omega^2 (4 + t_{2\gamma}^{-2} \Omega^{-2})^2 + 16\omega^2 t_{2\gamma}^{-2} \Omega^{-2} \right] \left[(4\Omega^2 + t_{2\gamma}^{-2} - \omega^2)^2 + (2\omega t_{2\gamma}^{-1})^2 \right]^{-1} \right\}. \quad (67)$$

Clearly, $|h_+^{\text{MP}}(\omega)|$ and $|h_\times^{\text{MP}}(\omega)|$ exhibit resonance at $\omega_{\text{R}}^2 = 4\Omega^2 + t_{2\gamma}^{-2}$. A similar calculation can be made for an *equatorial observer*, and the corresponding results are given by,

$$h_+^{\text{ME}}(t) = \frac{1}{2} h_0^{\text{M}} \sum_{\gamma=1}^{\infty} \kappa_{2\gamma} \left[-4\omega_{2\gamma} E^{\frac{1}{2}} \sin(2\Omega t) + (4 - E\omega_{2\gamma}^2) \cos(2\Omega t) \right] e^{-E^{\frac{1}{2}} \omega_{2\gamma} \Omega t}, \quad (68)$$

⁹We have left the expression in condensed form since the contribution is of the order $O(E^{\frac{1}{2}})$ only, which is lower than the magnitudes we want to explore.

¹⁰Refer to section A.3 in Appendix for details of the calculation.

¹¹ δ_{D} is the Kronecker Delta function with units of Hz^{-1} .

$$h_{\times}^{\text{ME}}(t) = 2h_0^{\text{M}} \sum_{\gamma=1}^{\infty} \kappa_{1\gamma} \left[2\omega_{1\gamma} E^{\frac{1}{2}} \cos(\Omega t) + (1 - E\omega_{1\gamma}^2) \sin(\Omega t) \right] e^{-E^{\frac{1}{2}}\omega_{1\gamma}\Omega t}. \quad (69)$$

It is important to note the change of oscillating frequency for the \times polarization from 2Ω in case of a polar observer to Ω in case of an equatorial observer. Further, additional 1γ modes are seen by an equatorial observer, besides the 2γ modes that appear in the emission spectrum. In Fourier space for an equatorial observer, we have

$$|h_{+}^{\text{ME}}(\omega)|^2 = \frac{1}{4} h_0^{\text{M}2} \sum_{\gamma=1}^{\infty} |\kappa_{2\gamma}|^2 \left\{ \left[t_{2\gamma}^{-2} (4 + t_{2\gamma}^{-2} \Omega^{-2})^2 + \omega^2 (4 - t_{2\gamma}^{-2} \Omega^{-2})^2 \right] \left[(4\Omega^2 + t_{2\gamma}^{-2} - \omega^2)^2 + (2\omega t_{2\gamma}^{-1})^2 \right]^{-1} \right\}, \quad (70)$$

$$|h_{\times}^{\text{ME}}(\omega)|^2 = 4h_0^{\text{M}2} \sum_{\gamma=1}^{\infty} |\kappa_{1\gamma}|^2 \left\{ \left[\Omega^2 (1 + t_{1\gamma}^{-2} \Omega^{-2})^2 + \right. \right.$$

$$\left. 4\omega^2 t_{1\gamma}^{-2} \Omega^{-2} \right] \left[(\Omega^2 + t_{1\gamma}^{-2} - \omega^2)^2 + (2\omega t_{1\gamma}^{-1})^2 \right]^{-1} \Big\}, \quad (71)$$

In this case, $|h_{+}^{\text{ME}}(\omega)|$ exhibits resonance at $\omega_{\text{R}}^2 = 4\Omega^2 + t_{2\gamma}^{-2}$, while $|h_{\times}^{\text{ME}}(\omega)|$ exhibits resonance at $\omega_{\text{R}}^2 = \Omega^2 + t_{1\gamma}^{-2}$. It is worth noting that the factors $\kappa_{1\gamma}$, $\kappa_{2\gamma}$ decrease in magnitude with increasing index γ , and we can truncate the above expressions at leading order $\gamma = 1$. The maximum order-of-magnitude value of the amplitude of the emitted gravitational waves for both polarizations at a given frequency ω then depends strongly on the characteristic magnitude h_0^{M} and its amplification by the frequency terms in the Fourier transforms. There also exists a weak dependency on the pre-factors $|\kappa_{1\gamma}|$ and $|\kappa_{2\gamma}|$ ¹².

In figure 2 and figure 3, we plot the frequency characteristics¹³ of the emitted signal amplitudes for $|h_{+}^{\text{ME}}(\omega)|$, $|h_{\times}^{\text{ME}}(\omega)|$, $|h_{+}^{\text{CE}}(\omega)|$ and $|h_{\times}^{\text{CE}}(\omega)|$.

4.2 Gravitational wave emission via current-quadrupole

Gravitational wave emission, as traditionally understood, from mass-quadrupole occurs when the associated oscillating mass-quadrupole moment excites gravitational waves. However, time-variation in the intrinsic mass-distribution (also known as the *mass-currents*) of the bulk matter could also lead to gravitational wave radiation through ‘current-quadrupole’ contribution [70, 26]. This effect is a subset of the *gravitomagnetic effects* – the electromagnetic equivalent in gravitation. Similar to the case of electromagnetism, where electric charges and current multipoles emit electromagnetic radiation, time-varying mass-current multipoles also emit gravitational wave radiation, besides the well-known emission from mass-quadrupole moment. We straightaway produce the expressions for the $+$ and \times polarization following Thorne [70], Melatos and Peralta [51] and Bennett et al. [26] for a polar observer as follows¹⁴,

$$h_{+}^{\text{CP}}(t) = h_0^{\text{C}} \sum_{\gamma=1}^{\infty} V_{2\gamma} \left[-4t_{2\gamma}^{-1} \Omega^{-1} \cos(2\Omega t) - (4 - t_{2\gamma}^{-2} \Omega^{-2}) \sin(2\Omega t) \right] e^{-t_{2\gamma}^{-1} t}, \quad (72)$$

$$h_{\times}^{\text{CP}}(t) = h_0^{\text{C}} \sum_{\gamma=1}^{\infty} V_{2\gamma} \left[-4t_{2\gamma}^{-1} \Omega^{-1} \sin(2\Omega t) + (4 - t_{2\gamma}^{-2} \Omega^{-2}) \cos(2\Omega t) \right] e^{-t_{2\gamma}^{-1} t}, \quad (73)$$

and, for an equatorial observer by,

$$h_{+}^{\text{CE}}(t) = 2h_0^{\text{C}} \sum_{\gamma=1}^{\infty} V_{1\gamma} \left[2t_{1\gamma}^{-1} \Omega^{-1} \cos(\Omega t) + (1 - t_{1\gamma}^{-2} \Omega^{-2}) \sin(\Omega t) \right] e^{-t_{1\gamma}^{-1} t}, \quad (74)$$

$$h_{\times}^{\text{CE}}(t) = \frac{1}{2} h_0^{\text{C}} \sum_{\gamma=1}^{\infty} V_{2\gamma} \left[-4t_{2\gamma}^{-1} \Omega^{-1} \sin(2\Omega t) + (4 - t_{2\gamma}^{-2} \Omega^{-2}) \cos(2\Omega t) \right] e^{-t_{2\gamma}^{-1} t}, \quad (75)$$

where,

$$h_0^{\text{C}} = 2\pi\rho_0\Omega^3 L^6 \epsilon \frac{G}{3c^5 d_{\text{s}}}. \quad (76)$$

Note that we have restricted ourselves to the leading-order quadrupole term $l = 2$ of the mass-current multipole expansion. Once more, we write the above expressions for polar and equatorial observers in the Fourier space. In case of a polar observer, this reduces to

¹²The ‘weak’ dependency in this case refers to the fact that $|\kappa_{1\gamma}|$ and $|\kappa_{2\gamma}|$ are not as sensitive to variations in K_{s} or N^2 , as we will see in later sections.

¹³In order to show the frequency characteristics, we abbreviate the remaining factors for simplicity such that $\left[\frac{|h_{\mp}^{\text{L}}(\omega)|}{h_0^{\text{L}} |\kappa_{\alpha\gamma}|} \right]^2 \equiv G_{\mp|\alpha\gamma}^{\text{L}}$.

¹⁴Refer to section A.4 in Appendix for more details of the calculation, and for expressions of the pre-factors $V_{1\gamma}$ and $V_{2\gamma}$.

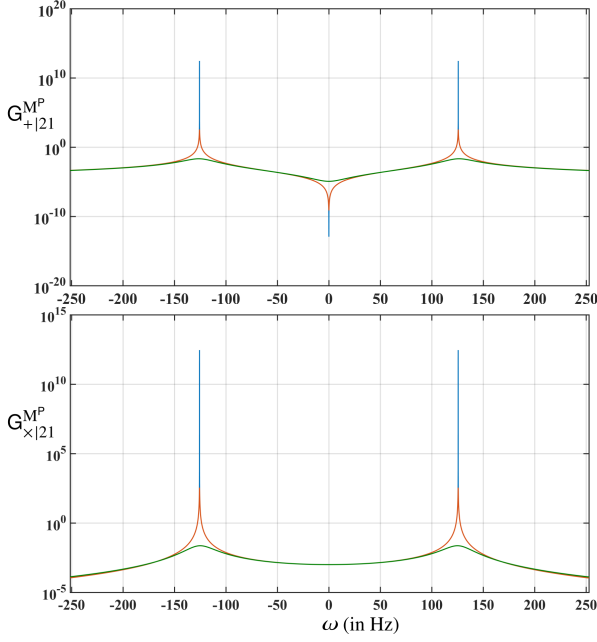


Figure 2: Frequency characteristics of emitted signals for polar observer: 3 different set of data are plotted for $\Omega/2\pi = 10$ Hz and $\partial_z \eta \sim 10^{-11}$. The respective color-coded time-scales are 9.8 (blue), 1.1×10^{-4} (red) and 8.5×10^{-7} (green) days. The corresponding resonant frequencies are ± 125.66371 , ± 125.66375 and ± 126.39611 Hz respectively. Note that the values of time-scales are calculated for specifically chosen physical parameters of the system – v_c , $\partial_z \eta$, v_{eq} , K , and F , in order to cover a large range of time-scales. A similar result for an equatorial observer is shown in figure 3.

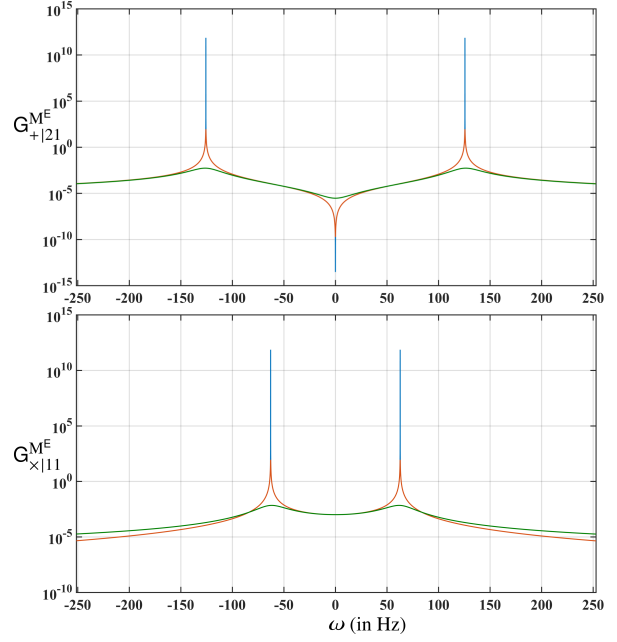


Figure 3: Frequency characteristics of emitted signals for equatorial observer: 3 different set of data are plotted for $\Omega/2\pi = 10$ Hz and $\partial_z \eta \sim 10^{-11}$. The respective color-coded time-scales are 9.8 (blue), 1.1×10^{-4} (red) and 8.5×10^{-7} (green) days. Moreover, the corresponding resonant frequencies for \times polarization are ± 62.83185 , ± 62.83188 and ± 63.19805 Hz respectively, whereas the resonant frequencies for the $+$ polarization remain exactly the same as they were for the case of a polar observer. Other physical parameters are chosen to be the same as in figure 2.

$$|h_+^{CP}(\omega)|^2 = h_0^2 \sum_{\gamma=1}^{\infty} |V_{2\gamma}|^2 \left\{ \left[4\Omega^2 (4 + t_{2\gamma}^{-2} \Omega^{-2})^2 + 16\omega^2 t_{2\gamma}^{-2} \Omega^{-2} \right] \left[(4\Omega^2 + t_{2\gamma}^{-2} - \omega^2)^2 + (2\omega t_{2\gamma}^{-1})^2 \right]^{-1} \right\}, \quad (75)$$

$$|h_{\times}^{CP}(\omega)|^2 = h_0^2 \sum_{\gamma=1}^{\infty} |V_{2\gamma}|^2 \left\{ \left[t_{2\gamma}^{-2} (4 + t_{2\gamma}^{-2} \Omega^{-2})^2 + \omega^2 (4 - t_{2\gamma}^{-2} \Omega^{-2})^2 \right] \left[(4\Omega^2 + t_{2\gamma}^{-2} - \omega^2)^2 + (2\omega t_{2\gamma}^{-1})^2 \right]^{-1} \right\}. \quad (76)$$

It should be noted that the resonant frequencies for current-quadrupole contribution from $|h_+^{MP}(\omega)|$ and $|h_{\times}^{MP}(\omega)|$ are the same as they were for mass-quadrupole contribution. Further, for the case of *equatorial observers*,

$$|h_+^{CE}(\omega)|^2 = 4h_0^2 \sum_{\gamma=1}^{\infty} |V_{1\gamma}|^2 \left\{ \left[\Omega^2 (1 + t_{1\gamma}^{-2} \Omega^{-2})^2 + 4\omega^2 t_{1\gamma}^{-2} \Omega^{-2} \right] \left[(\Omega^2 + t_{1\gamma}^{-2} - \omega^2)^2 + (2\omega t_{1\gamma}^{-1})^2 \right]^{-1} \right\}, \quad (77)$$

$$|h_{\times}^{CE}(\omega)|^2 = \frac{1}{4} h_0^2 \sum_{\gamma=1}^{\infty} |V_{2\gamma}|^2 \left\{ \left[t_{2\gamma}^{-2} (4 + t_{2\gamma}^{-2} \Omega^{-2})^2 + \omega^2 (4 - t_{2\gamma}^{-2} \Omega^{-2})^2 \right] \left[(4\Omega^2 + t_{2\gamma}^{-2} - \omega^2)^2 + (2\omega t_{2\gamma}^{-1})^2 \right]^{-1} \right\}. \quad (78)$$

We see that the emitted signals from the mass-quadrupole and the current-quadrupole are similar in nature in terms of the resonant frequencies and the general behavior of the frequency responses¹⁵. However, there is a notable switch in the $+$ and \times polarizations. Additionally, $V_{1\gamma}$ and $V_{2\gamma}$ pre-factors now appear instead of $\kappa_{1\gamma}$ and $\kappa_{2\gamma}$, besides the different characteristic amplitudes. Lastly, the frequency characteristics for $|h_+^{CP}(\omega)|$, $|h_{\times}^{CP}(\omega)|$, $|h_{\times}^{CE}(\omega)|$ and $|h_+^{CE}(\omega)|$ follow the same shapes as shown previously in figure 2 and figure 3.

4.3 A verdict on parameter space

It is clear from the general expressions of $\kappa_{\alpha\gamma}$ (in section A.5 in Appendix) and $V_{\alpha\gamma}$ (in section A.4 in Appendix)

¹⁵The characteristic amplitudes for mass and current quadrupole are related by $\frac{|h_0^C|}{|h_0^M|} = \frac{2g}{3\Omega c}$.

that their calculations are cumbersome to perform unless we could make some simplifying assumptions. Ideally, one would like to explore the range of parameter space where the first derivative of η – i.e. $\partial_z \eta$ in (51), and $\partial_z K_s$ are constants, and follow

$$\begin{aligned} |\partial_z \eta| &\ll FN^2 \ll \eta < 1 & \text{for } \forall z \in (0, 1], \\ |\partial_z K_s| &\ll |K_s| & \text{for } \forall z \in (0, 1]. \end{aligned} \quad (79)$$

Such a choice of a regime is physically reasonable and it makes the calculations analytically feasible, without compromising the generality of the model. These assumptions allow us to reduce the parameter space and explore the model in its simplest form. Meanwhile, since we do not have any prior functional forms of v_c and v_{eq} with respect to z -coordinate, we assume a simple scenario where v_c is linear in z and takes the form¹⁶,

$$v_c(z) = v_c^0 + z \times \partial_z v_c, \quad (80)$$

while, at the same time, N^2 is taken to be a constant. These assumptions leave v_{eq} implicitly varying in z according to (28). It must be noted that this doesn't imply constancy of η . In fact, it is simply that $\partial_z \eta \sim 2v_c(z)\partial_z v_c$, and $\partial_z^2 \eta \sim 2(\partial_z v_c)^2$. Lastly, we are left with N^2 , v_c^0 and $\partial_z v_c$ as free parameters in our model. K_s (or, v_{eq}) in this case becomes a dependent parameter varying in z according to (28), as previously stated. Thus, we restrict ourselves to the domain where

$$|\partial_z v_c| \ll v_c^0 < 1 \implies |\partial_z K_s| \ll |K_s|, \partial_z \eta \sim 2v_c^0 \partial_z v_c. \quad (81)$$

Under such assumptions, the calculations for the factors $\kappa_{\alpha\gamma}$ and $V_{\alpha\gamma}$ become analytic and relatively simpler¹⁷. The simplification occurs because $\partial_z \eta$ is now invariant in z according to (81). To further validate our choice, we find that numerical errors dominate significantly when calculating $\kappa_{\alpha\gamma}$ and $V_{\alpha\gamma}$ numerically, especially toward lower ranges of v_c^0 . These numerical errors are catalysed by large corresponding magnitudes of K_s when v_c^0 becomes very small. This effect is shown in detail in section A.6 in Appendix where we have compared numerical and analytic results for $\kappa_{\alpha\gamma}$ and $V_{\alpha\gamma}$, assuming (81) to be true. In nutshell, the analytic approximation in (81) enables us to selectively explore the more crucial aspects of the improved model, such as $\partial_z v_c$, while ignoring the less crucial degrees of freedom of the system, such as spatial variations in N^2 . The complete reduced expressions for $\kappa_{\alpha\gamma}$ and $V_{\alpha\gamma}$ are given in section A.5 in Appendix.

It must be noted that such an assumption of constancy of $\partial_z \eta$ isn't applied while calculating $\omega_{\alpha\gamma}$ and the corresponding time-scales $t_{\alpha\gamma}$, via (50). However, the time-scales $t_{\alpha\gamma}$ are not prone to the errors from numerical computations, as opposed to $\kappa_{\alpha\gamma}$ and $V_{\alpha\gamma}$. It

remains straightforward to compute them numerically and accurately. Nonetheless, the approximated expression for the time-scales is given in section A.5 in Appendix [see (A.5.11)].

5 Time-scales of emitted signals and corresponding amplitudes

In this section, we explore the decay time-scales of the emitted signals. We see from the expressions in (62)-(69) for the mass-quadrupole contribution, and (72)-(75) for the current-quadrupole contribution, that the decay time-scale $t_{\alpha\gamma}$ for a given $\{\alpha, \gamma\}$ mode – as defined previously in (64) – is given by,

$$t_{\alpha\gamma} = E^{-\frac{1}{2}} \Omega^{-1} \omega_{\alpha\gamma}^{-1}. \quad (82)$$

The emitted gravitational wave signal amplitude at a given frequency ω depends intrinsically on the time-scale; this is shown in the expressions in (62)-(78). Following the discussion in the previous section, we have 3 independent parameters to vary: v_c^0 , $\partial_z v_c$ and N^2 , under the analytic approximations introduced by (81). In figure 4, we plot the characteristics for the involved time-scales t_{11} and t_{21} , and the corresponding gravitational wave amplitudes for mass-quadrupole and current-quadrupole contributions at resonant frequencies i.e. $\omega = \omega_R$ (denoted by subscript **R**). Note that the resonant frequencies ω_R are also a function of $t_{\alpha\gamma}$, as shown in section 4.1. This corresponds to the effect where $|h_{\times}^{\text{ME}}|$, $|h_{+}^{\text{CE}}|$ emit at different resonant frequencies and different time-scales than $|h_{\times}^{\text{MP}}|$, $|h_{+}^{\text{MP}}|$, $|h_{+}^{\text{ME}}|$, $|h_{\times}^{\text{CP}}|$, $|h_{+}^{\text{CP}}|$ and $|h_{\times}^{\text{CE}}|$, as shown in figure 4. We also find that only a very small fraction of mechanical energy [$O(10^{-9} - 10^{-7})$] from the glitch is converted into gravitational wave emission¹⁸.

Note that in the case of $\partial_z v_c < 0$ in figure 4 (rightmost panels), the apparent outlier in the plots for $\partial_z v_c = -10^{-4} cL^{-1}$ is an artifact of low resolution in parameter space. In figure 5, we show the characteristics in the vicinity of the outlier for clarity.

5.1 Growing modes

In figure 4, for $\partial_z v_c < 0$ (rightmost panels), we see that it is possible for the system to exhibit *growing modes*. The growing modes refer to the cases where perturbations become unstable and grow monotonically, denoted by + marker in figure 4 and figure 5. *Growing modes* are characterised by negative time-scales, i.e. $t_{\alpha\gamma} < 0$. In standard Oceanography and Fluid Mechanics literature, growing modes are associated with convection and overturning¹⁹. They represent a system that gains energy from

¹⁶Note that any functional form of $v_c(z)$ can be reduced to this expression at the leading order as long as $|\partial_z v_c| \ll v_c^0$. This is equivalent to a “stiff” polytropic equation of state with the polytropic exponent $\gamma \rightarrow 1$.

¹⁷See section A.5 in Appendix for details, and for full expressions of $\kappa_{\alpha\gamma}$ and $V_{\alpha\gamma}$.

¹⁸The energetics of the emitted amplitudes is discussed in detail in section 6.2.

¹⁹See *An Introduction to Dynamic Meteorology* by **J.R. Holton**, and *Waves in Fluids* by **J. Lighthill**.

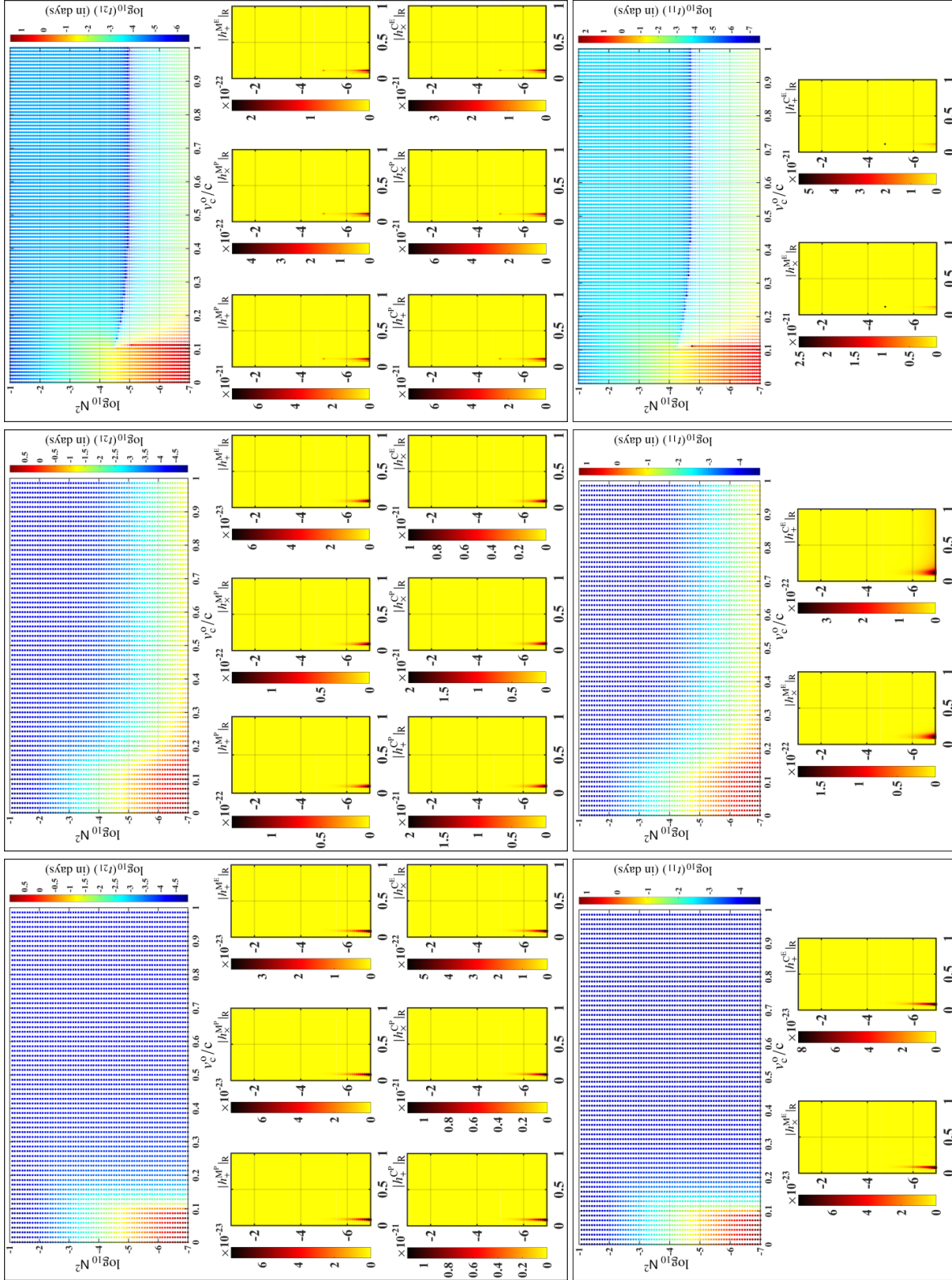


Figure 4: Emitted gravitational wave strain (*turn page sideways*): The top panel represents the time-scales for the t_{21} mode and the corresponding gravitational wave strain amplitudes for 3 sets of values for $\partial_c v_c$ at 0 , $10^{-3} cL^{-1}$, $-10^{-4} cL^{-1}$ (left to right) respectively. The bottom panel shows the t_{11} modes, and corresponding gravitational wave strain amplitudes. The parameters are set to: $f = 100$ Hz, $E = 10^{-7}$, $\epsilon = 10^{-4}$, $d_s = 1.0$ kpc, $L = 10^4$ m, $g = 10^{12}$ m/sec², $\rho_0 = 10^{17}$ kg/m³. All positive time-scales as well as the corresponding emitted amplitudes are marked by \bullet , while the negative time-scales and corresponding amplitudes are marked by $+$. Negative time-scales correspond to the scenario of growing modes²⁰.

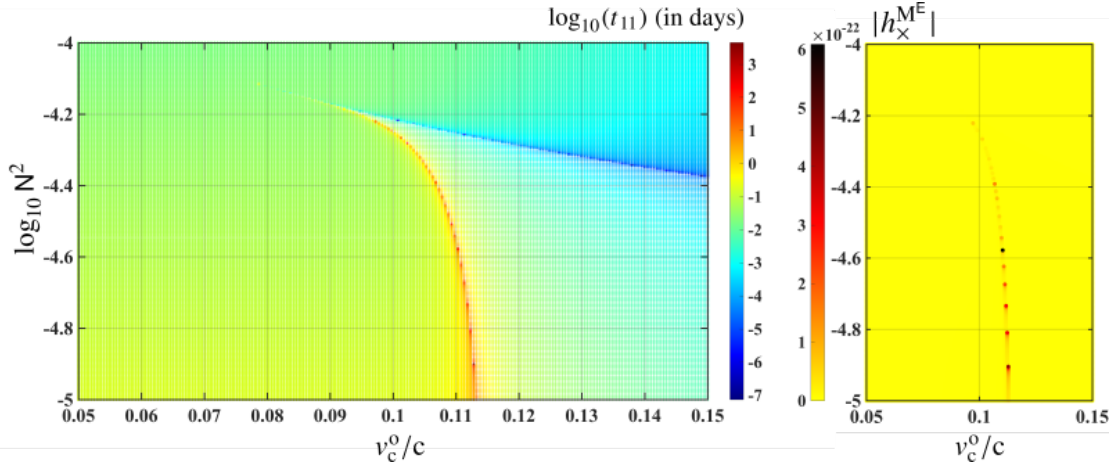


Figure 5: Outlier zoomed in: The characteristics of the parameter space in the vicinity of the apparent outlier in figure 4 for the case of $\partial_z v_c = -10^{-4} cL^{-1}$ (rightmost panels in figure 4) are shown in higher resolution. All positive time-scales as well as corresponding emitted amplitudes are marked by \bullet , while the negative time-scales and corresponding strain amplitudes are marked by $+$.

its surroundings and is not in an adiabatic state. However, this is not true for our system since it is an isolated neutron star. For this reason, these growing modes are unphysical²⁰ and the corresponding regions in the parameter space are gravitationally inaccessible.

6 Discussion

To conclude our study, one can broadly make the following reiterations and conclusions. We have extended the previous works by van Eysden and Melatos [73] and Bennett et al. [26], by incorporating a more general equation of state (characterized by v_c) and stratification length (characterized by K_s) in sections 2 and 3. We derived the expected time-scales of emission of gravitational wave signals and the corresponding strain amplitudes from mass-quadrupole and current-quadrupole formalisms in section 4. In order to better visualize the results, we explored the properties of emission in N^2 and v_c^0 parameter space by making some simplifying approximations given by (81) in section 4.3. The results are shown in figure 4, where we find that it is possible for such a hydrodynamic system to emit gravitational waves at a ground-based detector with a strain amplitude greater than $O(10^{-25})$ for a source at a distance of roughly 1 kpc. The corresponding time-scales for the loudest signals are as long as $O(300)$ days, also shown in figure 4. The results in figure 4 are explored for favorable values of physical parameters, such as at glitch magnitude $\epsilon = O(10^{-4})$, $d_s = 1$ kpc and $f = 100$ Hz. The analysis yields a strain amplitude as high as $O(10^{-21})$ toward lower magnitudes of N^2 , i.e. $N^2 \leq O(10^{-5})$, and v_c^0 approximately equaling $0.09c - 0.11c$,

for the majority of individual amplitudes²¹. Besides, in broader range of values of N^2 and v_c^0 different from the aforementioned ranges, we expect emission of the order of $O(10^1 - 10^{1.5})$ days in duration with amplitudes in the range of $O(10^{-23.5} - 10^{-26.5})$. It must be noted that the current-quadrupole contribution tends to be larger than the corresponding mass-quadrupole contribution to the emitted signal, as shown in section 4 and figure 4. This is largely because of the characteristic amplitude h_o^C being larger than h_o^M by a factor²² of $\frac{2g}{3\Omega c}$. Furthermore, very low values of N^2 (as low as $10^{-6} - 10^{-7}$) are debatable since no physical phenomenon account for such magnitudes of N^2 . Note that the ‘classical’ Brunt-Väisälä frequency N_c^2 is expected to lie loosely in the range of (0.01, 1) [73]. The equivalent magnitude of the lower bound on redefined Brunt-Väisälä frequency N^2 is then given by: $N^2 \sim \eta_o N_c^2 = 10^{-4}$, for $v_c^0 = 0.1c$. Thus, very low values of N^2 lie outside the current estimates on equivalent values of N_c^2 . In fact, very loud signals of amplitude $O(10^{-25})$ and higher lie near the lower bound of current estimates on N_c^2 , roughly in the range $10^{-4} - 10^{-7}$ for N^2 . However, the value of Ekman number E could lie anywhere in the range of $10^{-17} - 10^{-7}$ [73, 26, 33, 22, 19, 48, 20, 42, 50], whereas we have based our analysis on the assumption of $E = 10^{-7}$. The time-scales and the corresponding gravitational wave amplitudes depend on E such that, $E \downarrow \Rightarrow t_{\alpha\gamma} \uparrow \Rightarrow h_R \uparrow$. Thus, for lower values of E , stronger emissions could occur even at higher values of N^2 . This effect is shown in figure 6 where we have regenerated parts of figure 4 for $E = 10^{-14}$. Note that since Ekman number is directly proportional to the shear viscosity of the bulk matter [37, 33] and

²⁰A brief explanation and interpretation of the existence of growing modes is discussed in section A.8 in Appendix and section 6 respectively.

²¹See section A.8 in Appendix for more details.

²²This factor yields a value of the order $O(10^1 - 10^2)$ for $\Omega = O(10^2 \text{Hz})$, assuming $g = O(10^{12} \text{m/sec}^2)$.

inversely proportional to the square of its temperature [50], we expect higher values of E (10^{-7}) for colder neutron stars ($T \sim 10^6$ K) [50], and vice versa. Thus, in principle, hotter neutron stars should be better candidates for transient gravitational waves than colder neu-

tron stars. However, this is not entirely true since it is expected that hotter and younger neutron stars undergo post-glitch relaxation via crust-core dynamics aided by magnetic field rather than bulk hydrodynamics [75][36].

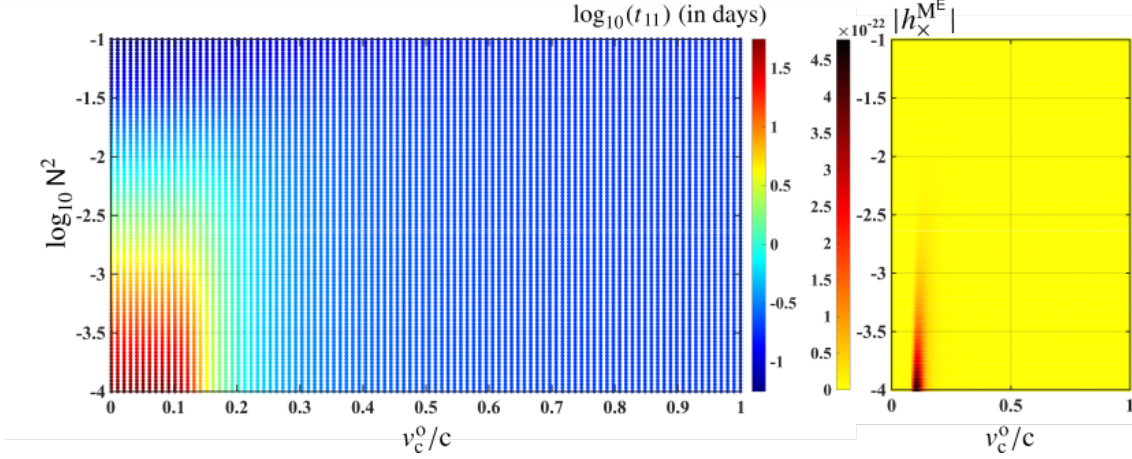


Figure 6: Sensitivity to E : The characteristics of emitted signals for $E = 10^{-14}$ and $\partial_z v_c = 0$ are shown, setting $f = 100$ Hz, $\epsilon = 10^{-4}$, $d_s = 1$ kpc, $L = 10^4$ m, $g = 10^{12}$ m/sec², $\rho_0 = 10^{17}$ kg/m³. Note the emission of loud amplitudes within the range $N_c^2 \in (10^{-4}, 10^{-2})$; the equivalent classical Brunt-Väisälä frequency N_c^2 for this range lies within permitted physical expectations.

6.1 Detectability of emitted signals

We can also derive characteristics of emitted signals as a function of rotational frequency f of the neutron star. It has been shown that the minimum strain amplitude h_0^{\min} of a continuous gravitational wave detectable by a network of 2 detectors searched over a large parameter space with a coherent search duration of T_{obs} hours during which the signal is present is given by [7, 41]

$$h_0^{\min}(\omega) = K_t \left[\frac{S_h(\omega)}{T_{\text{obs}}(\omega)} \right]^{\frac{1}{2}}, \quad (83)$$

where, $\sqrt{S_h(\omega)}$ is the *multi-detector amplitude spectral density* for a network of 2 detectors (H1, L1), and K_t is roughly equal to 30. Given this relation, we can compare the strength of emitted gravitational wave signals with the strain detectable by aLIGO. We again restrict ourselves to emission at resonant frequencies only, i.e. $\omega = \omega_R$. Note that we can express h_0^{\min} as a function of f instead of ω since ω_R is an implicit function of f . This allows us to rewrite h_0^{\min} as,

$$h_0^{\min}(f) \sim 30.0 \left[\frac{S_h(f)}{t_{\alpha\gamma}(f)} \right]^{\frac{1}{2}}. \quad (84)$$

where, $t_{\alpha\gamma}$ is expressed in hours²³. In figure 7, we plot $h_0^{\min}(f)$ and compare it with the emitted gravitational wave amplitudes²⁴ as a function of f . We have set the parameters E , v_c^0 and N_c^2 at nominal values of 10^{-10} , $0.1c$ and 10^{-4} respectively. We find that for the selected region in parameter space in figure 7, it is possible to detect the gravitational wave emission with current aLIGO sensitivity, especially in the mid to high frequency range.

One must carefully note that we have assumed an invariant N_c^2 in space and time in order to simplify our results for easier graphical visualization and understanding. In principle, one could vary all featuring parameters, i.e. N_c^2 or K_s , v_c , v_{eq} , in all possible ways. This is because all analytically derived results in sections 2-4.2 are general in nature and assume none of the approximations described in section 4.3. However, such a thorough and complete analysis will require extensive numerical computations and better priors on the parameter space. More importantly, the main aim of this study was to estimate the strength of the emitted gravitational wave signals and their time-scales as a function of spatial variation in the adiabatic sound speed v_c and stratification length z_s . This is shown in detail in figure 4 and

²³Refer to section A.7 in Appendix for discussion on properties of $t_{\alpha\gamma}$ as a function of f .

²⁴Note that the resonant frequencies of emitted modes for mass-quadrupole and current-quadrupole contributions, and for a given orientation of the observer (polar, equatorial, or otherwise), depend on the polarizations (+ and \times), which in turn depend on the featuring time-scales $t_{\alpha\gamma}$, as seen in figure 4 and section 4. The overall signal is a superposition of all such individual emissions shown in figure 7, possibly at multiple resonant frequencies for a single source with a given orientation. In this regard, (84) assumes that these individual emissions are resolvable in frequency; this usually holds true when the featuring time-scales $t_{\alpha\gamma}$ are not very small (see 4.1, 4.2).

figure 5. We find that signal characteristics are more sensitive to small spatial variations in v_c and K_S in some regions of the parameter space than others. In fact, for these regions in the parameter space, the maximum duration of the emission increases by a factor of 300 when

$\partial_z v_c = -10^{-4} cL^{-1}$, as compared to when $\partial_z v_c = 0$. The corresponding amplitudes also increase by a similar factor, as seen in figure 4,5. In parts of the parameter space characterized by growing modes, no gravitational emission is possible due to hydrodynamic instability.

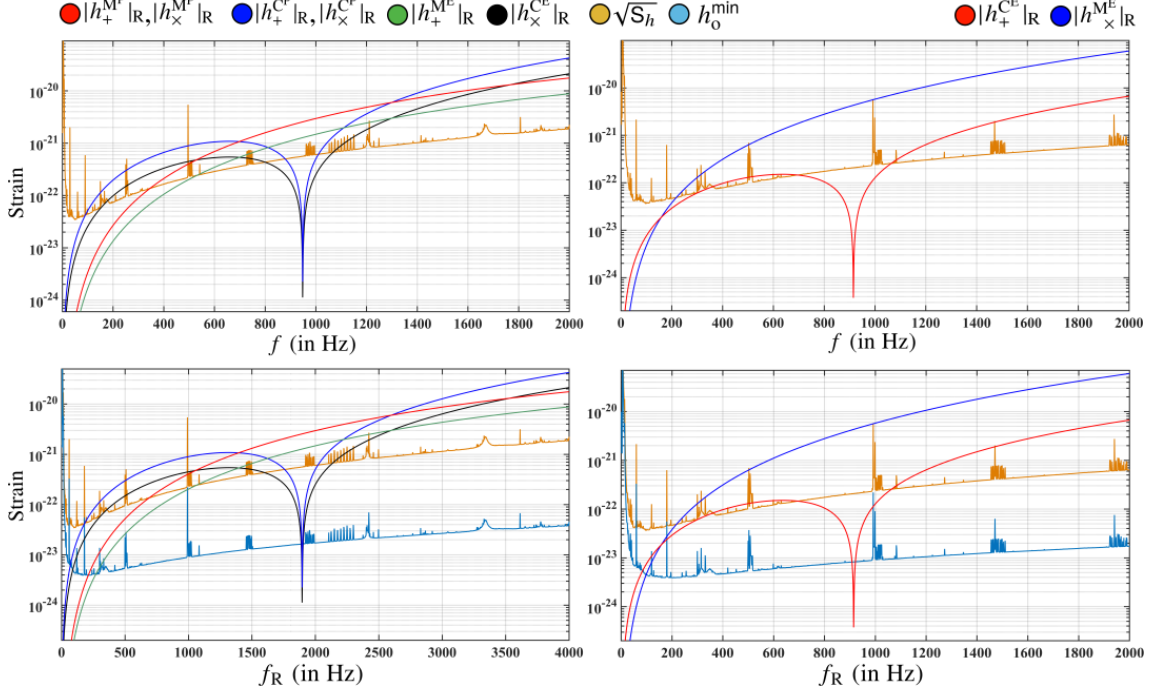


Figure 7: Sensitivity vs. f : The characteristics of emitted signals²⁴ and h_0^{\min} are shown as a function of neutron star's rotational frequency f as well as the emitted resonant frequency f_R , given by $f_R = \omega_R/2\pi$. We have set $v_c^0 = 0.1c$, $N^2 = 10^{-4}$, $E = 10^{-10}$, $\epsilon = 10^{-4}$, $d_s = 1$ kpc, $L = 10^4$ m, $g = 10^{12}$ m/sec², $\rho_0 = 10^{17}$ kg/m³, $\partial_z v_c = 0$. Note that the emitted amplitudes are largely insensitive to $\partial_z v_c$ for the chosen points in $\{v_c^0, N^2\}$ parameter space. The *multi-detector amplitude spectral density* $\sqrt{S_h(\omega)}$ is calculated by taking the harmonic mean of the individual amplitude spectral densities of H1 (aLIGO Hanford) and L1 detectors (aLIGO Livingston) measured during initial days of the O1 run i.e. Sept 12 – Oct 20, 2015.

6.2 Energetics of the system

It is an interesting exercise to estimate the fraction of mechanical energy (from the glitch) that gets converted into gravitational wave emission. For instance, the total gravitational wave energy emitted by a waveform $h(t) \propto e^{i\Omega_w t} e^{-\gamma_w t}$ is given by [70, 61]

$$E_{\text{GW}} = \frac{c^3}{8G} [\Omega_w^2 + \gamma_w^2] d_s^2 \int_0^\infty |h(\omega)|^2 d\omega, \quad (85)$$

where, we have used Parseval's theorem such that

$$\int_0^\infty |h(t)|^2 dt = \frac{1}{2\pi} \int_0^\infty |h(\omega)|^2 d\omega.$$

We can easily calculate E_{GW} by integrating (numerically or analytically) the total emitted waveform²⁵ over

time, or by integrating its Fourier transform in frequency space. Note that the expression (85) assumes an isotropic distribution of signal as a function of the observation angle i . In our case, the emission is not isotropically distributed as a function of i . In fact, the amplitude for a given polarization varies as a linear combination of sines and cosines of i , as briefly discussed in section A.4 in Appendix [26]. In order to simplify this to an order-of-magnitude estimate, the total emission can be constrained by an isotropic limit, such that²⁶

$$|h(\omega)|^2 \sim 2 \sum_{\mathcal{P}=+, \times} \left[\sum_{\mathcal{L}=M, C} |h_{\mathcal{P}}^{\mathcal{L}}(\omega)|^2 \right]. \quad (86)$$

Combining (85) and (86), we get

²⁵Note the total emission is a sum of the mass-quadrupole and current-quadrupole emission.

²⁶This approximation assumes that the amplitude measured by a polar observer is isotropically distributed as a function i . This is a reasonable assumption for an order-of-magnitude estimate of emitted energy considering that the observed amplitudes for polar and equatorial observers are of the same order of magnitude, as seen in figure 2,3 and figure 7.

$$E_{\text{GW}} \sim \frac{c^3}{4G} [\Omega_w^2 + \gamma_w^2] d_s^2 \int_0^\infty \sum_{\mathcal{P}=\pm, \times} \left[\sum_{\mathcal{L}=\text{M,C}} |h_{\mathcal{P}}^{\mathcal{L}}(\omega)| \right]^2 d\omega. \quad (87)$$

On the other hand, the total mechanical energy E_{glitch} imparted by the glitch is written as²⁷

$$E_{\text{glitch}} \sim \Gamma M_{\text{total}} L^2 \Omega_r \Delta \Omega_r = 2\pi \epsilon \Gamma \rho_o L^5 \Omega_r^2, \quad (88)$$

where, Γ is the fraction of total neutron star mass ($M_{\text{total}} \sim 2\pi\rho_o L^3$) contained within the crust; this is assumed to be a small fiducial value of 10^{-2} . Then, the fraction of mechanical energy E_C ($= E_{\text{GW}}/E_{\text{glitch}}$) converted into gravitational waves is given by

$$E_C \sim \frac{c^3}{8\pi G} \frac{[\Omega_w^2 + \gamma_w^2] d_s^2}{\epsilon \Gamma \rho_o L^5 \Omega_r^2} \int_0^\infty \sum_{\mathcal{P}=\pm, \times} \left[\sum_{\mathcal{L}=\text{M,C}} |h_{\mathcal{P}}^{\mathcal{L}}(\omega)| \right]^2 d\omega. \quad (89)$$

We find that the ratio E_C yields values of the order of $O(10^{-7})$, assuming $\Omega_w \sim 2\Omega_r$. This suggests that a large fraction of the energy from the glitch is converted into the kinetic and potential energy of bulk fluid. We also note that the value of E_C in the $\{N^2, v_c^o, \partial_z v_c\}$ parameter space depends only on the pre-factors $\kappa_{\alpha\gamma}$ and $V_{\alpha\gamma}$ ²⁸. In figure 8, we show an example of the characteristics of E_C .

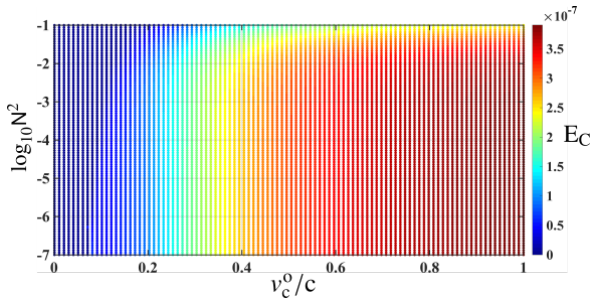


Figure 8: Energetics: We have set $E = 10^{-7}$, $\epsilon = 10^{-4}$, $d_s = 1$ kpc, $L = 10^4$ m, $g = 10^{12}$ m/sec², $\rho_o = 10^{17}$ kg/m³, and $\partial_z v_c = 0$. We find that similar results, i.e. $E_C = O(10^{-7})$, are achieved when we set $0 < |\partial_z v_c| \ll 1$; this is due to the fact that $\kappa_{\alpha\gamma}$ and $V_{\alpha\gamma}$ show very weak dependence on $\partial_z v_c$ when $|\partial_z v_c| \ll 1$.

6.3 Choice of equation of state

In (4), we assumed a simple form of the equation of state where the adiabatic speed of sound v_c is slowly and linearly varying with z . It may be useful to compare this choice with a general polytropic equation of state with polytropic index n , polytropic exponent $\gamma = (n + 1)/n$, and polytropic constant K_p , i.e. $p = K_p \rho^\gamma$. The adiabatic speed of sound v_p for the polytropic equation

is given by: $v_p^2 = K_p \rho^{1/n}$. Clearly, our model of equation of state resembles the polytropic model for $n \rightarrow \infty$. We also know that neutron star interiors are generally well-modeled for values of the polytropic index $n \in (0.5, 1.5)$. Thus, we should inquire whether our assumption of $n \rightarrow \infty$ is reasonable. In order to answer this question, consider that the gravitational wave emission is almost entirely dominated by the processes occurring at the viscous boundary layer, such as the exchange of fluid across this layer, as discussed in great detail in sections A.8, A.1, 3.8. These processes determine the time-scales of relaxation, which in turn determine the peak gravitational wave amplitudes (at resonant frequencies). We also note that the pre-factors $\kappa_{\alpha\gamma}$ and $V_{\alpha\gamma}$ are largely insensitive to these processes, as discussed in section 6.2. Thus, our choice of equation of state particularly encodes physical processes at the viscous boundary layer. In the vicinity of this viscous boundary layer, i.e. $z \sim 1$, any polytropic equation of state can be reduced to linear order in z . In this limit, the true form of the equation of state becomes irrelevant. For example, for a $n = 1$ polytrope,

$$v_p|_{z \sim 1} = \sqrt{K_p \rho|_{z \sim 1}} \sim v_c^o + \partial_z v_c. \quad (90)$$

In particular, for typical crust density of $\rho|_{z \sim 1} \sim 10^9$ kg m⁻³, $v_c^o \sim c$ and $\partial_z v_c \sim 0$, we find $K_p \sim 10^7$ kg⁻¹ m⁵ s⁻².

However, there are certain aspects that we have overlooked, such as the effects of the magnetic field and the superfluid nature of the core. The strong magnetic field in neutron stars affect the crust-core interactions and coupling dynamics of the superfluid [75][36], possibly shortening the duration of the emission, especially in young and hot neutron stars such as the Vela pulsar [18]. Recent works by van Eysden [72] have explored the effect of magnetic field on post-glitch relaxation phase but in a slightly different context. Note that we have assumed that non-axisymmetric modes are equally likely to be excited by the glitch as the axisymmetric ones ($C_\alpha = 1$). If this assumption does not hold, the gravitational amplitudes should be re-scaled by the same factor. In conclusion, we believe this to be a viable model to predict the expected order of magnitude of the amplitude and duration of the emitted gravitational wave signals from glitching neutron stars that involve relaxation via Ekman pumping. It lays down a basic approach to predict the approximate internal state of the neutron star and first-order variations in it, if any such transient signal is detected by gravitational wave detectors from the post-glitch relaxation phase.

²⁷This approximation assumes that only the crust of the neutron star gains angular momentum from the glitch while the bulk fluid is decoupled from the crust at the time of the glitch. Moreover, we also assume that the crust is very thin compared to the radius of the cylinder and it contains only a fraction of the mass [$O(10^{-2})$] of the entire neutron star.

²⁸Note that this dependence is generally biased toward $V_{\alpha\gamma}$ since the current-quadrupole emission is significantly louder than the mass-quadrupole emission.

Appendix

A.1 Time-evolution

In this section, we derive the time-evolution of the $\chi(r, \phi, z, t)$ function. We begin by isolating the time-dependence in $\chi(r, \phi, z, t)$ by separating the variables as follows,

$$\chi(r, \phi, z, t) \equiv \bar{\chi}(r, \phi, z)\mathbb{T}(t). \quad (\text{A.1.1})$$

In parallel, we take the time-derivative of (42),

$$\begin{aligned} \partial_t(\delta v_z)|_{z=\pm 1} &= \mp \frac{1}{2}E^{\frac{1}{2}}\partial_t(\nabla \times \delta \vec{v})|_{z=\pm 1} = \\ &\pm \frac{1}{2}E^{\frac{1}{2}}\left[\frac{1}{r}\frac{\partial}{\partial r}(r\partial_t[\delta v_\phi]) - \frac{1}{r}\frac{\partial}{\partial \phi}(\partial_t[\delta v_r])\right]\Bigg|_{z=\pm 1}. \end{aligned} \quad (\text{A.1.2})$$

Ignoring all the $O(E^1)$ or higher order terms on the right-hand side in (A.1.2) and using results from sections 3.4, 3.5 and (44), we get

$$\begin{aligned} \partial_t[\delta v_z^{(1)}]|_{z=\pm 1} &= \mp \frac{1}{4F}\left[\frac{1}{r^2}\frac{\partial^2 \chi}{\partial \phi^2} + \frac{1}{r}\frac{\partial}{\partial r}\left(r\frac{\partial \chi}{\partial r}\right)\right]\Bigg|_{z=\pm 1} \\ &= \pm \frac{1}{4F}\lambda_{\alpha\gamma}^2\chi|_{z=\pm 1}. \end{aligned} \quad (\text{A.1.3})$$

Moreover, we use (39) to further simplify (A.1.3) as

$$\begin{aligned} \left[\frac{\eta(z)}{FN^2(z)}\frac{\partial \dot{\chi}}{\partial z} + \left\{\frac{-\partial_z \eta}{FN^2(z)} - 1\right\}\dot{\chi}\right]\Bigg|_{z=\pm 1} &= \\ \mp \frac{1}{4F}\lambda_{\alpha\gamma}^2\chi|_{z=\pm 1}. \end{aligned} \quad (\text{A.1.4})$$

Now, introducing the separation of variables from (A.1.1), we re-write the above equation (A.1.4) as

$$\begin{aligned} \left[\frac{\eta(z)}{FN^2(z)}\frac{\partial \bar{\chi}}{\partial z} + \left\{\frac{-\partial_z \eta}{FN^2(z)} - 1\right\}\bar{\chi}\right]\Bigg|_{z=\pm 1} \dot{\mathbb{T}}(t) &= \\ \mp \frac{1}{4F}\lambda_{\alpha\gamma}^2\bar{\chi}|_{z=\pm 1}\mathbb{T}(t). \end{aligned} \quad (\text{A.1.5})$$

We further reduce the previous expression (A.1.5) by separating the variables into (r, ϕ) and z to

$$\begin{aligned} \left[\frac{\eta(\pm 1)}{FN^2(\pm 1)}\frac{\partial Z_{\alpha\gamma}}{\partial z}\right]\Bigg|_{z=\pm 1} + \left\{\frac{-\partial_z \eta|_{z=\pm 1}}{FN^2(\pm 1)} - 1\right\} \times \\ Z_{\alpha\gamma}(\pm 1)\Bigg] \dot{\mathbb{T}}(t) = \mp \frac{1}{4F}\lambda_{\alpha\gamma}^2 Z_{\alpha\gamma}(\pm 1)\mathbb{T}(t). \end{aligned} \quad (\text{A.1.6})$$

The equation (A.1.6) can now be solved to yield $\mathbb{T}(t)$ as,

$$\mathbb{T}(t) \propto e^{-\omega_{\alpha\gamma}t}, \quad (\text{A.1.7})$$

such that $\omega_{\alpha\gamma}$ is given by

$$\begin{aligned} \omega_{\alpha\gamma} = \frac{1}{4F}\lambda_{\alpha\gamma}^2 Z_{\alpha\gamma}(1) \left[\frac{\eta(1)}{FN^2(1)}\frac{\partial Z_{\alpha\gamma}}{\partial z}\right]\Bigg|_{z=1} + \\ \left\{\frac{-\partial_z \eta|_{z=1}}{FN^2(1)} - 1\right\} Z_{\alpha\gamma}(1) \Bigg]^{-1}. \end{aligned} \quad (\text{A.1.8})$$

Note that $Z_{\alpha\gamma}(z)$ is symmetric about $z = 0$ plane and

we have evaluated the expression at $z = 1$.

A.2 Bessel-Fourier Coefficients

In this section, we will calculate the Bessel-Fourier coefficients introduced in (52). We use the orthogonality property of the Bessel functions, which states that Bessel functions are orthogonal with respect to the inner product as follows²⁹,

$$\langle J_\alpha(\lambda_{\alpha\gamma}r), J_\alpha(\lambda_{\alpha\alpha}r) \rangle = \int_0^1 r J_\alpha(\lambda_{\alpha\gamma}r)J_\alpha(\lambda_{\alpha\alpha}r)dr = \frac{1}{2}\delta_{\gamma\alpha}[J_{\alpha+1}(\lambda_{\alpha\gamma}r)]^2. \quad (\text{A.2.1})$$

For a Fourier-Bessel series of the form $f(r) = \sum_{\alpha=1}^\infty C_\alpha J_\alpha(\lambda_{\alpha\alpha}r)$, the coefficients C_α can be calculated by taking projection of the function $f(r)$ over the corresponding Bessel functions as,

$$C_\alpha = \frac{\langle f(r), J_\alpha(\lambda_{\alpha\alpha}r) \rangle}{\langle J_\alpha(\lambda_{\alpha\gamma}r), J_\alpha(\lambda_{\alpha\gamma}r) \rangle}. \quad (\text{A.2.2})$$

Using the above relation in combination with (53), we can substitute for $f(r)$,

$$\begin{aligned} f(r) = \delta P_0 - \delta P_\infty = \sum_{\alpha=0}^\infty \sum_{\gamma=1}^\infty \omega_{\alpha\gamma}^{-1} J_\alpha(\lambda_{\alpha\gamma}r) \times \\ [A_{\alpha\gamma} \cos(\alpha\phi) + B_{\alpha\gamma} \sin(\alpha\phi)] Z_{\alpha\gamma}(z) = \\ \left[\sum_{\alpha=0}^\infty C_\alpha r^\alpha (r^2 - 1) \cos(\alpha\phi) Z_{\alpha\gamma}(z) \right] - r^2, \end{aligned} \quad (\text{A.2.3})$$

which, when applied to (A.2.2), gives

$$\begin{aligned} \omega_{\alpha\gamma}^{-1} A_{\alpha\gamma} \cos(\alpha\phi) Z_{\alpha\gamma}(z) = \frac{2}{J_{\alpha+1}^2(\lambda_{\alpha\gamma})} \int_0^1 r \times \\ J_\alpha(\lambda_{\alpha\gamma}r) [\delta P_0 - \delta P_\infty] dr. \end{aligned} \quad (\text{A.2.4})$$

We multiply both sides with $\cos(\alpha\phi)$ and integrate the resulting expression in ϕ and z variables assuming that $A_{\alpha\gamma}$ is an absolute constant, and arrive at the following result:

$$\begin{aligned} A_{\alpha\gamma} = \frac{2\omega_{\alpha\gamma}}{\pi J_{\alpha+1}^2(\lambda_{\alpha\gamma})} \int_0^{2\pi} d\phi \int_0^1 dz \int_0^1 r dr \times \\ J_\alpha(\lambda_{\alpha\gamma}r) \cos(\alpha\phi) [\delta P_0 - \delta P_\infty] Z_{\alpha\gamma}^{-1}(z). \end{aligned} \quad (\text{A.2.5})$$

Similarly, for $B_{\alpha\gamma}$,

$$\begin{aligned} B_{\alpha\gamma} = \frac{2\omega_{\alpha\gamma}}{\pi J_{\alpha+1}^2(\lambda_{\alpha\gamma})} \int_0^{2\pi} d\phi \int_0^1 dz \int_0^1 r dr \times \\ J_\alpha(\lambda_{\alpha\gamma}r) \sin(\alpha\phi) [\delta P_0 - \delta P_\infty] Z_{\alpha\gamma}^{-1}(z). \end{aligned} \quad (\text{A.2.6})$$

²⁹ $\delta_{\gamma\alpha}$ is the Dirac-delta function.

A.3 Quadrupole moment formalism

In this section, we will underline the formalism for calculating the expressions (62)-(71) for gravitational wave emission. In the reference frame of a polar observer at a distance d , the components of the gravitational wave strain in Einstein’s quadrupole moment formalism in the transverse traceless gauge (abbreviated as ‘TT’) are given by

$$h_+(t) = h_{xx}^{\text{TT}}(t) = -h_{yy}^{\text{TT}}(t) = \frac{G}{c^4 d} [\ddot{I}_{xx}(t) - \ddot{I}_{yy}(t)], \quad (\text{A.3.1})$$

$$h_{\times}(t) = h_{xy}^{\text{TT}}(t) = \frac{2G}{c^4 d} \ddot{I}_{xy}(t), \quad (\text{A.3.2})$$

where, $I_{ik}(t)$ is the reduced quadrupole moment of inertia, and it is given in terms of stress-energy tensor component T^{00} by,

$$I_{ik}(t) = \frac{1}{c^2} \int d^3 \vec{x} \left[x_i x_k - \delta_{ik} \frac{|\vec{x}|^2}{3} \right] T^{00}(\vec{x}, t). \quad (\text{A.3.3})$$

Combining (A.3.1), (A.3.2) and (A.3.3), we get

$$h_+^{\text{P}}(t) = \frac{G}{c^6 d} \int d^3 \vec{x} [x^2 - y^2] \ddot{T}^{00}(\vec{x}, t) = \frac{G}{c^6 d} \int d^3 \vec{r} r^2 \cos(2\phi) \ddot{T}_{\text{NA}}^{00}(\vec{r}, t), \quad (\text{A.3.4})$$

$$h_{\times}^{\text{P}}(t) = \frac{2G}{c^6 d} \int d^3 \vec{x} [xy] \ddot{T}^{00}(\vec{x}, t) = \frac{G}{c^6 d} \int d^3 \vec{r} r^2 \sin(2\phi) \ddot{T}_{\text{NA}}^{00}(\vec{x}, t), \quad (\text{A.3.5})$$

where, the sub-script NA refers to non-axisymmetric terms. Moreover, in case of a perfect fluid, we neglect the viscous terms while evaluating $T^{\mu\nu}$ since they are of the order $O(\epsilon)$, and the stress-energy tensor component T^{00} is then given by

$$T^{00} = \left[\rho + \frac{p}{c^2} \right] u^0 u^0 + p g^{00}, \quad (\text{A.3.6})$$

where, the 0-component u^0 of the 4-velocity \vec{u} is given by

$$u^0 = \frac{c}{\sqrt{1 - \frac{\vec{v} \cdot \vec{v}}{c^2}}}. \quad (\text{A.3.7})$$

We break the expression (A.3.6) into separate terms describing the constitutive equilibrium and perturbative terms, i.e. $\rho \rightarrow \rho_e + \epsilon \delta \rho$, $p \rightarrow p_e + \epsilon \delta p$ and $\vec{v} \rightarrow \vec{v}_r + \delta \vec{v}$, as described in section 3.2. Here, \vec{v}_r is simply the velocity of a fluid element given in cylindrical coordinates by $\vec{v}_r = (0, \Omega r, 0)$, assuming co-rotation with the neutron star crust. Note that equilibrium state is axisymmetric in nature and doesn’t contribute to the signal emission. The contributing non-axisymmetric terms in T^{00}

are then given by³⁰

$$\begin{aligned} T_{\text{NA}}^{00} = & \epsilon \delta \rho c^2 + (\rho_e c^2 + p_e) \left[2 \frac{\delta \vec{v} \cdot \vec{v}_r}{c^2} + \frac{\delta \vec{v} \cdot \delta \vec{v}}{c^2} \right] + \\ & \epsilon (\delta \rho c^2 + \delta p) \left[2 \frac{\delta \vec{v} \cdot \vec{v}_r}{c^2} + \frac{\vec{v}_r \cdot \vec{v}_r}{c^2} + \frac{\delta \vec{v} \cdot \delta \vec{v}}{c^2} \right] \sim \\ & \epsilon \delta \rho c^2 + (\rho_e c^2 + p_e) \left[2 \frac{\delta \vec{v} \cdot \vec{v}_r}{c^2} + \frac{\delta \vec{v} \cdot \delta \vec{v}}{c^2} \right] + \\ & (\epsilon \delta \rho c^2 + \delta p) \left[\frac{\vec{v}_r \cdot \vec{v}_r}{c^2} \right]. \end{aligned} \quad (\text{A.3.8})$$

Note that there exists no explicit factor of ϵ when it comes to $\delta \vec{v}$, as discussed previously in section 3.2. The factor of ϵ in the order of magnitude of $\delta \vec{v}$ is implicitly contained within $\delta \vec{v}$. Further, combining the expressions (A.3.4), (A.3.5) and (A.3.8), we calculate the gravitational wave emission up to the order $O(\epsilon^1)$ given by (62)-(71).

A.4 Current-quadrupole moment

In this section, we briefly describe the method to derive strain amplitude for the current-quadrupole contribution quoted in (72)-(76). We follow [70, 51, 26], and make appropriate modifications corresponding to our assumption of spatially varying stratification length and adiabatic sound speed. The general expression for the + and \times polarizations contributed by the current-quadrupole moment (labeled by the super-script C) for a general observer at distance d is given by [26, 51, 70],

$$h_+^{\text{C}}(t) = \frac{G}{2c^5 d} \left[\frac{5}{2\pi} \right]^{\frac{1}{2}} [\text{Im}\{\ddot{\mathbf{C}}^{21}(t)\} \sin(i) + \text{Im}\{\ddot{\mathbf{C}}^{22}(t)\} \cos(i)], \quad (\text{A.4.1})$$

$$h_{\times}^{\text{C}}(t) = \frac{G}{4c^5 d} \left[\frac{5}{2\pi} \right]^{\frac{1}{2}} [\text{Re}\{\ddot{\mathbf{C}}^{21}(t)\} \sin(2i) + \text{Re}\{\ddot{\mathbf{C}}^{22}(t)\} [1 + \cos^2(i)]], \quad (\text{A.4.2})$$

where, $C^{lv}(t)$ are the (l, v) -multipoles of the mass-current distribution. Note that we have only considered the leading order quadrupole moment ($l = 2$), which is the lowest multipole moment that contributes to the gravitational wave emission via its non-vanishing second-order time-derivative $\ddot{\mathbf{C}}^{2v}(t)$. The presence of additional c^5 factor, as opposed to c^4 in case of the mass-quadrupole moment, suggests that the current-quadrupole contribution is much smaller than the mass-quadrupole moment. This is true for systems with low density. However, for high-density systems such as a neutron star, current-quadrupole emission may be larger than mass-quadrupole contribution, as described in section 4.2. We have also ignored the $v = 0$ mode which contributes at the order of $O(\epsilon^1)$ while retaining the

³⁰Here, we have assumed $g^{00} = -1$ and $|v^2| \ll c^2$.

more significant $v = 1, 2$ modes. Moreover, i denotes the angle between neutron star's rotation axis and the observer's line of sight, such that $i = 0$ for a polar observer, and $i = 90^\circ$ for an equatorial observer. The $C^{2v}(t)$ terms are explicitly given by [26]³¹

$$C^{2v}(t) = \frac{(-1)^{v+1} 8\pi(10\pi)^{\frac{1}{2}}}{15v\rho_0^{-1}L^{-6}(\delta\Omega)^{-1}} \sum_{\gamma=1}^{\infty} V_{v\gamma} e^{-(E^{\frac{1}{2}}\omega_{v\gamma} + iv)\Omega t}, \quad (\text{A.4.3})$$

where,

$$V_{v\gamma} = 2A_{v\gamma}\omega_{v\gamma}^{-1} \int_0^1 dr \int_0^1 dz r^{v+1} z^{2-v} \times \hat{U} \left[J_v(\lambda_{v\gamma} r) Z_{v\gamma}(z) \rho_e(z) \right]. \quad (\text{A.4.4})$$

$$\begin{aligned} \kappa_{v\gamma} = 2\omega_{v\gamma}^{-1} A_{v\gamma} \left[\int_0^1 dr r^3 J_v(\lambda_{v\gamma} r) \int_0^1 dz \partial_z [-Z_{v\gamma}(z) \rho_e(z)] + K \int_0^1 dr r^4 \partial_r [J_v(\lambda_{v\gamma} r)] \times \right. \\ \left. \int_0^L dz \left[1 + \frac{K}{K_s(z)} \right] Z_{v\gamma}(z) \rho_e(z) + \frac{\Omega^2 L^2}{c^2} \int_0^1 dr r^5 J_v(\lambda_{v\gamma} r) \times \right. \\ \left. \int_0^1 dz \left[\partial_z [-Z_{v\gamma}(z) \rho_e(z)] + K Z_{v\gamma}(z) \rho_e(z) \right] \right] \end{aligned} \quad (\text{A.5.1})$$

Moreover, following the assumptions described in (81) in section 4.3, the above expression for $\kappa_{v\gamma}$ can be further reduced to a simpler and easier form. The simplifying assumptions lead to the case where all coefficients in (46) become effectively invariant with respect to the z -

$$\begin{aligned} \kappa_{v\gamma} = 2\omega_{v\gamma}^{-1} A_{v\gamma} \left[\mathcal{L}_1 \int_0^1 dr r^3 J_v(\lambda_{v\gamma} r) + K \left[1 + \frac{K}{K_s} \right] \mathcal{L}_2 \int_0^1 dr r^4 \partial_r [J_v(\lambda_{v\gamma} r)] + \right. \\ \left. \frac{\Omega^2 L^2}{c^2} \left[\mathcal{L}_1 + K \mathcal{L}_2 \right] \int_0^1 dr r^5 J_v(\lambda_{v\gamma} r) \right], \end{aligned} \quad (\text{A.5.2})$$

where, \mathcal{L}_1 and \mathcal{L}_2 are given in terms of \mathcal{K}_\pm by

$$\mathcal{L}_1 = \frac{(FN^2 - \mathcal{K}_-)[1 - e^{-\mathcal{K}_-}] - (FN^2 - \mathcal{K}_+)[1 - e^{-\mathcal{K}_+}]}{(FN^2 - \mathcal{K}_-)e^{\mathcal{K}_+} - (FN^2 - \mathcal{K}_+)e^{\mathcal{K}_-}}, \quad (\text{A.5.3})$$

$$\mathcal{L}_2 = \frac{(FN^2 - \mathcal{K}_-) \frac{1 - e^{-\mathcal{K}_-}}{\mathcal{K}_-} - (FN^2 - \mathcal{K}_+) \frac{1 - e^{-\mathcal{K}_+}}{\mathcal{K}_+}}{(FN^2 - \mathcal{K}_-)e^{\mathcal{K}_+} - (FN^2 - \mathcal{K}_+)e^{\mathcal{K}_-}}. \quad (\text{A.5.4})$$

Further, \mathcal{K}_\pm in (A.5.3) and (A.5.4) is given by

$$\mathcal{K}_\pm = \frac{1}{2} \left[K_s \pm (K_s^2 + \eta_0^{-1} [N^2 \lambda_{v\gamma}^2 + \partial_z \eta - \partial_z^2 \eta])^{\frac{1}{2}} \right], \quad (\text{A.5.5})$$

where, $\eta_0 = (v_c^0/c)^2$, $\partial_z \eta \sim 2v_c^0 \partial_z v_c$ and $\partial_z^2 \eta \sim 2(\partial_z v_c)^2$. Similarly, we calculate the reduced expres-

Moreover, the operator \hat{U} is written as

$$\begin{aligned} \hat{U} = \left[z \frac{\partial^2}{\partial r^2} + \frac{z}{r} \frac{\partial}{\partial r} - z \frac{v^2}{r^2} - r \frac{\partial^2}{\partial r \partial z} \right] + \\ 2F \left[r^2 \frac{\partial^2}{\partial z^2} - rz \frac{\partial^2}{\partial r \partial z} - 2z \frac{\partial}{\partial z} \right]. \end{aligned} \quad (\text{A.4.5})$$

Finally, the expressions for + and \times polarizations can now be reduced using the above relations to the expressions quoted in (72)-(76).

A.5 $\kappa_{v\gamma}$ and $V_{v\gamma}$

In this section, we quote the full expression of $\kappa_{v\gamma}$ ³².

coordinate. This leaves the solution for $Z_{v\gamma}(z)$ straightforward to achieve. Moreover, the integrals in the exponents involving K_s in (A.5.1) are dissolved, and the resulting exponential terms can be folded into $Z_{v\gamma}(z)$ to yield

sion for $V_{v\gamma}$ in terms of $\mathcal{L}_3^{(g)}$, $\mathcal{L}_4^{(g)}$ and $\mathcal{L}_5^{(g)}$. We define $\mathcal{L}_3^{(g)}$, $\mathcal{L}_4^{(g)}$ and $\mathcal{L}_5^{(g)}$ as follows:

$$\mathcal{L}_3^{(g)} = \frac{(FN^2 - \mathcal{K}_-) \mathcal{H}_g(\mathcal{K}_-) - (FN^2 - \mathcal{K}_+) \mathcal{H}_g(\mathcal{K}_-)}{(FN^2 - \mathcal{K}_-)e^{\mathcal{K}_+} - (FN^2 - \mathcal{K}_+)e^{\mathcal{K}_-}}, \quad (\text{A.5.6})$$

$$\mathcal{L}_4^{(g)} = \frac{(FN^2 - \mathcal{K}_-) \frac{\mathcal{H}_g(\mathcal{K}_-)}{\mathcal{K}_-^{-1}} - (FN^2 - \mathcal{K}_+) \frac{\mathcal{H}_g(\mathcal{K}_+)}{\mathcal{K}_+^{-1}}}{(FN^2 - \mathcal{K}_-)e^{\mathcal{K}_+} - (FN^2 - \mathcal{K}_+)e^{\mathcal{K}_-}}, \quad (\text{A.5.7})$$

$$\mathcal{L}_5^{(g)} = \frac{(FN^2 - \mathcal{K}_-) \frac{\mathcal{H}_g(\mathcal{K}_-)}{\mathcal{K}_-^{-2}} - (FN^2 - \mathcal{K}_+) \frac{\mathcal{H}_g(\mathcal{K}_+)}{\mathcal{K}_+^{-2}}}{(FN^2 - \mathcal{K}_-)e^{\mathcal{K}_+} - (FN^2 - \mathcal{K}_+)e^{\mathcal{K}_-}}, \quad (\text{A.5.8})$$

³¹In case of current-quadrupole contribution, it is possible to have continuous emission of gravitational waves at large time-scales, $t \gg t_{2v}$, as shown by Bennett et al. [26]. This continuous residual emission is not artificial (cf. van Eysden and Melatos [73]). In calculating the expression for $C^{2v}(t)$, we have ignored terms responsible for this residual continuous contribution since we concern ourselves solely with transient emission.

³²The pre-factor of 2 in $\kappa_{v\gamma}$ comes from extending the symmetric integral to $z \in [-1, 1]$.

where, $\mathcal{H}_g(\mathcal{K}_\pm)$ is defined by the integral given below³³ The resulting complete expression for $V_{\nu\gamma}$ is then expanded and written in terms of $\mathcal{L}_3^{(g)}$, $\mathcal{L}_4^{(g)}$ and $\mathcal{L}_5^{(g)}$ as follows:

$$\mathcal{H}_g(\mathcal{K}_\pm) = \int_0^1 dz z^g e^{-\mathcal{K}_\pm z}. \quad (\text{A.5.9})$$

$$V_{\nu\gamma} = 2A_{\nu\gamma}\omega_{\nu\gamma}^{-1} \left[\mathcal{L}_3^{(3-\nu)} \int_0^1 dr r^{\nu-1} [r^2 \partial_r^2 [J_\nu(\lambda_{\nu\gamma} r)] + r \partial_r [J_\nu(\lambda_{\nu\gamma} r)] - \nu^2 J_\nu(\lambda_{\nu\gamma} r)] + \mathcal{L}_4^{(2-\nu)} \times \int_0^1 dr r^{\nu+2} \partial_r [J_\nu(\lambda_{\nu\gamma} r)] + 2F \left[\mathcal{L}_5^{(2-\nu)} \int_0^1 dr r^{\nu+3} J_\nu(\lambda_{\nu\gamma} r) + \mathcal{L}_4^{(3-\nu)} \int_0^1 dr r^{\nu+1} [r \partial_r [J_\nu(\lambda_{\nu\gamma} r)] + 2J_\nu(\lambda_{\nu\gamma} r)] \right] \right]. \quad (\text{A.5.10})$$

Moreover, the approximated expression of $t_{\nu\gamma}$ can also be calculated following (81), and is given by

$$t_{\nu\gamma} = \frac{4E^{-\frac{1}{2}}\Omega^{-1}F^2N^2[(FN^2 - \mathcal{K}_-)e^{\mathcal{K}_+} - (FN^2 - \mathcal{K}_+)e^{\mathcal{K}_-}]}{\lambda_{\nu\gamma}^2[(\eta_1\mathcal{K}_+ - \partial_z\eta|_{z=1} - FN^2)(FN^2 - \mathcal{K}_-)e^{\mathcal{K}_+} - (\eta_1\mathcal{K}_- - \partial_z\eta|_{z=1} - FN^2)(FN^2 - \mathcal{K}_+)e^{\mathcal{K}_-}]}, \quad (\text{A.5.11})$$

where,

$$\eta_1 \sim \eta_0 + \partial_z\eta + \frac{1}{2}\partial_z^2\eta; \quad \partial_z\eta|_{z=1} \sim \partial_z\eta + \partial_z^2\eta; \quad \eta_0 = (v_c^0/c)^2, \quad \partial_z\eta \sim 2v_c^0\partial_z v_c \text{ and } \partial_z^2\eta \sim 2(\partial_z v_c)^2.$$

given,

A.6 Error characterization

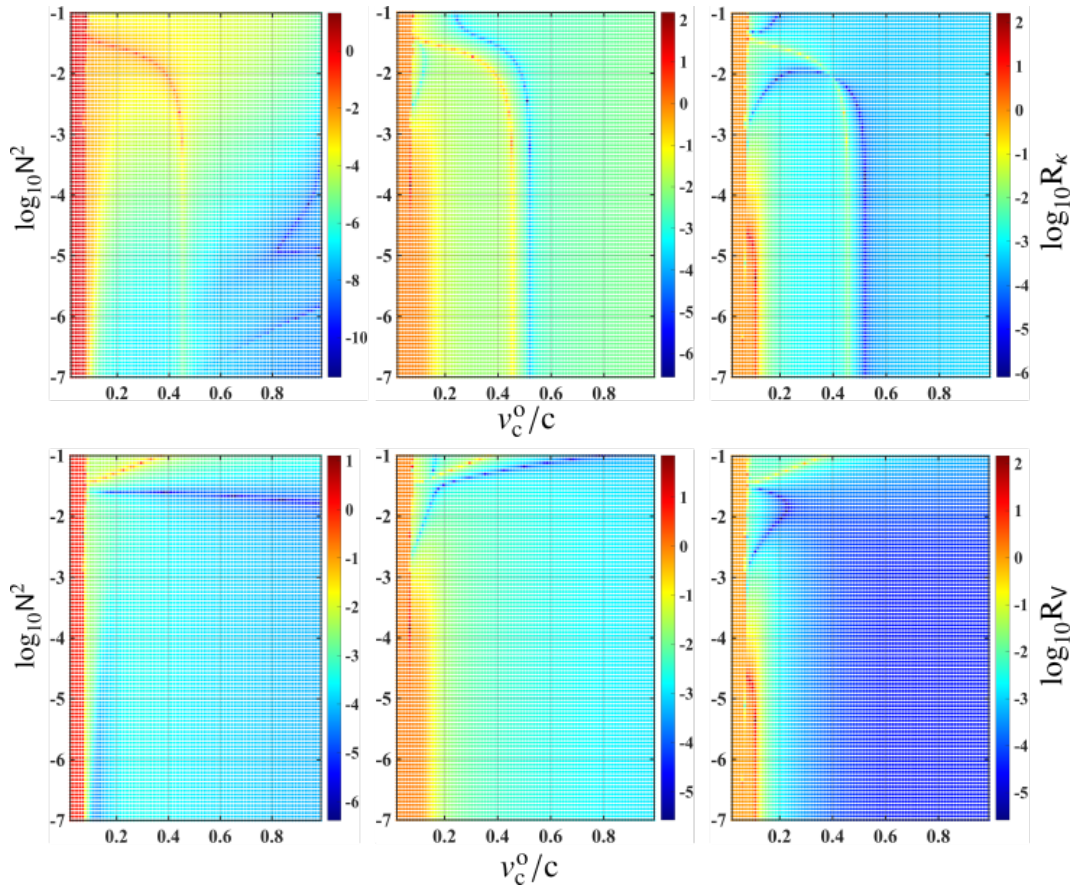


Figure 9: Error characteristics: 3 different sets of data are plotted for the t_{21} mode at a rotational frequency of 100 Hz, and for a set of values of $\partial_z v_c$ of 0, $10^{-3} cL^{-1}$ and $-10^{-4} cL^{-1}$ from left to right. Other relevant physical parameters are chosen from astrophysical priors, as in all previous figures. The top panel represents R_k while the bottom panel represents R_v . Note that larger values of R_k and R_v signify large mismatch between approximated analytic and numerical results.

³³Note that the occurrences of (g) in expressions of $\mathcal{L}_3^{(g)}$, $\mathcal{L}_3^{(g)}$ and $\mathcal{L}_3^{(g)}$ are intended as super-scripts and not exponents.

In this section, we show the comparison between analytically approximated and numerically computed results for $\kappa_{\nu\gamma}$ and $V_{\nu\gamma}$. We have explored the results for the t_{21} mode since this is sufficient for our purposes. We define the differences between analytically approximated ($\kappa_{\nu\gamma}^t, V_{\nu\gamma}^t$) and numerical ($\kappa_{\nu\gamma}^n, V_{\nu\gamma}^n$) results as follows,

$$R_\kappa = \left| \frac{\kappa_{\nu\gamma}^t - \kappa_{\nu\gamma}^n}{\kappa_{\nu\gamma}^t + \kappa_{\nu\gamma}^n} \right|, \quad (\text{A.6.1})$$

$$R_V = \left| \frac{V_{\nu\gamma}^t - V_{\nu\gamma}^n}{V_{\nu\gamma}^t + V_{\nu\gamma}^n} \right|. \quad (\text{A.6.2})$$

In figure 9, we plot the characteristics of R_κ and R_V for three cases, i.e when $\partial_z v_c \in \{0, 10^{-3}cL^{-1}, -10^{-4}cL^{-1}\}$. The leftmost panels show a baseline mismatch between approximated analytic values and numerically calculated values of $\kappa_{\nu\gamma}$ and $V_{\nu\gamma}$. Note that since $\partial_z v_c = 0$ for these two panels, the numerical and approximated analytic results should not have a high mismatch. However, the results deviate from accuracy for certain regions in parameter space, especially for lower values of v_c^0 . The center and rightmost panels show similar characteristics. Note that the mismatch in $\kappa_{\nu\gamma}$ and $V_{\nu\gamma}$ follows somewhat similar characteristics to the time-scales plotted in figure 4. The underlying reason is fairly straightforward: larger time-scales occur when K_s becomes large in magnitude, and this large magnitude of K_s tends to throw off the numerical results from accuracy while the approximated analytic results continue to follow an accurate description. Note that the factor $\rho_e(z)$ in the expressions of $\kappa_{\nu\gamma}$ and $V_{\nu\gamma}$ tends to fall very rapidly with z from a large value ρ_0 at $z = 0$ for large magnitudes of K_s ³⁴. We also find that the numerical values of $Z_{\nu\gamma}(z)$ tend to wander inaccurately into negative domain from tolerance-induced numerical errors nearing $z = 0$. This small discrepancy between the values calculated by numerical methods and approximate analytic expressions is amplified by the larger value of $\rho_e(z)$ nearing $z = 0$, especially when K_s is large, leading to a large mismatch. This affect also contributes to figure 9 for the case of $\partial_z v_c = 0$, i.e. leftmost panels.

A.7 $t_{\nu\gamma}$ vs f

In this section, we elaborate on the characteristics of emitted signals as a function of neutron star's rotational frequency f . In figure 10, we plot the time-scales for $\{2,1\}$ and $\{1,1\}$ modes, i.e. t_{21} and t_{11} , as a function of f . These time-scales have been calculated and implicitly included in the results via (84) in figure 7. We can conclude from figure 10 that these time-scales may span orders of magnitudes. For (84) to be a valid measure of minimum detectable strain for such signals, the observation time for the coherent search must be larger than these time-scales, i.e. $T_{\text{obs}} \geq t_{\nu\gamma}$.

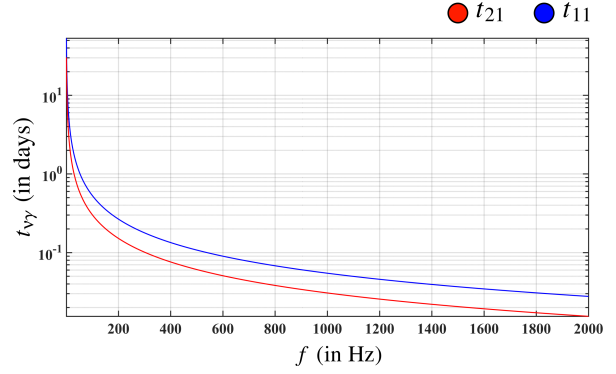


Figure 10: $t_{\nu\gamma}$ characteristics: t_{21} and t_{11} are plotted as a function of neutron star's rotational frequency f . We have set $v_c^0 = 0.1c$, $N^2 = 10^{-4}$, $E = 10^{-10}$, $\epsilon = 10^{-4}$, $d_s = 1$ kpc, $L = 10^4$ m, $g = 10^{12}$ m/sec², $\rho_0 = 10^{17}$ kg/m³, $\partial_z v_c = 0$.

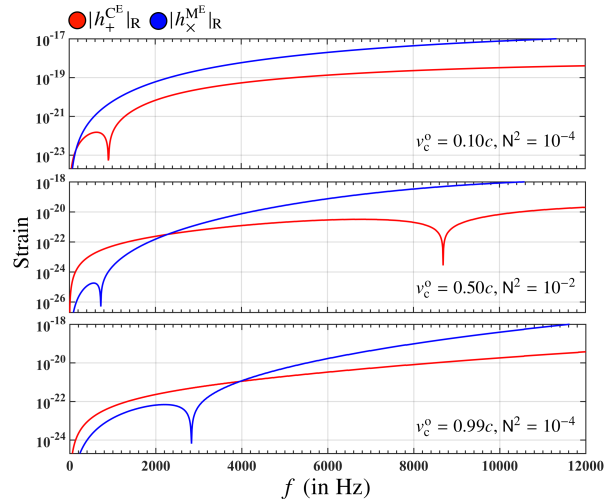


Figure 11: Emission characteristics: We have set $E = 10^{-10}$, $\epsilon = 10^{-4}$, $d_s = 1$ kpc, $L = 10^4$ m, $g = 10^{12}$ m/sec², $\rho_0 = 10^{17}$ kg/m³, $\partial_z v_c = 0$, and 3 different sets of values of v_c^0 and N^2 are explored. Note the appearance of dips in one or both the contributions in frequency space i.e. mass-quadrupole and current-quadrupole emissions, due to variation in v_c^0 and N^2 .

Moreover, there is a noticeable dip in emission from current-quadrupole contribution in the mid-frequency range in figure 7. This dip is caused by $V_{\nu\gamma}$ becoming negative with increasing frequency. The sharp dip occurs due to the inclusion of $V_{\nu\gamma}$ in (72)–(75) via its absolute magnitude. This affect is not limited to $V_{\nu\gamma}$ and current-quadrupole contribution only. In fact, the presence of this dip in current-quadrupole or mass-quadrupole emission depends upon the values of v_c^0 and N^2 . Like $V_{\nu\gamma}$, $\kappa_{\nu\gamma}$ may also show similar effect for alternative values of v_c^0 and N^2 . Furthermore, the location of this dip in frequency space is found to vary with v_c^0 as well as N^2 . We also find that the location of this dip is less sensitive to variation in N^2 as compared to v_c^0 .

³⁴While this affects the numerical results of $\kappa_{\nu\gamma}$ and $V_{\nu\gamma}$, no such effect is present in the expression for time-scale $t_{\nu\gamma}$.

In figure 11 above, we plot a part of figure 7 (top-right panel) to demonstrate the aforementioned effect.

A.8 Dependence of emission properties on $\partial_z v_c$

The significant and critical affect of $\partial_z v_c$ on the properties of the gravitational wave emission discussed in section 5 and section 6 is best estimated by looking at (42) and the discussion in section A.1. For instance, (A.1.2) equates the rate of flow into the viscous boundary layer at the top and bottom faces of the cylinder with the rate of flow out of this boundary layer back into the bulk; this is a direct consequence of the conservation of mass across the viscous boundary layer [17, 73, 76, 26]. This rate of exchange of fluid determines the dissipation time-scale of a certain perturbed $\{\alpha, \gamma\}$ mode – faster exchange of fluid leads to faster dissipation of the perturbation. The value of $\partial_z v_c$ bears a direct consequence on this process at the boundary layer. For example, from (A.1.8) and (46), we see that $\partial_z v_c$ contributes via the “slope term” $\partial Z_{\alpha\gamma}/\partial z$, and $\partial_z \eta$ term in the denominator in (A.1.8). In fact, the $\partial Z_{\alpha\gamma}/\partial z$ term is the dominant determinant in deciding the speed of exchange since $|\partial_z \eta| \ll 1$. When the slope term is large and positive, the exchange of fluid is slow, as clearly seen in (A.1.8). This is simply because the fluid flowing out of the boundary layer and back into the bulk has to work against high pressure gradient at

$z = \pm 1$, which is set by the positive value of the slope term. Note that positive slope of $Z_{\alpha\gamma}$ implies decreasing pressure in z -direction, as seen in (41). Similarly, when the slope term is positive but small, the exchange of fluid is faster since the pressure gradient decreases in value. Note that when the slope term becomes negative, we may see growing modes although this is neither a sufficient nor a necessary condition; the growing modes could also occur when $N^2 < 0$ despite the slope being positive. This effect is seen in figure 4, where the value $\partial_z v_c = -10^{-4} cL^{-1}$ increases the characteristic time-scales as well as the corresponding gravitational wave amplitudes in some regions of the parameter space. It is important to remember here that this increase in gravitational wave amplitude occurs at the resonance frequency only, and the amplitudes decay in the sidebands. Hence, while increasing time-scales increase the gravitational wave amplitude at the resonance frequency, they also decrease the effective bandwidth of the signal frequency.

Acknowledgments

I would like to extend my hearty thanks to Maria Alessandra Papa at the Max-Planck-Institut für Gravitationsphysik for her support throughout, and to Andrew Melatos for his input through the course of this work.

* * *

III Results of an all-sky high-frequency Einstein@Home search for continuous gravitational waves in LIGO’s fifth Science Run

Avneet Singh^{1,2,3,†}, Maria Alessandra Papa^{1,2,4,‡}, Heinz-Bernd Eggenstein^{2,3}, Sylvia Zhu^{1,2}, Holger Pletsch^{2,3}, Bruce Allen^{2,4,3}, Oliver Bock^{2,3}, Bernd Maschenschalk^{2,3}, Reinhard Prix^{2,3}, Xavier Siemens⁴

¹ Max-Planck-Institut für Gravitationsphysik, am Mühlenberg 1, 14476, Potsdam-Golm

² Max-Planck-Institut für Gravitationsphysik, Callinstraße 38, 30167, Hannover

³ Leibniz Universität Hannover, Welfengarten 1, 30167, Hannover

⁴ University of Wisconsin-Milwaukee, Milwaukee, Wisconsin 53201, USA

Abstract

We present results of a high-frequency all-sky search for continuous gravitational waves from isolated compact objects in LIGO’s 5th Science Run (S5) data, using the computing power of the Einstein@Home volunteer computing project. This is the only dedicated continuous gravitational wave search that probes this high frequency range on S5 data. We find no significant candidate signal, so we set 90%-confidence level upper-limits on continuous gravitational wave strain amplitudes. At the lower end of the search frequency range, around 1250 Hz, the most constraining upper-limit is 5.0×10^{-24} , while at the higher end, around 1500 Hz, it is 6.2×10^{-24} . Based on these upper-limits, and assuming a fiducial value of the principal moment of inertia of 10^{38} kg m^2 , we can exclude objects with ellipticities higher than roughly 2.8×10^{-7} within 100 pc of Earth with rotation periods between 1.3 and 1.6 milliseconds.

1 Introduction

Ground-based gravitational wave (GW) detectors will be able to detect a continuous gravitational wave signal from a spinning deformed compact object provided that it is spinning with a rotational period between roughly 1 and 100 milliseconds, that it is sufficiently close to Earth and it is sufficiently “bumpy”. Blind searches for continuous gravitational waves probe the whole sky and broad frequency ranges, looking for this type of objects.

In this paper, we present the results of an all-sky Einstein@Home search for continuous, nearly monochromatic, high-frequency gravitational waves in data from LIGO’s 5th Science Run (S5). A number of searches have been carried out on LIGO data [11, 10, 5, 4, 8, 7] targeting lower frequency ranges. The only other search covering frequencies up to 1500 Hz was conducted on S6 data [12] taken at least 3 years apart from the data used here. Our search results are only 33% less sensitive than those of Abbot *et al* [12], even though the S5 data is less sensitive than the S6 data by more than a factor of 2. The search method presented here anticipates the procedure that will be used on the advanced detector (aLIGO) data.

This search can be considered an extension of the S5 Einstein@Home search [4] although it employs a different search technique: this search uses the *Global Correlation Transform* (GCT) method to combine results from coherent \mathcal{F} -*statistic* searches [57, 58], as opposed to the previous Einstein@Home search [4] that employed the *Hough-transform* method to perform this combination. In the end, at fixed computing resources, these two search methods are comparable in sensitivity. However a semi-coherent \mathcal{F} -*statistic* search is more ef-

ficient when considering a broad spin-down range so for the Einstein@Home searches we have decided to adopt it as our “work horse”.

We do not find any significant signal(s) among the set of searched waveforms. Thus, we set 90%-confidence upper-limits on continuous gravitational wave strain amplitudes; near the lower end of the search frequency range between 1253.217–1255.217 Hz, the most constraining upper-limit is 5.0×10^{-24} , while toward the higher end of the search frequency range nearing 1500 Hz, the upper-limit value is roughly 6.2×10^{-24} . Based on these upper-limits, we can exclude certain combinations of signal frequency, star deformation (ellipticity) and distance values. We show with this search that even with S5 data from the first generation of GW detectors, such constraints do probe interesting regions of source parameter space.

2 The data

The LIGO gravitational wave network consists of two detectors, H1 in Hanford (Washington) and L1 in Livingston (Louisiana), separated by a 3000-km baseline. The S5 run lasted roughly two years between GPS time 815155213 sec (Fri, Nov 04, 16:00:00 UTC 2005) and 875145614 sec (Sun, Sep 30, 00:00:00 UTC 2007). This search uses data spanning this observation period, and during this time, H1 and L1 had duty-factors of 78% and 66% respectively [9, 6]. The gaps in this data-set are due to environmental or instrumental disturbances, or scheduled maintenance periods.

We follow [4, 7], where the calibrated and high-pass filtered data from each detector is partitioned in 30-minute chunks and each chunk is Fourier-transformed

[†]avneet.singh@aei.mpg.de

[‡]maria.alessandra.papa@aei.mpg.de

after the application of a steep Tukey window. The set of Short (time-baseline) Fourier Transforms (*abbrev.* SFT) that ensues, is the input data for our search.

We further follow [4], where frequency bands known to contain spectral disturbances have been removed from the analysis. In fact, such data has been substituted with fake Gaussian noise at the same level as the neighboring undisturbed data; in table 3, we list these bands.

3 The search

The search presented here is similar to the search on S6 data, reported in [11]. Our reference target signal is given by (1)-(4) in [10]; at emission, the signal is nearly monochromatic, typically with a small ‘spin-down’. The signal waveform in the detector data is modulated in frequency because of the relative motion between the compact object and the detector; a modulation in amplitude also occurs because of the variation of the sensitivity of the detector with time across the sky.

The most sensitive search technique that one could use is a fully-coherent combination of the detectors’ data, matched to the waveform that one is looking for. The (amplitude) sensitivity of such a method increases with the square-root of the time-span of the data used. However, the computational cost to resolve different waveforms increases very rapidly with increasing time-span of the data, and this makes a fully-coherent search over a large frequency range computationally unfeasible when using months of data. This is the main reason why *semi-coherent search* methods have been developed. These methods perform coherent searches over shorter stretches of data, called *segments*, and then combine the results with incoherent techniques.

This search covers waveforms from the entire sky, with frequencies in a 250 Hz range from 1249.717 Hz to 1499.717 Hz, and with a first-order spin-down between -2.93×10^{-9} Hz/s and 5.53×10^{-10} Hz/s, similar to previous Einstein@Home searches. We use a ‘stack-slide’ semi-coherent search procedure implemented with the GCT method [57, 58].

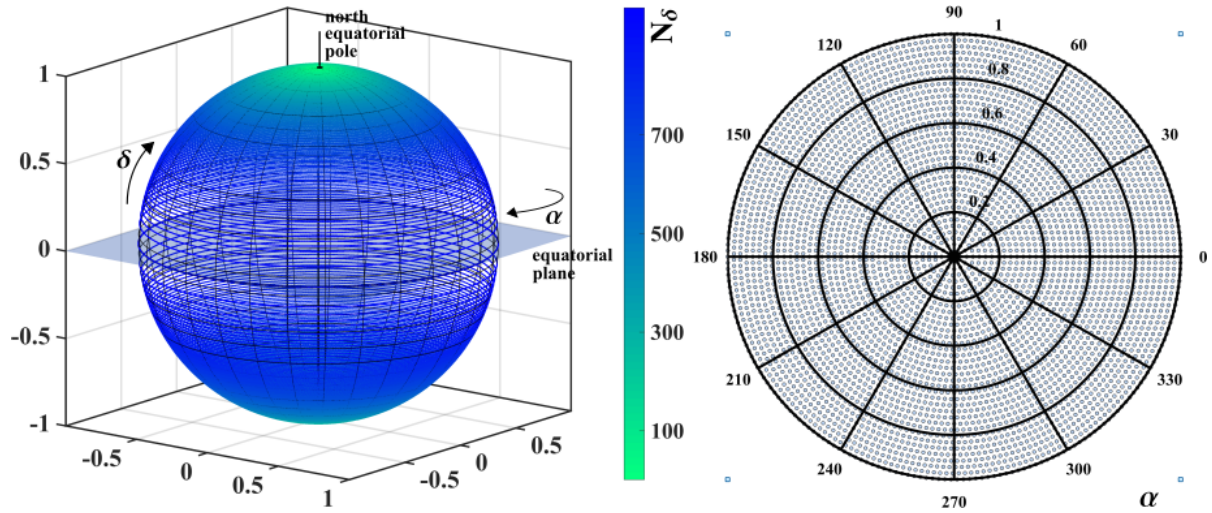


Figure 1: Tiling of sky-grid for the frequency band 1240-1250 Hz; $d_{\text{sky}} = 6.6 \times 10^{-4}$ for this band. In the left panel, we show the sky-grid points on the celestial sphere; the color-code traces the number of sky-grid points, N_δ , as a function of equatorial latitude δ . The right panel is a polar plot of the northern equatorial hemisphere of the same sky-grid but with density scaled down by a factor of 4 to allow for better viewing. In the polar plot, $\theta = \alpha$ and $r = \cos(\delta)$.

The data is divided into N_{seg} segments, each spanning T_{coh} in time. The coherent multi-detector \mathcal{F} -statistic [34] is computed on each segment for all the points on a coarse $\lambda_c \equiv \{f_c, \dot{f}_c, \alpha_c, \delta_c\}$ signal waveform parameter grid, and then results from the individual segments are summed, one per segment, to yield the final core detection-statistic $\overline{\mathcal{F}}$, as shown in (1); α, δ are the equatorial sky coordinates of the source position, while f and \dot{f} are the frequency and first-order spin-down of the signal respectively. Depending on which λ_c parameter points are taken on the coarse grid for each segment in this sum, the result will approximate the detection-statistic computed on a λ_f parameter point on a finer

grid:

$$\overline{\mathcal{F}}(\lambda_f) := \frac{1}{N_{\text{seg}}} \sum_{i=1}^{N_{\text{seg}}} \mathcal{F}(\lambda_c^i) \quad (1)$$

In a ‘stack-slide’ search in Gaussian noise, $N_{\text{seg}} \times 2\overline{\mathcal{F}}$ follows a $\chi_{4N_{\text{seg}}}^2$ chi-squared distribution with $4N_{\text{seg}}$ degrees of freedom.

The most important search parameters are then: $N_{\text{seg}}, T_{\text{coh}}$, the signal parameter search grids λ_c, λ_f , the total spanned observation time T_{obs} , and finally the ranking statistic used to rank parameter space cells i.e. $2\overline{\mathcal{F}}$.

The grid-spacing in frequency δf and spin-down $\delta \dot{f}$

are constant over the search range. The same frequency spacing and sky grid is used for the coherent analysis and in the incoherent summing. The spin-down spacing of the incoherent analysis is finer by a factor of γ with respect to that of the coherent analysis. In table 1, we summarize the search parameters.

The sky-grid for the search is constructed by tiling the projected equatorial plane uniformly with squares of edge length d_{sky} . The length of the edge of the squares is a function of the frequency f of the signal, and parameterized in terms of a so-called *sky-mismatch parameter* (m_{sky}) as

$$d_{\text{sky}} = \frac{1}{f} \frac{\sqrt{m_{\text{sky}}}}{\pi \tau_E} \quad (2)$$

where, $\tau_E = 0.021$ seconds and $m_{\text{sky}} = 0.3$, also given in table 1. The sky-grids are constant over 10 Hz-wide frequency bands, and are calculated for the highest frequency in the band. In figure 1, we illustrate an example of the sky-grid. The total number of templates in 50 mHz bands as a function of frequency is shown in figure 2. This search explores a total of 5.6×10^{16} waveform templates across the $\lambda_f \equiv \{f_f, \dot{f}_f, \alpha_f, \delta_f\}$ parameter space.

The search is divided into work-units (*abbrev.* WU), each searching a very small sub-set of template waveforms. The WU are sent to Einstein@Home volunteers and each WU occupies the volunteer/host computer for roughly 6 hours. One such WU covers a 50 mHz band, the entire spin-down range, and 139–140 points in the sky. 6.4 million different WU are necessary to cover the whole parameter space. Each WU returns a ranked list of the most significant 10^4 candidates found in the parameter space that it searched.

4 Identification of undisturbed bands

In table 3, we list the central frequencies and bandwidths of SFT data known to contain spectral lines from instrumental artefacts. These frequency regions were identified before the Einstein@Home run, and we were able to replace the corresponding data with Gaussian noise matching the noise level of neighbouring quiet bands. Consequently, some search results have contributions from this ‘fake data’. The intervals in signal-frequency where the search results come entirely from fake data are indicated as *All Fake Data* in table 4. In these intervals of signal-frequency, we effectively do not have search results. The other three columns in table 4 provide signal-frequency intervals where results *might* have contributions from fake data. In these regions, depending on the signal parameters, the detection efficiency might be affected.

Despite the removal of known disturbances from the data, it still contains unknown noise artefacts producing $2\overline{\mathcal{F}}$ values that do not follow the expected distribution for Gaussian noise. These artifacts usually have narrow-band characteristics; we identify such ‘dis-

turbed’ signal-frequency intervals in the search results and exclude them from further post-processing analysis.

Quantity	Value
T_{coh} (hours)	30.0
T_{obs} (days)	653.18
t_{ref} (GPS seconds)	847063082.5
N_{seg}	205
δf_c (Hz)	6.71×10^{-6}
$\delta \dot{f}_c$ (Hz/s)	5.78×10^{-10}
γ	1399
m_{sky}	0.30

Table 1: Search parameters for the search. t_{ref} is the reference time that defines the frequency and spin-down values.

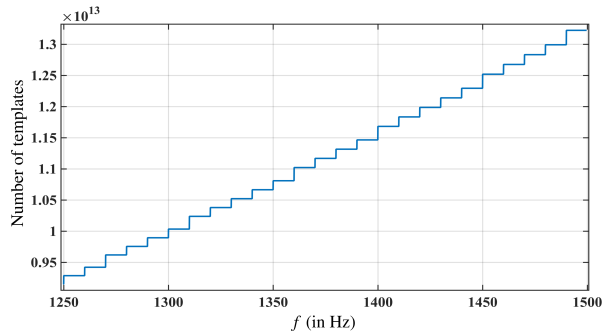


Figure 2: Number of templates searched in 50 mHz bands. The variation in template count arises from the variation in number of sky-grid points every 10 Hz in frequency. Each 50 mHz band contributes roughly 6.3×10^7 templates in frequency and spin-down (on the finer grid refined by *refinement factor* γ).

The benefit of such exclusions is that, in the remaining ‘undisturbed’ bands, we can rely on semi-analytic predictions for the significance of the observed $2\overline{\mathcal{F}}$ values, and we can set a uniform detection criterion across the entire parameter space. It is true that we forego the possibility of detecting a target signal in the ‘disturbed’ frequency intervals. However, to perform reliable analysis in these intervals, ad-hoc studies and tuning of the procedures would need to be set up. These additional procedures would require as much, if not longer, than the time spent on the ‘undisturbed’ data set. Moreover, since the ‘undisturbed’ intervals in data comprise over 95% of the total data, we believe this is a reasonable choice. In the future, a focused effort on the analysis of ‘disturbed bands’ could attempt to recover some sensitivity in those regions.

The identification of undisturbed bands is carried out via a visual inspection method. This visual inspection of the data is performed by two scientists who look at various distributions of the $2\overline{\mathcal{F}}$ values in the $\{f, \dot{f}\}$ parameter space in 50 mHz bands. They rank these 50 mHz bands with 4 numbers: 0,1,2,3; a ‘0’ ranking

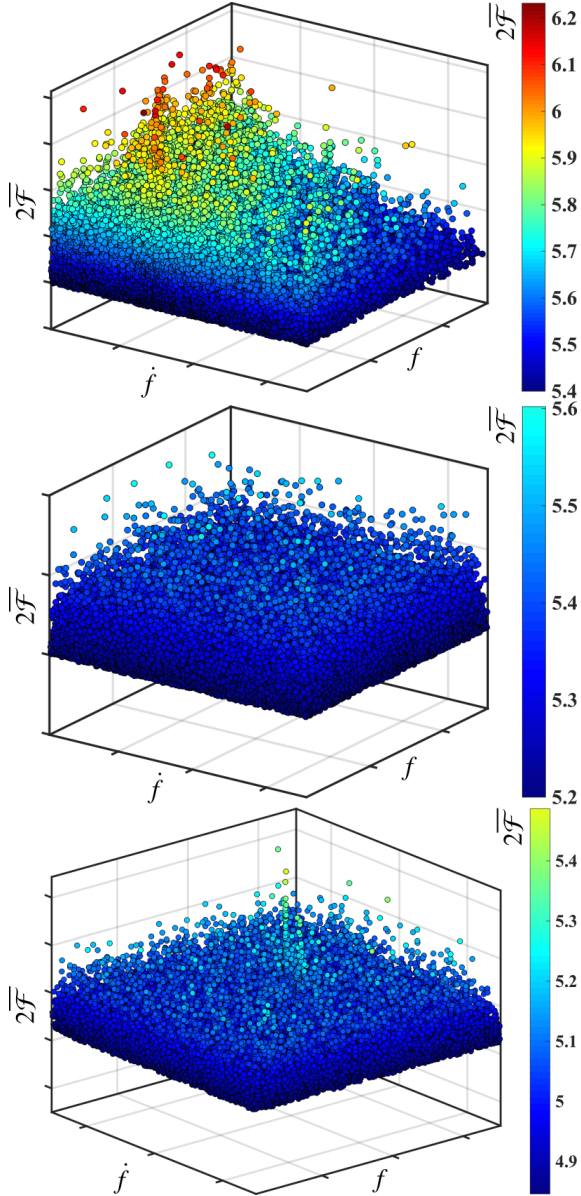


Figure 3: We plot the color-coded $2\overline{\mathcal{F}}$ values on the z-axis in three 50 mHz bands. The top-most band is marked as "disturbed"; the middle band is an example of an "undisturbed" band; the bottom-most band is an example of an "undisturbed" band but containing a simulated continuous gravitational wave signal.

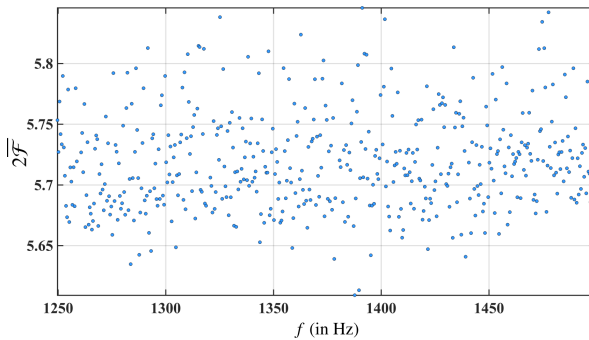


Figure 4: Highest values of $2\overline{\mathcal{F}}$ in every 0.5 Hz band as a function of starting frequency of the band.

marks the band as “undisturbed”, a ‘3’ ranks the band as ‘disturbed’, and rankings of ‘1’ or ‘2’ mark the band as “marginally disturbed”. A 50 mHz band is eventually considered to be undisturbed if it is marked as ‘0’ by both scientists. The criteria used for this inspection are based on training-sets of real data containing simulated signals. These criteria are designed to exclude disturbed set of results while retaining data sets with signal-like properties, and to err on the side of being conservative in terms of not falsely dismissing signals. A significant part of this visual inspection work can be automated [81], but at the time of this search, the procedure had not been fully tested and tuned. In figure 3, we empirically illustrate these criteria using three examples. Following this procedure, 3% of the total 5000 50 mHz bands are marked as “disturbed” by visual inspection. These excluded bands are listed in table 5 (Type D), together with the 50 mHz bands excluded as a result of the cleaning of known disturbances above (Type C), i.e. marked as “All Fake Data” in table 4. In consequence to these exclusions, there exist 0.5 Hz bands comprising results from less than ten 50 mHz bands. We define ‘fill-level’ as the percentage of 50 mHz bands that contribute to the results in 0.5 Hz intervals, where 100% fill-level signifies contribution by all ten 50 mHz bands. In figure 7, we show the distribution of fill-levels for the 0.5 Hz bands searched.

In figure 4, we plot the loudest observed candidate i.e. the candidate with the highest $2\overline{\mathcal{F}}$ value in each 0.5 Hz band in the search frequency range. The loudest candidate in our search has a detection-statistic value of $2\overline{\mathcal{F}} = 5.846$ at a frequency of roughly 1391.667 Hz. In order to determine the significance of this loudest candidate, we compare it to the expected value for the highest detection-statistic in our search. In order to determine this expected value, we have to estimate the number of independent trials performed in the search i.e. total number of independent realizations of our detection-statistic $2\overline{\mathcal{F}}$.

The number of independent realizations of the detection-statistic, N_{trials} , in a search through a bank of signal templates is smaller than the total number of searched templates, $N_{\text{templates}}$. We estimate N_{trials} as a function of frequency in 10 Hz frequency intervals. In each of these 10 Hz intervals, we fit the distribution of loudest candidates from 50 mHz bands to the expected distribution [3], and obtain the best-fitted value of N_{trials} . We perform this calculation in 10 Hz frequency intervals since the sky-grids, along with $N_{\text{templates}}$, are constant over 10 Hz frequency intervals. In figure 5, we plot the ratio $\mathcal{R} = N_{\text{trials}}/N_{\text{templates}}$, as a function of frequency.

With $\mathcal{R}(f)$ in hand, we evaluate the expected value for the loudest detection-statistic ($2\overline{\mathcal{F}}_{\text{exp}}$) in 0.5 Hz bands, and the standard deviation (σ_{exp}) of the associated distribution using (5)-(6) of [3], with $N_{\text{seg}} = 205$ and $N_{\text{trials}} = \mathcal{R} N_{\text{templates}}$. Based on these values, we can estimate the significance of the observed loudest candi-

dates (denoted by $2\overline{\mathcal{F}}_{\text{Loud}}$) as the ‘Critical Ratio’ (CR),

$$\text{CR} := \frac{2\overline{\mathcal{F}}_{\text{Loud}} - 2\overline{\mathcal{F}}_{\text{exp}}}{\sigma_{\text{exp}}}. \quad (3)$$

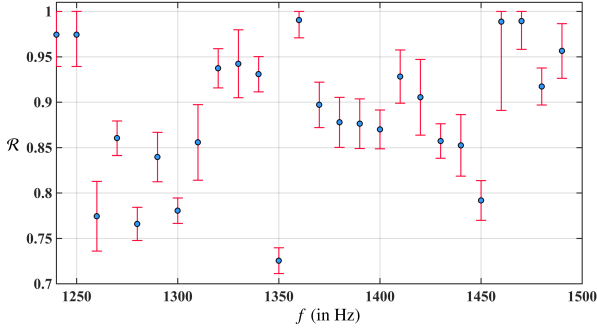


Figure 5: Plotted ratio $\mathcal{R} = N_{\text{trials}}/N_{\text{templates}}$ as a function of frequency in 10 Hz intervals. The error bars represent the $1\text{-}\sigma$ statistical errors from the fitting procedure described in the text.

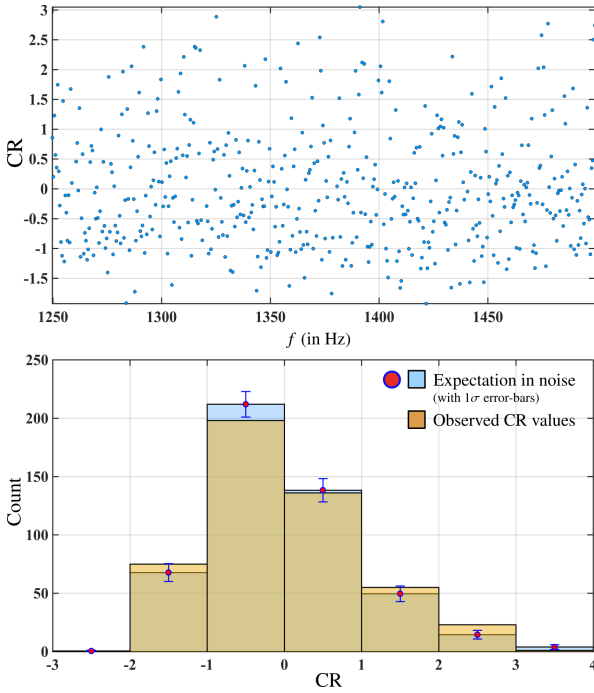


Figure 6: In the top panel, we plot the significance of the loudest observed candidate in every 0.5 Hz band as a function of starting frequency of the band. In the bottom panel, we show the distribution of CR values (top brown histogram bars), and the expected distribution of CR values for pure noise for reference (bottom blue histogram bars with markers). The significance folds in the expected value for the loudest $2\overline{\mathcal{F}}$ and its standard deviation.

In figure 6, we plot the CR values of the observed loudest candidates in 0.5 Hz bands as a function of frequency (top panel) and their distribution (bottom panel).

In this search, the overall loudest candidate with $2\overline{\mathcal{F}} = 5.846$ is also the most significant candidate, with $\text{CR} = 3.05$. A deviation of 3.05σ from the expected $2\overline{\mathcal{F}}$ value would not be significant enough to claim a detection if we had only searched a single 0.5 Hz band; in

fact, it is even less significant considering the fact that a total of 485 0.5 Hz bands were searched.

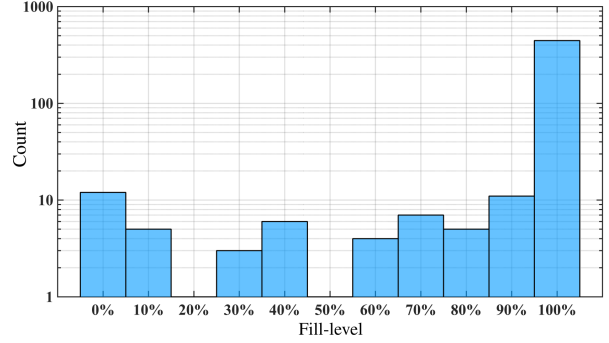


Figure 7: Distribution of fill-levels of 0.5 Hz bands.

We define the p -value associated with a CR as the probability of observing that particular value of CR or higher by random chance in a search over one 0.5 Hz band, performed over N_{trials} independent trials using N_{seg} segments. In figure 8, we see that the distribution of p -values associated with the loudest observed candidates in 0.5 Hz bands is consistent with what we expect from the noise-only scenario across the explored parameter space. In particular, we see in figure 8 that across 485 0.5 Hz bands searched by our set up, we expect 2.3 ± 1.5 candidates at least as significant as $\text{CR} = 3.05$ (p -value bin 10^{-2} for that band) by random chance, which makes our observed loudest candidate completely consistent with expectations from the noise-only case.

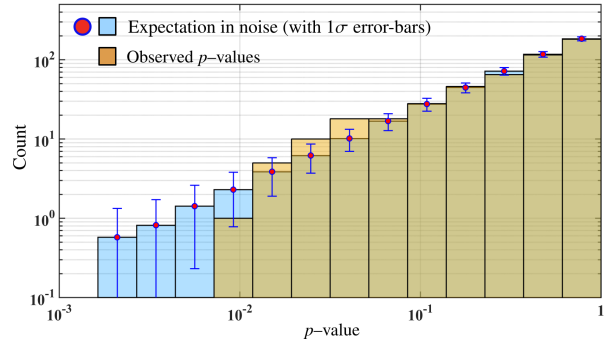


Figure 8: p -values for the loudest observed candidates in 0.5 Hz bands in the data (top brown histogram bars), and the expected distribution of p -values for pure noise for reference (bottom blue histogram bars with markers).

5 Upper-limits

Our search results do not deviate from the expectations from noise-only data. Hence, we set frequentist upper-limits on the maximum gravitational wave amplitude, $h_o^{90\%}$, from the target source population consistent with this null result at 90%-confidence in 0.5 Hz bands. Here, $h_o^{90\%}$ is the gravitational wave amplitude for which 90% of the target population of signals would

have produced a value of the detection statistic higher than the observed value.

Hence, we set frequentist upper-limits on the maximum detectable gravitational wave amplitude, $h_o^{90\%}$, at 90%-confidence in 0.5 Hz bands. Here, $h_o^{90\%}$ is the gravitational wave amplitude for which 90% of a population of signals with parameter values in our search range would have been produced a value of the detection statistic higher than the observed one in that search range.

Ideally, in order to estimate the $h_o^{90\%}$ values in each 0.5 Hz band across the 250 Hz signal-frequency search range, we would perform Monte-Carlo injection-and-recovery simulations in each of those bands. However, this is computationally very intensive. Therefore, we perform Monte-Carlo simulations in six 0.5 Hz bands spread evenly across the 250 Hz-wide frequency range, and in each of these six bands labeled by the index k , we estimate the $h_{o,CR_i}^{90\%,k}$ upper-limit value corresponding to eight different CR_i ‘significance bins’ for the putative observed loudest candidate: (0.0, 0.5, 1.0, 1.5, 2.0, 2.5, 3.0, 3.5). In each of these six bands and for each of the eight detection criteria, we calculate the so-called ‘sensitivity-depth’, defined in [3]: $\mathcal{D}_{CR_i}^{90\%,k}$. Lastly, we average these sensitivity-depths over the six bands and derive the average sensitivity-depth $\mathcal{D}_{CR_i}^{90\%}$ for each detection criterion. The values of the sensitivity-depths range between $\mathcal{D}_{CR_{0,0}}^{90\%} = 30.6 \text{ Hz}^{-1/2}$ and $\mathcal{D}_{CR_{3,5}}^{90\%} = 28.8 \text{ Hz}^{-1/2}$. We use these $\mathcal{D}_{CR_i}^{90\%}$ values to set upper-limits in the bands (labeled by l) where we have not performed any Monte-Carlo simulations as follows:

$$h_o^{90\%}(f_l) = \frac{\sqrt{S_h(f_l)}}{\mathcal{D}_{CR_i(l)}^{90\%}} \quad (4)$$

where, $CR_i(l)$ is the ‘significance bin’ i corresponding to the loudest observed candidate in the l -th frequency band, and $S_h(f_l)$ is the average power spectral density of the data in that band, measured in $\text{Hz}^{-1/2}$. The uncertainties on the $h_o^{90\%}$ upper-limit values introduced by this procedure amount to roughly 10% of the nominal $h_o^{90\%}$ upper-limit value. The final $h_o^{90\%}$ upper-limit values for this search, including an additional 10% calibration uncertainty, are given in table 2, and shown in figure 9.

Note that we do not set upper limits in 0.5 Hz bands where the results are entirely produced with fake Gaussian data inserted by the cleaning procedure described in section 4; $h_o^{90\%}$ upper-limit values for such bands do not appear either in table 2, or in figure 9.

Moreover, there also exist 50 mHz bands that contain results contributed by entirely fake data as a result of the cleaning procedure, or that have been excluded from the analysis because they are marked as

‘disturbed’ by the *visual inspection method* described in section 4. We mark the 0.5 Hz bands which host these particular 50 mHz bands with empty circles in figure 9. In table 5, we provide a complete list of such 50 mHz bands, highlighting that the upper-limit values do not apply to these bands. Finally, we note that, because of the cleaning procedure, there exist signal-frequency bands where the search results *may* have contributions from some fake data. We list these signal-frequency ranges in table 4. In line with the remarks in section 4, and for the sake of completeness, table 4 also contains the cleaned bands that featured under Type C in table 5, under the column header “All Fake Data”.

6 Conclusions

This search did not yield any evidence of continuous gravitational waves in the LIGO 5th Science Run data in the high-frequency range of 1250–1500 Hz. The lowest value for the upper-limit is 5.0×10^{-24} for signal frequencies between 1253.217–1255.217 Hz. We show in figure 9 that these $h_o^{90\%}$ upper-limits are about 33% higher than the upper-limits¹ [12] set in the same frequency range but using S6 data. In this frequency range, the S6 run data is about a factor 2.4 more sensitive compared to the S5 data used in this search.

We can express the $h_o^{90\%}$ upper-limits as bounds on the maximum distance from Earth within which we can exclude a rotating compact object emitting continuous gravitational waves at a given frequency f due to a fixed and non-axisymmetric mass quadrupole moment, characterised by $\epsilon \mathcal{I}$, with \mathcal{I} being the principal moment of inertia, and ϵ the ellipticity of the object. The ‘GW-spindown’ is the fraction of spin-down, $x|\dot{f}|$, responsible for continuous gravitational wave emission [53]. The ellipticity (ϵ) of the compact object necessary to sustain such emission is given by

$$\epsilon(f, x|\dot{f}|) = \sqrt{\frac{5c^5}{32\pi^4 G} \frac{x|\dot{f}|}{\mathcal{I} f^5}} \quad (5)$$

where, c is the speed of light, G is the Gravitational constant. Moreover, since the gravitational wave amplitude for an object at a distance d_{source} , with an ellipticity ϵ given by (5), is expressed as

$$h_o(f, x|\dot{f}|, d_{\text{source}}) = \frac{1}{d_{\text{source}}} \sqrt{\frac{5\mathcal{I}G}{2c^3} \frac{x|\dot{f}|}{f}} \quad (6)$$

we can recast the $h_o^{90\%}$ upper-limit curves as $(f, x|\dot{f}|)$ curves, or as (f, ϵ) curves, both parametrised by different values of the distance d_{source} , as shown in figure 10. We find that within 100 pc of Earth, our upper-limits exclude objects with ellipticities higher than roughly

¹The upper-limit values of [12] have been re-scaled according to [78] in order to allow a direct comparison with our $h_o^{90\%}$ upper-limit results.

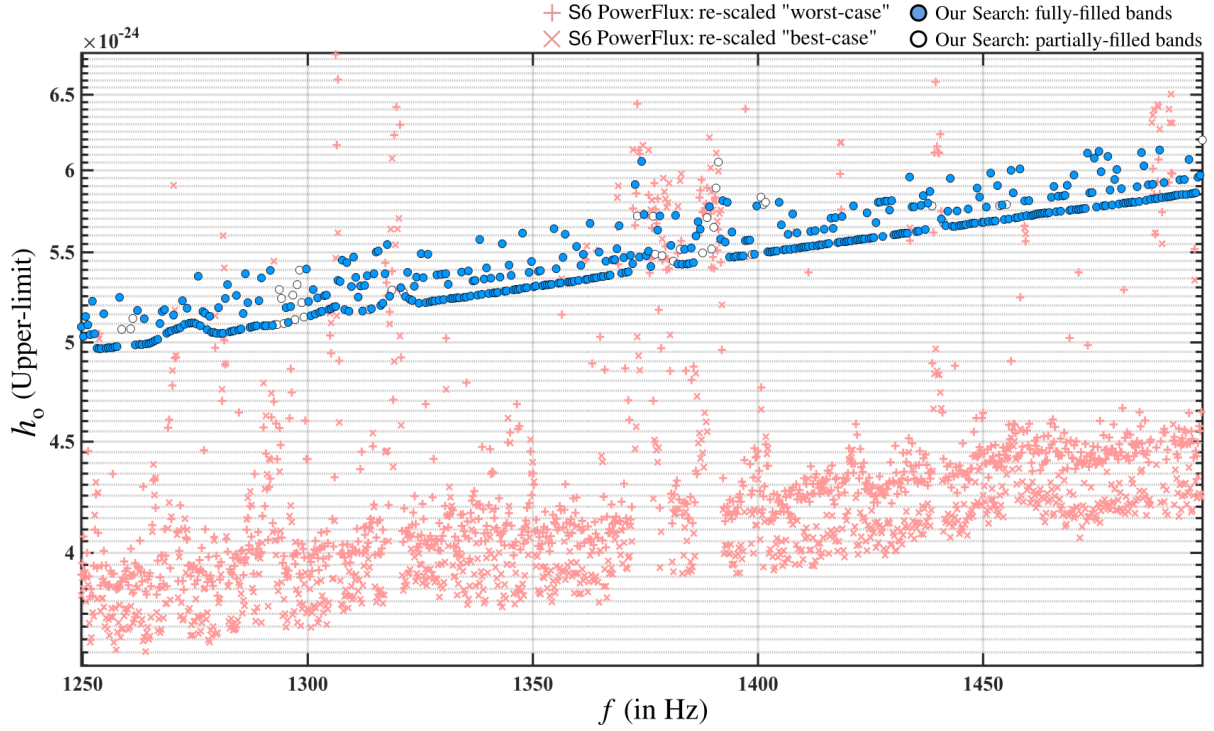


Figure 9: 90%-confidence upper-limits on the gravitational wave amplitude for signals with frequency within 0.5 Hz bands, over the entire sky, and within the spin-down range of the search described in section 3. The empty circular markers denote 0.5 Hz bands where the upper-limit value does not hold for all frequencies in that interval; the list of corresponding excluded frequencies is given in table 4. For reference, we also plot the upper-limit results (with non-circular markers) from the only other high-frequency search, on significantly more sensitive S6 data. It should be noted that the upper-limits from the *Power-Flux* search [12] are set at 95%-confidence rather than 90%-confidence level as in this search, but refer to 0.25 Hz bands rather than 0.5 Hz bands.

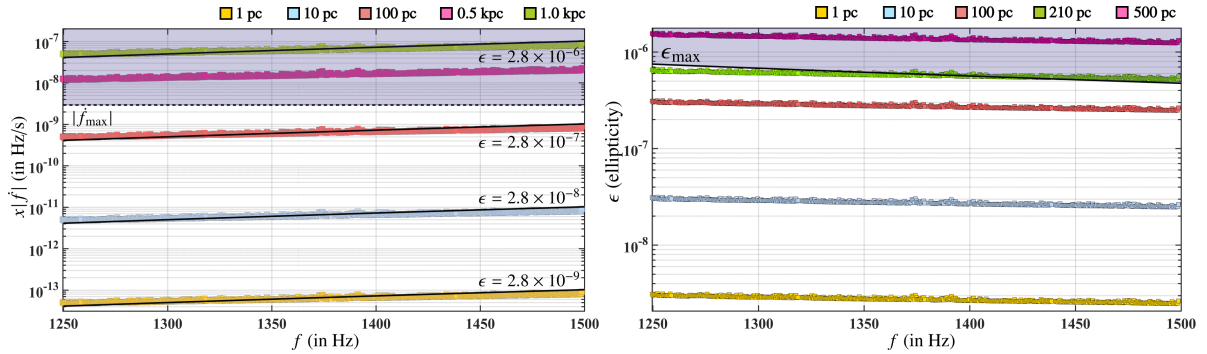


Figure 10: Gravitational wave amplitude upper-limits recast as curves in the $\{f, x|\dot{f}|\}$ -plane (left panel) for sources at given distances, where f is the signal-frequency and $x|\dot{f}|$ is the gravitational wave spin-down i.e. the fraction of the actual spin-down $|\dot{f}|$ that accounts for the rotational energy loss due to gravitational wave emission. We have superimposed curves of constant ellipticity ϵ . The dotted line at $|\dot{f}_{\max}|$ indicates the maximum magnitude of searched spin-down, namely 2.93×10^{-9} Hz/s. The right panel shows the corresponding $\{f, \epsilon\}$ upper-limit curves for sources at various distances. The $\epsilon_{\max} = 41.3 \times f^{-5/2}$ curve is the ellipticity corresponding to the highest $|\dot{f}|$ searched.

$2.8 \times 10^{-7} \left[\frac{10^{38} \text{kg m}^2}{\mathcal{I}} \right]$, corresponding to GW-spindown values between roughly 4.0×10^{-10} and 1.0×10^{-9} Hz/s. This value is well below the maximum elastic deformation that a relativistic star could sustain, see [39] and references therein.

The search presented here is probably the last all-sky search on S5 data, and by inspecting the higher frequency range for continuous gravitational wave emis-

sion, it concludes the Einstein@Home observing campaign on this data. Consistent with the recent results on S6 data [12], we also find no continuous GW signal in the S5 data. However, mechanisms for transient or intermittent GW emission have been proposed [65, 60, 41] which would not *a priori* exclude a signal that is “ON” during the S5 run and “OFF” during the S6 run. The estimates for the time-scales, frequencies, and spin-downs of continuous gravitational wave sig-

nals from isolated neutron stars lasting weeks to months span a very broad range of values – orders of magnitude. There are several different mechanisms that could sustain such emission at a level that this search could have detected, and with spin-down values consistent with the total energy emitted in the process, and with the spin-down range spanned by this search.

Acknowledgments

Maria Alessandra Papa, Bruce Allen and Xavier Siemens gratefully acknowledges the support from NSF

PHY Grant 1104902. All the post-processing computational work for this search was carried out on the ATLAS super-computing cluster at the Max-Planck-Institut für Gravitationsphysik/ Leibniz Universität Hannover. We also acknowledge the Continuous Wave Group of the LIGO Scientific Collaboration for useful discussions, and in particular, its chair Keith Riles for his careful reading of the manuscript. This paper has been assigned the LIGO Document Number P1600196.

Appendix: Tabular data

A.1 Upper-limit $h_0^{90\%}$ values

f (in Hz)	$h_0^{90\%} \times 10^{24}$	f (in Hz)	$h_0^{90\%} \times 10^{24}$	f (in Hz)	$h_0^{90\%} \times 10^{24}$	f (in Hz)	$h_0^{90\%} \times 10^{24}$
1249.717	5.1 ± 1.0	1250.217	5.0 ± 1.0	1250.717	5.1 ± 1.0	1251.217	5.1 ± 1.0
1251.717	5.0 ± 1.0	1252.217	5.2 ± 1.1	1252.717	5.0 ± 1.0	1253.217	5.0 ± 0.9
1253.717	5.0 ± 0.9	1254.217	5.0 ± 0.9	1254.717	5.2 ± 1.0	1255.217	5.0 ± 0.9
1255.717	5.0 ± 0.9	1256.217	5.0 ± 0.9	1256.717	5.0 ± 0.9	1257.217	5.0 ± 0.9
1257.717	5.0 ± 0.9	1258.217	5.2 ± 1.1	1258.717	5.1 ± 1.0	1260.717	5.1 ± 1.0
1261.217	5.1 ± 1.0	1261.717	5.0 ± 0.9	1262.217	5.2 ± 1.0	1262.717	5.0 ± 0.9
1263.217	5.0 ± 0.9	1263.717	5.1 ± 1.0	1264.217	5.0 ± 0.9	1264.717	5.0 ± 0.9
1265.217	5.0 ± 0.9	1265.717	5.0 ± 0.9	1266.217	5.0 ± 0.9	1266.717	5.0 ± 0.9
1267.217	5.1 ± 1.0	1267.717	5.2 ± 1.0	1268.217	5.2 ± 1.0	1268.717	5.0 ± 0.9
1269.217	5.1 ± 0.9	1269.717	5.1 ± 0.9	1270.217	5.1 ± 1.0	1270.717	5.1 ± 0.9
1271.217	5.1 ± 0.9	1271.717	5.1 ± 0.9	1272.217	5.2 ± 1.0	1272.717	5.1 ± 0.9
1273.217	5.2 ± 1.0	1273.717	5.1 ± 0.9	1274.217	5.1 ± 0.9	1274.717	5.1 ± 0.9
1275.217	5.1 ± 0.9	1275.717	5.4 ± 1.1	1276.217	5.1 ± 0.9	1276.717	5.2 ± 1.0
1277.217	5.2 ± 1.0	1277.717	5.1 ± 0.9	1278.217	5.1 ± 1.0	1278.717	5.1 ± 0.9
1279.217	5.1 ± 0.9	1279.717	5.0 ± 0.9	1280.217	5.2 ± 1.0	1280.717	5.0 ± 0.9
1281.217	5.0 ± 0.9	1281.717	5.2 ± 1.0	1282.217	5.3 ± 1.1	1282.717	5.1 ± 0.9
1283.217	5.1 ± 0.9	1283.717	5.1 ± 0.9	1284.217	5.3 ± 1.0	1284.717	5.1 ± 0.9
1285.217	5.1 ± 0.9	1285.717	5.2 ± 1.0	1286.217	5.4 ± 1.1	1286.717	5.2 ± 1.0
1287.217	5.1 ± 0.9	1287.717	5.1 ± 0.9	1288.217	5.1 ± 0.9	1288.717	5.1 ± 0.9
1289.217	5.2 ± 1.0	1289.717	5.4 ± 1.1	1290.217	5.1 ± 0.9	1290.717	5.1 ± 0.9
1291.217	5.1 ± 0.9	1291.717	5.4 ± 1.1	1292.217	5.1 ± 0.9	1292.717	5.1 ± 0.9
1293.217	5.1 ± 0.9	1293.717	5.3 ± 1.0	1294.217	5.2 ± 1.0	1294.717	5.1 ± 0.9
1295.217	5.2 ± 1.0	1295.717	5.1 ± 0.9	1296.217	5.2 ± 1.0	1296.717	5.3 ± 1.0
1297.217	5.1 ± 0.9	1297.717	5.3 ± 1.0	1298.217	5.4 ± 1.1	1298.717	5.2 ± 1.0
1299.217	5.1 ± 0.9	1299.717	5.4 ± 1.1	1300.217	5.2 ± 1.0	1300.717	5.1 ± 0.9
1301.217	5.3 ± 1.0	1301.717	5.2 ± 0.9	1302.217	5.2 ± 1.0	1302.717	5.2 ± 0.9
1303.217	5.2 ± 0.9	1303.717	5.3 ± 1.0	1304.217	5.3 ± 1.0	1304.717	5.2 ± 0.9
1305.217	5.2 ± 0.9	1305.717	5.2 ± 0.9	1306.217	5.2 ± 0.9	1306.717	5.3 ± 1.0
1307.217	5.3 ± 1.0	1307.717	5.5 ± 1.1	1308.217	5.2 ± 0.9	1308.717	5.4 ± 1.1
1309.217	5.2 ± 0.9	1309.717	5.3 ± 1.0	1310.217	5.5 ± 1.1	1310.717	5.4 ± 1.0
1311.217	5.2 ± 1.0	1311.717	5.3 ± 1.0	1312.217	5.2 ± 0.9	1312.717	5.3 ± 1.0
1313.217	5.4 ± 1.0	1313.717	5.2 ± 0.9	1314.217	5.2 ± 0.9	1314.717	5.4 ± 1.0
1315.217	5.5 ± 1.1	1315.717	5.5 ± 1.1	1316.217	5.2 ± 0.9	1316.717	5.2 ± 0.9
1317.217	5.4 ± 1.0	1317.717	5.5 ± 1.1	1318.217	5.2 ± 0.9	1318.717	5.3 ± 0.9
1320.717	5.3 ± 0.9	1321.217	5.3 ± 0.9	1321.717	5.2 ± 0.9	1322.217	5.4 ± 1.0
1322.717	5.2 ± 0.9	1323.217	5.2 ± 0.9	1323.717	5.3 ± 1.0	1324.217	5.4 ± 1.0
1324.717	5.2 ± 0.9	1325.217	5.5 ± 1.1	1325.717	5.4 ± 1.0	1326.217	5.2 ± 0.9
1326.717	5.5 ± 1.1	1327.217	5.2 ± 0.9	1327.717	5.2 ± 0.9	1328.217	5.2 ± 0.9
1328.717	5.4 ± 1.0	1329.217	5.2 ± 0.9	1329.717	5.4 ± 1.0	1330.217	5.2 ± 0.9

f (in Hz)	$h_0^{90\%} \times 10^{24}$	f (in Hz)	$h_0^{90\%} \times 10^{24}$	f (in Hz)	$h_0^{90\%} \times 10^{24}$	f (in Hz)	$h_0^{90\%} \times 10^{24}$
1330.717	5.4 ± 1.0	1331.217	5.3 ± 1.0	1331.717	5.2 ± 0.9	1332.217	5.2 ± 0.9
1332.717	5.2 ± 0.9	1333.217	5.2 ± 0.9	1333.717	5.2 ± 0.9	1334.217	5.4 ± 1.0
1334.717	5.2 ± 0.9	1335.217	5.2 ± 0.9	1335.717	5.4 ± 1.0	1336.217	5.3 ± 0.9
1336.717	5.3 ± 1.0	1337.217	5.3 ± 1.0	1337.717	5.3 ± 0.9	1338.217	5.6 ± 1.1
1338.717	5.3 ± 0.9	1339.217	5.3 ± 1.0	1339.717	5.4 ± 1.0	1340.217	5.3 ± 0.9
1340.717	5.4 ± 1.0	1341.217	5.3 ± 0.9	1341.717	5.3 ± 0.9	1342.217	5.3 ± 0.9
1342.717	5.4 ± 1.0	1343.217	5.6 ± 1.1	1343.717	5.3 ± 0.9	1344.217	5.3 ± 0.9
1344.717	5.4 ± 1.0	1345.217	5.4 ± 1.0	1345.717	5.3 ± 0.9	1346.217	5.3 ± 0.9
1346.717	5.3 ± 0.9	1347.217	5.3 ± 0.9	1347.717	5.6 ± 1.2	1348.217	5.3 ± 0.9
1348.717	5.3 ± 0.9	1349.217	5.4 ± 1.0	1349.717	5.4 ± 1.0	1350.217	5.3 ± 0.9
1350.717	5.3 ± 0.9	1351.217	5.4 ± 1.0	1351.717	5.4 ± 1.0	1352.217	5.3 ± 0.9
1352.717	5.3 ± 0.9	1353.217	5.3 ± 0.9	1353.717	5.3 ± 0.9	1354.217	5.3 ± 0.9
1354.717	5.6 ± 1.2	1355.217	5.4 ± 1.0	1355.717	5.3 ± 0.9	1356.217	5.3 ± 0.9
1356.717	5.5 ± 1.1	1357.217	5.6 ± 1.1	1357.717	5.3 ± 0.9	1358.217	5.3 ± 0.9
1358.717	5.3 ± 0.9	1359.217	5.3 ± 0.9	1359.717	5.5 ± 1.1	1360.217	5.3 ± 0.9
1360.717	5.4 ± 1.0	1361.217	5.5 ± 1.1	1361.717	5.3 ± 0.9	1362.217	5.3 ± 0.9
1362.717	5.7 ± 1.2	1363.217	5.4 ± 0.9	1363.717	5.4 ± 0.9	1364.217	5.4 ± 0.9
1364.717	5.5 ± 1.1	1365.217	5.4 ± 0.9	1365.717	5.4 ± 0.9	1366.217	5.4 ± 1.1
1366.717	5.4 ± 0.9	1367.217	5.4 ± 0.9	1367.717	5.5 ± 1.1	1368.217	5.5 ± 1.1
1368.717	5.5 ± 1.1	1369.217	5.7 ± 1.1	1369.717	5.4 ± 0.9	1370.217	5.5 ± 1.1
1370.717	5.4 ± 0.9	1371.217	5.4 ± 0.9	1371.717	5.5 ± 1.1	1372.217	5.4 ± 0.9
1372.717	5.9 ± 1.1	1373.217	5.7 ± 1.2	1373.717	5.5 ± 1.0	1374.217	6.1 ± 1.2
1374.717	5.7 ± 1.1	1375.217	5.5 ± 1.0	1375.717	5.5 ± 1.1	1376.217	5.4 ± 0.9
1376.717	5.7 ± 1.1	1377.217	5.5 ± 1.0	1377.717	5.6 ± 1.1	1378.217	5.7 ± 1.0
1378.717	5.5 ± 1.0	1380.717	5.5 ± 1.1	1381.217	5.4 ± 0.9	1381.717	5.7 ± 1.2
1382.217	5.4 ± 0.9	1382.717	5.5 ± 1.1	1383.217	5.4 ± 0.9	1383.717	5.5 ± 1.1
1384.217	5.4 ± 0.9	1384.717	5.4 ± 0.9	1385.217	5.5 ± 1.1	1385.717	5.4 ± 0.9
1386.217	5.6 ± 1.1	1386.717	5.7 ± 1.1	1387.217	5.6 ± 1.0	1387.717	5.5 ± 1.0
1388.717	5.7 ± 1.1	1389.217	5.8 ± 1.2	1389.717	5.5 ± 1.0	1390.217	5.6 ± 1.1
1390.717	5.9 ± 1.2	1391.217	6.1 ± 1.1	1391.717	5.6 ± 1.0	1392.217	5.8 ± 1.2
1392.717	5.6 ± 1.1	1393.217	5.8 ± 1.2	1393.717	5.5 ± 1.0	1394.217	5.6 ± 1.1
1394.717	5.5 ± 1.0	1395.217	5.5 ± 1.0	1395.717	5.5 ± 1.0	1396.217	5.5 ± 1.0
1396.717	5.5 ± 1.0	1397.217	5.6 ± 1.1	1397.717	5.6 ± 1.1	1398.217	5.6 ± 1.1
1398.717	5.5 ± 1.0	1399.217	5.5 ± 1.0	1399.717	5.8 ± 1.2	1400.717	5.8 ± 1.2
1401.217	5.8 ± 1.2	1401.717	5.8 ± 1.1	1402.217	5.5 ± 1.0	1402.717	5.5 ± 1.0
1403.217	5.5 ± 1.0	1403.717	5.5 ± 1.0	1404.217	5.5 ± 1.0	1404.717	5.8 ± 1.2
1405.217	5.7 ± 1.1	1405.717	5.5 ± 1.0	1406.217	5.5 ± 1.0	1406.717	5.6 ± 1.1
1407.217	5.5 ± 1.0	1407.717	5.7 ± 1.1	1408.217	5.5 ± 1.0	1408.717	5.6 ± 1.1
1409.217	5.5 ± 1.0	1409.717	5.5 ± 1.0	1410.217	5.5 ± 1.0	1410.717	5.5 ± 1.0
1411.217	5.5 ± 1.0	1411.717	5.6 ± 1.1	1412.217	5.5 ± 1.0	1412.717	5.6 ± 1.1
1413.217	5.5 ± 1.0	1413.717	5.5 ± 1.0	1414.217	5.5 ± 1.0	1414.717	5.6 ± 1.1
1415.217	5.5 ± 1.0	1415.717	5.6 ± 1.0	1416.217	5.7 ± 1.1	1416.717	5.6 ± 1.1
1417.217	5.7 ± 1.1	1417.717	5.6 ± 1.0	1418.217	5.6 ± 1.0	1418.717	5.7 ± 1.1
1419.217	5.6 ± 1.0	1419.717	5.6 ± 1.0	1420.217	5.6 ± 1.0	1420.717	5.6 ± 1.0
1421.217	5.8 ± 1.1	1421.717	5.6 ± 1.0	1422.217	5.6 ± 1.0	1422.717	5.6 ± 1.0
1423.217	5.6 ± 1.0	1423.717	5.6 ± 1.0	1424.217	5.7 ± 1.1	1424.717	5.6 ± 1.0
1425.217	5.6 ± 1.0	1425.717	5.6 ± 1.0	1426.217	5.7 ± 1.1	1426.717	5.8 ± 1.1
1427.217	5.8 ± 1.1	1427.717	5.6 ± 1.0	1428.217	5.8 ± 1.1	1428.717	5.8 ± 1.1
1429.217	5.8 ± 1.1	1429.717	5.8 ± 1.1	1430.217	5.6 ± 1.0	1430.717	5.6 ± 1.0
1431.217	5.6 ± 1.0	1431.717	5.6 ± 1.0	1432.217	5.6 ± 1.0	1432.717	5.6 ± 1.0
1433.217	5.6 ± 1.0	1433.717	6.0 ± 1.2	1434.217	5.8 ± 1.1	1434.717	5.8 ± 1.1
1435.217	5.6 ± 1.0	1435.717	5.6 ± 1.0	1436.217	5.8 ± 1.1	1436.717	5.8 ± 1.1
1437.217	5.6 ± 1.0	1437.717	5.8 ± 1.1	1438.217	5.9 ± 1.1	1438.717	5.8 ± 1.1
1440.717	5.7 ± 1.0	1441.217	5.7 ± 1.0	1441.717	5.7 ± 1.0	1442.217	5.7 ± 1.1
1442.717	5.9 ± 1.2	1443.217	5.7 ± 1.0	1443.717	5.7 ± 1.0	1444.217	5.7 ± 1.1
1444.717	5.7 ± 1.0	1445.217	5.7 ± 1.0	1445.717	5.7 ± 1.0	1446.217	5.7 ± 1.0
1446.717	5.8 ± 1.1	1447.217	5.7 ± 1.0	1447.717	5.7 ± 1.0	1448.217	5.7 ± 1.0
1448.717	5.9 ± 1.1	1449.217	5.8 ± 1.1	1449.717	5.7 ± 1.0	1450.217	5.7 ± 1.0
1450.717	5.8 ± 1.1	1451.217	5.7 ± 1.0	1451.717	6.0 ± 1.2	1452.217	5.7 ± 1.0

f (in Hz)	$h_0^{90\%} \times 10^{24}$	f (in Hz)	$h_0^{90\%} \times 10^{24}$	f (in Hz)	$h_0^{90\%} \times 10^{24}$	f (in Hz)	$h_0^{90\%} \times 10^{24}$
1452.717	5.7 ± 1.0	1453.217	5.9 ± 1.1	1453.717	5.8 ± 1.1	1454.217	5.8 ± 1.1
1454.717	5.7 ± 1.0	1455.217	5.8 ± 1.1	1455.717	5.7 ± 1.0	1456.217	6.0 ± 1.2
1456.717	5.9 ± 1.1	1457.217	5.7 ± 1.0	1457.717	5.7 ± 1.0	1458.217	6.0 ± 1.2
1458.717	5.7 ± 1.0	1459.217	5.8 ± 1.1	1459.717	5.7 ± 1.0	1460.217	5.8 ± 1.1
1460.717	5.7 ± 1.0	1461.217	5.7 ± 1.0	1461.717	5.7 ± 1.0	1462.217	5.7 ± 1.0
1462.717	5.7 ± 1.0	1463.217	5.7 ± 1.0	1463.717	5.7 ± 1.0	1464.217	5.7 ± 1.0
1464.717	5.7 ± 1.0	1465.217	5.8 ± 1.1	1465.717	5.9 ± 1.1	1466.217	5.7 ± 1.0
1466.717	5.8 ± 1.1	1467.217	5.7 ± 1.0	1467.717	5.8 ± 1.1	1468.217	5.8 ± 1.1
1468.717	5.9 ± 1.1	1469.217	5.8 ± 1.0	1469.717	5.8 ± 1.0	1470.217	6.0 ± 1.2
1470.717	5.8 ± 1.0	1471.217	5.8 ± 1.0	1471.717	5.8 ± 1.0	1472.217	5.8 ± 1.0
1472.717	5.8 ± 1.0	1473.217	6.1 ± 1.3	1473.717	5.9 ± 1.1	1474.217	5.9 ± 1.1
1474.717	6.1 ± 1.2	1475.217	5.8 ± 1.0	1475.717	6.1 ± 1.3	1476.217	6.0 ± 1.2
1476.717	5.8 ± 1.0	1477.217	5.8 ± 1.0	1477.717	6.1 ± 1.2	1478.217	5.9 ± 1.1
1478.717	5.8 ± 1.0	1479.217	5.9 ± 1.1	1479.717	6.0 ± 1.2	1480.217	5.8 ± 1.0
1480.717	5.9 ± 1.1	1481.217	5.8 ± 1.0	1481.717	5.8 ± 1.0	1482.217	5.8 ± 1.0
1482.717	5.8 ± 1.0	1483.217	5.8 ± 1.0	1483.717	5.8 ± 1.0	1484.217	5.9 ± 1.1
1484.717	5.8 ± 1.0	1485.217	6.1 ± 1.2	1485.717	6.0 ± 1.2	1486.217	5.8 ± 1.0
1486.717	5.9 ± 1.1	1487.217	5.8 ± 1.0	1487.717	5.9 ± 1.1	1488.217	5.8 ± 1.0
1488.717	5.8 ± 1.0	1489.217	6.1 ± 1.2	1489.717	5.8 ± 1.0	1490.217	5.9 ± 1.1
1490.717	5.8 ± 1.0	1491.217	5.8 ± 1.0	1491.717	5.8 ± 1.0	1492.217	5.8 ± 1.0
1492.717	5.8 ± 1.0	1493.217	5.8 ± 1.0	1493.717	5.9 ± 1.1	1494.217	5.8 ± 1.0
1494.717	5.9 ± 1.1	1495.217	5.8 ± 1.0	1495.717	6.1 ± 1.2	1496.217	5.9 ± 1.0
1496.717	5.9 ± 1.0	1497.217	5.9 ± 1.0	1497.717	6.0 ± 1.2	1498.217	6.0 ± 1.2
1498.717	6.2 ± 1.3	–	–	–	–	–	–

Table 2: Left column denotes the starting frequency of each 0.5 Hz signal-frequency band in which we set upper-limits; right column states the upper-limit value i.e. $h_0^{90\%}$, for that 0.5 Hz band. Note: the $h_0^{90\%}$ values quoted here include additional 10% uncertainty introduced by data calibration procedure.

A.2 Detector Lines

Source	f (Hz)	Harmonics	LFS (Hz)	HFS (Hz)	IFO
Power Mains	60.0	5	1.0	1.0	L,H
Violin Mode	1373.75	1	0.1	0.1	H
Violin Mode	1374.44	1	0.1	0.1	H
Violin Mode	1377.14	1	0.1	0.1	H
Violin Mode	1378.75	1	0.1	0.1	H
Violin Mode	1379.52	1	0.1	0.1	H
Violin Mode	1389.06	1	0.06	0.06	H
Violin Mode	1389.82	1	0.07	0.07	H
Violin Mode	1391.5	1	0.2	0.2	H
Violin Mode	1372.925	1	0.075	0.075	L
Violin Mode	1374.7	1	0.1	0.1	L
Violin Mode	1375.2	1	0.1	0.1	L
Violin Mode	1378.39	1	0.1	0.1	L
Violin Mode	1387.4	1	0.05	0.05	L
Violin Mode	1388.5	1	0.3	0.3	L

Table 3: Instrumental lines identified and cleaned before the Einstein@Home analysis. The different columns represent: (I) the source of the line; (II) the central frequency of the instrumental line; (III) the number of harmonics in the signal-frequency range, i.e. 1249.7 Hz and 1499.7 Hz; (IV) Low-Frequency-Side (LFS) of the knockout band; (V) High-Frequency-Side (HFS) of the knockout band; (VI) the interferometer where the instrumental lines were identified. Note that when there are higher harmonics present, the knockout bandwidth remains constant.

A.3 Signal-frequency ranges and Data Quality

Source	Mixed (Isolated)	Mixed (Left)	All Fake Data	Mixed (Right)	IFO
Power Mains	--	1258.7976 – 1259.2024	1259.2024 – 1260.7974	1260.7974 – 1261.2026	H,L
Power Mains	--	1318.7915 – 1319.2085	1319.2085 – 1320.7913	1320.7913 – 1321.2087	H,L
Violin Mode	1372.6360 – 1373.2140	--	--	--	L
Violin Mode	1373.4359 – 1374.0641	--	--	--	H
Violin Mode	1374.1259 – 1375.5142	--	--	--	H,L
Violin Mode	1376.8256 – 1377.4554	--	--	--	H
Violin Mode	1378.0755 – 1379.0646	--	--	--	H,L
Violin Mode	1379.2054 – 1379.8347	--	--	--	H
Power Mains	--	1378.7854 – 1379.2146	1379.2146 – 1380.7852	1380.7852 – 1381.2148	H,L
Violin Mode	1387.1346 – 1387.6655	--	--	--	L
Violin Mode	--	1387.9845 – 1388.4155	1388.4155 – 1388.5844	1388.5844 – 1389.0156	H,L
Violin Mode	1388.7844 – 1389.3356	--	--	--	H,L
Violin Mode	1389.5343 – 1390.1057	--	--	--	H
Violin Mode	1391.0842 – 1391.9159	--	--	--	H,L
Power Mains	--	1438.7793 – 1439.2207	1439.2207 – 1440.7791	1440.7791 – 1441.2209	H,L
Power Mains	--	1498.7732 – 1499.2268	1499.2268 – 1499.7170	--	H,L

Table 4: Signal-frequency ranges where the results might have contributions from fake data. When the results are entirely due to artificial data, the band is listed in the “All Fake Data” column; bands where the results comprise of contributions from both fake and real data are listed in the other three columns. The “Mixed (Left)” and “Mixed (Right)” columns are populated only when there is a matching “All Fake Data” entry, which highlights the same physical cause for the fake data, i.e. the cleaning. The “Mixed (Isolated)” column lists isolated ranges of mixed data. The list of input data frequencies where the data was substituted with artificial noise are given in table 3.

A.4 Omitted 50 mHz bands from Signal-frequency

f_{start} (in Hz)	f_{end} (in Hz)	Type	f_{start} (in Hz)	f_{end} (in Hz)	Type
1258.617	1258.717	D	1259.217	1260.717	C
1291.017	1291.067	D	1292.567	1292.867	D
1293.267	1293.567	D	1293.917	1294.217	D
1296.367	1296.817	D	1297.517	1297.717	D
1298.667	1298.967	D	1313.467	1313.517	D
1318.567	1318.667	D	1319.217	1320.717	C
1372.867	1373.167	D	1376.417	1376.817	D
1378.517	1378.617	D	1379.217	1380.717	C
1382.567	--	D	1387.317	--	D
1387.767	1388.217	D	1388.417	1388.517	C
1389.467	--	D	1389.767	1390.217	D
1390.467	1390.867	D	1390.967	1391.117	D
1395.217	1395.467	D	1398.417	1398.667	D
1399.967	1400.867	D	1400.967	1401.267	D
1438.417	1438.517	D	1439.267	1440.717	C
1453.467	1453.517	D	1454.967	1455.067	D
1498.317	1498.467	D	1499.267	1499.667	C

Table 5: 50 mHz search-frequency bands that were identified as “disturbed” based on Visual Inspection (Type D), or where the results were produced from “All Fake Data”, as detailed in table 4 (Type C). Both sets of bands (Type D and C) were excluded from the analysis. The first two columns list the starting frequency of the first and last 50 mHz band in the contiguous range of excluded bands.

* * *

IV Adaptive clustering algorithm for continuous gravitational wave searches

Avneet Singh^{1,2,3,†}, Maria Alessandra Papa^{1,2,4,‡}, Heinz-Bernd Eggenstein^{2,3}, Sinéad Walsh^{1,2}

¹ Max-Planck-Institut für Gravitationsphysik, am Mühlenberg 1, 14476, Potsdam-Golm

² Max-Planck-Institut für Gravitationsphysik, Callinstraße 38, 30167, Hannover

³ Leibniz Universität Hannover, Welfengarten 1, 30167, Hannover

⁴ University of Wisconsin-Milwaukee, Milwaukee, Wisconsin 53201, USA

Abstract

In hierarchical searches for continuous gravitational waves, clustering of candidates is an important post-processing step because it reduces the number of noise candidates that are followed-up at successive stages [3][25][55]. Previous clustering procedures bundled together nearby candidates ascribing them to the same root cause (be it a signal or a disturbance), based on a predefined cluster volume. In this paper, we present a procedure that adapts the cluster volume to the data itself and checks for consistency of such volume with what is expected from a signal. This significantly improves the noise rejection capabilities at fixed detection threshold, and at fixed computing resources for the follow-up stages, this results in an overall more sensitive search. This new procedure was employed in the first Einstein@Home search on data from the first science run of the advanced LIGO detectors (O1) [45].

1 Introduction

In searches for continuous gravitational wave (CW) signals (e.g. [11, 55, 68, 81, 16, 14, 4, 2, 3]), like in many other gravitational wave searches, the detection statistic can be triggered both by signals and by noise disturbances. Furthermore, when the signal or disturbance is strong, it typically does not trigger only a single template waveform but also many nearby ones.

‘Clustering’ is the procedure through which we assess elevated detection statistic template points close enough to each other in parameter space that might arise from the same root cause, i.e. signal or noise disturbance. The reason for doing this is that the clustering properties help discriminate candidates due to signals from the candidates due to disturbances, and in certain cases (e.g. loud disturbances), bundle together large numbers of candidates together which one does not need to assess separately. In case of hierarchical sub-threshold searches (e.g. [25, 55]), clustering is performed on the candidates from the first stage. This significantly reduces the number of candidates for subsequent follow-up at fixed threshold on the detection statistic. Hence, at fixed computing budget for the follow-up stages, clustering allows to lower the threshold and increase the sensitivity of the search.

In previous searches using a clustering procedure, the cluster volume was defined once and for all, based on the average clustering properties of signals [25, 55]. In this paper, we present a clustering method that is adaptive, i.e. it adapts the clustering size in each dimension to the local distribution of candidates in parameter space, and then it requires consistency in clustering among the different dimensions. We have named it AdCl procedure (*Adaptive Clustering Procedure*).

As the name suggests, the AdCl procedure adapts its parameters to the data. If the data were pure Gaus-

sian noise, all this sophistication would not be necessary. Hence, in order to illustrate the AdCl under realistic and relevant conditions, throughout this paper we use small (50 mHz) frequency-domain snippets of data from the first Advanced LIGO observing run (O1).

The paper is organised as follows. In section 2, we introduce the fundamental idea behind the adaptive clustering procedure; in section 3, we detail how it functions and introduce the various parameters that characterise it. In section 4, we present and compare the performance of this procedure against the clustering procedure used in previous searches. The last section summarises the main findings and discusses prospects.

2 Clustering of candidates

A typical all-sky CW search covers the entire sky, a large frequency range and a certain range of spin-down values. In this parameter space, grids are set up and a detection statistic is computed at each grid point.

We indicate a generic grid point with $\lambda_i \equiv (f_i, \dot{f}_i, \alpha_i, \delta_i)$, with $i = 1 \dots N$, and the detection statistic calculated at that grid point with Γ_i . Here, α_i, δ_i are the equatorial sky coordinates of the signal template, while f_i and \dot{f}_i denote the frequency and the first-order spin-down respectively. The result of the search are the ensemble of $\kappa_i \equiv (\lambda_i, \Gamma_i)$. We concentrate on the subset of these results that are interesting, i.e. where the detection statistic values are elevated above some predefined threshold (Γ_L). Let’s assume that there are M such results. We will refer to these as the candidates.

Operationally, the clustering procedure is an iterative process and it was first introduced in [25]: we begin with the highest detection statistic value in our results, corresponding to, say, candidate $\kappa_{i(1)}$, where ‘1’ identifies the first iteration of the clustering procedure (i.e.

[†]avneet.singh@aei.mpg.de; [‡]maria.alessandra.papa@aei.mpg.de

the first cluster). The candidate $\kappa_{i(1)}$ is also called the *seed* for the first cluster. We then find elevated detection statistic values “nearby” λ_i , and we associate them with $\kappa_{i(1)}$. These set of points will form the first cluster, and they – along with the seed $\kappa_{i(1)}$ – will be referred to as the *occupants* of the cluster. We proceed to remove these occupants associated with $\kappa_{i(1)}$ from the original set of candidates. In the next iteration, we consider the highest detection statistic value among the remaining

set of candidates, now $\kappa_{i(2)}$, i.e. the seed for the second cluster. We again find elevated detection statistic values nearby $\kappa_{i(2)}$ and associate them with it. The occupants of the second cluster are again removed from the set of remaining candidates. This process is repeated with $\kappa_{i(3)}$, $\kappa_{i(4)}$, $\kappa_{i(5)}$ and so on. The process ends when we have no more seeds left above a certain predefined detection statistic threshold (Γ_S).

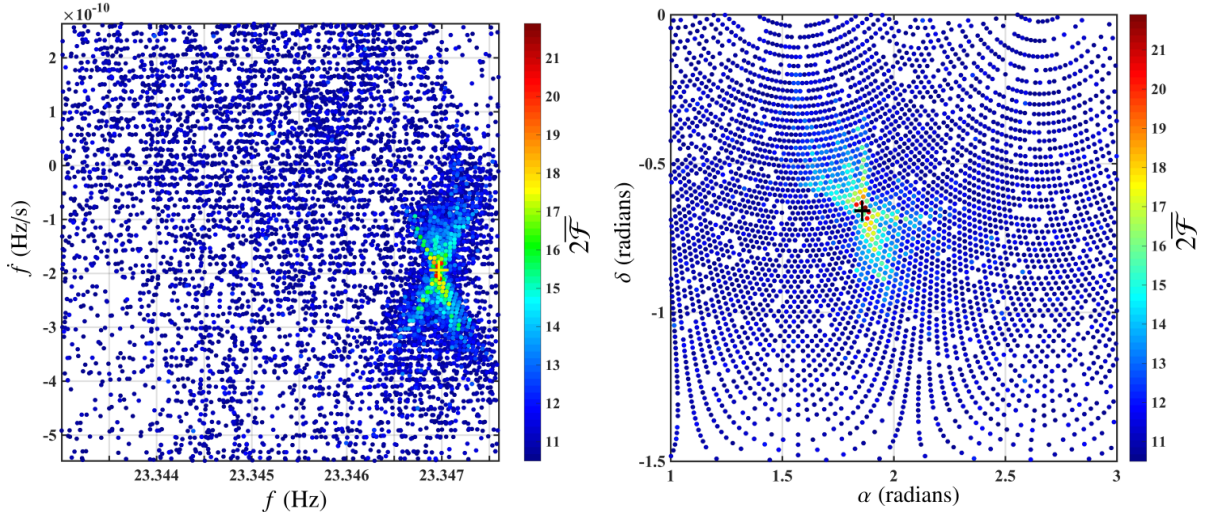


Figure 1: (top panel) Distribution of \mathcal{F} -statistic values ($2\overline{\mathcal{F}}$) in the parameter space near a fake signal in noise (from LIGO O1 data). Note the elevated $2\overline{\mathcal{F}}$ values in the neighborhood of the injection. The elevated $2\overline{\mathcal{F}}$ values are clearly coincident in frequency-spindown and the sky. The location of the injection is marked with ‘+’.

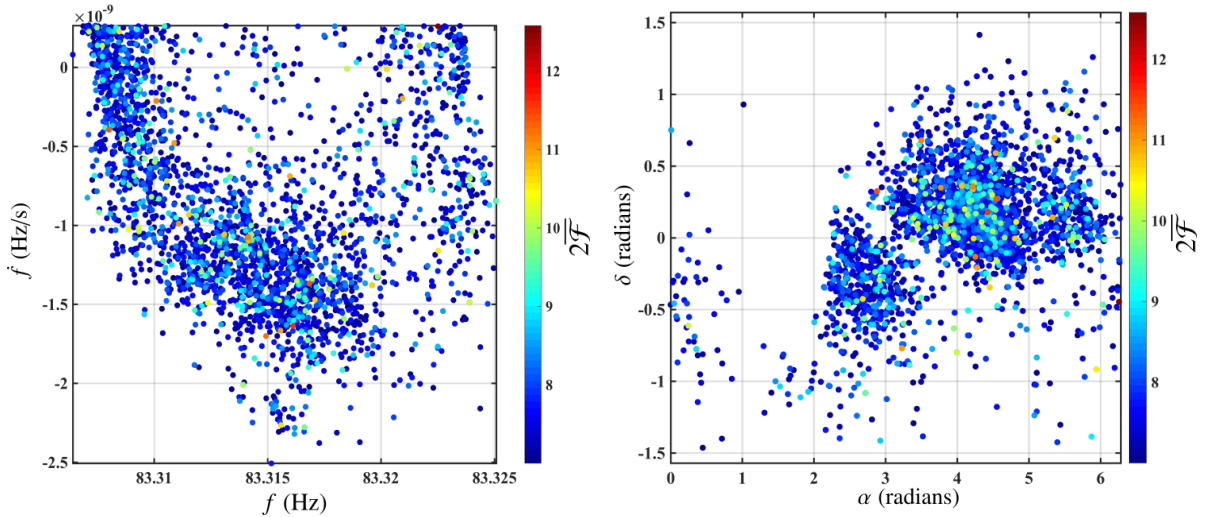


Figure 1: (bottom panel) Distribution of \mathcal{F} -statistic values ($2\overline{\mathcal{F}}$) in the parameter space in the vicinity of a typical noise disturbance in LIGO O1 data. In contrast with the top panel, the elevated $2\overline{\mathcal{F}}$ values due to the disturbance are not coincident between frequency-spindown and sky.

The core of the AdCl procedure procedure lies in identifying an over-density of candidates in frequency and spin-down around each seed, in determining its extension, and in checking whether that set of candidates

also presents an over-density in sky around its seed. These features are trademark signatures of signals (e.g. see figure 1 top panel), and they are not shared by most noise fluctuations/disturbances (e.g. see figure 1 bot-

tom panel). We note that previous clustering algorithms did not require such coincident over-densities between frequency-spindown and the sky, and hence, lead to a higher number of false alarms.

Furthermore, the AdCl procedure dynamically defines the clustering neighbourhood based on the data itself. In contrast, previous procedures derived a static clustering neighbourhood around the seed based on average clustering properties of the signals independently of the data. Thus, the AdCl procedure enables us to bundle together any over-density that extends over large volumes of parameter space as a single follow-up candidate, and hence, the number of candidates to follow-up from highly populated parameter space regions decreases significantly.

3 The cluster size

3.1 A measure of distance in frequency and spin-down space (F-space)

The clustering is applied to a set of candidates χ_1 whose detection statistic value is above a certain threshold Γ_L ; Let's assume that there are M such candidates:

$$\chi_1 := \{\kappa_\ell\} \quad | \quad \Gamma_\ell \geq \Gamma_L, \quad (1)$$

where $1 \leq \ell \leq M$.

In general, at each iteration i , the clustering procedure defines a new cluster, and it does this by operating on a set of candidates χ_i . We indicate the seed for the i -th cluster with $\kappa_{\ell(i)}$, with $\ell(i)$ being the index that corresponds to the candidate with the loudest detection statistic value among the candidates in χ_i . We constrain the cluster seed to exceed a fixed threshold Γ_S , which in general is larger than Γ_L . The clustering procedure stops at iteration $N_c + 1$ when there are no more candidates with detection statistic values above Γ_S in χ_{N_c+1} , i.e. when $\Gamma_{\ell(N_c+1)} < \Gamma_S$.

At each iteration i , we define as Euclidean distance $\mathcal{R}_{i,k}^F$ in frequency and spin-down space (F-space) between the cluster seed $\kappa_{\ell(i)}$ and every other candidate κ_k in χ_i :

$$\mathcal{R}_{i,k}^F := \sqrt{\left[\frac{f_k - f_{\ell(i)}}{\delta f}\right]^2 + \left[\frac{\dot{f}_k - \dot{f}_{\ell(i)}}{\delta \dot{f}}\right]^2} \quad \forall \quad \kappa_k \in \chi_i, \quad (2)$$

where, δf and $\delta \dot{f}$ are the frequency and spin-down grid spacings used in the search. Note that at fixed $\mathcal{R}_{i,k}^F$, (2) is an ellipse in F-space centered at $(f_{\ell(i)}, \dot{f}_{\ell(i)})$ and with axes of half-length $\delta f \times \mathcal{R}_{i,k}^F$ and $\delta \dot{f} \times \mathcal{R}_{i,k}^F$.

3.2 Distribution of distances in F-space

We define the cluster radius for the i -th cluster based on the distribution of the distances $\mathcal{R}_{i,k}^F$ in F-space. In order to derive such a distribution, we must bin the distances $\mathcal{R}_{i,k}^F$ appropriately.

The binning in F-space naturally takes the form of concentric elliptical annuli (f^r, \dot{f}^r) at distances $\mathcal{B}_{i,r}^F$ from the seed. The index r denotes the different bins. The edges (f^1, \dot{f}^1) of the first bin are defined by the equation

$$\sqrt{\left[\frac{f^1 - f_{\ell(i)}}{\mathcal{B}_{i,1}^F \delta f}\right]^2 + \left[\frac{\dot{f}^1 - \dot{f}_{\ell(i)}}{\mathcal{B}_{i,1}^F \delta \dot{f}}\right]^2} = 1. \quad (3)$$

The successive bins are defined by the recursive relation

$$[\mathcal{B}_{i,r+1}^F]^2 - [\mathcal{B}_{i,r}^F]^2 = [\mathcal{B}_{i,1}^F]^2 \quad \text{for all bins } r = 1, 2, 3 \dots, \quad (4)$$

which requires that the area of the annuli is constant and equal to $\pi[\mathcal{B}_{i,1}^F]^2$ (see figure 2). Note that each annulus encloses an equal number of parameter space points. The relation (4) can be explicitly solved to yield

$$\mathcal{B}_{i,r}^F = \sqrt{r} \mathcal{B}_{i,1}^F \quad \text{for all bins } r = 1, 2, 3 \dots, \quad (5)$$

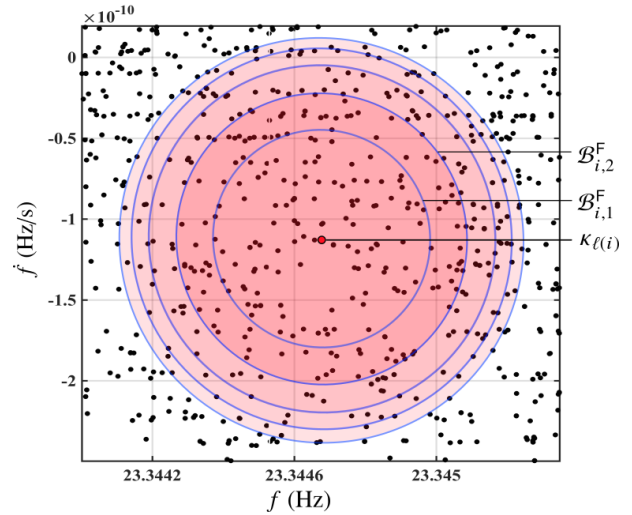


Figure 2: Example of annular binning in F-space, defined by (3)–(5). The values of the parameters are: $\delta f = 8.3 \times 10^{-7}$ Hz, $\delta \dot{f} = 1.3 \times 10^{-13}$ Hz/s. An ad-hoc value for $\mathcal{B}_{i,1}^F$ of 1.2×10^3 ($N_F = 50$) is taken. The area within each annuli is constant, hence the annuli get thinner with distance from the center. Note that the figure shows only the first 5 annuli for clarity; in total, there are $N_F^2 = 2500$ such annuli.

The value of $\mathcal{B}_{i,1}^F$ is chosen as

$$\mathcal{B}_{i,1}^F = \frac{1}{N_F} \mathcal{R}_{i,\max}^F \quad \text{with} \quad \mathcal{R}_{i,\max}^F = \max_k \{\mathcal{R}_{i,k}^F\}. \quad (6)$$

Comparing (6) with (5) and setting $\mathcal{R}_{i,\max}^F = \mathcal{B}_{i,r}^F$, we find that N_F^2 is equal to the total number of r bins. N_F is determined as follows: the candidate count $n_{i,r}^F$ in the various r bins is determined for a test value of N_F , say N_{F_t} . If the condition,

$$n_{i,1}^F(N_{F_t}) \geq C_F \langle n_{i,r}^F(N_{F_t}) \rangle \quad \text{where } r = 1, 2, 3 \dots, \quad (7)$$

is not satisfied, we iteratively decrease N_{F_t} by one ($N_{F_t} \rightarrow N_{F_t} - 1$) until (7) is verified, and set $N_F = N_{F_t}$. In (7), the angled brackets indicate the average over the

r bins, and $C_F > 1$. Note that N_{F_t} should be large enough such that $\mathcal{B}_{i,1}^F$ is comparable with the signal containment region in F-space [55]. Further, C_F encodes the over-density requirement, and for low amplitude signals, this requirement is very lax: $C_F \gtrsim 1$, which means that the procedure picks the finest binning for which we at least do not have an under-density around the seed.

We note that in a sub-threshold search, the clustering procedures are in principle sensitive to the parameter Γ_L : the over-densities of signal candidates due to a weak signal will only be observable down to certain detection statistic values, below which the density of noise candidates will be high enough that the over-density due to the signal candidates will not be appreciable. The threshold Γ_L could, in principle, be optimally placed at the level just above when this effect begins to take place. However, this is difficult to determine. By setting $C_F \gtrsim 1$, we appreciate the smallest over-density possible, and hence, ease the dependency of the procedure on Γ_L .

If for some i -th cluster, no resolution (no N_F value) can be found that meets the requirement of (7), then only the seed $\kappa_{\ell(i)}$ is removed from χ_i and the resulting set of candidates defines χ_{i+1} . The i -th cluster, ϕ_i , is classified as a *single-occupant-cluster*.

In figure 3, we compare the distribution of $\mathcal{R}_{i,k}^F$ values from searches ran on noise data (blue curve), and on fake noise plus a CW signal (red curve). The red distribution presents a clear maximum near the seed $\kappa_{\ell(i)}$, i.e. there is an evident over-density of candidates near the seed. We want to estimate the extent of this over-density, and cluster the candidates that form this over-density together.

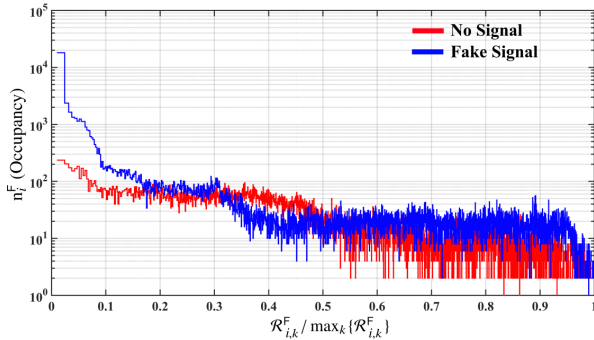


Figure 3: Distribution of $\mathcal{R}_{i,k}^F$ for a noise-only data-set (red) and for a data-set also containing a fake signal (blue). The grid spacing $\mathcal{B}_{i,1}^F$ in F-space is defined by $N_F = 50$.

3.3 Cluster size in F-space

For every i -th cluster, we use the distribution of distances $\mathcal{R}_{i,k}^F$ in order to determine the cluster radius in F-space: the cluster radius \mathcal{R}_i^{F*} is the value of the distance defined in (2) at which we have the first local minimum of $n_{i,r}^F$. Since the $\mathcal{R}_{i,k}^F$ histogram has typically many fluctuations, in order to estimate more accurately the

position of the first minimum of the underlying distribution, we determine its shape with a fitting procedure which smoothens out the random fluctuations.

We fit the data $n_{i,r}^F$ in two stages. In the first stage, the data is separately fitted with two functions G (a superposition of Gaussians) and S (a superposition of sinusoids):

$$G(x) = \sum_{l=1}^{m_1} G_l(x); \quad S(x) = \sum_{l=1}^{m_2} S_l(x). \quad (8)$$

This step is implemented using a compiled MATLAB executable (using the package *fit*), which provides support for $m_1, m_2 \in [1, 8]$. For each fit, we choose the highest value of m_1 and m_2 that is able to fit the data within the standard tolerances defined by the program. The fitted curves G and S are summed and re-normalised, and the output is then fit again with a Gaussian function, yielding g_i^F . This second fit smoothens out the small scale fluctuations and leaves us with a clear view of the over-densities in F-space.

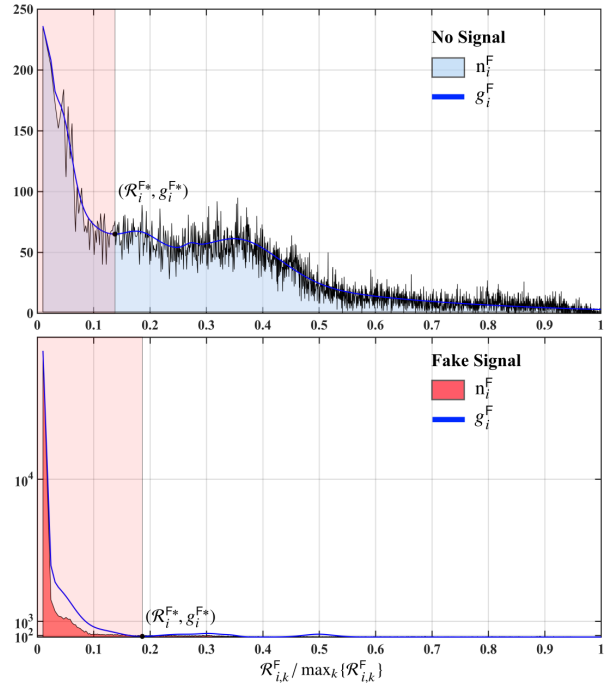


Figure 4: Fit to the distribution of $\mathcal{R}_{i,k}^F$ for a noise-only data-set (top panel) and for a data-set also containing a fake signal (bottom panel). The grid spacing $\mathcal{B}_{i,1}^F$ is defined by $N_F = 50$. We can see that the fitting procedure contours the shape of the distribution while ignoring small scale fluctuations, and returns a good measure of the over-density.

Finally, we can identify the local minimum of g_i^F closest to the origin and take that as the radius \mathcal{R}_i^{F*} in F-space of the i -th cluster. In figure 4, we show an example of the fitting procedure on purely noise data (top panel) and in data containing a fake signal (bottom panel).

3.4 Hill parameters in F-space and further constraints

The distribution of candidates in parameter space is very diverse, depending on the nature of the noise in the data. Because of this, even an adaptive procedure, such as the one described above, may still generate clusters that spuriously assemble together candidates that are actually independent. In order to counter this, instead of setting more stringent criteria, for example a higher threshold C_F , it is more effective to produce a first estimate of the cluster based on liberal parameters, and then scrutinize its topological properties in detail, and further accept, discard or modify the cluster based on these.. The topological properties that we consider for a cluster i are the so-called ‘‘hill parameters’’¹ *prominence* P_i , *dominance* D_i and *goodness* G_i :

$$P_i := \frac{\mathcal{R}_i^{F*}}{\max_k \{\mathcal{R}_{i,k}^F\}}, \quad (9)$$

$$D_i := \frac{g_i^F(\mathcal{B}_{i,1}^F) - g_i^F(\mathcal{R}_i^{F*})}{g_i^F(\mathcal{B}_{i,1}^F)}, \quad (10)$$

$$G_i := \frac{|\ln_{i,1}^F - g_i^F(\mathcal{B}_{i,1}^F)|}{\ln_{i,1}^F + g_i^F(\mathcal{B}_{i,1}^F)}. \quad (11)$$

The cluster candidates from the set χ_i are further inspected to check if:

$$P_i \leq P_{\text{th}}, \quad D_i \geq D_{\text{th}}, \quad G_i \leq G_{\text{th}}. \quad (12)$$

These thresholds (P_{th} , D_{th} , G_{th}) on the hill parameters restrict the topology of clusters: P_{th} restricts the fraction of the available parameter space that the cluster occupies; D_{th} bounds the contrast between the density of candidates near the seed and at the cluster edge; G_{th} specifies the minimum agreement between the fitted curve and the observed density near the seed. The nature and the values of the constraints in (12) is such that they exclude clusters that extend too far in the F-space, and at the same time, show very little contrast with respect to the local noise background; thus we shortlist the kind of clusters that we typically expect from signals.

When a cluster in F-space fails to meet any of the criteria given by (12), we shortlist candidates $n_{i,1}^F$ from the distribution that fall within the first bin $\mathcal{B}_{i,1}^F$ around the seed and discard all other candidates from the iteration. This is equivalent to resetting $\mathcal{R}_i^{F*} = \mathcal{B}_{i,1}^F$. This choice is justified because the failing of the hill parameters means that the shortlisted cluster is not topologically consistent with what we require from a cluster of that extent. However, the initial over-density still remains near the seed and it might be due to a low amplitude signal. In this regard, we do not discard the whole

cluster. On the other hand, if the criteria in (12) are met, we shortlist all the candidates, including the seed, that fall within our estimated cluster radius \mathcal{R}_i^{F*} , and discard all other candidates outside the cluster radius.

The candidates clustered in F-space will constitute the χ_i^{sky} set and their clustering properties in the sky will be considered further.

3.5 A measure of distance in the sky (S-space)

We now want to determine whether the shortlisted candidates in χ_i^{sky} show any over-density in sky around the seed. If any over-density is found, the candidates constituting this over-density will form the final i -th cluster.

As in F-space, for each candidate $\kappa_k \in \chi_i^{\text{sky}}$, we introduce a distance in the sky, $\mathcal{R}_{i,k}^S$, to the seed of the i -th cluster under consideration:

$$\mathcal{R}_{i,k}^S := \sqrt{[x_k - x_{\ell(i)}]^2 + [y_k - y_{\ell(i)}]^2} \quad \forall \kappa_k \in \chi_i^{\text{sky}}. \quad (13)$$

This definition is justified when the search grids are uniform on some plane (x, y) , for example the ecliptic plane (e.g. see [55]) or the equatorial plane (e.g. see [11]). The transformation equations between the sky coordinates (α, δ) and (x, y) for a uniform grid on ecliptic plane, are:

$$\begin{cases} x = \cos \lambda \cos \beta \\ y = \sin \lambda \cos \beta, \end{cases} \quad (14)$$

with

$$\begin{cases} \lambda = \tan^{-1} \left[\frac{\sin \alpha \cos \varphi + \tan \delta \sin \varphi}{\cos \alpha} \right] \\ \beta = \sin^{-1} [\sin \delta \cos \varphi - \sin \alpha \cos \delta \sin \varphi]. \end{cases} \quad (15)$$

In the expressions above, $\varphi = 23.4^\circ$ is the angle of obliquity of the ecliptic with respect to the celestial equatorial plane². The ecliptic plane represents the S-space after this transformation.

3.6 Distribution of distances in S-space

The binning of the $\mathcal{R}_{i,k}^S$ values is performed in a similar fashion as previously done in F-space. The edges of the bins, labeled by r , of the i -th cluster, satisfy the following relation:

$$[\mathcal{B}_{i,r+1}^S]^2 - [\mathcal{B}_{i,r}^S]^2 = [\mathcal{B}_{i,1}^S]^2 \quad \text{for all bins } r = 1, 2, 3 \dots \quad (16)$$

This recursive relation describes concentric circular annuli in the (x, y) plane enclosing equal areas; the annuli naturally get thinner as we move away from the seed, as shown in figure 2. The first bin is a circle and its area is proportional to $[\mathcal{B}_{i,1}^S]^2$.

¹We adopt the notion of hill parameters from the concept of ‘topographic prominence’ used in topography/geography, e.g. see [38].

²Note that in (15), λ must be translated to its correct quadrant by adding 180° or subtracting 180° .

$\mathcal{B}_{i,1}^S$ is chosen based on the clustering properties of signals. Precisely, it will depend on the 99% containment region of the search [55]. This region defines a neighbourhood around a cluster seed originating from a signal, within which the true signal parameters are contained with 99% confidence. If we indicate with d_{sky} the width of the search pixels in the (x, y) plane [11, 55], and with $N^{99\%}$ the diameter of the 99% containment region expressed in number of pixels, then we can express $\mathcal{B}_{i,1}$ as

$$\mathcal{B}_{i,1}^S := \frac{N^{99\%} + N_S}{2} d_{\text{sky}}, \quad (17)$$

where, N_S is a parameter that has to be tuned as shown in section 4. Further, (17) says that the first bin in the sky, i.e. the circle with radius $\mathcal{B}_{i,1}^S$, contains all sky pixels within the 99% containment region, plus (or minus) a tuning term N_S . We continue binning recursively according to (16) until the width of the bin becomes smaller than a sky-grid pixel; all candidates lying more distant than that point are ignored.

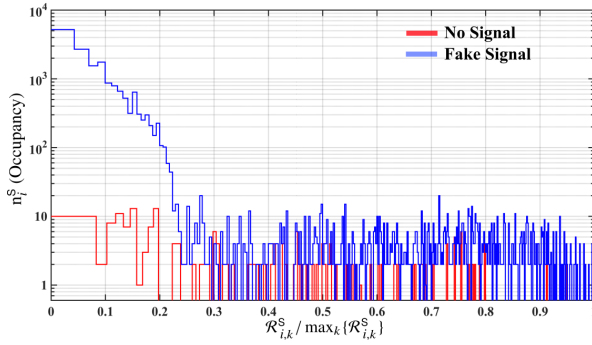


Figure 5: Distribution of $\mathcal{R}_{i,k}^S$ values for signal versus noise: $\mathcal{B}_{i,1}^S$ for the noise-only case is defined by $N_S = 0$, while for signal it is set to $N_S = 6$.

We find that in disturbed data that contains a large number of noise outliers, a single value of N_S independent of the loudness Γ_i of the cluster seed under consideration, makes this clustering procedure very slow. The reason is that very large values of Γ_i are often associated with many candidates clustered in F-space (highly populated χ_i^F) that are distributed almost isotropically in the sky. In this situation, if the resolution in the sky ($\mathcal{B}_{i,1}^S$) is high, the sky-clustering step eliminates one candidate at the time as a single-occupant-cluster, and this is very inefficient. The solution is to decrease the resolution (increase $\mathcal{B}_{i,1}^S$ by increasing N_S) with Γ_i .

In figure 5, we show the re-normalised distribution of $\mathcal{R}_{i,k}^S$ for a fake signal and LIGO O1 noise.

3.7 Cluster in S-space

In order to estimate the cluster radius in S-space, we check for over-densities by analysing the distribution of $\mathcal{R}_{i,k}^S$.

If the first bin is the most highly populated (i.e. $n_{i,1}^S = \max_r \{n_{i,r}^S\}$), all the candidates contained within

a distance \mathcal{R}_i^{S*} are clustered together:

$$\mathcal{R}_i^{S*} = \min_r \left\{ \mathcal{B}_{i,r}^S : \frac{n_{i,r}^S - n_{i,r+1}^S}{n_{i,r}^S} > C_S \right\}. \quad (18)$$

\mathcal{R}_i^{S*} is the smallest distance at which we have a relative drop in the density of candidates above a certain threshold C_S . All candidates within \mathcal{R}_i^{S*} constitute, together with the seed, the final i -th cluster, ϕ_i . The set of candidates considered for the next clustering iteration is $\chi_{i+1} = \chi_i - \phi_i$.

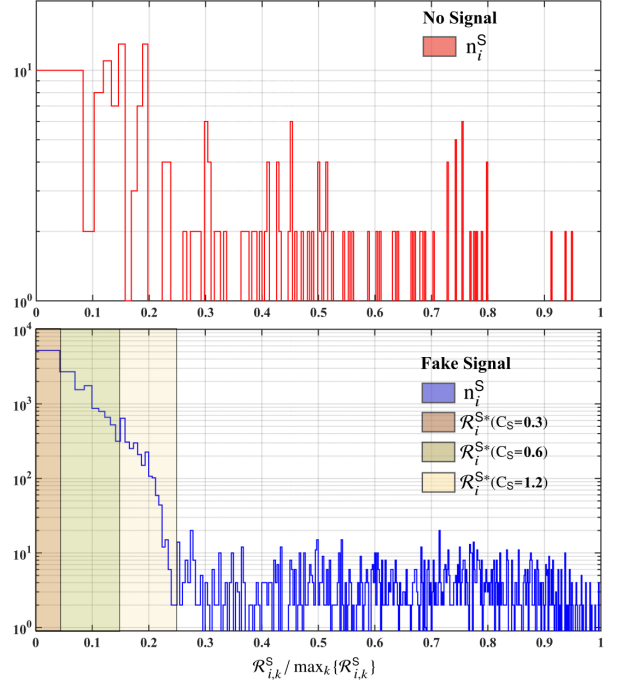


Figure 6: Clustering properties in the sky for a data-set containing a signal (lower panel) and a noise data-set (upper panel). The values of N_S are 6 and 0, respectively for the lower and upper panels. Note that the first bin in the pure noise case (top panel) is not the most highly populated, and hence failed the clustering criteria ($n_{i,1}^S \neq \max_r \{n_{i,r}^S\}$), irrespective of the value of C_S .

The value of C_S is chosen based on the localisation properties of signals and leaning on the conservative side, i.e. toward lower values of C_S . For instance, in the bottom panel of figure 6, we see that $\mathcal{R}_i^{S*}(1.2) > \mathcal{R}_i^{S*}(0.6) > \mathcal{R}_i^{S*}(0.3)$. Indeed, the lower value of C_S clusters less candidates, but the candidates excluded at this iteration will likely form their own separate cluster at the next iteration. If this second set of points were due a signal, with a lower C_S , they would be associated to the correct seed.

If the first bin is not the most highly populated, the final cluster ϕ_i will contain only the seed $\kappa_{\ell(i)}$. All the other candidates remain un-clustered, and available for association with another cluster in the set $\chi_{i+1} = \chi_i - \kappa_{\ell(i)}$.

This recursive procedure continues until there are no more candidate seeds, i.e. no more candidates with de-

tection statistic value above the threshold Γ_S . In figure 8, 9 in appendix A, we show a snapshot of the procedure for the first iteration on data χ_1 for a fake signal and near-Gaussian noise.

4 Performance

Quantity	Value
T_{obs}	4 months
T_{coh}	210 hours
N_{seg}	12
δf	8.3×10^{-7} Hz
$\delta \dot{f}$	1.3×10^{-13} Hz/s
$d_{\text{sky}} (f = 100 \text{ Hz})$	20 arcmin

Table 6: The clustering procedure is applied to the output from this all-sky search.

We characterise the performance of the AdCl procedure and compare it with the old clustering procedure, used in Papa *et al* [55]. We show how the tuning parameters were chosen in an actual search [45], with parameters given in table 6.

The two clustering procedures are compared at the same value of seed threshold Γ_S , and with the other parameters optimally tuned.

4.1 Clustering parameters

We will consider two different data inputs to the clustering procedure, one suitable for a high-significance search (loud signals), and the other for a sub-threshold search (weak signals). In the former search, the detection statistic is $2\overline{\mathcal{F}}$, the corresponding Γ_S and Γ_L thresholds are 12.0 and 10.5 respectively, and the value of N_S for the i -th cluster is:

$$N_S(2\overline{\mathcal{F}}_i) = \begin{cases} 0 & \text{if } 2\overline{\mathcal{F}}_i < 18 \\ 2\overline{\mathcal{F}}_i - 18 & \text{if } 18 \leq 2\overline{\mathcal{F}}_i \leq 48 \\ 30 & \text{if } 2\overline{\mathcal{F}}_i > 48. \end{cases} \quad (19)$$

Alternatively, for the second search, the detection statistic is the line- and the transient line-robust statistic $\hat{\beta}_{S/\text{GLIL}}$ [41, 45], the corresponding Γ_S and Γ_L thresholds are 5.5 and 4, respectively, and N_S for the i -th cluster is:

$$N_S(\hat{\beta}_{S/\text{GLIL}}^i) = \begin{cases} 0 & \text{if } \hat{\beta}_{S/\text{GLIL}}^i < 15 \\ \hat{\beta}_{S/\text{GLIL}}^i - 15 & \text{if } 15 \leq \hat{\beta}_{S/\text{GLIL}}^i \leq 35 \\ 31 & \text{if } \hat{\beta}_{S/\text{GLIL}}^i > 35. \end{cases} \quad (20)$$

This is the set-up appropriate for a search like [45].

The reason why we consider searches with different detection statistics is historical: at the time when we started characterising the AdCl procedure, we were

planning to use it for a high-significance search on quiet bands, as done in [11]. In this case, the simplest detection statistic to use is $2\overline{\mathcal{F}}$, and all the false alarm and detection efficiency studies were performed with this statistic. It was only later that we realised that the quality of the data in the low-frequency range was such that a high-significance search was not possible: we would have many candidates above threshold, and we would have to carry out a large scale follow-up. Due to these complications, for this search, the use of the $\hat{\beta}_{S/\text{GLIL}}$ was necessary. In the absence of large disturbances, the empirical relationship between the two detection statistics is $2\overline{\mathcal{F}} \equiv 0.419 \hat{\beta}_{S/\text{GLIL}} + 10.855$.

The other parameters are chosen as described in the previous sections and they are equal for both types of searches, and their values are:

$$\begin{cases} N_F \in [25, 50], C_F = 1.2 \\ C_S = 0.25 \\ P_{\text{th}} = 0.25, D_{\text{th}} = 0.05, G_{\text{th}} = 0.1. \end{cases} \quad (21)$$

On the other hand, the old clustering uses a fixed cluster size corresponding to the 99% containment regions in the various dimensions. In case of the high-threshold $2\overline{\mathcal{F}}$ search:

$$2\overline{\mathcal{F}} \equiv \begin{cases} \Delta f = 1.15 \times 10^{-4} \text{ Hz}, \\ \Delta \dot{f} = 5.6 \times 10^{-11} \text{ Hz/s}, \\ \Delta^{\text{sky}} = 6 \times 6 \text{ sky-pixels}, \end{cases} \quad (22)$$

while for the sub-threshold $\hat{\beta}_{S/\text{GLIL}}$ search:

$$\hat{\beta}_{S/\text{GLIL}} \equiv \begin{cases} \Delta f = 1.85 \times 10^{-4} \text{ Hz}, \\ \Delta \dot{f} = 8.5 \times 10^{-11} \text{ Hz/s}, \\ \Delta^{\text{sky}} = 9 \times 9 \text{ sky-pixels}. \end{cases} \quad (23)$$

4.2 Safety

Naturally, the clustering procedure needs to be safe, i.e. it should not discard real signals. Thus, we choose the clustering parameters to yield the lowest false alarm rate for a very low false dismissal rate. We now show the detection efficiencies for the clustering parameters outlined in (19), (20), (21).

We estimate the detection efficiency by performing Monte-Carlo simulations of gravitational wave signals in real data taken from the LIGO O1 run. By using the real LIGO data instead of fake Gaussian noise, we derive a realistic benchmark of the performance. In a nutshell, the fake signals are added to the real data, the search is run, and the clustering procedure is applied.

The population of signals has parameters reasonably uniformly distributed in frequency, spin-down and sky-position, and with amplitudes that yield the detection statistic values shown in figure 7.

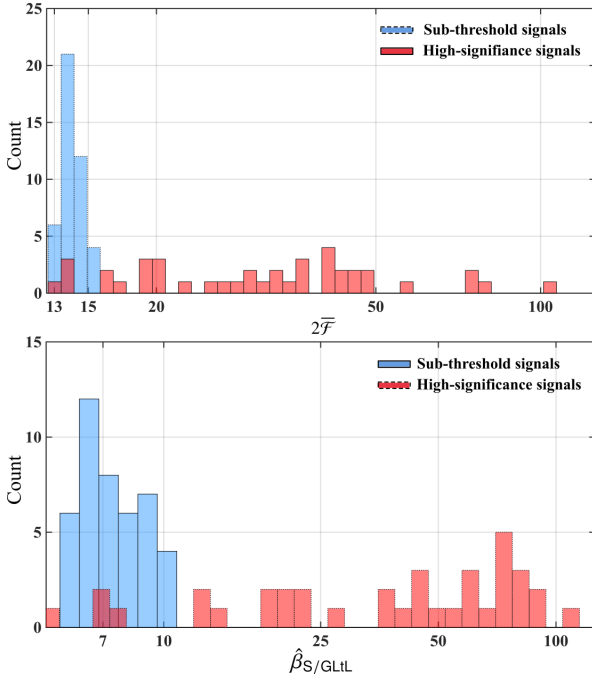


Figure 7: Distribution of the values of the detection statistics of the sub-threshold and high-significance signals added to the data to characterize the performance of the clustering procedure. Note that the high-significance signal population is not purely high-significance; it also contains a few signals at low values of the detection statistic (less than 10% below $2\bar{\mathcal{F}} = 14.0 \equiv \hat{\beta}_{S/GLTL} = 7.5$). Meanwhile, the sub-threshold search may be considered as purely sub-threshold (none above $\hat{\beta}_{S/GLTL} = 10.5 \equiv 2\bar{\mathcal{F}} = 15.3$).

The detection efficiency \mathcal{E} is defined as the ratio of the number of candidates from signals recovered by the clustering procedure with the total number of signals with detection statistic value above Γ_S . For a signal to be recovered by the clustering procedure, we require that the signal parameters lie within the 99% containment region of the seed parameters (we remind the reader that the detection statistic value of the seed must also exceed Γ_S). This means that if there were a follow-up stage on the cluster seeds, the true signal parameters would lie within the searched region, and if there were no follow-ups, the signal parameters would lie within the quoted parameter uncertainties.

4.3 Noise Rejection

We estimate the false alarm rate by applying the clustering procedure to the same search output data as described in the previous section, just without fake signals.

The input to the clustering procedure are \mathcal{N}_{in} candidates, with detection statistic values greater than Γ_S . At the output of the clustering procedure, we have \mathcal{N}_{out} candidates. We define the noise reduction factor NR as:

$$NR := 1 - \frac{\mathcal{N}_{out}}{\mathcal{N}_{in}} \quad \text{on noise.} \quad (24)$$

Naturally, $0 \leq NR \leq 1$, and higher values of NR denote lower number of noise candidates after the clustering procedure.

		AdCl Procedure	Old Procedure
High-significance $2\bar{\mathcal{F}}$ search	NR	65.9%	$\leq 40.0\%$
	\mathcal{E}	97.6%	95.1%
Sub-threshold $\hat{\beta}_{S/GLTL}$ search	NR	90.5%	$\leq 74.1\%$
	\mathcal{E}	95.5%	$> 95.0\%$

Table 7: Comparison of the noise rejection (NR) and the detection efficiencies (\mathcal{E}) of high-significance and sub-threshold searches between the new and old clustering procedures.

4.4 Results

The performance results for the AdCl and the old clustering procedures are shown in table 7. For a high-significance search, the detection efficiency, exceeding 95%, is high for both the procedures, but the new clustering has a noise rejection (NR) which is significantly higher (nearly 66% versus 40%) than the one achieved by the previous method.

In a sub-threshold search, we set a low enough threshold on the detection statistic of the seed (Γ_S) such that we expect a large number of candidates to exceed this limit, just due to random noise. The underlying idea behind this is that with successive follow-up stages, one is able to weed out the noise and identify a signal

that, at the first stage of the hierarchy, was hidden by a multitude of false alarms. In this regime, the clustering procedure operates in an environment of the most uniformly and densely populated candidates. The signal signature used by the clustering procedure are local over-densities around the cluster seed, coincident in F-space and S-space. But the cluster seed is, at every iteration i , the loudest candidate in the set χ_i , and when the signal is weak, i.e. its amplitude is comparable to the amplitude of many of the candidates, it might not be picked as a seed. For this reason, the detection efficiency is lower for a sub-threshold search with respect to a high-threshold search. In order to compare the performance of AdCl procedure with the old procedure, we

fix the detection efficiency at $> 95\%$ by lowering Γ_L to 3.4 for the old procedure (keeping $\Gamma_L = 4.0$ for AdCl procedure). In this case, the AdCl procedure improves the noise rejection (NR) by 22% over the old procedure.

The results of table 7 refer to signal-frequency bands where the data is fairly uniformly distributed in parameter space, i.e. there are no extended regions of the parameter space that host enhanced values of the detection statistic, as in the case of the top panel of figure 1. Moreover, the AdCl procedure performs very well in disturbed conditions, and this is important because the disturbed regions typically yield a lot of spurious candidates.

In noisy regions, the new clustering procedure has a NR of 98.9%, compared to $\leq 91.1\%$ for the old procedure in a $2\mathcal{F}$ search. We expect similar results for noisy data in a $\hat{\beta}_{S/GLIL}$ search. The NR values in the disturbed bands are higher than those in quiet bands because each cluster comprises more candidates above Γ_S in noisy bands than in the quiet bands. This is expected merely due to higher density of disturbances. The new clustering procedure has a higher NR than the old method because it adapts the cluster size to the local over-density and can get as big (or small) as it needs, in order to accommodate the features in the data.

A rigorous quantitative assessment of the detection efficiency in disturbed bands is hard to make because the results would depend not only on the location of the fake signals in parameter space but also their numbers with respect to the disturbances. In such scenarios, there is no unbiased way to pick the fake signal population. However, based on the fact that for a cluster to be identified, we only require a seed above threshold and concurrent clustering around that seed in both F-space and S-space, we do not expect the presence of more candidates due to disturbances (which generally do not cluster in the parameter space) to interfere too much with the identification of the signal clusters. On the contrary, the old procedure does not require a local over-density around the seed and it might happen that a signal candidate gets associated with a higher random fluctuation; this cluster may not satisfy the over-density criteria in the AdCl procedure which may have led to a wrong estimation of the follow-up region. Thus, by requiring the seed to be centered at a local over-density, the new procedure avoids this type of occurrence. This might slightly favour the detection efficiency of the AdCl procedure with respect to the old one.

5 Conclusions

The clustering procedure that we propose in this paper is more effective at reducing the number of candidates to be considered in follow-up stages while achieving comparable, if not better, detection efficiency with respect to the procedure used in previous searches. Since we operate at fixed computing budget, the number of candidates that a given follow-up stage can search, is

fixed. Hence, a higher noise rejection means a lower detection threshold. In a search like the Einstein@Home O1 low-frequency search [45], the new clustering has allowed us to lower the $\hat{\beta}_{S/GLIL}$ threshold. In disturbed bands, the noise rejection is even higher.

There are two main reasons for the observed improvements. The first reason is that the AdCl procedure is more demanding than the old one, i.e. a cluster has to display a more pronounced over-density of candidates compared to nearby noise. The second reason is that, since the cluster size is estimated on the data itself, the clustering algorithm adapts itself to it and is capable of bundling together a large number of candidates arising from extended regions of parameter space.

Another advantage of the AdCl procedure compared to the old one is that, by relying on local over-densities of candidates, the false alarm rate does not increase with a decreasing value of the threshold Γ_L , which is significantly necessary for low-significance searches.

However, the AdCl procedure may well go through many iterations before discarding a single candidate as a single occupancy cluster and restoring the rest of the candidates for future consideration. This, especially in noisy bands, can make it rather slow. The variable sky-binning depending on the seed amplitude is a way to ease this issue, and quite certainly, further use will inspire other ways to make the procedure faster in all noise conditions.

Currently, the tuning parameters (N_F , C_F , N_S , C_S) and the hill parameters (P_{th} , D_{th} , G_{th}) are chosen to represent the approximate topology of the clusters that we expect from signals. These approximate values are chosen upon visual inspection of the fake signals injected in LIGO data at many values of the signal amplitude h_o . To improve the estimates on these parameters, one would require to perform a much larger number of Monte-Carlo simulations (in λ and h_o), and then estimate the cluster properties. This remains a difficult task due to limited computational resources and very large parameter space of the tuning and hill parameters. The modeling of clusters arising from non-Gaussian noise (such as instrumental artifacts) is even more difficult, especially for unknown sources of disturbances. In principle, this modeling could however help better discern between signals and noise.

There are certainly other possible ways to perform adaptive clustering. One of the methods is to employ machine learning. Besides that, one could also perform more complex parameter space correlation studies of the detection statistic values, similar to the studies done for cosmic microwave background (CMB) surveys [71] and large scale structure (LSS) surveys [44]. However, such complex analysis methods require much cleaner data, and they are certainly an overkill for the current data-sets.

Appendix

of data from the LIGO O1 run with and without a fake signal (figure 8, figure 9).

A.1 The first cluster

We now illustrate the different phases of the first iteration of the clustering procedure on two small snippets

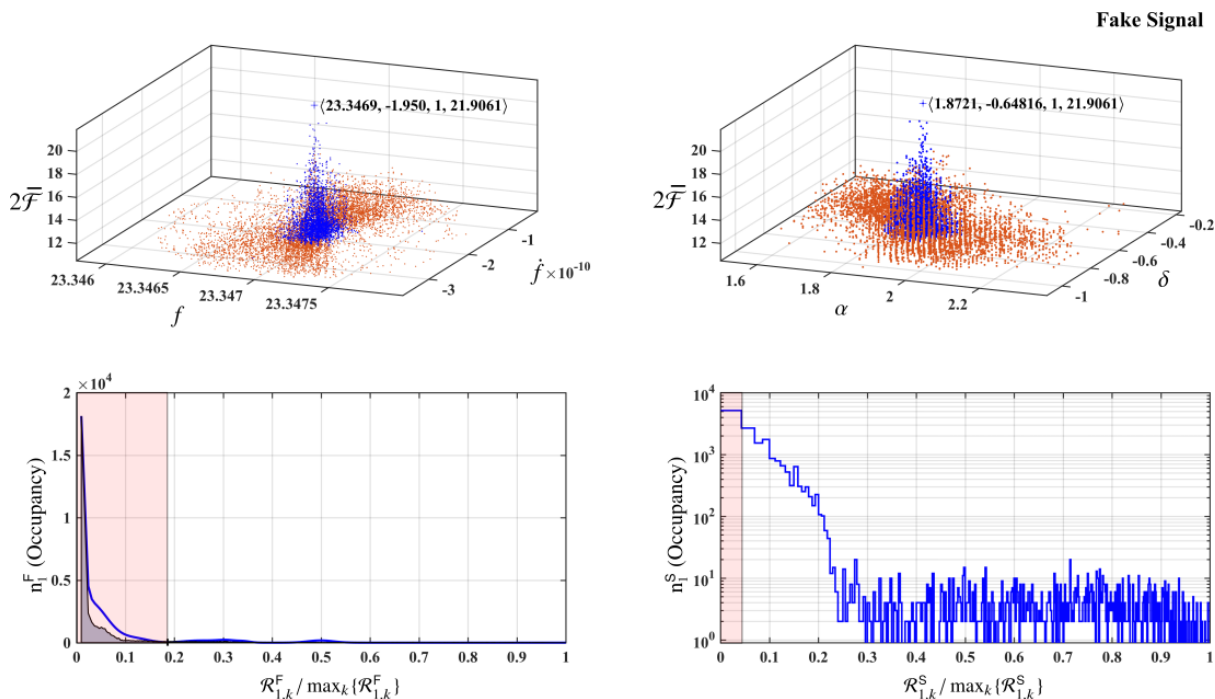


Figure 8: (*Signal case*) The orange points are the candidates in χ_1^{sky} ; the blue points are the subset of these that form the final cluster ϕ_1 . The corresponding distributions for $\mathcal{R}_{i,k}^F$ and $\mathcal{R}_{i,k}^S$ are shown in the second row of plots. The shaded regions extend up to \mathcal{R}_i^{F*} (left plot) and \mathcal{R}_i^{S*} (right plot). The seed is marked with a '+'. The numbers in the brackets by the '+' denote: $\langle f, \dot{f}, i, \Gamma_i \rangle$ in F-space and $\langle \alpha, \delta, i, \Gamma_i \rangle$ in S-space, where $\Gamma \equiv 2\bar{\mathcal{F}}$.

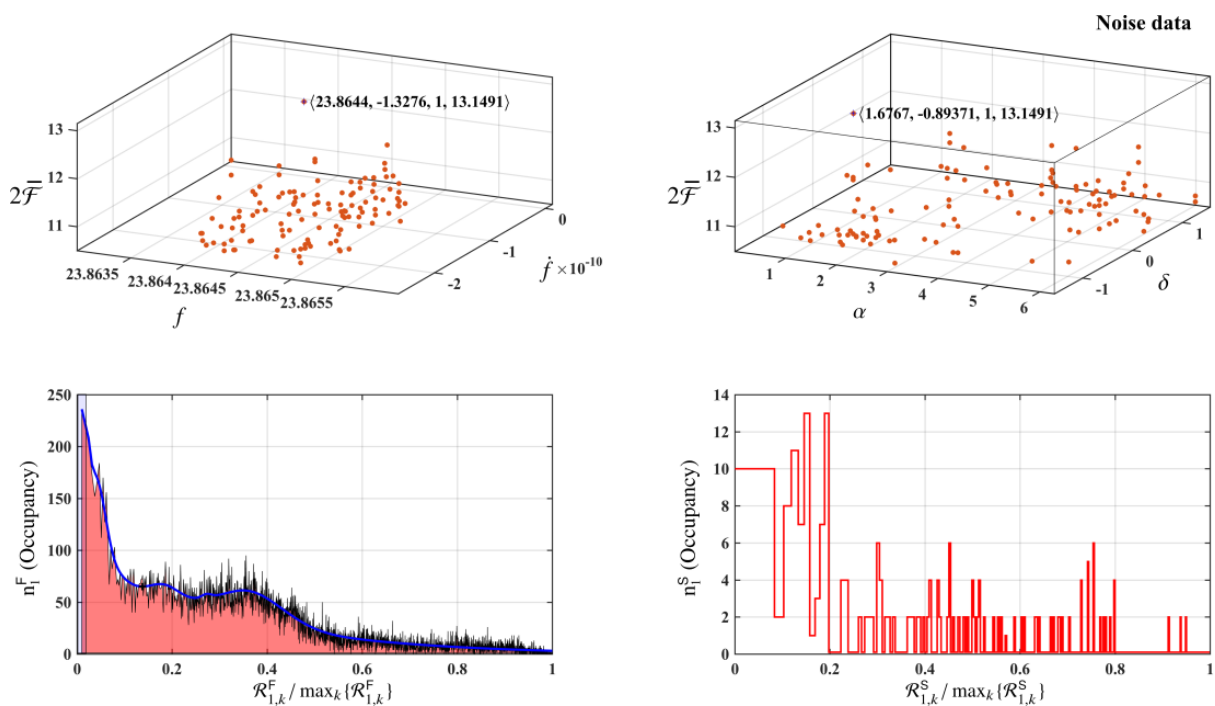


Figure 9 (previous page): (Noise only) The orange points are the candidates in χ_1^{sky} . The corresponding distributions for $\mathcal{R}_{i,k}^F$ and $\mathcal{R}_{i,k}^S$ are shown in the second row of plots. The shaded regions extend up to \mathcal{R}_i^{F*} (left plot) and \mathcal{R}_i^{S*} (right plot). Note that \mathcal{R}_i^{F*} fails the hill parameters test and is reset to $\mathcal{B}_{i,1}^F$. The distribution in S-space satisfies $n_{i,1}^S \neq \max_r \{n_{i,r}^S\}$ (i.e. no over-density is sky near the seed), so ϕ_1 is a single-occupant-cluster. The seed is marked with a '+'. The numbers in the brackets by the '+' denote: $\langle f, \hat{f}, i, \Gamma_i \rangle$ in F-space and $\langle \alpha, \delta, i, \Gamma_i \rangle$ in S-space, where $\Gamma \equiv 2\overline{\mathcal{F}}$.

Acknowledgements

This procedure was used in [45], and we thank Sergey Klimenko and Evan Goetz for the review of the application of this new clustering procedure to the results of that search. M A Papa and S Walsh gratefully acknowl-

edge the support from NSF PHY Grant 1104902. All computational work for this search was carried out on the ATLAS super-computing cluster at the Max-Planck-Institut für Gravitationsphysik, Hannover and Leibniz Universität Hannover. This document has LIGO DCC number P1700123.

* * *

V The upper-limit procedure for the most recent Einstein@Home searches

Avneet Singh^{1,2,3,†}, Maria Alessandra Papa^{1,2,4,‡}, Sinéad Walsh^{1,2}, Sylvia Zhu^{1,2}, Heinz-Bernd Eggenstein^{2,3}

¹ Max-Planck-Institut für Gravitationsphysik, am Mühlenberg 1, 14476, Potsdam-Golm

² Max-Planck-Institut für Gravitationsphysik, Callinstraße 38, 30167, Hannover

³ Leibniz Universität Hannover, Welfengarten 1, 30167, Hannover

⁴ University of Wisconsin-Milwaukee, Milwaukee, Wisconsin 53201, USA

Abstract

Several searches for continuous gravitational waves (CW) are underway targeting known and unknown isolated neutron stars in LIGO data [45, 15, 11, 55, 68, 81]. However, no direct detection of continuous gravitational waves have yet been made. Generally, in the absence of a signal, stringent upper-limits are placed on the continuous gravitational wave amplitudes attributable to a population of nearby spinning and slightly non-axisymmetric neutron stars. In this short document, we detail the procedure used to calculate these upper-limits on the CW amplitudes in the most recent Einstein@Home searches on LIGO S5 [68], S6 [11, 55] and O1 data [45].

1 Introduction

In searches for continuous gravitational wave (CW) signals, upper-limits on the CW amplitudes are an informative measure of the performance of a search as well as an astrophysical statement on the population of isolated neutron stars in our “neighborhood”. Generally, when no successful CW candidate is detected in a frequency range, an estimate can be made on the amplitude of the CW above which a source would have been detected (with a certain high statistical confidence), if it had been present. This estimate on the CW amplitude (h_o) is called the *upper-limit*, usually denoted by $h_o^{x\%}$, where x is the associated *level of confidence* in percentage. The value of x is typically 90% or higher.

No direct CW detections have yet been made in the LIGO data. Thus, the upper-limits are the most important quantitative measure that separate several search pipelines based on their sensitivity [77]. Typically, the Einstein@Home searches incorporate the most sensitive investigations of the LIGO data for CW signals [77, 45, 15], and these searches quote the most stringent upper-limits on the CW amplitudes for a nearby population of neutron stars [45, 11, 55, 77, 68, 81].

In this report, we provide the details of the upper-limit procedure used in the most recent Einstein@Home CW searches¹ [45, 11, 55, 68, 81]. Note that this document is drafted solely keeping in mind the recent and the upcoming Einstein@Home searches, and the terminology used herein must be interpreted accordingly.

1.1 A typical Einstein@Home search

Consider a typical Einstein@Home search spanning a broad search frequency range, such as [45, 11, 68] etc. In [45], [11], [68] and [81], the overall search frequency spanned 20–100 Hz, 50–550 Hz, 1.25–1.5 kHz and 50 Hz–1 kHz respectively. These searches employ

matched-filtering such that each parameter space point λ is denoted by four quantities characterising a template, i.e. $\lambda \equiv (f, \dot{f}, \alpha, \delta)$, and a ranking- and/or detection-statistic Γ is assigned to each parameter space point as a measure of its relative significance of being a CW signal [68, 66]. The fundamental aim in the post-processing stages of these searches is to compare the observed values of Γ (corresponding to the signal templates) against the expected background noise level. While the fundamental principle appears straightforward, the complexities that occur in the process of making such comparisons are numerous and analytically intractable. One can thus expect the post-processing of templates in typical Einstein@Home searches to be a highly statistics-oriented science.

2 The upper-limit procedure

Typically, the results of the Einstein@Home searches are reported in 0.5 Hz frequency bands. When no signal is found in a 0.5 Hz band, upper-limits are calculated on the amplitude h_o of the CW signals using Monte-Carlo simulations [45, 11, 55, 68, 81].

2.1 Monte-Carlo simulations

Currently, no analytical method is available to estimate the upper-limit on the CW amplitudes from the observations made by the aforementioned Einstein@Home searches, such as by converting the observed loudest Γ value to a h_o value. Due to this reason, Monte-Carlo simulations are employed to statistically determine the upper-limit values. However, it is nearly impossible to perform Monte-Carlo simulation for each of the 0.5 Hz bands due to the excessive computational requirements. Therefore, a subset of N_B 0.5 Hz bands are chosen as representatives and they are spread evenly across the total search frequency range. In these N_B bands, software

[†]avneet.singh@aei.mpg.de; [‡]maria.alessandra.papa@aei.mpg.de

¹The Einstein@Home search targeting Cassiopeia A in S6 data [81] uses an identical method with very minor differences from what is used in other searches [45, 11, 55, 68], such as different programming languages and numerical libraries.

injections are simulated in the real LIGO data at several values of the h_o (say, N_h) using the standard injection-and-recovery technique [1, 11]. Thus, in each 0.5 Hz band, N_I software injections are simulated at each of the N_h values of h_o , totaling $N_I \times N_h \times N_B$ injections. The parameters of the software injections are chosen such that they are uniformly distributed in frequency (within the 0.5 Hz range of the band), in spin-down range, in sky and in the nuisance parameters; this leaves the amplitude h_o as the only argument affecting the SNR of a candidate in the upper-limit procedure at this stage. Lastly, the loudest candidate corresponding to each of the simulated software injection is recovered at this stage.

2.2 Detection criteria

Once the loudest candidates from the software injections are recovered, a ‘detection criteria’ must be established. The said detection criteria is a qualifying test for determining whether the observed loudest candidate corresponding to the injection has been recovered as a signal and not a noise artifact. In the recent Einstein@Home searches, different detection criteria have been used depending partially on the quality of the data and partially on the nature of the searches.

In searches where the data is relatively well-behaved [11, 68], the detection criteria takes the form involving the ‘Critical Ratio’ (CR). The CR is defined as

$$\text{CR} := \frac{\Gamma_{\text{Loud}} - \Gamma_{\text{exp}}}{\sigma_{\text{exp}}}, \quad (1)$$

where, Γ_{Loud} is the observed loudest candidate, Γ_{exp} is the expected value of the loudest candidate from pure Gaussian noise [78], and σ_{exp} is the standard deviation of the expected distribution. The range of CR values are then binned in k reasonably spaced bins such that the detection criteria is defined as a function of CR_k . Under this definition, for each CR_k bin, an injected signal is considered detected if its recovered Γ value exceeds $\Gamma_{\text{exp}} + \text{CR}_k \sigma_{\text{exp}}$. In nutshell, the detection criteria is defined differently for each CR_k bin.

In searches where the data is somewhat disturbed [45, 55], the expectation of noise deviates significantly from Gaussianity. In such cases, Γ_{exp} cannot be calculated for unmodeled non-Gaussian noise. Consequently, all Monte-Carlo injections are subjected to the entire hierarchical post-processing pipeline and an injection is considered detected if it passes through all the follow-up stages [45].

2.3 Confidence level

Considering a given detection criteria, at each value of the injection h_o , we calculate the *detection rate* $\mathcal{R}(h_o)$ as simply the fraction of injections detected (N_I^{det}), i.e.

$\mathcal{R}(h_o) = N_I^{\text{det}}/N_I$. In total, there are N_h such values of \mathcal{R} for each 0.5 Hz band. At this stage, a threshold x is set on the detection rate, and this threshold corresponds to the level of confidence in our upper-limit statements; for Einstein@Home searches, typical value of $x \geq 90\%$ has been used. For example, a 90%-confidence upper-limit value of h_o means that at least 90% of the CW signals would be detected by the search if their amplitudes were $h_o^{90\%}$ or higher.

In order to calculate the $h_o^{x\%}$ for any arbitrary value of x in each 0.5 Hz band, we must fit the $\mathcal{R} - h_o$ curve with a smooth analytical function and interpolate at the value $x\%$. The values of \mathcal{R} versus h_o are expected to resemble a sigmoid function in their trend of variation of the form:

$$\mathcal{R} := \frac{1}{1 + e^{-(x-\mu)/\nu}}. \quad (2)$$

The \mathcal{R} versus h_o values are fitted to (2) using the non-linear regression algorithm `nlinfit` provided by MatLab. In figure 1, we show a typical example of such a fit from the OIAS² search [45].

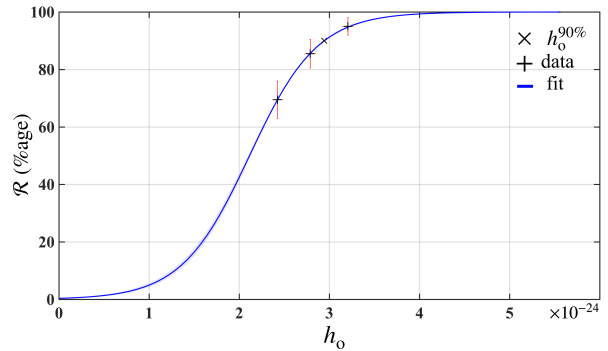


Figure 1: A typical sigmoid fit for 3 data points (+) at 21 Hz. The interpolated $h_o^{90\%}$ value is marked by \times . The red error bars on the data points represent the 2σ standard binomial error, and the thin blue shaded region around the fitted curve is the 2σ variance of the fit calculated according to (4) (see section 2.3.1 for more details).

2.3.1 Error characterisation

The observed detection rate at any value of h_o is calculated on a random population of signals. The detection rate thus follows a binomial distribution and the standard 1σ error (σ_B) is given by

$$\sigma_B^2 = \frac{1}{N_I} \mathcal{R}(1 - \mathcal{R}). \quad (3)$$

The `nlinfit` routine weighs each data point by its corresponding σ_B before performing the non-linear regression. The outcome of the routine is an estimate on the parameters μ and ν , along with the *covariance matrix* C . The routine assumes that all deviations from the fit are random variables and follow the normal distribution.

²abbrev. LIGO Scientific Collaboration and Virgo Collaboration [45].

The symmetric 1σ envelope (σ_F) on the fit (shown in figure 1 and 2) are then given by

$$\sigma_F = \pm \sqrt{[\partial_{\mu}\mathcal{R}]^2 C_{\mu\mu} + 2[\partial_{\mu\nu}\mathcal{R}]C_{\mu\nu} + [\partial_{\nu}\mathcal{R}]^2 C_{\nu\nu}}. \quad (4)$$

The error in the estimation of $h_0^{x\%}$ is then simply calculated analytically using (4) as shown below in figure 2.

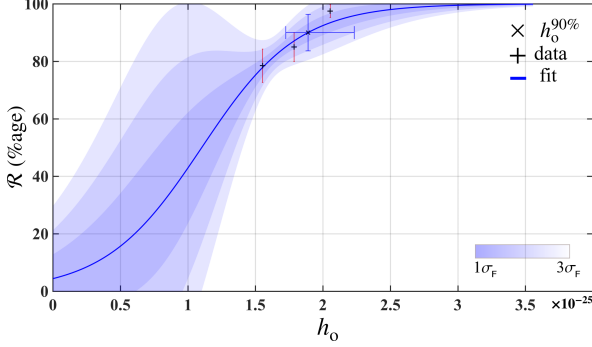


Figure 2: A badly fitted sigmoid for 3 data points (+) at 94.5 Hz. The interpolated $h_0^{90\%}$ point is marked by \times . The red error bars on the data points represent the $2\sigma_B$ standard binomial error, and the thin blue shaded envelopes around the fitted curve are the $1-3\sigma_F$ variances to the fit calculated according to (4). The value of $h_0^{90\%}$ is found to be $1.89^{+0.34}_{-0.16} \times 10^{-25}$, where the errors are simply the thickness of the $2\sigma_F$ envelope at $\mathcal{R} = 90\%$.

2.4 Sensitivity-depth

The $h_0^{x\%}$ values in every 0.5 Hz band (denoted by $h_{0,i}^{x\%}$) are then converted to the *sensitivity-depth* defined as

$$\mathcal{D}_i^{x\%} = \frac{\sqrt{S_{h,i}}}{h_{0,i}^{x\%}} \quad \text{where, } i = 1, 2, 3 \dots N_I, \quad (5)$$

where, $S_{h,i}$ is the average power spectral density of the data in the i th 0.5 Hz band. Further, an average value of the sensitivity-depth $\mathcal{D}^{x\%}$ may now be calculated which is representative of the entire search frequency range, i.e.

$$\mathcal{D}^{x\%} = \frac{1}{N_I} \sum_{i=1}^{N_I} \mathcal{D}_i^{x\%}. \quad (6)$$

With this average value $\mathcal{D}^{x\%}$ of the sensitivity-depth, we can invert the relation (5) to get the $h_0^{90\%}$ at any value f of the search frequency:

$$h_0^{x\%}(f) = \frac{\sqrt{S_h(f)}}{\mathcal{D}^{x\%}}. \quad (7)$$

Note that for searches [68, 11] where the detection criteria features the CR (as discussed before in section 2.2), the average value of $\mathcal{D}^{x\%}$ corresponds to the CR of the

loudest candidate observed in the 0.5 Hz band where the upper-limit is being calculated, i.e. $\mathcal{D}^{x\%} \rightarrow \mathcal{D}_{CR}^{x\%}$.

Lastly, $h_0^{x\%}(f)$ is the final upper-limit result quoted in the respective observational results [45, 15, 11, 55, 68, 81].

2.5 Uncertainty in the upper-limits

In order to estimate the uncertainty in the upper-limits, we note that the intrinsic uncertainty in $\mathcal{D}_i^{x\%}$ ($\delta\mathcal{D}_i^{x\%}$) is related to the uncertainty in $h_{0,i}^{x\%}$ ($\delta h_{0,i}^{x\%}$), according to (5). Remember that $\delta h_{0,i}^{x\%}$ are calculated analytically using (4), as shown in figure 2. In figure 3 below, we show the calculated values of $\mathcal{D}_i^{90\%} \pm \delta\mathcal{D}_i^{90\%}$ for the O1AS search [45].

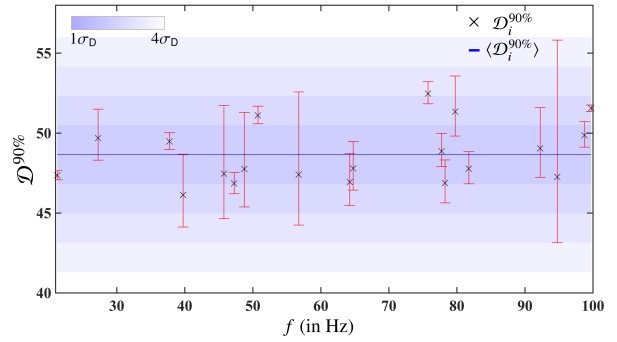


Figure 3: Calculated values of the sensitivity-depths (\times) in 20 0.5 Hz bands in the O1AS search, along with the 2σ uncertainties $\delta\mathcal{D}_i^{90\%} = 2\sigma_F$ in red markers. The envelopes represent the $1-4\sigma_D$ regions around $\langle \mathcal{D}_i^{90\%} \rangle$.

The standard deviation of the distribution of $\mathcal{D}_i^{x\%}$ values is denoted by σ_D , excluding the contribution from $\delta\mathcal{D}_i^{x\%}$. Note that while the deviation of $\mathcal{D}_i^{x\%}$ from $\mathcal{D}^{x\%}$ may be assumed to be random, the intrinsic uncertainties $\delta\mathcal{D}_i^{x\%}$ in the values $\mathcal{D}_i^{x\%}$ are clearly asymmetric and not random³. Due to this asymmetric nature of $\delta\mathcal{D}_i^{x\%}$, incorporating $\delta\mathcal{D}_i^{x\%}$ in the average value $\mathcal{D}^{x\%}$ of the sensitivity-depth is not straightforward. One way to make this incorporation is to quote an appropriate uncertainty ($\delta\mathcal{D}^{x\%} := N_D\sigma_D$) envelope in $\mathcal{D}^{x\%}$ that covers the individual errors $\delta\mathcal{D}_i^{x\%}$. For example, figure 3 also shows the average value $\mathcal{D}^{90\%} = \langle \mathcal{D}_i^{90\%} \rangle = 48.7 \text{ Hz}^{-1/2}$ of the sensitivity-depth and several envelopes corresponding to $N_D = 1, 2, 3, 4$. The uncertainties quoted in the observational paper ($\delta\mathcal{D}^{x\%} = \pm 5.5 \equiv \pm 11\%$) corresponded to $N_D = 3$ [45].

Lastly, according to (5), the equivalent uncertainty $\delta h_0^{x\%}$ in the $h_0^{x\%}$ value is related to $\delta\mathcal{D}_i^{x\%}$ by

$$\left| \frac{\delta h_0^{x\%}}{h_0^{x\%}} \right| = \left| \frac{\delta\mathcal{D}^{x\%}}{\mathcal{D}^{x\%}} \right|. \quad (8)$$

³It is because these uncertainties are related to random errors (normally distributed) in μ and ν (calculated via non-linear regression) by the sigmoid function. Consequently, the inverse sigmoid function skews the errors on $\mathcal{D}_i^{x\%}$, according to (2).

3 Conclusions

In conclusion, the final upper-limit values quoted in various Einstein@Home searches are of the form $h_o^{x\%} \pm \delta h_o^{x\%}$ calculated according to (7) and (8), where $x = 90\%$ in general [45, 11, 55, 68, 81]. These upper-limits on h_o may also be converted to what is known as the *astrophysical reach* of the search, which repre-

sents the upper-limits as a function of the distance to the source, the effective GW spin-down (\dot{f}_{GW}) and the source’s ellipticity ϵ ; these $(\epsilon, \dot{f}_{\text{GW}})$ contours are presented in the appropriate aforementioned references. We quickly quote the values of the 90%-confidence sensitivity-depth estimates of various searches that use this procedure below in table 8.

Search	Sensitivity-depth	$N_D \sigma_D$ (%)
O1AS[45]	$\mathcal{D}^{90\%} = 48.7 \pm 5.5 \text{ Hz}^{-1/2}$	$\pm 3\sigma_D$ (11%)
S6B0[11]	$[\mathcal{D}_{\text{CR}_{0,0}}^{90\%}, \mathcal{D}_{\text{CR}_{6,0}}^{90\%}] = [37.0 \pm 3.7, 33.0 \pm 3.3] \text{ Hz}^{-1/2}$	$\pm 2\sigma_D$ (10%)
S6FU[55]	$\mathcal{D}^{90\%} = 46.9 \pm 4.7 \text{ Hz}^{-1/2}$	$\pm 2\sigma_D$ (10%)
S5HF[68]	$[\mathcal{D}_{\text{CR}_{0,0}}^{90\%}, \mathcal{D}_{\text{CR}_{3,5}}^{90\%}] = [30.6 \pm 3.1, 28.8 \pm 2.9] \text{ Hz}^{-1/2}$	$\pm 2\sigma_D$ (10%)
S6CasA[81] ¹	$\mathcal{D}^{90\%} = 70.0 \text{ Hz}^{-1/2}$	–

Table 8: Calculated sensitivity-depths of the various searches using this upper-limit procedure.

3.1 Beyond 90% confidence level

In addition, we may also calculate 95% or higher confidence level upper-limits as an exercise to make com-

parison between the different percentages. In figure 4 below, we show the upper-limit values for several values of $x\%$ for the O1AS search. The associated values of the sensitivity-depths are quoted in table 9.

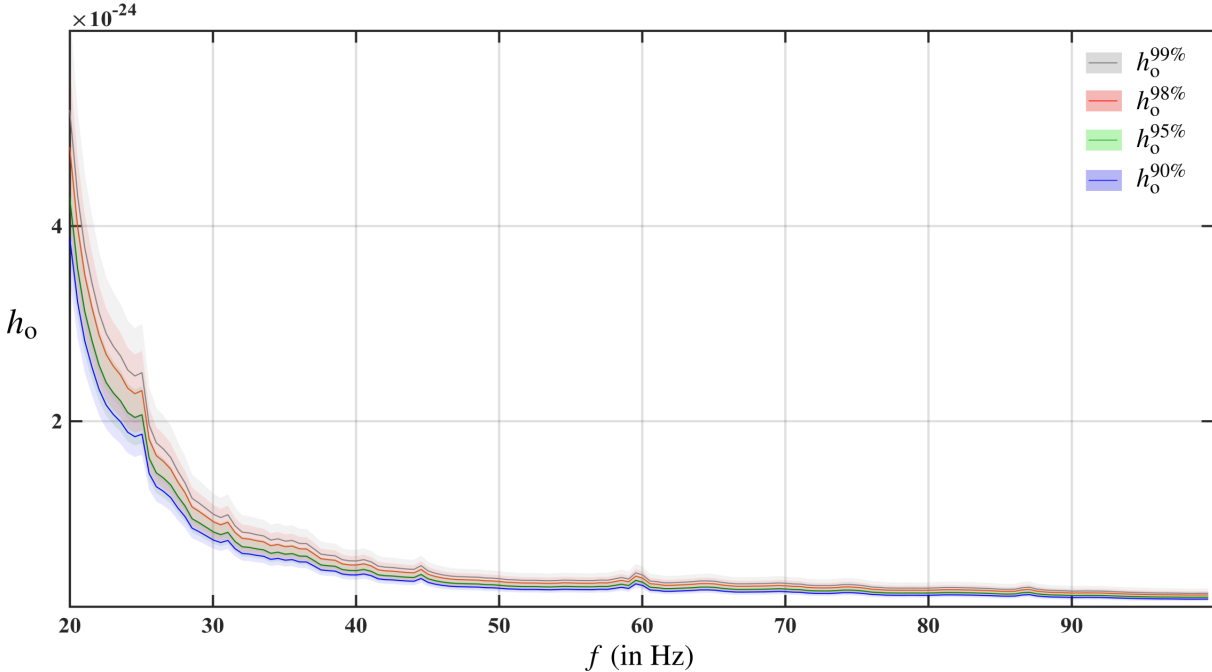


Figure 4: The 90%-, 95%-, 98%- and 99%-confidence level upper-limits on h_o in the O1AS search. The shaded areas around each curve indicate the $2\sigma_D$ uncertainties. The corresponding values of the sensitivity-depth are given in table 9.

Quantity	Sensitivity-depth value	$2\sigma_D$ (%)
$\mathcal{D}^{90\%}$	$48.7 \pm 5.5 \text{ Hz}^{-1/2}$	11%
$\mathcal{D}^{95\%}$	$44.0 \pm 6.2 \text{ Hz}^{-1/2}$	14%
$\mathcal{D}^{98\%}$	$39.3 \pm 6.9 \text{ Hz}^{-1/2}$	18%
$\mathcal{D}^{99\%}$	$36.4 \pm 7.2 \text{ Hz}^{-1/2}$	20%

Table 9: Calculated sensitivity-depths at different confidence levels for the OIAS search. Interestingly, the uncertainties on the sensitivity-depth values increase with increasing confidence. This occurs because the injected values of h_0 chosen in the Monte-Carlo simulations are tuned to yield optimal results for the 90%-confidence level, i.e. $\mathcal{R} = 90\%$ in (2). Thus, with a better re-tuning of the injected h_0 values, more robust estimates can be made for $x > 90\%$.

Acknowledgements

This procedure was most recently used in [45], and we thank Sergey Klimenko and Evan Goetz for the review of the application of this new clustering procedure to the results of that search. M A Papa and S Walsh gratefully acknowledge the support from NSF PHY Grant 1104902. All computational work for this search was carried out on the ATLAS super-computing cluster at the Max-Planck-Institut für Gravitationsphysik, Hannover and Leibniz Universität Hannover. This document has LIGO DCC number T1700389.

* * *

VI Implementation to CW searches

PHYSICAL REVIEW D 96, 122004 (2017)

1 First low-frequency Einstein@Home all-sky search for continuous gravitational waves in Advanced LIGO data

B. P. Abbott *et al.**

(LIGO Scientific Collaboration and Virgo Collaboration)

(Received 29 June 2017; revised manuscript received 14 September 2017; published 8 December 2017)

We report results of a deep all-sky search for periodic gravitational waves from isolated neutron stars in data from the first Advanced LIGO observing run. This search investigates the low frequency range of Advanced LIGO data, between 20 and 100 Hz, much of which was not explored in initial LIGO. The search was made possible by the computing power provided by the volunteers of the Einstein@Home project. We find no significant signal candidate and set the most stringent upper limits to date on the amplitude of gravitational wave signals from the target population, corresponding to a sensitivity depth of $48.7 [1/\sqrt{\text{Hz}}]$. At the frequency of best strain sensitivity, near 100 Hz, we set 90% confidence upper limits of 1.8×10^{-25} . At the low end of our frequency range, 20 Hz, we achieve upper limits of 3.9×10^{-24} . At 55 Hz we can exclude sources with ellipticities greater than 10^{-5} within 100 pc of Earth with fiducial value of the principal moment of inertia of 10^{38} kg m^2 .

DOI: 10.1103/PhysRevD.96.122004

I. INTRODUCTION

In this paper we report the results of a deep all-sky Einstein@Home [1] search for continuous, nearly monochromatic gravitational waves (GWs) in data from the first Advanced LIGO observing run (O1). A number of all-sky searches have been carried out on initial LIGO data, [2–15], of which [2,3,7,9,14] also ran on Einstein@Home. Einstein@Home is a distributed computing project which uses the idle time of computers volunteered by the general public to search for GWs.

The search presented here covers frequencies from 20 Hz through 100 Hz and frequency derivatives from $-2.65 \times 10^{-9} \text{ Hz/s}$ through $2.64 \times 10^{-10} \text{ Hz/s}$. A large portion of this frequency range was not explored in initial LIGO due to lack of sensitivity. By focusing the available computing power on a subset of the detector frequency range, this search achieves higher sensitivity at these low frequencies than would be possible in a search over the full range of LIGO frequencies. In this low-frequency range we establish the most constraining gravitational wave amplitude upper limits to date for the target signal population.

II. LIGO INTERFEROMETERS AND THE DATA USED

The LIGO gravitational wave network consists of two observatories, one in Hanford (Washington) and the other

in Livingston (Louisiana) separated by a 3000-km baseline [16]. The first observing run (O1) [17] of this network after the upgrade towards the Advanced LIGO configuration [18] took place between September 2015 and January 2016. The Advanced LIGO detectors are significantly more sensitive than the initial LIGO detectors. This increase in sensitivity is especially significant in the low-frequency range of 20 Hz through 100 Hz covered by this search: at 100 Hz the O1 Advanced LIGO detectors are about a factor 5 more sensitive than the Initial LIGO detectors during their last run (S6 [19]), and this factor becomes ≈ 20 at 50 Hz. For this reason all-sky searches did not include frequencies below 50 Hz on initial LIGO data.

Since interferometers sporadically fall out of operation (“lose lock”) due to environmental or instrumental disturbances or for scheduled maintenance periods, the data set is not contiguous and each detector has a duty factor of about 50%. To remove the effects of instrumental and environmental spectral disturbances from the analysis, the data in frequency bins known to contain such disturbances have been substituted with Gaussian noise with the same average power as that in the neighboring and undisturbed bands. This is the same procedure as used in [3]. These bands are identified in the Appendix.

III. THE SEARCH

The search described in this paper targets nearly monochromatic gravitational wave signals as described for example by Eqs. (1)–(4) of [9]. Various emission mechanisms could generate such a signal, as reviewed in Sec. IIA of [15]. In interpreting our results we will consider a spinning compact object with a fixed, nonaxisymmetric $\ell = m = 2$ mass quadrupole, described by an equatorial ellipticity ϵ .

*Full author list given at the end of the Letter.

Published by the American Physical Society under the terms of the *Creative Commons Attribution 4.0 International* license. Further distribution of this work must maintain attribution to the author(s) and the published article’s title, journal citation, and DOI.

B. P. ABBOTT *et al.*

We perform a stack-slide type of search using the global correlation transform (GCT) method [20–22]. In a stack-slide search the data is partitioned in segments, and each segment is searched with a matched-filter method [23]. The results from these coherent searches are combined by summing the detection statistic values from the different segments, one per segment (\mathcal{F}_i), and this determines the value of the core detection statistic:

$$\bar{\mathcal{F}} := \frac{1}{N_{\text{seg}}} \sum_{i=1}^{N_{\text{seg}}} \mathcal{F}_i. \quad (1)$$

The “stacking” part of the procedure is the summing, and the “sliding” (in parameter space) refers to the fact that the \mathcal{F}_i that are summed do not all come from the same template.

Summing the detection statistic values is not the only way to combine the results from the coherent searches; see for instance [4,24,25]. Independently of the way that this is done, this type of search is usually referred to as a “semicoherent search.” Important variables for this type of search are the coherent time baseline of the segments T_{coh} , the number of segments used N_{seg} , the total time spanned by the data T_{obs} , the grids in parameter space, and the detection statistic used to rank the parameter space cells. For a stack-slide search in Gaussian noise, $N_{\text{seg}} \times 2\bar{\mathcal{F}}$ follows a chi-squared distribution with $4N_{\text{seg}}$ degrees of freedom, $\chi^2_{4N_{\text{seg}}}$. These parameters are summarized in Table I. The grids in frequency and spin-down are each described by a single parameter, the grid spacing, which is constant over the search range. The same frequency grid spacings are used for the coherent searches over the segments and for the incoherent summing. The spin-down spacing for the incoherent summing, $\delta\dot{f}$, is finer than that used for the coherent searches, $\delta\dot{f}_c$, by a factor γ . The notation used here is consistent with that used in previous observational papers [2,3].

The sky grid is approximately uniform on the celestial sphere projected on the ecliptic plane. The tiling is a hexagonal covering of the unit circle with hexagons’ edge length d :

TABLE I. Search parameters rounded to the first decimal figure. T_{ref} is the reference time that defines the frequency and frequency derivative values.

Parameter	Value
T_{coh}	210 hr
T_{ref}	1132729647.5 GPS s
N_{seg}	12
δf	8.3×10^{-7} Hz
$\delta\dot{f}_c$	1.3×10^{-11} Hz/s
γ	100
m_{sky}	1×10^{-3}

PHYSICAL REVIEW D 96, 122004 (2017)

$$d(m_{\text{sky}}) = \frac{1}{f} \frac{\sqrt{m_{\text{sky}}}}{\pi\tau_E}, \quad (2)$$

with $\tau_E \simeq 0.021$ s being half of the light travel time across the Earth and m_{sky} a constant which controls the resolution of the sky grid. The sky grids are constant over 5 Hz bands and the spacings are the ones associated through Eq. (2) to the highest frequency in each 5 Hz. The resulting number of templates used to search 50 mHz bands as a function of frequency is shown in Fig. 1.

This search leverages the computing power of the Einstein@Home project, which is built upon the BOINC (Berkeley Open Infrastructure for Network Computing) architecture [26–28]: a system that exploits the idle time on volunteer computers to solve scientific problems that require large amounts of computer power. The search is split into work units (WUs) sized to keep the average Einstein@Home volunteer computer busy for about 8 CPU hours. Each WU performs 1.5×10^{11} semicoherent searches, one for each of the templates in 50 mHz band, the entire spin-down range and 118 points in the sky. Out of the semicoherent detection statistic values computed for the 1.5×10^{11} templates, it returns to the Einstein@Home server only the highest 10000 values. A total of 1.9×10^6 WUs are necessary to cover the entire parameter space. The total number of templates searched is 3×10^{17} .

A. The ranking statistic

Two detection statistics are used in the search: $\hat{\beta}_{S/\text{GLL}}$ and $2\bar{\mathcal{F}}$. $\hat{\beta}_{S/\text{GLL}}$ is the ranking statistic which defines the

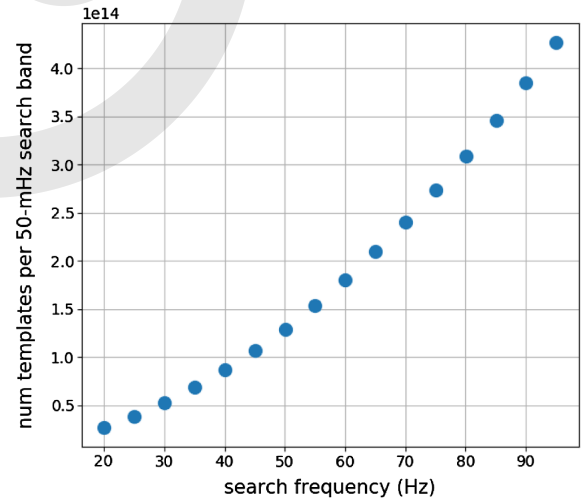


FIG. 1. Number of searched templates in 50 mHz band as a function of frequency. The sky resolution increases with frequency causing the variation in the number of templates. $N_f \times N_{\dot{f}} \sim 1.3 \times 10^9$, where N_f and $N_{\dot{f}}$ are the number of f and \dot{f} templates searched in 50 mHz bands. The total number of templates searched between 20 and 100 Hz is 3×10^{17} .

FIRST LOW-FREQUENCY EINSTEIN@HOME ALL-SKY ...

top-candidate list; it is a line- and transient-robust statistic that tests the signal hypothesis against a noise model which, in addition to Gaussian noise, also includes single-detector continuous or transient spectral lines. Since the distribution of $\hat{\beta}_{S/GLIL}$ is not known in closed form even in Gaussian noise, when assessing the significance of a candidate against Gaussian noise, we use the average $2\bar{\mathcal{F}}$ statistic over the segments, $2\bar{\mathcal{F}}$ [23]; see Eq. (1). This is in essence, at every template point, the log-likelihood of having a signal with the shape given by the template versus having Gaussian noise.

Built from the multi- and single-detector $\hat{\mathcal{F}}$ statistics, $\hat{\beta}_{S/GLIL}$ is the \log_{10} of $\hat{B}_{S/GLIL}$, the full definition of which is given by Eq. (23) of [29]. This statistic depends on a few tuning parameters that we describe in the remainder of the paragraph for the reader interested in the technical details: A transition-scale parameter $\hat{\mathcal{F}}_*^{(0)}$ is used to tune the behavior of the $\hat{\beta}_{S/GLIL}$ statistic to match the performance of the standard average $2\bar{\mathcal{F}}$ statistic in Gaussian noise while still statistically outperforming it in the presence of continuous or transient single-detector spectral disturbances. Based on injection studies of fake signals in Gaussian-noise data, we set an average $2\bar{\mathcal{F}}$ transition scale of $\hat{\mathcal{F}}_*^{(0)} = 65.826$. According to Eq. (67) of [30], with $N_{\text{seg}} = 12$ this $2\bar{\mathcal{F}}$ value corresponds to a Gaussian false-alarm probability of 10^{-9} . Furthermore, we assume equal-odds priors between the various noise hypotheses (“L” for line, “G” for Gaussian, “tL” for transient line).

B. Identification of undisturbed bands

Even after the removal of disturbed data caused by spectral artifacts of known origin, the statistical properties of the results are not uniform across the search band. In what follows we concentrate on the subset of the signal-frequency bands having reasonably uniform statistical properties, or containing features that are not immediately identifiable as detector artifacts. This comprises the large majority of the search parameter space.

Our classification of “clean” versus “disturbed” bands has no pretense of being strictly rigorous, because strict rigor here is neither useful nor practical. The classification serves the practical purpose of discarding from the analysis regions in parameter space with evident disturbances and must not dismiss detectable real signals. The classification is carried out in two steps: an automated identification of undisturbed bands and a visual inspection of the remaining bands.

An automatic procedure, described in Sec. II F of [31], identifies as undisturbed the 50-mHz bands whose maximum density of outliers in the $f - \dot{f}$ plane and average $2\bar{\mathcal{F}}$ are well within the bulk distribution of the values for these quantities in the neighboring frequency bands. This procedure identifies 1233 of the 1600 50-mHz bands as

PHYSICAL REVIEW D 96, 122004 (2017)

undisturbed. The remaining 367 bands are marked as potentially disturbed, and in need of visual inspection.

A scientist performs the visual inspection by looking at various distributions of the $\hat{\beta}_{S/GLIL}$ statistic over the entire sky and spin-down parameter space in the 367 potentially disturbed 50-mHz bands. She ranks each band with an integer score 0,1,2 ranging from “undisturbed” (0) to “disturbed” (2). A band is considered “undisturbed” if the distribution of detection statistic values does not show a visible trend affecting a large portion of the $f - \dot{f}$ plane. A band is considered “mildly disturbed” if there are outliers in the band that are localized in a small region of the $f - \dot{f}$ plane. A band is considered “disturbed” if there are outliers that are not well localized in the $f - \dot{f}$ plane.

Figure 2 shows the $\hat{\beta}_{S/GLIL}$ for each type of band. Figure 3 shows the $\hat{\beta}_{S/GLIL}$ for a band that harbors a fake signal injected in the data to verify the detection pipelines. In the latter case, the detection statistic is elevated in a small region around the signal parameters.

Based on this visual inspection, 1% of the bands between 20 and 100 Hz are marked as “disturbed” and excluded from the current analysis. A further 6% of the bands are marked as “mildly disturbed.” These bands contain features that cannot be classified as detector disturbances without further study; therefore, these are included in the analysis.

Figure 4 shows the highest values of the detection statistic in half-Hz signal-frequency bands compared to the expectations. The set of candidates from which the highest detection statistic values are picked does not include the 50-mHz signal-frequency bands that stem entirely from fake data, from the cleaning procedure, or that were marked as disturbed. Two 50-mHz bands that contained a hardware injection [32] were also excluded, as the high amplitude of the injected signal caused it to dominate the list of candidates recovered in those bands. In this paper we refer to the candidates with the highest value of the detection statistic as the *loudest* candidates.

The highest expected value from Gaussian noise over N_{trials} independent trials of $2\bar{\mathcal{F}}$ is determined¹ by numerical integration of the probability density function given, for example, by Eq. (7) of [33]. Fitting to the distribution of the highest $2\bar{\mathcal{F}}$ values suggests that $N_{\text{trials}} \approx N_{\text{templ}}$, with N_{templ} being the number of templates searched.

The p value for the highest $2\bar{\mathcal{F}}$ measured in any half-Hz band searched with N_{trials} independent trials is obtained by integrating the expected noise distribution ($\chi_{4N_{\text{seg}}}^2$ given in Sec. III) between the observed value and infinity, as done in Eq. (6) of [33]. The distribution of these p values is shown in Fig. 5 and it is not consistent with what we expect from Gaussian noise across the measured range. Therefore, we cannot exclude the presence of a signal in this data based on this distribution alone, as was done in [3].

¹After a simple change of variable from $2\bar{\mathcal{F}}$ to $N_{\text{seg}} \times 2\bar{\mathcal{F}}$.

B. P. ABBOTT *et al.*

PHYSICAL REVIEW D 96, 122004 (2017)

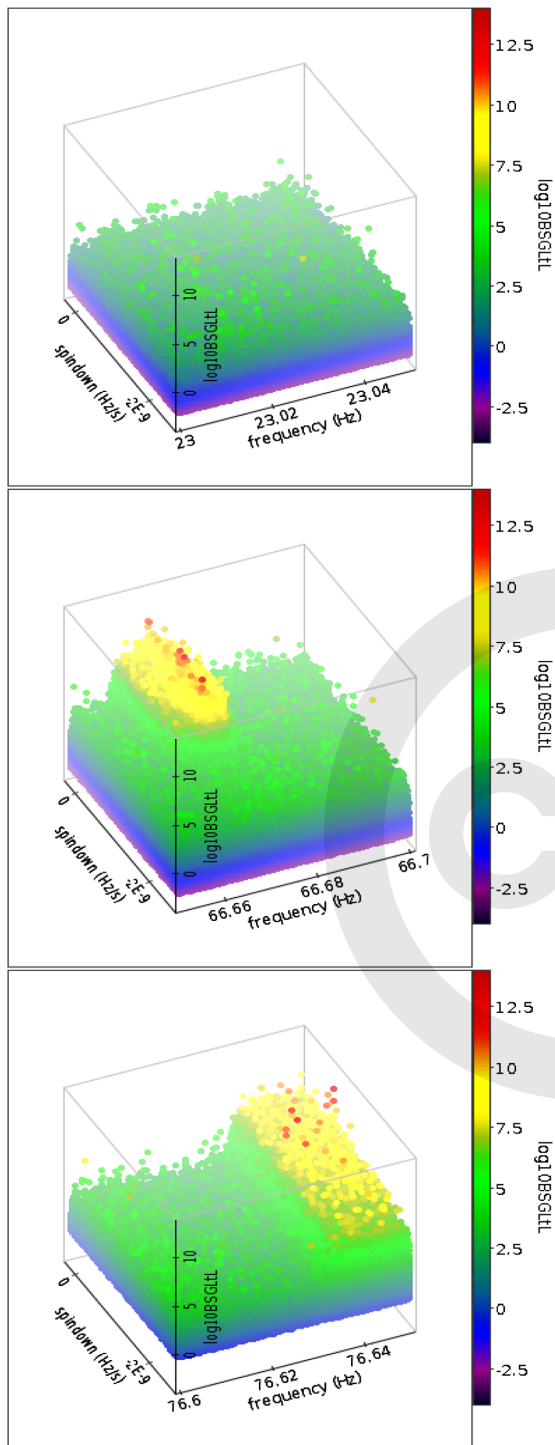


FIG. 2. On the vertical axis and color-coded is the $\hat{\beta}_{S/GLL}$ in three 50-mHz bands. The top band was marked as “undisturbed.” The middle band is an example of a “mildly disturbed band.” The bottom band is an example of a “disturbed band.”

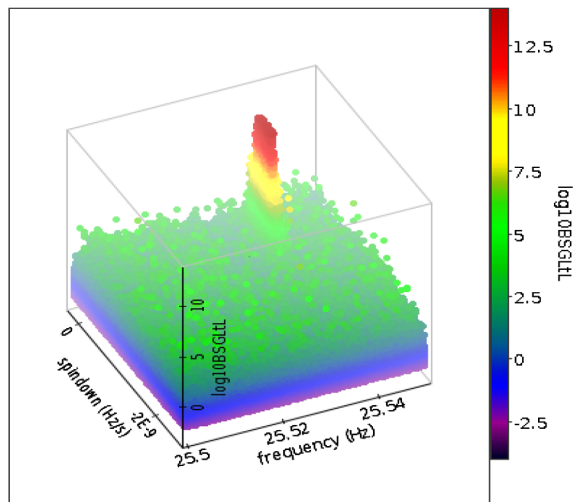


FIG. 3. This is an example of an “undisturbed band” but containing a fake signal. On the z axis and color coded is the $\hat{\beta}_{S/GLL}$.

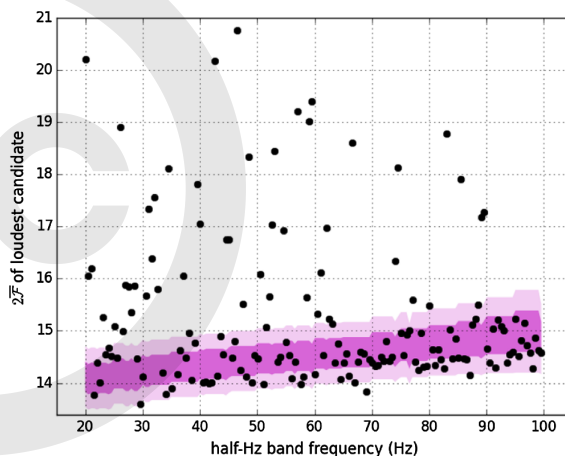


FIG. 4. Highest $2\bar{F}$ value (also referred to as the $2\bar{F}$ of the loudest candidate) in every half-Hz band as a function of band frequency. Since the number of templates increases with frequency, so does the highest $2\bar{F}$. The highest expected $2\bar{F} \pm 1\sigma(2\sigma)$ over N_{trials} independent trials is indicated by the darker (faded) band. Two half-mHz bands have $2\bar{F}$ values greater than the axes boundaries. The half-Hz bands beginning at 33.05 Hz and 35.55 Hz have loudest $2\bar{F}$ values of 159 and 500, respectively, due to features in the 33.3 Hz and 35.75 Hz 50-mHz bands which were marked “mildly disturbed” in the visual inspection.

IV. HIERARCHICAL FOLLOW UP

Since the significance of candidates is not consistent with what we expect from Gaussian noise only, we must investigate “significant” candidates to determine if they are

FIRST LOW-FREQUENCY EINSTEIN@HOME ALL-SKY ...

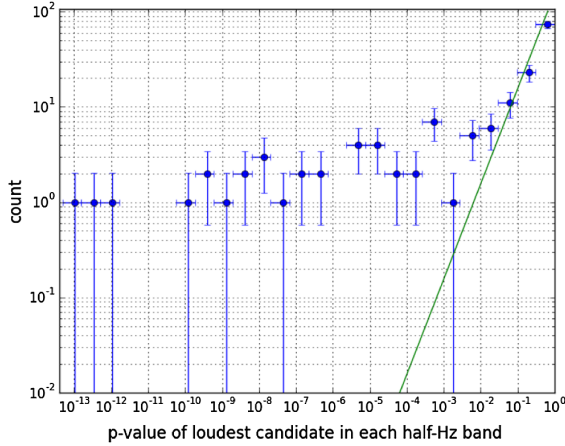


FIG. 5. Distribution of p values, with binomial uncertainties, for the highest detection statistic values measured in half-Hz bands (circles) and expected from pure Gaussian noise (line). We note that the measured p values for the highest $2\mathcal{F}$ in the 33.05 Hz and 35.55 Hz bands are not shown because they are outside of the x axis boundaries.

produced by a signal or by a detector disturbance. This is done using a hierarchical approach similar to what was used for the hierarchical follow-up of subthreshold candidates from the Einstein@Home S6 all-sky search [2].

At each stage of the hierarchical follow-up a semi-coherent search is performed, the top ranking candidates are marked and then searched in the next stage. If the data harbors a real signal, the significance of the recovered candidate will increase with respect to the significance that it had in the previous stage. On the other hand, if the candidate is not produced by a continuous-wave signal, the significance is not expected to increase consistently over the successive stages.

The hierarchical approach used in this search consists of four stages. This is the smallest number of stages within which we could achieve a fully coherent search, given the available computing resources. Directly performing a fully coherent follow-up of all significant candidates from the all-sky search would have been computationally unfeasible.

A. Stage 0

We bundle together candidates from the all-sky search that can be ascribed to the same root cause. This clustering step is a standard step in a multistage approach [2]: Both a loud signal and a loud disturbance produce high values of the detection statistic at a number of different template grid points, and it is a waste of compute cycles to follow up each of these independently.

We apply a clustering procedure that associates together multiple candidates close to each other in parameter space, and assigns them the parameters of the loudest among them, the seed. We use a new procedure with respect to [2]

PHYSICAL REVIEW D 96, 122004 (2017)

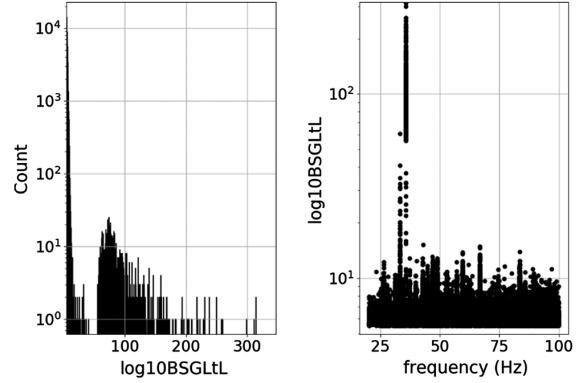


FIG. 6. Candidates that are followed up in stage 1: the distribution of their detection statistic values $\hat{\beta}_{S/GLtL}$ (left) and their distribution as a function of frequency (right).

that adapts the cluster size to the data and checks for consistency of the cluster volume with what is expected from a signal [34]. A candidate must have a $\hat{\beta}_{S/GLtL} > 5.5$ to be a cluster seed. This threshold is chosen such that only a handful of candidates per 50 mHz would be selected if the data were consistent with Gaussian noise. In this search, there are 15×10^6 candidates with $\hat{\beta}_{S/GLtL} > 5.5$. A lower threshold of $\hat{\beta}_{S/GLtL} > 4.0$ is applied to candidates that can be included in a cluster. If a cluster has at least two occupants (including the seed), the seed is marked for follow-up. In total, 35963 seeds are marked for follow-up. The $\hat{\beta}_{S/GLtL}$ values of these candidates are shown in Fig. 6 as well as their distribution in frequency.

Monte Carlo studies, using simulated signals added into the data, are conducted to determine how far from the signal parameters a signal candidate is recovered. These signals are simulated at a fixed strain amplitude for which most have $\hat{\beta}_{S/GLtL} \gtrsim 10.0$. We find that 1282 of 1294 signal candidates recovered after clustering (99%) are recovered within

$$\begin{cases} \Delta f = \pm 9.25 \times 10^{-5} \text{ Hz} \\ \Delta \dot{f} = \pm 4.25 \times 10^{-11} \text{ Hz/s} \\ \Delta \text{sky} \approx 4.5 \text{ sky grid points} \end{cases} \quad (3)$$

of the signal parameters. This confidence region² defines the parameter space around each candidate which will be searched in the first stage of the hierarchical follow-up. For weaker signals the confidence associated with this uncertainty region decreases. For signals close to the threshold used here, namely with $\hat{\beta}_{S/GLtL}$ between 5.5 and 10, the

²We pick 99% confidence rather than, say, 100%, because to reach the 100% confidence level would require an increase in a containment region too large for the available computing resources.

B. P. ABBOTT *et al.*

TABLE II. Search parameters for each stage. The follow-up stages are stages 1, 2, and 3. Also shown are the parameters for stage 0, taken from Table I.

	T_{coh} hr	N_{seg}	δf Hz	$\delta \dot{f}_c$ Hz/s	γ	m_{sky}
Stage 0	210	12	8.3×10^{-7}	1.3×10^{-11}	100	1×10^{-3}
Stage 1	500	5	6.7×10^{-7}	2.9×10^{-12}	80	8×10^{-6}
Stage 2	1260	2	1.9×10^{-7}	9.3×10^{-13}	30	1×10^{-6}
Stage 3	2512	1	6.7×10^{-8}	9.3×10^{-14}	1	4×10^{-7}

detection confidence only drops by a few percent (see bottom panel of Fig. 7 and last row of Table II in [34]).

B. Stage 1

In this stage we search a volume of parameter space [Eqs. (3)] around each cluster seed. We fix the run time per candidate to be 4 hr on an average CPU of the ATLAS computing cluster [35]. This yields an optimal search setup having a coherent baseline of 500 hr, with 5 segments and the grid spacings shown in Table II. We use the same ranking statistic as the original search, $\hat{\beta}_{S/GLL}$, with tunings updated for $N_{\text{seg}} = 5$.

For the population of simulated signals that passed the previous stage, stage 0, 1268 of 1282 (99%) are recovered within the uncertainty region

$$\begin{cases} \Delta f = \pm 1.76 \times 10^{-5} \text{ Hz} \\ \Delta \dot{f} = \pm 9.6 \times 10^{-12} \text{ Hz/s} \\ \Delta \text{sky} \approx 0.23 \Delta \text{sky}^{\text{stage } 0}. \end{cases} \quad (4)$$

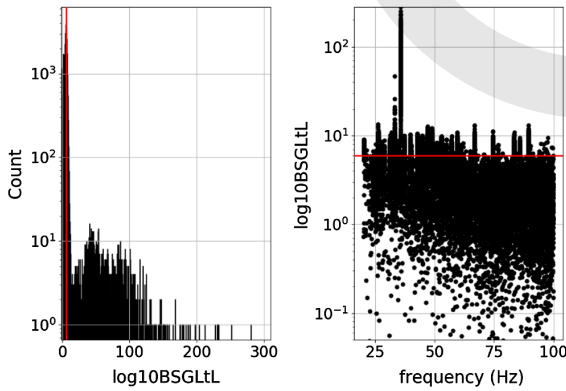


FIG. 7. Detection statistic of the loudest candidate from each stage 1 search: the distribution of their detection statistic values $\hat{\beta}_{S/GLL}$ (left) and their distribution as a function of frequency (right). 411 candidates have $\hat{\beta}_{S/GLL}$ values lower than the axes boundaries on the right plot. The red line marks $\hat{\beta}_{S/GLL} = 6.0$ which is the threshold at and above which candidates are passed on to stage 2.

PHYSICAL REVIEW D 96, 122004 (2017)

From each of the 35963 follow-up searches we record the most significant candidate in $\hat{\beta}_{S/GLL}$. The distribution of these is shown in Fig. 7. A threshold at $\hat{\beta}_{S/GLL} = 6.0$, derived from Monte Carlo studies, is applied to select the candidates to consider in the next stage. There are 14456 candidates above this threshold.

C. Stage 2

In this stage we search a volume of parameter space [Eqs. (4)] around each candidate from stage 1. We fix the run time per candidate to be 4 hr on an average CPU of the ATLAS computing cluster [35]. This yields an optimal search setup having a coherent baseline of 1260 hr, with 2 segments and the grid spacings shown in Table II. We use a different ranking statistic from the original search, because with 2 segments the transient line veto is not useful. Instead we use the ranking statistic $\hat{\beta}_{S/GL} := \log_{10} \hat{B}_{S/GL}$, introduced in [30] and previously used in [3], with tunings updated for $N_{\text{seg}} = 2$.

For the population of signals that passed the previous stage, 1265 of 1268 (>99%) are recovered within the uncertainty region

$$\begin{cases} \Delta f = \pm 8.65 \times 10^{-6} \text{ Hz} \\ \Delta \dot{f} = \pm 7.8 \times 10^{-12} \text{ Hz/s} \\ \Delta \text{sky} \approx 0.81 \Delta \text{sky}^{\text{stage } 1}. \end{cases} \quad (5)$$

From each of the follow-up searches we record the most significant candidate in $\hat{\beta}_{S/GL}$. The distribution of these is shown in Fig. 8. A threshold at $\hat{\beta}_{S/GL} = 6.0$ is applied to determine what candidates to consider in the next stage. There are 8486 candidates above threshold.

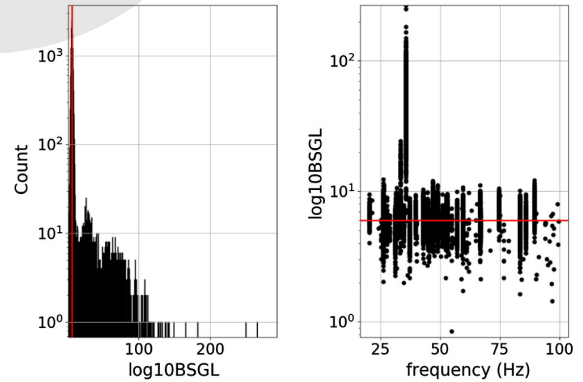


FIG. 8. Detection statistic of the loudest candidate from each stage 2 search: the distribution of their detection statistic values $\hat{\beta}_{S/GL}$ (left) and their distribution as a function of frequency (right). The red line marks $\hat{\beta}_{S/GL} = 6.0$ which is the threshold at and above which candidates are passed on to stage 3.

D. Stage 3

In this stage we search a volume of parameter space [Eqs. (5)] around each candidate. We perform a fully coherent search, with a coherent baseline of 2512 hr. The grid spacings are shown in Table II. We use the same ranking statistic as the previous stage, $\hat{\beta}_{S/GL}$, with tunings updated for $N_{seg} = 1$.

For the population of signals that passed the previous stage, 1265 of 1265 (>99%) are recovered within the uncertainty region

$$\begin{cases} \Delta f = \pm 7.5 \times 10^{-6} \text{ Hz} \\ \Delta \dot{f} = \pm 7 \times 10^{-12} \text{ Hz/s} \\ \Delta \text{sky} \approx 0.99 \Delta \text{sky}^{\text{stage } 2}. \end{cases} \quad (6)$$

This uncertainty region assumes candidates are within the uncertainty regions shown in Eqs. (3), (4), and (5) for each of the corresponding follow-up stages. It is possible that a strong candidate which is outside these uncertainty regions would be significant enough to pass through all follow-up stages. In this case the uncertainty on the signal parameters would be larger than the uncertainty region defined in Eq. (6).

From each of the follow-up searches we record the most significant candidate in $\hat{\beta}_{S/GL}$. The distribution of these is shown in Fig. 9. A threshold at $\hat{\beta}_{S/GL} = 6.0$ is applied to determine what candidates require further study. There are 6349 candidates above threshold. Many candidates appear to be from the same feature at a specific frequency. There are 57 distinct narrow frequency regions at which these 6349 candidates have been recovered.

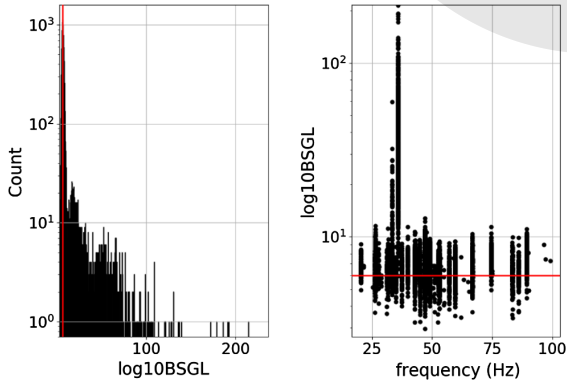


FIG. 9. Detection statistic of the loudest candidate from each stage 3 search: the distribution of their detection statistic values $\hat{\beta}_{S/GL}$ (left) and their distribution as a function of frequency (right). The red line marks $\hat{\beta}_{S/GL} = 6.0$ which is the threshold below which candidates are discarded.

E. Doppler modulation off veto

We employ a newly developed Doppler modulation off (DM-off) veto [36] to determine if the surviving candidates are of terrestrial origin. When searching for CW signals, the frequency of the signal template at any point in time is demodulated for the Doppler effect from the motion of the detectors around the Earth and around the Sun. If this demodulation is disabled, a candidate of astrophysical origin would not be recovered with the same significance. In contrast, a candidate of terrestrial origin could potentially become more significant. This is the basis of the DM-off veto.

For each candidate, the search range of the DM-off searches includes all detector frequencies that could have contributed to the original candidate, accounting for \dot{f} and Doppler corrections. The \dot{f} range includes the original all-sky search range, and extends into large positive values of \dot{f} to allow for a wider range of detector artifact behavior.

For a candidate to pass the DM-off veto it must be that its $2\mathcal{F}_{DM-off} \leq 2\mathcal{F}_{DM-off}^{thr}$. The $2\mathcal{F}_{DM-off}^{thr}$ is picked to be safe, i.e. to not veto any signal candidate with $2\mathcal{F}_{DM-on}$ in the range of the candidates under consideration. In particular we find that for candidates with $2\mathcal{F}_{DM-on} < 500$, after the third follow-up, $2\mathcal{F}_{DM-off}^{thr} = 62$. The threshold increases for candidates with $2\mathcal{F}_{DM-on} > 500$, scaling linearly with the candidates $2\mathcal{F}_{DM-on}$ (see Fig. 4 of [36]).

As described in [36], the DM-off search is first run using data from both detectors and a search grid which is ten times coarser in f and \dot{f} than the stage 3 search. The coarser search grid is used to minimize computational cost. 653 of the 6349 candidates pass the $2\mathcal{F}_{DM-off}^{thr}$ threshold. These surviving candidates undergo another similar search, except that the search is performed separately on the data from each of the LIGO detectors. We search each detector separately because a detector artifact present only in one detector may still pass the previous, multidetector search, as its significance is “diluted” by the clean data of the other detector. 101 candidates survive, and undergo a final DM-off search stage. This search uses the fine grid parameters of the stage 3 search (Table II), covers the parameter space which resulted in the largest $2\mathcal{F}_{DM-off}$ from the previous DM-off steps, and is performed three times, once using both detectors jointly and once for each of the two LIGO detectors. For a candidate to survive this stage it has to pass all three stage 3 searches.

Four candidates survive the full DM-off veto. Such veto is designed to be safe, i.e. not falsely dismiss real signals. However, its false alarm rate for noise disturbances is not fully characterized because very little is known about such weak and rare spectral disturbances, which this type of deep search unveils. This means that we cannot exclude that the four surviving candidates are in fact noise disturbances. The parameters of the candidates, after the third follow-up, are given in Table III. The $2\mathcal{F}_{DM-off}$ values are also given in this table.

B. P. ABBOTT *et al.*

PHYSICAL REVIEW D **96**, 122004 (2017)

TABLE III. Stage 3 follow-up results for each of the 4 candidates that survive the DM-off veto. For illustration purposes, in the 7th and 8th column we show the values of the average single-detector detection statistics. Typically, for signals, the single-detector values do not exceed the multidetector $2\bar{\mathcal{F}}$.

ID	f [Hz]	α [rad]	δ [rad]	\dot{f} [Hz/s]	$2\bar{\mathcal{F}}$	$2\bar{\mathcal{F}}_{\text{H1}}$	$2\bar{\mathcal{F}}_{\text{L1}}$	$2\mathcal{F}_{\text{DM-off}}$
1	58.970435900	1.87245	-0.51971	-1.081102×10^{-9}	81.4	48.5	33.4	55
2	62.081409292	4.98020	0.58542	-2.326246×10^{-9}	81.9	45.5	39.0	52
3	97.197674733	5.88374	-0.76773	2.28614×10^{-10}	86.5	55.0	31.8	58
4	99.220728369	2.842702	-0.469603	-2.498113×10^{-9}	80.2	41.4	45.8	55

TABLE IV. Search parameters, rounded to the first decimal place, for the follow-up of surviving LIGO O1 candidates in LIGO O2 data. T_{ref} is the reference time that defines the frequency and frequency derivative values.

Parameter	Value
T_{coh}	2160 hrs
T_{ref}	1168447494.5 GPS sec
N_{seg}	1
δf	9.0×10^{-8} Hz
δf_c	1.1×10^{-13} Hz/s
γ	1
m_{sky}	4×10^{-7}

TABLE V. Highest $2\bar{\mathcal{F}}$ expected after the follow-up in O2 data, if the candidates were due to a signal, compared with the highest $2\bar{\mathcal{F}}$ recovered from the follow-up. The $2\bar{\mathcal{F}}$ expected in Gaussian noise data is 52 ± 3 .

Candidate	Expected $2\bar{\mathcal{F}} \pm 1\sigma$	Loudest $2\bar{\mathcal{F}}$ recovered
1	85 ± 18	44
2	90 ± 19	52
3	84 ± 18	49
4	77 ± 17	47

F. Follow-up in LIGO O2 data

If the signal candidates surviving the O1 search are standard continuous wave signals, i.e. continuous wave signals arising from sources that radiate steadily over many years, they should be present in data from the Advanced LIGO’s second observing run (O2) with the same parameters. We perform a follow-up search using three months of O2 data, collected from November 30, 2016 to February 28, 2017.

The candidate parameters in Table III are translated to the O2 midtime, which is the reference time of the new search. The parameter space covered by the search is determined by the uncertainty on the candidate parameters in Eq. (5). The frequency region is widened to account for the spin-down uncertainty. The O2 follow-up covers a frequency range of $\pm 5.15 \times 10^{-4}$ Hz around the candidates.

The search parameters of the O2 follow-up are given in Table IV. The expected loudest $2\bar{\mathcal{F}}$ per follow-up search due to Gaussian noise alone is 52 ± 3 , assuming independent search templates.

If a candidate in Table III were due to a signal, the loudest $2\bar{\mathcal{F}}$ expected after the follow-up would be the value given in the second column of Table V. This expected value is obtained by scaling the $2\bar{\mathcal{F}}$ in Table III according to the different duration and the different noise levels between the data set used for the third follow-up and the O2 data set. The expected $2\bar{\mathcal{F}}$ also folds in a conservative factor of 0.9 due to a different mismatch of the O2 template grid with

respect to the template grid used for the third follow-up. Thus the expected $2\bar{\mathcal{F}}$ in Table V is a conservative estimate for the minimum $2\bar{\mathcal{F}}$ that we would expect from a signal candidate.

The loudest $2\bar{\mathcal{F}}$ after the follow-up in O2 data is also given in Table V. The loudest $2\bar{\mathcal{F}}$ recovered for each candidate are $\approx 2\sigma$ below the expected $2\bar{\mathcal{F}}$ for a signal candidate. The recovered $2\bar{\mathcal{F}}$ are consistent with what is expected from Gaussian data. We conclude that it is unlikely that any of the candidates in Table III arises from a long-lived astronomical source of continuous gravitational waves.

V. RESULTS

A. Upper limits on the gravitational wave amplitude

The search did not reveal any continuous gravitational wave signal in the parameter volume that was searched. We hence set frequentist 90% confidence upper limits on the maximum gravitational wave amplitude consistent with this null result in 0.5 Hz bands of the O1 data, $h_0^{90\%}(f)$. Specifically, $h_0^{90\%}(f)$ is the GW amplitude such that 90% of a population of signals with parameter values in our search range would have been detected by our search. We determined the upper limits in bands that were marked as undisturbed in Sec. III B. These upper limits may not hold for frequency bands that were marked as mildly disturbed, which we now consider disturbed as they were excluded by the analysis. These bands, as well as bands which were excluded from further analysis, are identified in Appendix A 3, Table VIII.

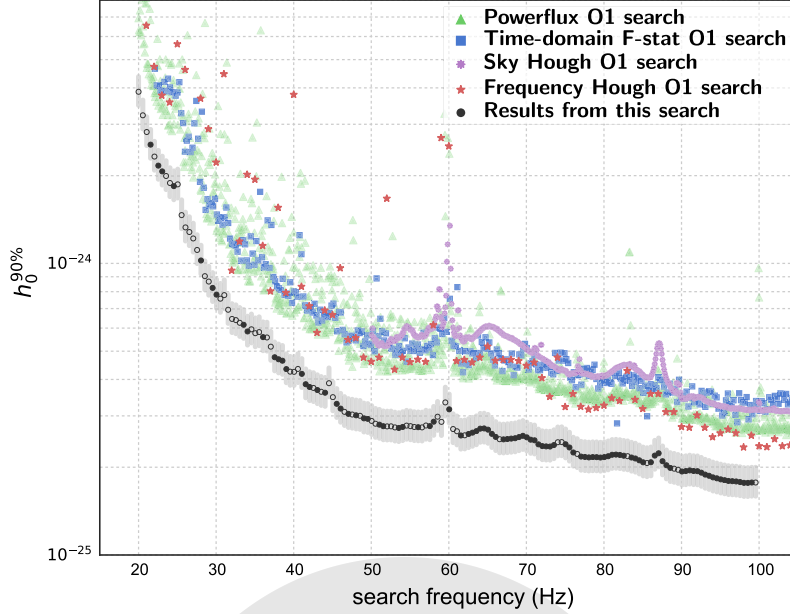


FIG. 10. 90% confidence upper limits on the gravitational wave amplitude of continuous gravitational wave signals with frequency in 0.5 Hz bands and with spin-down values within the searched range. The lowest set of points (black circles) are the results of this search. The empty circles denote half-Hz bands where the upper limit value does not hold for all frequencies in that interval. A list of the excluded frequencies is given in the Appendix. The lighter grey region around the upper limit points shows the 11% relative difference bracket between upper limits inferred with the procedure described in Sec. V and upper limits that would have been derived (at great computational expense) with direct measurements in all half-Hz bands. We estimate that less than $\sim 0.5\%$ of the upper limit points would fall outside of this bracket if they were derived with the direct-measurement method in Gaussian noise. For comparison we also plot the most recent upper limits results in this frequency range from O1 data obtained with various search pipelines [38]. The better sensitivity of this search is due to the long coherent observation time used. We note also that the searches of [38] cover a broader frequency and spin-down range than the search presented here. All upper limits presented here are population-averaged limits over the full sky and source polarization.

Since an actual full-scale fake-signal injection-and-recovery Monte Carlo for the entire set of follow-ups in every 0.5 Hz band is prohibitive, in the same spirit as [2,5,31], we perform such a study in a limited set of trial bands. We choose 20 half-Hz bands to measure the upper limits. If these half-Hz bands include 50 mHz bands which were not marked undisturbed, no upper limit injections are made in those 50 mHz bands.

The amplitudes of the fake signals bracket the 90% confidence region typically between 70% and 100%. The h_0 versus confidence data is fit in this region with a sigmoid of the form

$$C(h_0) = \frac{1}{1 + \exp\left(\frac{a-h_0}{b}\right)} \quad (7)$$

and the $h_0^{90\%}$ value is read off of this curve. The fitting procedure³ yields the best-fit a and b values and the covariance matrix. Given the binomial confidence values uncertainties,

³We used the `linfit` Matlab routine.

using the covariance matrix we estimate the $h_0^{90\%}$ uncertainty.

For each of these frequency bands we determine the sensitivity depth $\mathcal{D}^{90\%}$ [37] of the search corresponding to $h_0^{90\%}(f)$:

$$\mathcal{D}^{90\%} := \frac{\sqrt{S_h(f)}}{h_0^{90\%}(f)} [1/\sqrt{\text{Hz}}], \quad (8)$$

where $\sqrt{S_h(f)}$ is the noise level of the data as a function of frequency.

As representative of the sensitivity depth of this hierarchical search, we take the average of the measured depths at different frequencies: $48.7 [1/\sqrt{\text{Hz}}]$. We then determine the 90% upper limits by substituting this value in Eq. (8) for $\mathcal{D}^{90\%}$.

The upper limit that we get with this procedure, in general, yields a different number compared to the upper limit directly measured as done in the 20 test bands. An 11% relative error bracket comprises the range of variation observed on the measured sensitivity depths, including the

B. P. ABBOTT *et al.*

uncertainties on the single measurements. So we take this as a generous estimate of the range of variability of the upper limit values introduced by the estimation procedure. If the data were Gaussian this bracket would yield a $\sim 0.5\%$ probability of a *measured* upper limit falling outside of this bracket.

As a sanity check we measure the upper limits in five half-Hz bands which were not used to determine the average sensitivity depth. In each case we find that the measured sensitivity depth falls well within 11% of the average: $48.7 [1/\sqrt{\text{Hz}}]$.

Figure 10 shows the upper limits as a function of frequency. They are also presented in tabular form in the Appendix with the uncertainties indicating the range of variability introduced by the estimation procedure. The associated uncertainties amount to $\sim 20\%$ when also including 10% amplitude calibration uncertainty. The most constraining upper limit in the band 98.5–99 Hz, close to the highest frequency, where the detector is most sensitive, is 1.8×10^{-25} . At the lowest end of the frequency range, at 20 Hz, the upper limit rises to 3.9×10^{-24} .

B. Upper limits on the source ellipticity

In general not all the rotational kinetic energy lost is due to GW emission. Following [39], we define x to be the fraction of the spin-down rotational energy emitted in gravitational waves. The star's ellipticity necessary to sustain such emission is

$$\varepsilon(f, x\dot{f}) = \sqrt{\frac{5c^5}{32\pi^4 G} \frac{x|\dot{f}|}{If^5}}, \quad (9)$$

where c is the speed of light, G is the gravitational constant, f is the GW frequency, and I is the principal moment of inertia of the star. Correspondingly, $x\dot{f}$ is the spin-down rate that accounts for the emission of GWs and this is why we refer to it as the GW spin-down. The gravitational wave amplitude h_0 at the detector coming from a GW source at a distance D from Earth is

$$h_0(f, D) = \frac{4GI\pi^2}{c^4} \frac{\varepsilon f^2}{D}. \quad (10)$$

Based on this last equation, we can use the GW amplitude upper limits to bound the minimum distance for compact objects emitting continuous gravitational waves under different assumptions on the ellipticity of the objects. This is shown in Fig. 11. Above 55 Hz we can exclude sources with ellipticities larger than 10^{-5} (corresponding to x values larger than $3.2 \times 10^{-5} \frac{2.6 \times 10^{-9} \text{ Hz/s}}{|\dot{f}|}$) within 100 pc of Earth. Rough estimates are that there should be of order 10^4 neutron stars within this volume.

The dashed line in Fig. 11 is the spin-down ellipticity [$x = 1$ in Eq. (9)] for an object spinning down at half the

PHYSICAL REVIEW D 96, 122004 (2017)

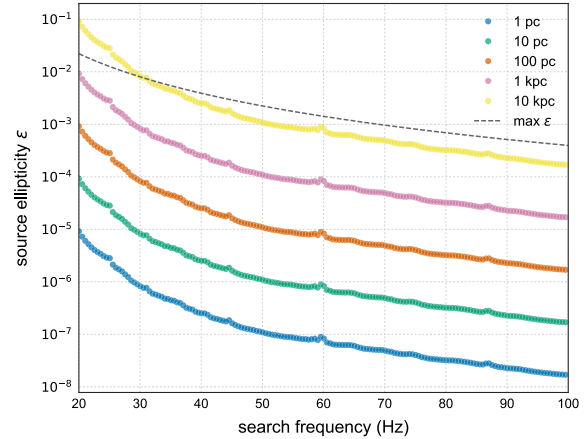


FIG. 11. Ellipticity ε of a source at a distance D emitting continuous gravitational waves that would have been detected by this search, assuming a source \dot{f} within the range covered by this search. The dashed line shows the spin-down ellipticity for the highest magnitude spin-down parameter value searched, $2.6 \times 10^{-9} \text{ Hz/s}$. The spin-down ellipticity is the ellipticity necessary for all the lost rotational kinetic energy to be emitted in gravitational waves. If we assume that the observed spin-down is all actual spin-down of the object, then no ellipticities could be possible above the dashed curve. In reality the observed and actual spin-down could differ due to radial acceleration of the source. In this case the actual spin-down of the object may even be larger than the apparent one. In this case our search would be sensitive to objects with ellipticities above the dashed line.

maximum searched gravitational wave signal spin-down value ($|\dot{f}| = 2.6 \times 10^{-9} \text{ Hz/s}$). This is the maximum ellipticity that this search probes; we can make no claim on sources with ellipticities greater than this. For a normal neutron star one might expect the majority of the spin-down to be due to non gravitational-wave emission. If, for instance, one believes that only 1% of the spin-down is due to gravitational wave emission ($x = 0.01$) then, from Eq. (9), the maximum ellipticity needs to be divided by ten and the dashed line in Fig. 11 drops by the same factor.

The results in Fig. 11 assume a fiducial value of the principal moment of inertia of 10^{38} kg m^2 . The upper limits can be scaled to any assumption for I using Eq. (10).

VI. CONCLUSIONS

This search concentrates the computing power of Einstein@Home in a relatively small frequency range at low frequencies where all-sky searches are significantly “cheaper” than at higher frequencies. For this reason, the initial search could be set up with a very long coherent observation time of 210 hr and this yields a record sensitivity depth of $48.7 [1/\sqrt{\text{Hz}}]$.

The O1 data set in the low frequency range investigated with this search is significantly more polluted by coherent

FIRST LOW-FREQUENCY EINSTEIN@HOME ALL-SKY ...

spectral artifacts than most of the data sets from the Initial-LIGO science runs. Because of this, even a relatively high threshold on the detection statistic of the first search yields tens of thousands of candidates, rather than just $O(100)$. We follow each of them up through a hierarchy of three further stages at the end of which $O(7000)$ survive. After the application of a newly developed Doppler-modulation-off veto, four survive.

Due to the presence of coherent spectral artifacts, no assumption can be made about the noise background of the search. On the other hand, we cannot run an Einstein@Home search many times to estimate such background.⁴ Because of this, measuring the significance of the four candidates at the end of the third follow-up stage is not trivial. However, the parameter uncertainty around the four candidates after the third follow-up stage is small [Eq. (6)], so with an independent data set we can verify the findings of the third stage *and* estimate its background. This means that we could assign a measure of confidence to any candidate that might survive the search on the new data set.

The four candidates which survive the Doppler-modulation-off veto are followed up with a fully coherent search using three months of O2 data, which produces results completely consistent with Gaussian noise and falls short of the predictions under the signal hypothesis. We hence proceed to set upper limits on the intrinsic GW amplitude h_0 . The hierarchical follow-up procedure presented here has also been used to follow-up outliers from other all-sky searches in O1 data with various search pipelines [38].

The smallest value of the GW amplitude upper limit is 1.8×10^{-25} in the band 98.5–99 Hz. Figure 10 shows the upper limit values as a function of search frequency. Our upper limits are the tightest ever placed for this population of signals, and are a factor 1.5–2 smaller than the most recent upper limits [38]. We note that [38] presents results from four different all-sky search pipelines covering a broader frequency and spin-down range than the one explored here. The coherent time baseline for all these pipelines is significantly shorter than the 210 hr used by the very first stage of this search. This limits the sensitivity of those searches but it makes them more robust to deviations in the signal waveform from the target waveform, compared to this search. We finally note that because the data is plagued in this low frequency region by coherent disturbances, the two procedures [34,36] are essential to reach the final sensitivity: without them a much higher detection threshold would have been needed, ultimately resulting in a degraded sensitivity/astrophysical reach.

Translating the upper limits on the GW amplitude to upper limits on the ellipticity of the GW source, we find that for frequencies above 55 Hz our results exclude isolated compact objects with spin-down ellipticities of

⁴By producing many (off-source) realizations of the search results.

PHYSICAL REVIEW D 96, 122004 (2017)

$10^{-5} \sqrt{10^{38} \text{ kg m}^2 / I}$ (corresponding to GW spin-downs between 10^{-14} Hz/s and 10^{-13} Hz/s) or higher, within 100 pc of Earth. For the population of known pulsars we know that the spin-down ellipticity is generally an overestimate of the actual ellipticity. However, for other objects, belonging to the population of possible continuous wave emitters that we do *not* see, this might not be the case. So we present the bounds on our results (the dashed line in Fig. 11) in terms of the spin-down ellipticity and leave it to the reader to derive the reach for the ellipticity value that best represents the class of sources in which they are interested.

ACKNOWLEDGMENTS

The authors gratefully acknowledge the support of the United States National Science Foundation (NSF) for the construction and operation of the LIGO Laboratory and Advanced LIGO as well as the Science and Technology Facilities Council (STFC) of the United Kingdom, the Max-Planck-Society (MPS), and the State of Niedersachsen/Germany for support of the construction of Advanced LIGO and construction and operation of the GEO600 detector. Additional support for Advanced LIGO was provided by the Australian Research Council. The authors gratefully acknowledge the Italian Istituto Nazionale di Fisica Nucleare (INFN), the French Centre National de la Recherche Scientifique (CNRS) and the Foundation for Fundamental Research on Matter supported by the Netherlands Organisation for Scientific Research, for the construction and operation of the Virgo detector and the creation and support of the EGO consortium. The authors also gratefully acknowledge research support from these agencies as well as by the Council of Scientific and Industrial Research of India, Department of Science and Technology, India, Science & Engineering Research Board (SERB), India, Ministry of Human Resource Development, India, the Spanish Ministerio de Economía y Competitividad, the Vicepresidència i Conselleria d’Innovació, Recerca i Turisme and the Conselleria d’Educació i Universitat del Govern de les Illes Balears, the National Science Centre of Poland, the European Commission, the Royal Society, the Scottish Funding Council, the Scottish Universities Physics Alliance, the Hungarian Scientific Research Fund (OTKA), the Lyon Institute of Origins (LIO), the National Research Foundation of Korea, Industry Canada and the Province of Ontario through the Ministry of Economic Development and Innovation, the Natural Science and Engineering Research Council Canada, Canadian Institute for Advanced Research, the Brazilian Ministry of Science, Technology, and Innovation, International Center for Theoretical Physics South American Institute for Fundamental Research (ICTP-SAIFR), Russian Foundation for Basic Research, the Leverhulme Trust, the Research Corporation, Ministry of Science and Technology (MOST), Taiwan and the Kavli Foundation. The authors gratefully acknowledge the support

B. P. ABBOTT *et al.*

PHYSICAL REVIEW D **96**, 122004 (2017)

of the NSF, STFC, MPS, INFN, CNRS and the State of Niedersachsen/Germany for provision of computational resources. The authors also gratefully acknowledge the support of the many thousands of Einstein@Home

volunteers, without whom this search would not have been possible.

This document has been assigned LIGO Laboratory document No. LIGO-P1700127.

APPENDIX: TABULAR DATA

1. Upper limit values

See Table VI.

TABLE VI. First frequency of each half-Hz signal frequency band in which we set upper limits and upper limit value for that band. The uncertainties correspond to the 11% relative difference bracket discussed in Sec. V.

f (Hz)	$h_0^{90\%} \times 10^{25}$	f (Hz)	$h_0^{90\%} \times 10^{25}$	f (Hz)	$h_0^{90\%} \times 10^{25}$	f (Hz)	$h_0^{90\%} \times 10^{25}$
20.00	38.8 ± 4.9	20.55	32.2 ± 4.1	21.05	28.2 ± 3.6	21.55	25.5 ± 3.3
22.05	23.3 ± 3.0	22.55	21.6 ± 2.8	23.05	20.7 ± 2.6	23.55	19.9 ± 2.5
24.05	18.9 ± 2.4	24.55	18.4 ± 2.3	25.05	18.7 ± 2.4	25.55	14.6 ± 1.9
26.05	13.3 ± 1.7	26.55	12.8 ± 1.6	27.05	12.2 ± 1.6	27.55	11.1 ± 1.4
28.05	10.2 ± 1.3	28.55	9.0 ± 1.2	29.05	8.7 ± 1.1	29.55	8.2 ± 1.0
30.05	7.8 ± 1.0	30.55	7.6 ± 1.0	31.05	7.8 ± 1.0	31.55	6.9 ± 0.9
32.05	6.5 ± 0.8	32.55	6.4 ± 0.8	33.05	6.3 ± 0.8	33.55	6.2 ± 0.8
34.05	5.8 ± 0.7	34.55	5.9 ± 0.8	35.05	5.8 ± 0.7	35.55	5.8 ± 0.7
36.05	5.6 ± 0.7	36.55	5.6 ± 0.7	37.05	5.2 ± 0.7	37.55	4.8 ± 0.6
38.05	4.7 ± 0.6	38.55	4.6 ± 0.6	39.05	4.3 ± 0.6	39.55	4.3 ± 0.5
40.05	4.2 ± 0.5	40.55	4.3 ± 0.6	41.05	4.2 ± 0.5	41.55	3.9 ± 0.5
42.05	3.8 ± 0.5	42.55	3.7 ± 0.5	43.05	3.7 ± 0.5	43.55	3.6 ± 0.5
44.05	3.6 ± 0.5	44.55	3.9 ± 0.5	45.05	3.5 ± 0.4	45.55	3.3 ± 0.4
46.05	3.2 ± 0.4	46.55	3.1 ± 0.4	47.05	3.0 ± 0.4	47.55	3.0 ± 0.4
48.05	3.0 ± 0.4	48.55	3.0 ± 0.4	49.05	2.9 ± 0.4	49.55	2.9 ± 0.4
50.05	2.9 ± 0.4	50.55	2.8 ± 0.4	51.05	2.8 ± 0.4	51.55	2.8 ± 0.4
52.05	2.8 ± 0.4	52.55	2.8 ± 0.4	53.05	2.7 ± 0.3	53.55	2.7 ± 0.3
54.05	2.7 ± 0.3	54.55	2.8 ± 0.4	55.05	2.8 ± 0.4	55.55	2.7 ± 0.3
56.05	2.7 ± 0.3	56.55	2.7 ± 0.3	57.05	2.8 ± 0.4	57.55	2.8 ± 0.4
58.05	2.9 ± 0.4	58.55	3.0 ± 0.4	59.05	2.9 ± 0.4	59.55	3.3 ± 0.4
60.05	3.2 ± 0.4	60.55	2.7 ± 0.3	61.05	2.7 ± 0.3	61.55	2.6 ± 0.3
62.05	2.6 ± 0.3	62.55	2.6 ± 0.3	63.05	2.6 ± 0.3	63.55	2.7 ± 0.3
64.05	2.7 ± 0.3	64.55	2.7 ± 0.3	65.05	2.7 ± 0.3	65.55	2.6 ± 0.3
66.05	2.5 ± 0.3	66.55	2.5 ± 0.3	67.05	2.5 ± 0.3	67.55	2.5 ± 0.3
68.05	2.5 ± 0.3	68.55	2.5 ± 0.3	69.05	2.5 ± 0.3	69.55	2.6 ± 0.3
70.05	2.5 ± 0.3	70.55	2.5 ± 0.3	71.05	2.5 ± 0.3	71.55	2.4 ± 0.3
72.05	2.4 ± 0.3	72.55	2.4 ± 0.3	73.05	2.4 ± 0.3	73.55	2.4 ± 0.3
74.05	2.4 ± 0.3	74.55	2.4 ± 0.3	75.05	2.4 ± 0.3	75.55	2.3 ± 0.3
76.05	2.2 ± 0.3	76.55	2.2 ± 0.3	77.05	2.2 ± 0.3	77.55	2.2 ± 0.3
78.05	2.2 ± 0.3	78.55	2.2 ± 0.3	79.05	2.2 ± 0.3	79.55	2.2 ± 0.3
80.05	2.2 ± 0.3	80.55	2.2 ± 0.3	81.05	2.2 ± 0.3	81.55	2.2 ± 0.3
82.05	2.2 ± 0.3	82.55	2.2 ± 0.3	83.05	2.2 ± 0.3	83.55	2.2 ± 0.3
84.05	2.1 ± 0.3	84.55	2.1 ± 0.3	85.05	2.1 ± 0.3	85.55	2.1 ± 0.3
86.05	2.1 ± 0.3	86.55	2.2 ± 0.3	87.05	2.2 ± 0.3	87.55	2.1 ± 0.3
88.05	2.0 ± 0.3	88.55	2.0 ± 0.3	89.05	2.0 ± 0.3	89.55	2.0 ± 0.2
90.05	1.9 ± 0.2	90.55	1.9 ± 0.2	91.05	2.0 ± 0.2	91.55	1.9 ± 0.2
92.05	1.9 ± 0.2	92.55	1.9 ± 0.2	93.05	1.9 ± 0.2	93.55	1.9 ± 0.2
94.05	1.8 ± 0.2	94.55	1.8 ± 0.2	95.05	1.8 ± 0.2	95.55	1.8 ± 0.2
96.05	1.8 ± 0.2	96.55	1.8 ± 0.2	97.05	1.8 ± 0.2	97.55	1.8 ± 0.2
98.05	1.8 ± 0.2	98.55	1.8 ± 0.2	99.05	1.8 ± 0.2	99.55	1.8 ± 0.2

FIRST LOW-FREQUENCY EINSTEIN@HOME ALL-SKY ...

PHYSICAL REVIEW D 96, 122004 (2017)

2. Cleaned-out frequency bins

See Table VII

TABLE VII. Instrumental lines identified and cleaned before the Einstein@Home runs. The different columns represent (I) the central frequency of the instrumental line; (II) low-frequency side (LFS) of the knockout band; (III) high-frequency side (HFS) of the knockout band; (IV) the interferometer in which the instrumental lines were identified.

f_L (Hz)	LFS (Hz)	HFS (Hz)	IFO
19.9995	0.001	0.001	L
20.0	0.001	0.001	H
20.24999	0.001	0.001	H
20.25014	0.001	0.001	L
20.5	0.001	0.001	H
20.5	0.001	0.001	L
20.7163	0.002	0.002	L
20.73	0.002	0.002	L
20.74121875	0.001	0.001	H
20.7423125	0.001	0.001	H
20.9995	0.001	0.001	L
21.0	0.001	0.001	H
21.24998	0.001	0.001	H
21.25011	0.001	0.001	L
21.3575	0.001	0.001	L
21.3842	0.001	0.001	L
21.41043	0.001	0.001	L
21.41043	0.001	0.001	L
21.4374	0.001	0.001	L
21.4639	0.001	0.001	L
21.499987	0.001	0.001	L
21.5	0.001	0.001	H
21.7028	0.002	0.002	L
21.7165	0.002	0.002	L
21.7344	0.001	0.001	L
21.9995	0.001	0.001	L
22.0	0.001	0.001	H
22.24997	0.001	0.001	H
22.25008	0.001	0.001	L
22.499974	0.001	0.001	L
22.5	0.001	0.001	H
22.6893	0.002	0.002	L
22.7	0.0005	0.0005	L
22.703	0.002	0.002	L
22.72233	0.001	0.001	L
22.815340625	0.001	0.001	H
22.81654375	0.001	0.001	H
22.9995	0.001	0.001	L
23.0	0.001	0.001	H
23.24996	0.001	0.001	H
23.25005	0.001	0.001	L
23.3039	0.001	0.001	L
23.3306	0.001	0.001	L
23.35683	0.001	0.001	L

(Table continued)

TABLE VII. (Continued)

f_L (Hz)	LFS (Hz)	HFS (Hz)	IFO
23.35683	0.001	0.001	L
23.3838	0.001	0.001	L
23.4103	0.001	0.001	L
23.499961	0.001	0.001	L
23.5	0.001	0.001	H
23.6758	0.002	0.002	L
23.6895	0.002	0.002	L
23.71026	0.001	0.001	L
23.97079	0.0016	0.0008	L
23.9995	0.001	0.001	L
24.0	0.0005	0.0005	H
24.0	0.001	0.001	H
24.24995	0.001	0.001	H
24.25002	0.001	0.001	L
24.499948	0.001	0.001	L
24.5	0.001	0.001	H
24.6623	0.002	0.002	L
24.676	0.002	0.002	L
24.69819	0.001	0.001	L
24.8894625	0.001	0.001	H
24.890775	0.001	0.001	H
24.9995	0.001	0.001	L
25.0	0.001	0.001	H
25.24994	0.001	0.001	H
25.24999	0.001	0.001	L
25.2503	0.001	0.001	L
25.277	0.001	0.001	L
25.30323	0.001	0.001	L
25.30323	0.001	0.001	L
25.3302	0.001	0.001	L
25.3567	0.001	0.001	L
25.499935	0.001	0.001	L
25.5	0.001	0.001	H
25.6	0.0005	0.0005	L
25.6488	0.002	0.002	L
25.6625	0.002	0.002	L
25.68612	0.001	0.001	L
25.9995	0.001	0.001	L
26.0	0.001	0.001	H
26.24993	0.001	0.001	H
26.24996	0.001	0.001	L
26.499922	0.001	0.001	L
26.5	0.001	0.001	H
26.6353	0.002	0.002	L
26.649	0.002	0.002	L
26.67405	0.001	0.001	L
26.963584375	0.001	0.001	H
26.96500625	0.001	0.001	H
26.9995	0.001	0.001	L
27.0	0.001	0.001	H
27.1967	0.001	0.001	L
27.2234	0.001	0.001	L
27.24963	0.001	0.001	L
27.24963	0.001	0.001	L
27.24992	0.001	0.001	H

(Table continued)

B. P. ABBOTT *et al.*

PHYSICAL REVIEW D **96**, 122004 (2017)

TABLE VII. (Continued)

f_L (Hz)	LFS (Hz)	HFS (Hz)	IFO
27.24993	0.001	0.001	L
27.2766	0.001	0.001	L
27.3031	0.001	0.001	L
27.499909	0.001	0.001	L
27.5	0.001	0.001	H
27.6218	0.002	0.002	L
27.6355	0.002	0.002	L
27.66198	0.001	0.001	L
27.9995	0.001	0.001	L
28.0	0.001	0.001	H
28.2499	0.001	0.001	L
28.24991	0.001	0.001	H
28.499896	0.001	0.001	L
28.5	0.001	0.001	H
28.5	0.0005	0.0005	L
28.6083	0.002	0.002	L
28.622	0.002	0.002	L
28.64991	0.001	0.001	L
28.9995	0.001	0.001	L
29.0	0.001	0.001	H
29.03770625	0.001	0.001	H
29.0392375	0.001	0.001	H
29.1431	0.001	0.001	L
29.1698	0.001	0.001	L
29.19603	0.001	0.001	L
29.19603	0.001	0.001	L
29.223	0.001	0.001	L
29.2495	0.001	0.001	L
29.24987	0.001	0.001	L
29.2499	0.001	0.001	H
29.2767	0.001	0.001	L
29.3031	0.001	0.001	L
29.499883	0.001	0.001	L
29.5	0.001	0.001	H
29.5948	0.002	0.002	L
29.6085	0.002	0.002	L
29.63784	0.001	0.001	L
29.9995	0.001	0.001	L
30.0	0.001	0.001	H
30.24984	0.001	0.001	L
30.24989	0.001	0.001	H
30.49987	0.001	0.001	L
30.5	0.001	0.001	H
30.5813	0.002	0.002	L
30.595	0.002	0.002	L
30.62577	0.001	0.001	L
30.943	0.001	0.001	H
30.9738	0.001	0.001	H
30.9995	0.001	0.001	L
31.0	0.001	0.001	H
31.0895	0.001	0.001	L
31.111828125	0.001	0.001	H
31.11346875	0.001	0.001	H
31.1162	0.001	0.001	L
31.14243	0.001	0.001	L

(Table continued)

TABLE VII. (Continued)

f_L (Hz)	LFS (Hz)	HFS (Hz)	IFO
31.14243	0.001	0.001	L
31.1694	0.001	0.001	L
31.1959	0.001	0.001	L
31.2231	0.001	0.001	L
31.2495	0.001	0.001	L
31.24981	0.001	0.001	L
31.24988	0.001	0.001	H
31.4	0.0005	0.0005	L
31.4127	0.003	0.003	H
31.4149	0.003	0.003	H
31.499857	0.001	0.001	L
31.5	0.001	0.001	H
31.5678	0.002	0.002	L
31.5815	0.002	0.002	L
31.6137	0.001	0.001	L
31.94116	0.001	0.001	H
31.973	0.001	0.001	H
31.9995	0.001	0.001	L
32.0	0.0005	0.0005	H
32.0	0.001	0.001	H
32.24978	0.001	0.001	L
32.24987	0.001	0.001	H
32.499844	0.001	0.001	L
32.5	0.001	0.001	H
33.7	0.01556	0.01556	L
33.8	0.0005	0.0005	L
34.3	0.0005	0.0005	L
34.7	0.02778	0.02778	H
34.7	0.13	0.13	L
35.3	0.02778	0.02778	H
35.3	0.13	0.13	L
35.706385	0.003055	0.003055	L
35.7095265	0.01222	0.01222	H
35.9	0.10222	0.10222	H
35.958055	0.009165	0.009165	L
36.7	0.10722	0.10722	H
36.7	0.0005	0.0005	L
37.3	0.01	0.01	H
38.955	0.001	0.001	L
38.9674	0.001	0.001	H
38.9815	0.001	0.001	L
38.9995	0.001	0.001	L
39.0	0.001	0.001	H
39.0087	0.001	0.001	L
39.0351	0.001	0.001	L
39.24957	0.001	0.001	L
39.2498	0.001	0.001	H
39.408315625	0.001	0.001	H
39.41039375	0.001	0.001	H
39.4598	0.002	0.002	L
39.4735	0.002	0.002	L
39.499753	0.001	0.001	L
39.5	0.001	0.001	H
39.51714	0.001	0.001	L
39.6	0.0005	0.0005	L

(Table continued)

FIRST LOW-FREQUENCY EINSTEIN@HOME ALL-SKY ...

PHYSICAL REVIEW D 96, 122004 (2017)

TABLE VII. (Continued)

f_L (Hz)	LFS (Hz)	HFS (Hz)	IFO
39.92644	0.001	0.001	H
39.9666	0.001	0.001	H
39.9995	0.001	0.001	L
40.0	0.0005	0.0005	H
40.0	0.001	0.001	H
40.24954	0.001	0.001	L
40.24979	0.001	0.001	H
40.4463	0.002	0.002	L
40.46	0.002	0.002	L
40.49974	0.001	0.001	L
40.5	0.001	0.001	H
40.50507	0.001	0.001	L
40.8215	0.001	0.001	L
40.8482	0.001	0.001	L
40.87443	0.001	0.001	L
40.87443	0.001	0.001	L
40.9014	0.001	0.001	L
40.9246	0.001	0.001	H
40.9279	0.001	0.001	L
40.9551	0.001	0.001	L
40.9658	0.001	0.001	H
40.9815	0.001	0.001	L
40.9995	0.001	0.001	L
41.0	0.001	0.001	H
41.24951	0.001	0.001	L
41.24978	0.001	0.001	H
41.4328	0.002	0.002	L
41.4465	0.002	0.002	L
41.4824375	0.001	0.001	H
41.484625	0.001	0.001	H
41.493	0.001	0.001	L
41.499727	0.001	0.001	L
41.5	0.001	0.001	H
41.92276	0.001	0.001	H
41.965	0.001	0.001	H
41.9995	0.001	0.001	L
42.0	0.001	0.001	H
42.24948	0.001	0.001	L
42.24977	0.001	0.001	H
42.4193	0.002	0.002	L
42.433	0.002	0.002	L
42.48093	0.001	0.001	L
42.499714	0.001	0.001	L
42.5	0.001	0.001	H
42.5	0.0005	0.0005	L
42.7679	0.001	0.001	L
42.7946	0.001	0.001	L
42.82083	0.001	0.001	L
42.82083	0.001	0.001	L
42.8478	0.001	0.001	L
42.8743	0.001	0.001	L
42.9015	0.001	0.001	L
42.92092	0.001	0.001	H
42.9279	0.001	0.001	L
42.9642	0.001	0.001	H

(Table continued)

TABLE VII. (Continued)

f_L (Hz)	LFS (Hz)	HFS (Hz)	IFO
42.9995	0.001	0.001	L
43.0	0.001	0.001	H
43.24945	0.001	0.001	L
43.24976	0.001	0.001	H
43.4058	0.002	0.002	L
43.4195	0.002	0.002	L
43.46886	0.001	0.001	L
43.499701	0.001	0.001	L
43.5	0.001	0.001	H
43.556559375	0.001	0.001	H
43.55885625	0.001	0.001	H
43.91908	0.001	0.001	H
43.9634	0.001	0.001	H
43.9995	0.001	0.001	L
44.0	0.001	0.001	H
44.24942	0.001	0.001	L
44.24975	0.001	0.001	H
44.3923	0.002	0.002	L
44.406	0.002	0.002	L
44.45679	0.001	0.001	L
44.499688	0.001	0.001	L
44.5	0.001	0.001	H
44.7143	0.001	0.001	L
44.741	0.001	0.001	L
44.76723	0.001	0.001	L
44.76723	0.001	0.001	L
44.7942	0.001	0.001	L
44.8207	0.001	0.001	L
44.8479	0.001	0.001	L
44.8743	0.001	0.001	L
44.91724	0.001	0.001	H
44.9626	0.001	0.001	H
44.9995	0.001	0.001	L
45.0	0.001	0.001	H
45.24939	0.001	0.001	L
45.24974	0.001	0.001	H
45.3788	0.002	0.002	L
45.3925	0.002	0.002	L
45.4	0.0005	0.0005	L
45.44472	0.001	0.001	L
45.499675	0.001	0.001	L
45.5	0.001	0.001	H
45.63068125	0.001	0.001	H
45.6330875	0.001	0.001	H
45.9	0.0005	0.0005	L
45.9154	0.001	0.001	H
45.9618	0.001	0.001	H
45.9995	0.001	0.001	L
46.0	0.001	0.001	H
46.24936	0.001	0.001	L
46.24973	0.001	0.001	H
46.3653	0.002	0.002	L
46.379	0.002	0.002	L
46.43265	0.001	0.001	L
46.499662	0.001	0.001	L

(Table continued)

B. P. ABBOTT *et al.*

PHYSICAL REVIEW D 96, 122004 (2017)

TABLE VII. (Continued)

f_L (Hz)	LFS (Hz)	HFS (Hz)	IFO
46.5	0.001	0.001	H
46.6607	0.001	0.001	L
46.6874	0.001	0.001	L
46.71363	0.001	0.001	L
46.71363	0.001	0.001	L
46.7406	0.001	0.001	L
46.7671	0.001	0.001	L
46.7943	0.001	0.001	L
46.8207	0.001	0.001	L
46.91356	0.001	0.001	H
46.961	0.001	0.001	H
46.9995	0.001	0.001	L
47.0	0.001	0.001	H
47.24933	0.001	0.001	L
47.24972	0.001	0.001	H
47.3518	0.002	0.002	L
47.3655	0.002	0.002	L
47.42058	0.001	0.001	L
47.499649	0.001	0.001	L
47.5	0.001	0.001	H
47.704803125	0.001	0.001	H
47.70731875	0.001	0.001	H
47.8	0.0005	0.0005	L
47.91172	0.001	0.001	H
47.94158	0.0032	0.0016	L
47.9602	0.001	0.001	H
47.9995	0.001	0.001	L
48.0	0.0005	0.0005	H
48.0	0.001	0.001	H
48.2493	0.001	0.001	L
48.24971	0.001	0.001	H
48.3	0.0005	0.0005	L
48.3383	0.002	0.002	L
48.352	0.002	0.002	L
48.40851	0.001	0.001	L
48.499636	0.001	0.001	L
48.5	0.001	0.001	H
48.6071	0.001	0.001	L
48.6338	0.001	0.001	L
48.66003	0.001	0.001	L
48.66003	0.001	0.001	L
48.687	0.001	0.001	L
48.7135	0.001	0.001	L
48.7407	0.001	0.001	L
48.7671	0.001	0.001	L
48.90988	0.001	0.001	H
48.9594	0.001	0.001	H
48.9995	0.001	0.001	L
49.0	0.001	0.001	H
49.24927	0.001	0.001	L
49.2497	0.001	0.001	H
49.3248	0.002	0.002	L
49.3385	0.002	0.002	L
49.499623	0.001	0.001	L
49.5	0.001	0.001	H

(Table continued)

TABLE VII. (Continued)

f_L (Hz)	LFS (Hz)	HFS (Hz)	IFO
49.778925	0.001	0.001	H
49.78155	0.001	0.001	H
49.90804	0.001	0.001	H
49.9995	0.001	0.001	L
50.0	0.001	0.001	H
50.24924	0.001	0.001	L
50.3113	0.002	0.002	L
50.325	0.002	0.002	L
50.49961	0.001	0.001	L
50.5	0.001	0.001	H
50.5535	0.001	0.001	L
50.5802	0.001	0.001	L
50.60643	0.001	0.001	L
50.60643	0.001	0.001	L
50.6334	0.001	0.001	L
50.6599	0.001	0.001	L
50.6871	0.001	0.001	L
50.7135	0.001	0.001	L
50.9062	0.001	0.001	H
51.0	0.001	0.001	H
51.2	0.0005	0.0005	L
51.24921	0.001	0.001	L
51.2978	0.002	0.002	L
51.3115	0.002	0.002	L
51.499597	0.001	0.001	L
51.5	0.001	0.001	H
51.853046875	0.001	0.001	H
51.85578125	0.001	0.001	H
51.90436	0.001	0.001	H
52.0	0.001	0.001	H
52.24918	0.001	0.001	L
52.2843	0.002	0.002	L
52.298	0.002	0.002	L
52.499584	0.001	0.001	L
52.4999	0.001	0.001	L
52.5	0.001	0.001	H
52.5266	0.001	0.001	L
52.55283	0.001	0.001	L
52.55283	0.001	0.001	L
52.5798	0.001	0.001	L
52.6063	0.001	0.001	L
52.6335	0.001	0.001	L
52.6599	0.001	0.001	L
52.90252	0.001	0.001	H
53.0	0.001	0.001	H
53.24915	0.001	0.001	L
53.2708	0.002	0.002	L
53.2845	0.002	0.002	L
53.499571	0.001	0.001	L
53.5	0.001	0.001	H
53.90068	0.001	0.001	H
53.92716875	0.001	0.001	H
53.9300125	0.001	0.001	H
54.0	0.001	0.001	H
54.1	0.0005	0.0005	L

(Table continued)

FIRST LOW-FREQUENCY EINSTEIN@HOME ALL-SKY ...

PHYSICAL REVIEW D 96, 122004 (2017)

TABLE VII. (Continued)

f_L (Hz)	LFS (Hz)	HFS (Hz)	IFO
54.2573	0.002	0.002	L
54.271	0.002	0.002	L
54.4463	0.001	0.001	L
54.473	0.001	0.001	L
54.49923	0.001	0.001	L
54.49923	0.001	0.001	L
54.499558	0.001	0.001	L
54.5	0.001	0.001	H
54.5262	0.001	0.001	L
54.5527	0.001	0.001	L
54.5799	0.001	0.001	L
54.6063	0.001	0.001	L
54.89884	0.001	0.001	H
55.0	0.001	0.001	H
55.2438	0.002	0.002	L
55.2575	0.002	0.002	L
55.499545	0.001	0.001	L
55.5	0.001	0.001	H
55.897	0.001	0.001	H
56.0	0.0005	0.0005	H
56.0	0.001	0.001	H
56.001290625	0.001	0.001	H
56.00424375	0.001	0.001	H
56.3927	0.001	0.001	L
56.4194	0.001	0.001	L
56.44563	0.001	0.001	L
56.44563	0.001	0.001	L
56.4726	0.001	0.001	L
56.4991	0.001	0.001	L
56.499532	0.001	0.001	L
56.5	0.001	0.001	H
56.5	0.0005	0.0005	L
56.5263	0.001	0.001	L
56.5527	0.001	0.001	L
56.89516	0.001	0.001	H
57.0	0.001	0.001	H
57.0	0.0005	0.0005	L
57.499519	0.001	0.001	L
57.5	0.001	0.001	H
57.89332	0.001	0.001	H
58.0	0.001	0.001	H
58.0754125	0.001	0.001	H
58.078475	0.001	0.001	H
58.3391	0.001	0.001	L
58.3658	0.001	0.001	L
58.39203	0.001	0.001	L
58.39203	0.001	0.001	L
58.419	0.001	0.001	L
58.4455	0.001	0.001	L
58.499506	0.001	0.001	L
58.5	0.001	0.001	H
58.89148	0.001	0.001	H
59.0	0.001	0.001	H
59.499493	0.001	0.001	L
59.5	0.001	0.001	H

(Table continued)

TABLE VII. (Continued)

f_L (Hz)	LFS (Hz)	HFS (Hz)	IFO
59.88964	0.001	0.001	H
59.926975	0.004	0.002	L
60.0	0.001	0.001	H
60.0	0.06	0.06	H
60.0	0.06	0.06	L
60.149534375	0.001	0.001	H
60.15270625	0.001	0.001	H
60.2855	0.001	0.001	L
60.3122	0.001	0.001	L
60.33843	0.001	0.001	L
60.33843	0.001	0.001	L
60.3654	0.001	0.001	L
60.3919	0.001	0.001	L
60.49948	0.001	0.001	L
60.5	0.001	0.001	H
60.8878	0.001	0.001	H
61.0	0.001	0.001	H
61.499467	0.001	0.001	L
61.5	0.001	0.001	H
62.0	0.001	0.001	H
62.22365625	0.001	0.001	H
62.2269375	0.001	0.001	H
62.28483	0.001	0.001	L
62.28483	0.001	0.001	L
62.3	0.0005	0.0005	L
62.499454	0.001	0.001	L
62.5	0.001	0.001	H
62.8	0.0005	0.0005	L
62.8254	0.003	0.003	H
62.8298	0.003	0.003	H
63.0	0.001	0.001	H
63.499441	0.001	0.001	L
63.5	0.001	0.001	H
64.0	0.0005	0.0005	H
64.0	0.001	0.001	H
64.297778125	0.001	0.001	H
64.30116875	0.001	0.001	H
64.499428	0.001	0.001	L
64.5	0.001	0.001	H
65.0	0.001	0.001	H
65.2	0.0005	0.0005	L
65.499415	0.001	0.001	L
65.5	0.001	0.001	H
65.7	0.0005	0.0005	L
66.0	0.001	0.001	H
66.3719	0.001	0.001	H
66.3754	0.001	0.001	H
66.499402	0.001	0.001	L
66.5	0.001	0.001	H
66.665	0.001	0.001	L
67.0	0.001	0.001	H
67.499389	0.001	0.001	L
67.5	0.001	0.001	H
67.6	0.0005	0.0005	L
68.0	0.001	0.001	H

(Table continued)

B. P. ABBOTT *et al.*

PHYSICAL REVIEW D **96**, 122004 (2017)

TABLE VII. (Continued)

f_L (Hz)	LFS (Hz)	HFS (Hz)	IFO
68.1	0.0005	0.0005	L
68.499376	0.001	0.001	L
68.5	0.001	0.001	H
68.6	0.0005	0.0005	L
69.0	0.001	0.001	H
69.499363	0.001	0.001	L
69.5	0.001	0.001	H
70.0	0.001	0.001	H
70.49935	0.001	0.001	L
70.5	0.001	0.001	H
71.0	0.001	0.001	H
71.0	0.0005	0.0005	L
71.499337	0.001	0.001	L
71.5	0.001	0.001	H
71.5	0.0005	0.0005	L
71.91237	0.0048	0.0024	L
72.0	0.0005	0.0005	H
72.0	0.001	0.001	H
72.499324	0.001	0.001	L
72.5	0.001	0.001	H
73.0	0.001	0.001	H
73.499311	0.001	0.001	L
73.5	0.001	0.001	H
73.9	0.0005	0.0005	L
74.0	0.001	0.001	H
74.4	0.0005	0.0005	L
74.5	0.001	0.001	H
75.0	0.001	0.001	H
75.5	0.001	0.001	H
76.0	0.001	0.001	H
76.3	0.0005	0.0005	L
76.3235	0.001	0.001	H
76.3235	0.001	0.001	H
76.411925	0.001	0.001	H
76.5	0.001	0.001	H
76.50035	0.001	0.001	H
76.588775	0.001	0.001	H
76.6772	0.001	0.001	H
76.75	0.001	0.001	L
76.765625	0.001	0.001	H
76.8	0.0005	0.0005	L
76.85405	0.001	0.001	H
76.942475	0.001	0.001	H
77.0	0.001	0.001	H
77.0309	0.001	0.001	H
77.119325	0.001	0.001	H
77.20775	0.001	0.001	H
77.296175	0.001	0.001	H
77.3	0.0005	0.0005	L
77.3846	0.001	0.001	H
77.473025	0.001	0.001	H
77.5	0.001	0.001	H
77.56145	0.001	0.001	H
77.749975	0.001	0.001	L
78.0	0.001	0.001	H

(Table continued)

TABLE VII. (Continued)

f_L (Hz)	LFS (Hz)	HFS (Hz)	IFO
78.5	0.001	0.001	H
78.74995	0.001	0.001	L
79.0	0.001	0.001	H
79.2	0.0005	0.0005	L
79.5	0.001	0.001	H
79.7	0.0005	0.0005	L
79.749925	0.001	0.001	L
80.0	0.0005	0.0005	H
80.0	0.001	0.001	H
80.5	0.001	0.001	H
80.7499	0.001	0.001	L
81.0	0.001	0.001	H
81.5	0.001	0.001	H
81.749875	0.001	0.001	L
82.0	0.001	0.001	H
82.1	0.0005	0.0005	L
82.5	0.001	0.001	H
82.6	0.0005	0.0005	L
82.74985	0.001	0.001	L
83.0	0.001	0.001	H
83.5	0.001	0.001	H
83.749825	0.001	0.001	L
83.897765	0.0056	0.0028	L
84.0	0.001	0.001	H
84.5	0.001	0.001	H
84.7498	0.001	0.001	L
85.0	0.001	0.001	H
85.0	0.0005	0.0005	L
85.5	0.001	0.001	H
85.5	0.0005	0.0005	L
85.749775	0.001	0.001	L
86.0	0.001	0.001	H
86.5	0.001	0.001	H
86.74975	0.001	0.001	L
87.0	0.001	0.001	H
87.5	0.001	0.001	H
87.749725	0.001	0.001	L
87.9	0.0005	0.0005	L
88.0	0.0005	0.0005	H
88.0	0.001	0.001	H
88.4	0.0005	0.0005	L
88.5	0.001	0.001	H
88.7497	0.001	0.001	L
89.0	0.001	0.001	H
89.5	0.001	0.001	H
89.749675	0.001	0.001	L
90.0	0.001	0.001	H
90.3	0.0005	0.0005	L
90.5	0.001	0.001	H
90.74965	0.001	0.001	L
90.8	0.0005	0.0005	L
91.0	0.001	0.001	H
91.3	0.0005	0.0005	L
91.5	0.001	0.001	H
91.749625	0.001	0.001	L

(Table continued)

FIRST LOW-FREQUENCY EINSTEIN@HOME ALL-SKY ...

PHYSICAL REVIEW D 96, 122004 (2017)

TABLE VII. (Continued)

f_L (Hz)	LFS (Hz)	HFS (Hz)	IFO
92.0	0.001	0.001	H
92.5	0.001	0.001	H
92.7496	0.001	0.001	L
93.0	0.001	0.001	H
93.5	0.001	0.001	H
93.7	0.0005	0.0005	L
93.749575	0.001	0.001	L
94.0	0.001	0.001	H
94.2	0.0005	0.0005	L
94.2381	0.003	0.003	H
94.2447	0.003	0.003	H
94.5	0.001	0.001	H
94.74955	0.001	0.001	L
95.0	0.001	0.001	H
95.5	0.001	0.001	H
95.749525	0.001	0.001	L
95.88316	0.0064	0.0032	L
96.0	0.0005	0.0005	H
96.0	0.001	0.001	H
96.5	0.001	0.001	H
96.6	0.0005	0.0005	L
96.7495	0.001	0.001	L
97.0	0.001	0.001	H
97.1	0.0005	0.0005	L
97.5	0.001	0.001	H
97.749475	0.001	0.001	L
98.0	0.001	0.001	H
98.5	0.001	0.001	H
98.74945	0.001	0.001	L
99.0	0.001	0.001	H
99.0	0.0005	0.0005	L
99.5	0.001	0.001	H
99.5	0.0005	0.0005	L
99.749425	0.001	0.001	L
99.9989	0.001	0.001	H
100.0	0.001	0.001	H

3. 50-mHz signal-frequency bands where the upper limit value does not hold

See Table VII

TABLE VIII. 50-mHz search-frequency bands that are excluded from the results. Bands are excluded from the results if they were identified as disturbed based on visual inspection (D), if they were identified as mildly disturbed based on visual inspection then excluded later in the analysis (M), if they contained a hardware injection (I), or where the results were produced from entirely fake data as detailed in Table I (C). Bands labeled D, C, or I are excluded from the analysis.

Start band	Band type	Start band	Band type	Start band	Band type	Start band	Band type
20.40	M	20.90	D	20.80	M	21.45	M
22.40	D	23.90	M	24.45	D	24.20	M
25.25	M	25.60	M	26.05	M	26.90	M
27.50	D	27.45	M	27.85	D	27.55	M
28.55	D	28.90	M	29.15	D	30.60	D
30.85	M	31.10	M	31.40	I	31.75	M
32.35	M	32.90	M	33.05	M	34.80	M
34.60	C	34.65	C	34.70	C	34.75	C
35.20	C	35.25	C	35.30	C	35.35	C
35.70	M	35.80	C	35.85	C	35.90	C
35.95	C	36.60	M	36.60	C	36.65	C
36.70	C	36.75	C	37.25	M	39.75	M
40.20	M	40.85	D	42.80	M	43.65	M
44.70	D	44.65	M	45.30	D	45.35	M
46.90	M	47.65	M	48.95	M	50.25	M
51.00	M	52.30	M	52.60	M	52.80	I
53.05	M	54.70	M	55.05	M	55.60	M
56.80	D	57.10	M	58.95	M	59.50	M
59.55	M	59.95	C	60.00	C	61.00	M
61.05	M	62.45	D	62.05	M	66.65	M
74.50	D	74.45	M	75.00	M	76.60	D
76.65	M	83.30	M	85.80	M	89.40	D
89.35	M	90.00	M	99.95	D		

[1] <https://www.einsteinathome.org/>.
 [2] M. A. Papa *et al.*, Hierarchical follow-up of subthreshold candidates of an all-sky Einstein@Home search for continuous gravitational waves on LIGO sixth science run data, *Phys. Rev. D* **94**, 122006 (2016).
 [3] B. P. Abbott *et al.* (LIGO Scientific Collaboration and Virgo Collaboration), Results of the deepest all-sky survey for continuous gravitational waves on LIGO S6 data running on the Einstein@Home volunteer distributed computing project, *Phys. Rev. D* **94**, 102002 (2016).
 [4] B. P. Abbott *et al.* (LIGO Scientific Collaboration and VIRGO Collaboration), Comprehensive all-sky search for

periodic gravitational waves in the sixth science run LIGO data, *Phys. Rev. D* **94**, 042002 (2016).
 [5] A. Singh, M. A. Papa, H.-B. Eggenstein, S. Zhu, H. Pletsch, B. Allen, O. Bock, B. Maschenchalk, R. Prix, and X. Siemens, Results of an all-sky high-frequency Einstein@Home search for continuous gravitational waves in LIGO 5th science run, *Phys. Rev. D* **94**, 064061 (2016).
 [6] J. Aasi *et al.* (LIGO Scientific Collaboration and VIRGO Collaboration), First low frequency all-sky search for continuous gravitational wave signals, *Phys. Rev. D* **93**, 042007 (2016).

B. P. ABBOTT *et al.*PHYSICAL REVIEW D **96**, 122004 (2017)

- [7] B. P. Abbott *et al.* (LIGO Scientific Collaboration), Einstein@Home all-sky search for periodic gravitational waves in LIGO S5 data, *Phys. Rev. D* **87**, 042001 (2013).
- [8] B. P. Abbott *et al.* (LIGO Scientific Collaboration and VIRGO Collaboration), All-sky Search for Periodic Gravitational Waves in the Full S5 Data, *Phys. Rev. D* **85**, 022001 (2012).
- [9] B. P. Abbott *et al.* (LIGO Scientific Collaboration), Einstein@Home search for periodic gravitational waves in early S5 LIGO data, *Phys. Rev. D* **80**, 042003 (2009).
- [10] B. P. Abbott *et al.* (LIGO Scientific Collaboration), All-sky LIGO Search for Periodic Gravitational Waves in the Early S5 Data, *Phys. Rev. Lett.* **102**, 111102 (2009).
- [11] J. Aasi *et al.* (LIGO Scientific Collaboration and Virgo Collaboration), Application of a Hough search for continuous gravitational waves on data from the 5th LIGO science run, *Classical Quantum Gravity* **31**, 085014 (2014).
- [12] J. Aasi *et al.* (LIGO Scientific Collaboration and Virgo Collaboration), Implementation of an \mathcal{F} -statistic all-sky search for continuous gravitational waves in Virgo VSR1 data, *Classical Quantum Gravity* **31**, 165014 (2014).
- [13] B. P. Abbott *et al.* (LIGO Scientific Collaboration), All-sky search for periodic gravitational waves in LIGO S4 data, *Phys. Rev. D* **77**, 022001 (2008).
- [14] B. P. Abbott *et al.* (LIGO Scientific Collaboration), Einstein@Home search for periodic gravitational waves in LIGO S4 data, *Phys. Rev. D* **79**, 022001 (2009).
- [15] B. Abbott *et al.* (LIGO Scientific Collaboration), Searches for periodic gravitational waves from unknown isolated sources and Scorpius X-1: Results from the second LIGO science run, *Phys. Rev. D* **76**, 082001 (2007).
- [16] LIGO Scientific Collaboration, LIGO: The Laser Interferometer Gravitational-Wave Observatory, *Rep. Prog. Phys.* **72**, 076901 (2009).
- [17] B. Abbott *et al.* (LIGO Scientific Collaboration), GW150914: The Advanced LIGO Detectors in the Era of First Discoveries, *Phys. Rev. Lett.* **116**, 131103 (2016).
- [18] J. Aasi *et al.* (LIGO Scientific Collaboration), Advanced LIGO, *Classical Quantum Gravity* **32**, 074001 (2015).
- [19] J. Abadie *et al.* (LIGO Scientific Collaboration and Virgo Collaboration), Sensitivity achieved by the LIGO and Virgo gravitational wave detectors during LIGO's sixth and Virgo's second and third science runs, [arXiv:1203.2674](https://arxiv.org/abs/1203.2674).
- [20] H. J. Pletsch and B. Allen, Exploiting Large-Scale Correlations to Detect Continuous Gravitational Waves, *Phys. Rev. Lett.* **103**, 181102 (2009).
- [21] H. J. Pletsch, Parameter-space correlations of the optimal statistic for continuous gravitational-wave detection, *Phys. Rev. D* **78**, 102005 (2008).
- [22] H. J. Pletsch, Parameter-space metric of semicoherent searches for continuous gravitational waves, *Phys. Rev. D* **82**, 042002 (2010).
- [23] C. Cutler and B. F. Schutz, The generalized \mathcal{F} -statistic: multiple detectors and multiple gravitational wave pulsars, *Phys. Rev. D* **72**, 063006 (2005).
- [24] B. Krishnan, A. M. Sintes, M. A. Papa, B. F. Schutz, S. Frasca, and C. Palomba, The Hough transform search for continuous gravitational waves, *Phys. Rev. D* **70**, 082001 (2004).
- [25] P. Astone, A. Colla, S. D'Antonio, S. Frasca, and C. Palomba, Method for all-sky searches of continuous gravitational wave signals using the frequency-Hough transform, *Phys. Rev. D* **90**, 042002 (2014).
- [26] <http://boinc.berkeley.edu/>.
- [27] D. P. Anderson, BOINC: A System for Public-Resource Computing and Storage, in *Proceedings of the Fifth IEEE/ACM International Workshop on Grid Computing (GRID04)*, pp. 4–10 (2004).
- [28] D. P. Anderson, C. Christensen, and B. Allen, Designing a Runtime System for Volunteer Computing, in *Proceedings of the 2006 ACM/IEEE conference on Supercomputing*, pp. 126–136 (2006).
- [29] D. Keitel, Robust semicoherent searches for continuous gravitational waves with noise and signal models including hours to days long transients, *Phys. Rev. D* **93**, 084024 (2016).
- [30] D. Keitel, R. Prix, M. A. Papa, P. Leaci, and M. Siddiqi, Search for continuous gravitational waves: Improving robustness versus instrumental artifacts, *Phys. Rev. D* **89**, 064023 (2014).
- [31] S. J. Zhu *et al.*, An Einstein@Home search for continuous gravitational waves from Cassiopeia A, *Phys. Rev. D* **94**, 082008 (2016).
- [32] C. Biwer *et al.*, Validating gravitational-wave detections: The Advanced LIGO hardware injection system, *Phys. Rev. D* **95**, 062002 (2017).
- [33] J. Aasi *et al.* (LIGO Scientific Collaboration and VIRGO Collaboration), Directed search for continuous gravitational waves from the Galactic center, *Phys. Rev. D* **88**, 102002 (2013).
- [34] A. Singh, M. A. Papa, H.-B. Eggenstein, and S. Walsh, Adaptive clustering algorithm for continuous gravitational wave searches, [arXiv:1707.02676](https://arxiv.org/abs/1707.02676).
- [35] <http://www.aei.mpg.de/24838/02> Computing and ATLAS.
- [36] S. J. Zhu, M. A. Papa, and S. Walsh, preceding article, New veto for continuous gravitational wave searches, *Phys. Rev. D* **96**, 124007 (2017).
- [37] B. Behnke, M. A. Papa, and R. Prix, Postprocessing methods used in the search for continuous gravitational-wave signals from the Galactic Center, *Phys. Rev. D* **91**, 064007 (2015).
- [38] J. Aasi *et al.* (LIGO Scientific Collaboration and VIRGO Collaboration), All-sky search for periodic gravitational waves in the O1 LIGO Data, [arXiv:1707.02667](https://arxiv.org/abs/1707.02667).
- [39] J. Ming, B. Krishnan, M. A. Papa, C. Aulbert, and H. Fehrmann, Optimal directed searches for continuous gravitational waves, *Phys. Rev. D* **93**, 064011 (2016).

B. P. Abbott,¹ R. Abbott,¹ T. D. Abbott,² F. Acernese,^{3,4} K. Ackley,⁵ C. Adams,⁶ T. Adams,⁷ P. Addesso,⁸ R. X. Adhikari,¹ V. B. Adya,⁹ C. Affeldt,⁹ M. Afrough,¹⁰ B. Agarwal,¹¹ K. Agatsuma,¹² N. Aggarwal,¹³ O. D. Aguiar,¹⁴ L. Aiello,^{15,16}

FIRST LOW-FREQUENCY EINSTEIN@HOME ALL-SKY ...

PHYSICAL REVIEW D 96, 122004 (2017)

A. Ain,¹⁷ B. Allen,^{9,18,19} G. Allen,¹¹ A. Allocca,^{20,21} P. A. Altin,²² A. Amato,²³ A. Ananyeva,¹ S. B. Anderson,¹ W. G. Anderson,¹⁸ S. Antier,²⁴ S. Appert,¹ K. Arai,¹ M. C. Araya,¹ J. S. Areeda,²⁵ N. Arnaud,^{24,26} S. Ascenzi,^{27,16} G. Ashton,⁹ M. Ast,²⁸ S. M. Aston,⁶ P. Astone,²⁹ P. Aufmuth,¹⁹ C. Aubert,⁹ K. AultONeal,³⁰ A. Avila-Alvarez,²⁵ S. Babak,³¹ P. Bacon,³² M. K. M. Bader,¹² S. Bae,³³ P. T. Baker,^{34,35} F. Baldaccini,^{36,37} G. Ballardini,²⁶ S. W. Ballmer,³⁸ S. Banagiri,³⁹ J. C. Barayoga,¹ S. E. Barclay,⁴⁰ B. C. Barish,¹ D. Barker,⁴¹ F. Barone,^{3,4} B. Barr,⁴⁰ L. Barsotti,¹³ M. Barsuglia,³² D. Barta,⁴² J. Bartlett,⁴¹ I. Bartos,⁴³ R. Bassiri,⁴⁴ A. Basti,^{20,21} J. C. Batch,⁴¹ C. Baune,⁹ M. Bawaj,^{45,37} M. Bazzan,^{46,47} B. Bécsy,⁴⁸ C. Beer,⁹ M. Bejger,⁴⁹ I. Belahcene,²⁴ A. S. Bell,⁴⁰ B. K. Berger,¹ G. Bergmann,⁹ C. P. L. Berry,⁵⁰ D. Bersanetti,^{51,52} A. Bertolini,¹² J. Betzwieser,⁶ S. Bhagwat,³⁸ R. Bhandare,⁵³ I. A. Bilenko,⁵⁴ G. Billingsley,¹ C. R. Billman,⁵ J. Birch,⁶ R. Birney,⁵⁵ O. Birnholtz,⁹ S. Biscans,¹³ A. Bisht,¹⁹ M. Bitossi,^{26,21} C. Biwer,³⁸ M. A. Bizouard,²⁴ J. K. Blackburn,¹ J. Blackman,⁵⁶ C. D. Blair,⁵⁷ D. G. Blair,⁵⁷ R. M. Blair,⁴¹ S. Bloemen,⁵⁸ O. Bock,⁹ N. Bode,⁹ M. Boer,⁵⁹ G. Bogaert,⁵⁹ A. Bohe,³¹ F. Bondu,⁶⁰ R. Bonnard,⁷ B. A. Boom,¹² R. Bork,¹ V. Boschi,^{20,21} S. Bose,^{61,17} Y. Bouffanais,³² A. Bozzi,²⁶ C. Bradaschia,²¹ P. R. Brady,¹⁸ V. B. Braginsky,^{†,54} M. Branchesi,^{62,63} J. E. Brau,⁶⁴ T. Briant,⁶⁵ A. Brilliet,⁵⁹ M. Brinkmann,⁹ V. Brisson,²⁴ P. Brockill,¹⁸ J. E. Broida,⁶⁶ A. F. Brooks,¹ D. A. Brown,³⁸ D. D. Brown,⁵⁰ N. M. Brown,¹³ S. Brunett,¹ C. C. Buchanan,² A. Buikema,¹³ T. Bulik,⁶⁷ H. J. Bulten,^{68,12} A. Buonanno,^{31,69} D. Buskulic,⁷ C. Buy,³² R. L. Byer,⁴⁴ M. Cabero,⁹ L. Cadonati,⁷⁰ G. Cagnoli,^{23,71} C. Cahillane,¹ J. Calderón Bustillo,⁷⁰ T. A. Callister,¹ E. Calloni,^{72,4} J. B. Camp,⁷³ P. Canizares,⁷³ K. C. Cannon,⁷⁴ H. Cao,⁷⁵ J. Cao,⁷⁶ C. D. Capano,⁹ E. Capocasa,³² F. Carbognani,²⁶ S. Caride,⁷⁷ M. F. Carney,⁷⁸ J. Casanueva Diaz,²⁴ C. Casentini,^{27,16} S. Caudill,¹⁸ M. Cavaglia,¹⁰ F. Cavalier,²⁴ R. Cavalieri,²⁶ G. Cella,²¹ C. B. Cepeda,¹ L. Cerboni Baiardi,^{62,63} G. Cerretani,^{20,21} E. Cesarini,^{27,16} S. J. Chamberlin,⁷⁹ M. Chan,⁴⁰ S. Chao,⁸⁰ P. Charlton,⁸¹ E. Chassande-Mottin,³² D. Chatterjee,¹⁸ B. D. Cheeseboro,^{34,35} H. Y. Chen,⁸² Y. Chen,⁵⁶ H.-P. Cheng,⁵ A. Chincarini,⁵² A. Chiummo,²⁶ T. Chmiel,⁷⁸ H. S. Cho,⁸³ M. Cho,⁶⁹ J. H. Chow,²² N. Christensen,^{66,59} Q. Chu,⁵⁷ A. J. K. Chua,⁸⁴ S. Chua,⁸⁵ A. K. W. Chung,⁸⁵ S. Chung,⁵⁷ G. Ciani,⁵ R. Ciolfi,^{86,87} C. E. Cirelli,⁴⁴ A. Cirone,^{51,52} F. Clara,⁴¹ J. A. Clark,⁷⁰ F. Cleva,⁵⁹ C. Cocchieri,¹⁰ E. Coccia,^{15,16} P.-F. Cohadon,⁶⁵ A. Colla,^{88,29} C. G. Collette,⁸⁹ L. R. Cominsky,⁹⁰ M. Constancio Jr.,¹⁴ L. Conti,⁴⁷ S. J. Cooper,⁵⁰ P. Corban,⁶ T. R. Corbitt,² K. R. Corley,⁴³ N. Cornish,⁹¹ A. Corsi,⁷⁷ S. Cortese,²⁶ C. A. Costa,¹⁴ M. W. Coughlin,⁶⁶ S. B. Coughlin,^{92,93} J.-P. Coulon,⁵⁹ S. T. Countryman,⁴³ P. Couvares,¹ P. B. Covas,⁹⁴ E. E. Cowan,⁷⁰ D. M. Coward,⁵⁷ M. J. Cowart,⁶ D. C. Coyne,¹ R. Coyne,⁷⁷ J. D. E. Creighton,¹⁸ T. D. Creighton,⁹⁵ J. Cripe,² S. G. Crowder,⁹⁶ T. J. Cullen,²⁵ A. Cumming,⁴⁰ L. Cunningham,⁴⁰ E. Cuoco,²⁶ T. Dal Canton,⁷³ S. L. Danilishin,^{19,9} S. D'Antonio,¹⁶ K. Danzmann,^{19,9} A. Dasgupta,⁹⁷ C. F. Da Silva Costa,⁵ V. Dattilo,²⁶ I. Dave,⁵³ M. Davier,²⁴ D. Davis,³⁸ E. J. Daw,⁹⁸ B. Day,⁷⁰ S. De,³⁸ D. DeBra,⁴⁴ E. Deelman,⁹⁹ J. Degallaix,²³ M. De Laurentis,^{72,4} S. Deléglise,⁶⁵ W. Del Pozzo,^{50,20,21} T. Denker,⁹ T. Dent,⁹ V. Dergachev,³¹ R. De Rosa,^{72,4} R. T. DeRosa,⁶ R. DeSalvo,¹⁰⁰ J. Devenson,⁵⁵ R. C. Devine,^{34,35} S. Dhurandhar,¹⁷ M. C. Díaz,⁹⁵ L. Di Fiore,⁴ M. Di Giovanni,^{101,87} T. Di Girolamo,^{72,4,43} A. Di Lieto,^{20,21} S. Di Pace,^{88,29} I. Di Palma,^{88,29} F. Di Renzo,^{20,21} Z. Doctor,⁸² V. Dolique,²³ F. Donovan,¹³ K. L. Dooley,¹⁰ S. Doravari,⁹ I. Dorrington,⁹³ R. Douglas,⁴⁰ M. Dovale Álvarez,⁵⁰ T. P. Downes,¹⁸ M. Drago,⁹ R. W. P. Drever,^{†,1} J. C. Driggers,⁴¹ Z. Du,⁷⁶ M. Ducrot,⁷ J. Duncan,⁹² S. E. Dwyer,⁴¹ T. B. Edo,⁹⁸ M. C. Edwards,⁶⁶ A. Effler,⁶ H.-B. Eggenstein,⁹ P. Ehrens,¹ J. Eichholz,¹ S. S. Eikenberry,⁵ R. A. Eisenstein,¹³ R. C. Essick,¹³ Z. B. Etienne,^{34,35} T. Etzel,¹ M. Evans,¹³ T. M. Evans,⁶ M. Factourovich,⁴³ V. Fafone,^{27,16,15} H. Fair,³⁸ S. Fairhurst,⁹³ X. Fan,⁷⁶ S. Farinon,⁵² B. Farr,⁸² W. M. Farr,⁵⁰ E. J. Fauchon-Jones,⁹³ M. Favata,¹⁰² M. Fays,⁹³ H. Fehrmann,⁹ J. Feicht,¹ M. M. Fejer,⁴⁴ A. Fernandez-Galiana,¹³ I. Ferrante,^{20,21} E. C. Ferreira,¹⁴ F. Ferrini,²⁶ F. Fidecaro,^{20,21} I. Fiori,²⁶ D. Fiorucci,³² R. P. Fisher,³⁸ R. Flaminio,^{23,103} M. Fletcher,⁴⁰ H. Fong,¹⁰⁴ P. W. F. Forsyth,²² S. S. Forsyth,⁷⁰ J.-D. Fournier,⁵⁹ S. Frasca,^{88,29} F. Frasconi,²¹ Z. Frei,⁴⁸ A. Freise,⁵⁰ R. Frey,⁶⁴ V. Frey,²⁴ E. M. Fries,¹ P. Fritschel,¹³ V. V. Frolov,⁶ P. Fulda,^{5,73} M. Fyffe,⁶ H. Gabbard,⁹ M. Gabel,¹⁰⁵ B. U. Gadre,¹⁷ S. M. Gaebel,⁵⁰ J. R. Gair,¹⁰⁶ L. Gammaitoni,³⁶ M. R. Ganija,⁷⁵ S. G. Gaonkar,¹⁷ F. Garufi,^{72,4} S. Gaudio,³⁰ G. Gaur,¹⁰⁷ V. Gayathri,¹⁰⁸ N. Gehrels,^{†,73} G. Gemme,⁵² E. Genin,²⁶ A. Gennai,²¹ D. George,¹¹ J. George,⁵³ L. Gergely,¹⁰⁹ V. Germain,⁷ S. Ghonge,⁷⁰ Abhirup Ghosh,¹¹⁰ Archisman Ghosh,^{110,12} S. Ghosh,^{58,12} J. A. Giaime,^{2,6} K. D. Giardino,⁶ A. Giazotto,²¹ K. Gill,³⁰ L. Glover,¹⁰⁰ E. Goetz,⁹ R. Goetz,⁵ S. Gomes,⁹³ G. González,² J. M. Gonzalez Castro,^{20,21} A. Gopakumar,¹¹¹ M. L. Gorodetsky,⁵⁴ S. E. Gossan,¹ M. Gosselin,²⁶ R. Gouaty,⁷ A. Grado,^{112,4} C. Graef,⁴⁰ M. Granata,²³ A. Grant,⁴⁰ S. Gras,¹³ C. Gray,⁴¹ G. Greco,^{62,63} A. C. Green,⁵⁰ P. Groot,⁵⁸ H. Grote,⁹ S. Grunewald,³¹ P. Gruning,²⁴ G. M. Guidi,^{62,63} X. Guo,⁷⁶ A. Gupta,⁷⁹ M. K. Gupta,⁹⁷ K. E. Gushwa,¹ E. K. Gustafson,¹ R. Gustafson,¹¹³ B. R. Hall,⁶¹ E. D. Hall,¹ G. Hammond,⁴⁰ M. Haney,¹¹¹ M. M. Hanke,⁹ J. Hanks,⁴¹ C. Hanna,⁷⁹ O. A. Hannuksela,⁸⁵ J. Hanson,⁶ T. Hardwick,² J. Harms,^{62,63} G. M. Harry,¹¹⁴ I. W. Harry,³¹ M. J. Hart,⁴⁰ C.-J. Haster,¹⁰⁴ K. Haughian,⁴⁰ J. Healy,¹¹⁵ A. Heidmann,⁶⁵

122004-21

B. P. ABBOTT *et al.*PHYSICAL REVIEW D **96**, 122004 (2017)

M. C. Heintze,⁶ H. Heitmann,⁵⁹ P. Hello,²⁴ G. Hemming,²⁶ M. Hendry,⁴⁰ I. S. Heng,⁴⁰ J. Hennig,⁴⁰ J. Henry,¹¹⁵
A. W. Heptonstall,¹ M. Heurs,^{9,19} S. Hild,⁴⁰ D. Hoak,²⁶ D. Hofman,²³ K. Holt,⁶ D. E. Holz,⁸² P. Hopkins,⁹³ C. Horst,¹⁸
J. Hough,⁴⁰ E. A. Houston,⁴⁰ E. J. Howell,⁵⁷ Y. M. Hu,⁹ E. A. Huerta,¹¹ D. Huet,²⁴ B. Hughey,³⁰ S. Husa,⁹⁴ S. H. Huttner,⁴⁰
T. Huynh-Dinh,⁶ N. Indik,⁹ D. R. Ingram,⁴¹ R. Inta,⁷⁷ G. Intini,^{88,29} H. N. Isa,⁴⁰ J.-M. Isac,⁶⁵ M. Isi,¹ B. R. Iyer,¹¹⁰
K. Izumi,⁴¹ T. Jacqmin,⁶⁵ K. Jani,⁷⁰ P. Jaranowski,¹¹⁶ S. Jawahar,¹¹⁷ F. Jiménez-Forteza,⁹⁴ W. W. Johnson,² D. I. Jones,¹¹⁸
R. Jones,⁴⁰ R. J. G. Jonker,¹² L. Ju,⁵⁷ J. Junker,⁹ C. V. Kalaghatgi,⁹³ V. Kalogera,⁹² S. Kandhasamy,⁶ G. Kang,³³
J. B. Kanner,¹ S. Karki,⁶⁴ K. S. Karvinen,⁹ M. Kasprzak,² M. Katolik,¹¹ E. Katsavounidis,¹³ W. Katzman,⁶ S. Kaufer,¹⁹
K. Kawabe,⁴¹ F. Kéfélian,⁵⁹ D. Keitel,⁴⁰ A. J. Kember,¹¹ R. Kennedy,⁹⁸ C. Kent,⁹³ J. S. Key,¹¹⁹ F. Y. Khalili,⁵⁴ I. Khan,^{15,16}
S. Khan,⁹ Z. Khan,⁹⁷ E. A. Khazanov,¹²⁰ N. Kijbunchoo,⁴¹ Chunglee Kim,¹²¹ J. C. Kim,¹²² W. Kim,⁷⁵ W. S. Kim,¹²³
Y.-M. Kim,^{83,121} S. J. Kimbrell,⁷⁰ E. J. King,⁷⁵ P. J. King,⁴¹ R. Kirchhoff,⁹ J. S. Kissel,⁴¹ L. Kleybolte,²⁸ S. Klimenko,⁵
P. Koch,⁹ S. M. Koehlenbeck,⁹ S. Koley,¹² V. Kondrashov,¹ A. Kontos,¹³ M. Korobko,²⁸ W. Z. Korth,¹ I. Kowalska,⁶⁷
D. B. Kozak,¹ C. Krämer,⁹ V. Kringel,⁹ B. Krishnan,⁹ A. Królak,^{124,125} G. Kuehn,⁹ P. Kumar,¹⁰⁴ R. Kumar,⁹ S. Kumar,¹¹⁰
L. Kuo,⁸⁰ A. Kutynia,¹²⁴ S. Kwang,¹⁸ B. D. Lackey,³¹ K. H. Lai,⁸⁵ M. Landry,⁴¹ R. N. Lang,¹⁸ J. Lange,¹¹⁵ B. Lantz,⁴⁴
R. K. Lanza,¹³ A. Lartaux-Vollard,²⁴ P. D. Lasky,¹²⁶ M. Laxen,⁶ A. Lazzarini,¹ C. Lazzaro,⁴⁷ P. Leaci,^{88,29} S. Leavey,⁴⁰
C. H. Lee,⁸³ H. K. Lee,¹²⁷ H. M. Lee,¹²¹ H. W. Lee,¹²² K. Lee,⁴⁰ J. Lehmann,⁹ A. Lenon,^{34,35} M. Leonardi,^{101,87} N. Leroy,²⁴
N. Letendre,⁷ Y. Levin,¹²⁶ T. G. F. Li,⁸⁵ A. Libson,¹³ T. B. Littenberg,¹²⁸ J. Liu,⁵⁷ R. K. L. Lo,⁸⁵ N. A. Lockerbie,¹¹⁷
L. T. London,⁹³ J. E. Lord,³⁸ M. Lorenzini,^{15,16} V. Lorette,¹²⁹ M. Lormand,⁶ G. Losurdo,²¹ J. D. Lough,^{9,19} G. Lovelace,²⁵
H. Lück,^{19,9} D. Lumaca,^{27,16} A. P. Lundgren,⁹ R. Lynch,¹³ Y. Ma,⁵⁶ S. Macfoy,⁵⁵ B. Machenschalk,⁹ M. MacInnis,¹³
D. M. Macleod,² I. Magaña Hernandez,⁸⁵ F. Magaña-Sandoval,³⁸ L. Magaña Zertuche,³⁸ R. M. Magee,⁷⁹ E. Majorana,²⁹
I. Maksimovic,¹²⁹ N. Man,⁵⁹ V. Mandic,³⁹ V. Mangano,⁴⁰ G. L. Mansell,²² M. Manske,¹⁸ M. Mantovani,²⁶
F. Marchesoni,^{45,37} F. Marion,⁷ S. Márka,⁴³ Z. Márka,⁴³ C. Markakis,¹¹ A. S. Markosyan,⁴⁴ E. Maros,¹ F. Martelli,^{62,63}
L. Martellini,⁵⁹ I. W. Martin,⁴⁰ D. V. Martynov,¹³ K. Mason,¹³ A. Masserot,⁷ T. J. Massinger,¹ M. Masso-Reid,⁴⁰
S. Mastrogiovanni,^{88,29} A. Matas,³⁹ F. Matchard,¹³ L. Matone,⁴³ N. Mavalvala,¹³ R. Mayani,⁹⁹ N. Mazumder,⁶¹
R. McCarthy,⁴¹ D. E. McClelland,²² S. McCormick,⁶ L. McCuller,¹³ S. C. McGuire,¹³⁰ G. McIntyre,¹ J. McIver,¹
D. J. McManus,²² T. McRae,²² S. T. McWilliams,^{34,35} D. Meacher,⁷⁹ G. D. Meadors,^{31,9} J. Meidam,¹² E. Mejuto-Villa,⁸
A. Melatos,¹³¹ G. Mendell,⁴¹ R. A. Mercer,¹⁸ E. L. Merilh,⁴¹ M. Merzougui,⁵⁹ S. Meshkov,¹ C. Messenger,⁴⁰ C. Messick,⁷⁹
R. Metzdrorf,⁶⁵ P. M. Meyers,³⁹ F. Mezzani,^{29,88} H. Miao,⁵⁰ C. Michel,²³ H. Middleton,⁵⁰ E. E. Mikhailov,¹³² L. Milano,^{72,4}
A. L. Miller,⁵ A. Miller,^{88,29} B. B. Miller,⁹² J. Miller,¹³ M. Millhouse,⁹¹ O. Minazzoli,⁵⁹ Y. Minenkov,¹⁶ J. Ming,³¹
C. Mishra,¹³³ S. Mitra,¹⁷ V. P. Mitrofanov,⁵⁴ G. Mitselmakher,⁵ R. Mittleman,¹³ A. Moggi,²¹ M. Mohan,²⁶
S. R. P. Mohapatra,¹³ M. Montani,^{62,63} B. C. Moore,¹⁰² C. J. Moore,⁸⁴ D. Moraru,⁴¹ G. Moreno,⁴¹ S. R. Morris,⁹⁵
B. Mours,⁷ C. M. Mow-Lowry,⁵⁰ G. Mueller,⁵ A. W. Muir,⁹³ Arunava Mukherjee,⁹ D. Mukherjee,¹⁸ S. Mukherjee,⁹⁵
N. Mukund,¹⁷ A. Mullavey,⁶ J. Munch,⁷⁵ E. A. M. Muniz,³⁸ P. G. Murray,⁴⁰ K. Napier,⁷⁰ I. Nardecchia,^{27,16}
L. Naticchioni,^{88,29} R. K. Nayak,¹³⁴ G. Nelemans,^{58,12} T. J. N. Nelson,⁶ M. Neri,^{51,52} M. Nery,⁹ A. Neunzert,¹¹³
J. M. Newport,¹¹⁴ G. Newton,^{7,40} K. K. Y. Ng,⁸⁵ T. T. Nguyen,²² D. Nichols,⁵⁸ A. B. Nielsen,⁹ S. Nissanke,^{58,12} A. Nitz,⁹
A. Noack,⁹ F. Nocera,²⁶ D. Nolting,⁶ M. E. N. Normandin,⁹⁵ L. K. Nuttall,³⁸ J. Oberling,⁴¹ E. Ochsner,¹⁸ E. Oelker,¹³
G. H. Ogin,¹⁰⁵ J. J. Oh,¹²³ S. H. Oh,¹²³ F. Ohme,⁹ M. Oliver,⁹⁴ P. Oppermann,⁹ Richard J. Oram,⁶ B. O'Reilly,⁶
R. Ormiston,³⁹ L. F. Ortega,⁵ R. O'Shaughnessy,¹¹⁵ D. J. Ottaway,⁷⁵ H. Overmier,⁶ B. J. Owen,⁷⁷ A. E. Pace,⁷⁹ J. Page,¹²⁸
M. A. Page,⁵⁷ A. Pai,¹⁰⁸ S. A. Pai,⁵³ J. R. Palamos,⁶⁴ O. Palashov,¹²⁰ C. Palomba,²⁹ A. Pal-Singh,²⁸ H. Pan,⁸⁰ B. Pang,⁵⁶
P. T. H. Pang,⁸⁵ C. Pankow,⁹² F. Pannarale,⁹³ B. C. Pant,⁵³ F. Paoletti,²¹ A. Paoli,²⁶ M. A. Papa,^{31,18,9} H. R. Paris,⁴⁴
W. Parker,⁶ D. Pascucci,⁴⁰ A. Pasqualetti,²⁶ R. Passaquietti,^{20,21} D. Passuello,²¹ B. Patricelli,^{135,21} B. L. Pearlstone,⁴⁰
M. Pedraza,¹ R. Pedurand,^{23,136} L. Pekowsky,³⁸ A. Pele,⁶ S. Penn,¹³⁷ C. J. Perez,⁴¹ A. Perreca,^{1,101,87} L. M. Perri,⁹²
H. P. Pfeiffer,¹⁰⁴ M. Phelps,⁴⁰ O. J. Piccinni,^{88,29} M. Pichot,⁵⁹ F. Piergiorganni,^{62,63} V. Pierro,⁸ G. Pillant,²⁶ L. Pinard,²³
I. M. Pinto,⁸ M. Pitkin,⁴⁰ R. Poggiani,^{20,21} P. Popolizio,²⁶ E. K. Porter,³² A. Post,⁹ J. Powell,⁴⁰ J. Prasad,¹⁷ J. W. W. Pratt,³⁰
V. Predoi,⁹³ T. Prestegard,¹⁸ M. Prijatelj,⁹ M. Principe,⁸ S. Privitera,³¹ R. Prix,⁹ G. A. Prodi,^{101,87} L. G. Prokhorov,⁵⁴
O. Puncken,⁹ M. Punturo,³⁷ P. Puppo,²⁹ M. Pürer,³¹ H. Qi,¹⁸ J. Qin,⁵⁷ S. Qiu,¹²⁶ V. Quetschke,⁹⁵ E. A. Quintero,¹
R. Quitzow-James,⁶⁴ F. J. Raab,⁴¹ D. S. Rabeling,²² H. Radkins,⁴¹ P. Raffai,⁴⁸ S. Raja,⁵³ C. Rajan,⁵³ M. Rakhmanov,⁹⁵
K. E. Ramirez,⁹⁵ P. Rapagnani,^{88,29} V. Raymond,³¹ M. Razzano,^{20,21} J. Read,²⁵ T. Regimbau,⁵⁹ L. Rei,⁵² S. Reid,⁵⁵
D. H. Reitze,^{1,5} H. Rew,¹³² S. D. Reyes,³⁸ F. Ricci,^{88,29} P. M. Ricker,¹¹ S. Rieger,⁹ K. Riles,¹¹³ M. Rizzo,¹¹⁵
N. A. Robertson,^{1,40} R. Robie,⁴⁰ F. Robinet,²⁴ A. Rocchi,¹⁶ L. Rolland,⁷ J. G. Rollins,¹ V. J. Roma,⁶⁴ R. Romano,^{3,4}

FIRST LOW-FREQUENCY EINSTEIN@HOME ALL-SKY ...

PHYSICAL REVIEW D **96**, 122004 (2017)

C. L. Romel,⁴¹ J. H. Romie,⁶ D. Rosińska,^{138,49} M. P. Ross,¹³⁹ S. Rowan,⁴⁰ A. Rüdiger,⁹ P. Ruggi,²⁶ K. Ryan,⁴¹ M. Rynge,⁹⁹ S. Sachdev,¹ T. Sadecki,⁴¹ L. Sadeghian,¹⁸ M. Sakellariadou,¹⁴⁰ L. Salconi,²⁶ M. Saleem,¹⁰⁸ F. Salemi,⁹ A. Samajdar,¹³⁴ L. Sammut,¹²⁶ L. M. Sampson,⁹² E. J. Sanchez,¹ V. Sandberg,⁴¹ B. Sandeen,⁹² J. R. Sanders,³⁸ B. Sassolas,²³ B. S. Sathyaprakash,^{79,93} P. R. Saulson,³⁸ O. Sauter,¹¹³ R. L. Savage,⁴¹ A. Sawadsky,¹⁹ P. Schale,⁶⁴ J. Scheuer,⁹² E. Schmidt,³⁰ J. Schmidt,⁹ P. Schmidt,^{1,58} R. Schnabel,²⁸ R. M. S. Schofield,⁶⁴ A. Schönbeck,²⁸ E. Schreiber,⁹ D. Schuette,^{9,19} B. W. Schulte,⁹ B. F. Schutz,^{93,9} S. G. Schwalbe,³⁰ J. Scott,⁴⁰ S. M. Scott,²² E. Seidel,¹¹ D. Sellers,⁶ A. S. Sengupta,¹⁴¹ D. Sentenac,²⁶ V. Sequino,^{27,16} A. Sergeev,¹²⁰ D. A. Shaddock,²² T. J. Shaffer,⁴¹ A. A. Shah,¹²⁸ M. S. Shahriar,⁹² L. Shao,³¹ B. Shapiro,⁴⁴ P. Shawhan,⁶⁹ A. Sheperd,¹⁸ D. H. Shoemaker,¹³ D. M. Shoemaker,⁷⁰ K. Siellez,⁷⁰ X. Siemens,¹⁸ M. Sieniawska,⁴⁹ D. Sigg,⁴¹ A. D. Silva,¹⁴ A. Singer,¹ L. P. Singer,⁷³ A. Singh,^{31,9,19} R. Singh,² A. Singhal,^{15,29} A. M. Sintes,⁹⁴ B. J. J. Slagmolen,²² B. Smith,⁶ J. R. Smith,²⁵ R. J. E. Smith,¹ E. J. Son,¹²³ J. A. Sonnenberg,¹⁸ B. Sorazu,⁴⁰ F. Sorrentino,⁵² T. Souradeep,¹⁷ A. P. Spencer,⁴⁰ A. K. Srivastava,⁹⁷ A. Staley,⁴³ M. Steinke,⁹ J. Steinlechner,^{40,28} S. Steinlechner,²⁸ D. Steinmeyer,^{9,19} B. C. Stephens,¹⁸ R. Stone,⁹⁵ K. A. Strain,⁴⁰ G. Stratta,^{62,63} S. E. Strigin,⁵⁴ R. Sturani,¹⁴² A. L. Stuver,⁶ T. Z. Summerscales,¹⁴³ L. Sun,¹³¹ S. Sunil,⁹⁷ P. J. Sutton,⁹³ B. L. Swinkels,²⁶ M. J. Szczepańczyk,³⁰ M. Tacca,³² D. Talukder,⁶⁴ D. B. Tanner,⁵ M. Tápai,¹⁰⁹ A. Taracchini,³¹ J. A. Taylor,¹²⁸ R. Taylor,¹ T. Theeg,⁹ E. G. Thomas,⁵⁰ M. Thomas,⁶ P. Thomas,⁴¹ K. A. Thorne,⁶ K. S. Thorne,⁵⁶ E. Thrane,¹²⁶ S. Tiwari,^{15,87} V. Tiwari,⁹³ K. V. Tokmakov,¹¹⁷ K. Toland,⁴⁰ M. Tonelli,^{20,21} Z. Tornasi,⁴⁰ C. I. Torrie,¹ D. Töyrä,⁵⁰ F. Travasso,^{26,37} G. Traylor,⁶ D. Trifirò,¹⁰ J. Trinastic,⁵ M. C. Tringali,^{101,87} L. Trozzo,^{144,21} K. W. Tsang,¹² M. Tse,¹³ R. Tso,¹ D. Tuyenbayev,⁹⁵ K. Ueno,¹⁸ D. Ugolini,¹⁴⁵ C. S. Unnikrishnan,¹¹¹ A. L. Urban,¹ S. A. Usman,⁹³ K. Vahi,⁹⁹ H. Vahlbruch,¹⁹ G. Vajente,¹ G. Valdes,⁹⁵ M. Vallisneri,⁵⁶ N. van Bakel,¹² M. van Beuzekom,¹² J. F. J. van den Brand,^{68,12} C. Van Den Broeck,¹² D. C. Vander-Hyde,³⁸ L. van der Schaaf,¹² J. V. van Heijningen,¹² A. A. van Veggel,⁴⁰ M. Vardaro,^{46,47} V. Varma,⁵⁶ S. Vass,¹ M. Vasúth,⁴² A. Vecchio,⁵⁰ G. Vedovato,⁴⁷ J. Veitch,⁵⁰ P. J. Veitch,⁷⁵ K. Venkateswara,¹³⁹ G. Venugopalan,¹ D. Verkindt,⁷ F. Vetrano,^{62,63} A. Vicere,^{62,63} A. D. Viets,¹⁸ S. Vinciguerra,⁵⁰ D. J. Vine,⁵⁵ J.-Y. Vinet,⁵⁹ S. Vitale,¹³ T. Vo,³⁸ H. Vocca,^{36,37} C. Vorvick,⁴¹ D. V. Voss,⁵ W. D. Voudsen,⁵⁰ S. P. Vyatchanin,⁵⁴ A. R. Wade,¹ L. E. Wade,⁷⁸ M. Wade,⁷⁸ R. Walet,¹² M. Walker,² L. Wallace,¹ S. Walsh,¹⁸ G. Wang,^{15,63} H. Wang,⁵⁰ J. Z. Wang,⁷⁹ M. Wang,⁵⁰ Y.-F. Wang,⁸⁵ Y. Wang,⁵⁷ R. L. Ward,²² J. Warner,⁴¹ M. Was,⁷ J. Watchi,⁸⁹ B. Weaver,⁴¹ L.-W. Wei,^{9,19} M. Weinert,⁹ A. J. Weinstein,¹ R. Weiss,¹³ L. Wen,⁵⁷ E. K. Wessel,¹¹ P. Weßels,⁹ T. Westphal,⁹ K. Wette,⁹ J. T. Whelan,¹¹⁵ B. F. Whiting,⁵ C. Whittle,¹²⁶ D. Williams,⁴⁰ R. D. Williams,¹ A. R. Williamson,¹¹⁵ J. L. Willis,¹⁴⁶ B. Willke,^{19,9} M. H. Wimmer,^{9,19} W. Winkler,⁹ C. C. Wipf,¹ H. Wittel,^{9,19} G. Woan,⁴⁰ J. Woehler,⁹ J. Wofford,¹¹⁵ K. W. K. Wong,⁸⁵ J. Worden,⁴¹ J. L. Wright,⁴⁰ D. S. Wu,⁹ G. Wu,⁶ W. Yam,¹³ H. Yamamoto,¹ C. C. Yancey,⁶⁹ M. J. Yap,²² Hang Yu,¹³ Haocun Yu,¹³ M. Yvert,⁷ A. Zadrożny,¹²⁴ M. Zanolin,³⁰ T. Zelenova,²⁶ J.-P. Zendri,⁴⁷ M. Zevin,⁹² L. Zhang,¹ M. Zhang,¹³² T. Zhang,⁴⁰ Y.-H. Zhang,¹¹⁵ C. Zhao,⁵⁷ M. Zhou,⁹² Z. Zhou,⁹² S. J. Zhu,^{31,9} X. J. Zhu,⁵⁷ M. E. Zucker,^{1,13} and J. Zweizig¹

(LIGO Scientific Collaboration and Virgo Collaboration)

and D. P. Anderson¹⁴⁷¹LIGO, California Institute of Technology, Pasadena, California 91125, USA²Louisiana State University, Baton Rouge, Louisiana 70803, USA³Università di Salerno, Fisciano, I-84084 Salerno, Italy⁴INFN, Sezione di Napoli, Complesso Universitario di Monte S. Angelo, I-80126 Napoli, Italy⁵University of Florida, Gainesville, Florida 32611, USA⁶LIGO Livingston Observatory, Livingston, Louisiana 70754, USA⁷Laboratoire d'Annecy-le-Vieux de Physique des Particules (LAPP), Université Savoie Mont Blanc, CNRS/IN2P3, F-74941 Annecy, France⁸University of Sannio at Benevento, I-82100 Benevento, Italy and INFN, Sezione di Napoli, I-80100 Napoli, Italy⁹Albert-Einstein-Institut, Max-Planck-Institut für Gravitationsphysik, D-30167 Hannover, Germany¹⁰The University of Mississippi, University, Mississippi 38677, USA¹¹NCSA, University of Illinois at Urbana-Champaign, Urbana, Illinois 61801, USA¹²Nikhef, Science Park, 1098 XG Amsterdam, Netherlands¹³LIGO, Massachusetts Institute of Technology, Cambridge, Massachusetts 02139, USA

B. P. ABBOTT *et al.*PHYSICAL REVIEW D **96**, 122004 (2017)

- ¹⁴*Instituto Nacional de Pesquisas Espaciais, 12227-010 São José dos Campos, São Paulo, Brazil*
¹⁵*Gran Sasso Science Institute (GSSI), I-67100 L'Aquila, Italy*
¹⁶*INFN, Sezione di Roma Tor Vergata, I-00133 Roma, Italy*
¹⁷*Inter-University Centre for Astronomy and Astrophysics, Pune 411007, India*
¹⁸*University of Wisconsin-Milwaukee, Milwaukee, Wisconsin 53201, USA*
¹⁹*Leibniz Universität Hannover, D-30167 Hannover, Germany*
²⁰*Università di Pisa, I-56127 Pisa, Italy*
²¹*INFN, Sezione di Pisa, I-56127 Pisa, Italy*
²²*OzGrav, Australian National University, Canberra, Australian Capital Territory 0200, Australia*
²³*Laboratoire des Matériaux Avancés (LMA), CNRS/IN2P3, F-69622 Villeurbanne, France*
²⁴*LAL, Univ. Paris-Sud, CNRS/IN2P3, Université Paris-Saclay, F-91898 Orsay, France*
²⁵*California State University Fullerton, Fullerton, California 92831, USA*
²⁶*European Gravitational Observatory (EGO), I-56021 Cascina, Pisa, Italy*
²⁷*Università di Roma Tor Vergata, I-00133 Roma, Italy*
²⁸*Universität Hamburg, D-22761 Hamburg, Germany*
²⁹*INFN, Sezione di Roma, I-00185 Roma, Italy*
³⁰*Embry-Riddle Aeronautical University, Prescott, Arizona 86301, USA*
³¹*Albert-Einstein-Institut, Max-Planck-Institut für Gravitationsphysik, D-14476 Potsdam-Golm, Germany*
³²*APC, AstroParticule et Cosmologie, Université Paris Diderot, CNRS/IN2P3, CEA/Irfu, Observatoire de Paris, Sorbonne Paris Cité, F-75205 Paris Cedex 13, France*
³³*Korea Institute of Science and Technology Information, Daejeon 34141, Korea*
³⁴*West Virginia University, Morgantown, West Virginia 26506, USA*
³⁵*Center for Gravitational Waves and Cosmology, West Virginia University, Morgantown, West Virginia 26505, USA*
³⁶*Università di Perugia, I-06123 Perugia, Italy*
³⁷*INFN, Sezione di Perugia, I-06123 Perugia, Italy*
³⁸*Syracuse University, Syracuse, New York 13244, USA*
³⁹*University of Minnesota, Minneapolis, Minnesota 55455, USA*
⁴⁰*SUPA, University of Glasgow, Glasgow G12 8QQ, United Kingdom*
⁴¹*LIGO Hanford Observatory, Richland, Washington 99352, USA*
⁴²*Wigner RCP, RMKI, H-1121 Budapest, Konkoly Thege Miklós út 29-33, Hungary*
⁴³*Columbia University, New York, New York 10027, USA*
⁴⁴*Stanford University, Stanford, California 94305, USA*
⁴⁵*Università di Camerino, Dipartimento di Fisica, I-62032 Camerino, Italy*
⁴⁶*Università di Padova, Dipartimento di Fisica e Astronomia, I-35131 Padova, Italy*
⁴⁷*INFN, Sezione di Padova, I-35131 Padova, Italy*
⁴⁸*MTA Eötvös University, "Lendulet" Astrophysics Research Group, Budapest 1117, Hungary*
⁴⁹*Nicolaus Copernicus Astronomical Center, Polish Academy of Sciences, 00-716 Warsaw, Poland*
⁵⁰*University of Birmingham, Birmingham B15 2TT, United Kingdom*
⁵¹*Università degli Studi di Genova, I-16146 Genova, Italy*
⁵²*INFN, Sezione di Genova, I-16146 Genova, Italy*
⁵³*RRCAT, Indore Madhya Pradesh 452013, India*
⁵⁴*Faculty of Physics, Lomonosov Moscow State University, Moscow 119991, Russia*
⁵⁵*SUPA, University of the West of Scotland, Paisley PA1 2BE, United Kingdom*
⁵⁶*Caltech CaRT, Pasadena, California 91125, USA*
⁵⁷*OzGrav, University of Western Australia, Crawley, Western Australia 6009, Australia*
⁵⁸*Department of Astrophysics/IMAPP, Radboud University Nijmegen, P.O. Box 9010, 6500 GL Nijmegen, Netherlands*
⁵⁹*Artemis, Université Côte d'Azur, Observatoire Côte d'Azur, CNRS, CS 34229, F-06304 Nice Cedex 4, France*
⁶⁰*Institut de Physique de Rennes, CNRS, Université de Rennes 1, F-35042 Rennes, France*
⁶¹*Washington State University, Pullman, Washington 99164, USA*
⁶²*Università degli Studi di Urbino 'Carlo Bo', I-61029 Urbino, Italy*
⁶³*INFN, Sezione di Firenze, I-50019 Sesto Fiorentino, Firenze, Italy*
⁶⁴*University of Oregon, Eugene, Oregon 97403, USA*
⁶⁵*Laboratoire Kastler Brossel, UPMC-Sorbonne Universités, CNRS, ENS-PSL Research University, Collège de France, F-75005 Paris, France*
⁶⁶*Carleton College, Northfield, Minnesota 55057, USA*
⁶⁷*Astronomical Observatory Warsaw University, 00-478 Warsaw, Poland*
⁶⁸*VU University Amsterdam, 1081 HV Amsterdam, Netherlands*

- ⁶⁹University of Maryland, College Park, Maryland 20742, USA
- ⁷⁰Center for Relativistic Astrophysics and School of Physics, Georgia Institute of Technology, Atlanta, Georgia 30332, USA
- ⁷¹Université Claude Bernard Lyon 1, F-69622 Villeurbanne, France
- ⁷²Università di Napoli 'Federico II', Complesso Universitario di Monte S. Angelo, I-80126 Napoli, Italy
- ⁷³NASA Goddard Space Flight Center, Greenbelt, Maryland 20771, USA
- ⁷⁴RESCEU, University of Tokyo, Tokyo 113-0033, Japan.
- ⁷⁵OzGrav, University of Adelaide, Adelaide, South Australia 5005, Australia
- ⁷⁶Tsinghua University, Beijing 100084, China
- ⁷⁷Texas Tech University, Lubbock, Texas 79409, USA
- ⁷⁸Kenyon College, Gambier, Ohio 43022, USA
- ⁷⁹The Pennsylvania State University, University Park, Pennsylvania 16802, USA
- ⁸⁰National Tsing Hua University, Hsinchu City, 30013 Taiwan, Republic of China
- ⁸¹Charles Sturt University, Wagga Wagga, New South Wales 2678, Australia
- ⁸²University of Chicago, Chicago, Illinois 60637, USA
- ⁸³Pusan National University, Busan 46241, Korea
- ⁸⁴University of Cambridge, Cambridge CB2 1TN, United Kingdom
- ⁸⁵The Chinese University of Hong Kong, Shatin, NT, Hong Kong
- ⁸⁶INAF, Osservatorio Astronomico di Padova, Vicolo dell'Osservatorio 5, I-35122 Padova, Italy
- ⁸⁷INFN, Trento Institute for Fundamental Physics and Applications, I-38123 Povo, Trento, Italy
- ⁸⁸Università di Roma 'La Sapienza', I-00185 Roma, Italy
- ⁸⁹Université Libre de Bruxelles, Brussels 1050, Belgium
- ⁹⁰Sonoma State University, Rohnert Park, California 94928, USA
- ⁹¹Montana State University, Bozeman, Montana 59717, USA
- ⁹²Center for Interdisciplinary Exploration & Research in Astrophysics (CIERA), Northwestern University, Evanston, Illinois 60208, USA
- ⁹³Cardiff University, Cardiff CF24 3AA, United Kingdom
- ⁹⁴Universitat de les Illes Balears, IAC3—IEEC, E-07122 Palma de Mallorca, Spain
- ⁹⁵The University of Texas Rio Grande Valley, Brownsville, Texas 78520, USA
- ⁹⁶Bellevue College, Bellevue, Washington 98007, USA
- ⁹⁷Institute for Plasma Research, Bhat, Gandhinagar 382428, India
- ⁹⁸The University of Sheffield, Sheffield S10 2TN, United Kingdom
- ⁹⁹University of Southern California Information Sciences Institute, Marina Del Rey, California 90292, USA
- ¹⁰⁰California State University, Los Angeles, 5151 State University Dr, Los Angeles, California 90032, USA
- ¹⁰¹Università di Trento, Dipartimento di Fisica, I-38123 Povo, Trento, Italy
- ¹⁰²Montclair State University, Montclair, New Jersey 07043, USA
- ¹⁰³National Astronomical Observatory of Japan, 2-21-1 Osawa, Mitaka, Tokyo 181-8588, Japan
- ¹⁰⁴Canadian Institute for Theoretical Astrophysics, University of Toronto, Toronto, Ontario M5S 3H8, Canada
- ¹⁰⁵Whitman College, 345 Boyer Avenue, Walla Walla, Washington 99362 USA
- ¹⁰⁶School of Mathematics, University of Edinburgh, Edinburgh EH9 3FD, United Kingdom
- ¹⁰⁷University and Institute of Advanced Research, Gandhinagar Gujarat 382007, India
- ¹⁰⁸IISER-TVM, CET Campus, Trivandrum Kerala 695016, India
- ¹⁰⁹University of Szeged, Dóm tér 9, Szeged 6720, Hungary
- ¹¹⁰International Centre for Theoretical Sciences, Tata Institute of Fundamental Research, Bengaluru 560089, India
- ¹¹¹Tata Institute of Fundamental Research, Mumbai 400005, India
- ¹¹²INAF, Osservatorio Astronomico di Capodimonte, I-80131 Napoli, Italy
- ¹¹³University of Michigan, Ann Arbor, Michigan 48109, USA
- ¹¹⁴American University, Washington, D.C. 20016, USA
- ¹¹⁵Rochester Institute of Technology, Rochester, New York 14623, USA
- ¹¹⁶University of Białystok, 15-424 Białystok, Poland
- ¹¹⁷SUPA, University of Strathclyde, Glasgow G1 1XQ, United Kingdom
- ¹¹⁸University of Southampton, Southampton SO17 1BJ, United Kingdom
- ¹¹⁹University of Washington Bothell, 18115 Campus Way NE, Bothell, Washington 98011, USA
- ¹²⁰Institute of Applied Physics, Nizhny Novgorod, 603950, Russia
- ¹²¹Seoul National University, Seoul 08826, Korea
- ¹²²Inje University Gimhae, South Gyeongsang 50834, Korea
- ¹²³National Institute for Mathematical Sciences, Daejeon 34047, Korea

B. P. ABBOTT *et al.*PHYSICAL REVIEW D **96**, 122004 (2017)

- ¹²⁴NCBJ, 05-400 Świerk-Otwock, Poland
¹²⁵Institute of Mathematics, Polish Academy of Sciences, 00656 Warsaw, Poland
¹²⁶OzGrav, School of Physics & Astronomy, Monash University, Clayton 3800, Victoria, Australia
¹²⁷Hanyang University, Seoul 04763, Korea
¹²⁸NASA Marshall Space Flight Center, Huntsville, Alabama 35811, USA
¹²⁹ESPCI, CNRS, F-75005 Paris, France
¹³⁰Southern University and A&M College, Baton Rouge, Louisiana 70813, USA
¹³¹OzGrav, University of Melbourne, Parkville, Victoria 3010, Australia
¹³²College of William and Mary, Williamsburg, Virginia 23187, USA
¹³³Indian Institute of Technology Madras, Chennai 600036, India
¹³⁴IISER-Kolkata, Mohanpur, West Bengal 741252, India
¹³⁵Scuola Normale Superiore, Piazza dei Cavalieri 7, I-56126 Pisa, Italy
¹³⁶Université de Lyon, F-69361 Lyon, France
¹³⁷Hobart and William Smith Colleges, Geneva, New York 14456, USA
¹³⁸Janusz Gil Institute of Astronomy, University of Zielona Góra, 65-265 Zielona Góra, Poland
¹³⁹University of Washington, Seattle, Washington 98195, USA
¹⁴⁰King's College London, University of London, London WC2R 2LS, United Kingdom
¹⁴¹Indian Institute of Technology, Gandhinagar Ahmedabad Gujarat 382424, India
¹⁴²International Institute of Physics, Universidade Federal do Rio Grande do Norte, Natal RN 59078-970, Brazil
¹⁴³Andrews University, Berrien Springs, Michigan 49104, USA
¹⁴⁴Università di Siena, I-53100 Siena, Italy
¹⁴⁵Trinity University, San Antonio, Texas 78212, USA
¹⁴⁶Abilene Christian University, Abilene, Texas 79699, USA
¹⁴⁷University of California at Berkeley, Berkeley, California 94720, USA

†Deceased.



PHYSICAL REVIEW D 94, 102002 (2016)

2 Results of the deepest all-sky survey for continuous gravitational waves on LIGO S6 data running on the Einstein@Home volunteer distributed computing project

B. P. Abbott *et al.**

(LIGO Scientific Collaboration and Virgo Collaboration)

(Received 6 July 2016; published 18 November 2016)

We report results of a deep all-sky search for periodic gravitational waves from isolated neutron stars in data from the S6 LIGO science run. The search was possible thanks to the computing power provided by the volunteers of the Einstein@Home distributed computing project. We find no significant signal candidate and set the most stringent upper limits to date on the amplitude of gravitational wave signals from the target population. At the frequency of best strain sensitivity, between 170.5 and 171 Hz we set a 90% confidence upper limit of 5.5×10^{-25} , while at the high end of our frequency range, around 505 Hz, we achieve upper limits $\approx 10^{-24}$. At 230 Hz we can exclude sources with ellipticities greater than 10^{-6} within 100 pc of Earth with fiducial value of the principal moment of inertia of 10^{38} kg m². If we assume a higher (lower) gravitational wave spin-down we constrain farther (closer) objects to higher (lower) ellipticities.

DOI: 10.1103/PhysRevD.94.102002

I. INTRODUCTION

In this paper we report the results of a deep all-sky Einstein@Home [1] search for continuous, nearly monochromatic gravitational waves (GWs) in data from LIGO's sixth science (S6) run. A number of all-sky searches have been carried out on LIGO data, [2–11], of which [5,7,10] also ran on Einstein@Home. The search presented here covers frequencies from 50 Hz through 510 Hz and frequency derivatives from 3.39×10^{-10} Hz/s through -2.67×10^{-9} Hz/s. In this range we establish the most constraining gravitational wave amplitude upper limits to date for the target signal population.

II. LIGO INTERFEROMETERS AND THE DATA USED

The LIGO gravitational wave network consists of two observatories, one in Hanford (WA) and the other in Livingston (LA) separated by a 3000-km baseline [12]. The last science run (S6) [13] of this network before the upgrade towards the advanced LIGO configuration [14] took place between July 2009 and October 2010. The analysis in this paper uses a subset of this data: from GPS 949469977 (2010 Feb 6 05:39:22 UTC) through GPS 971529850 (2010 Oct 19 13:23:55 UTC), selected for good strain sensitivity [15]. Since interferometers sporadically fall out of operation (“lose lock”) due to environmental or

instrumental disturbances or for scheduled maintenance periods, the data set is not contiguous and each detector has a duty factor of about 50% [16].

As done in [7], frequency bands known to contain spectral disturbances have been removed from the analysis. Actually, the data has been substituted with Gaussian noise with the same average power as that in the neighboring and undisturbed bands. Table III identifies these bands.

III. THE SEARCH

The search described in this paper targets nearly monochromatic gravitational wave signals as described for example by Eqs. 1–4 of [7]. Various emission mechanisms could generate such a signal as reviewed in Sec. II A of [11]. In interpreting our results we will consider a spinning compact object with a fixed, nonaxisymmetric mass quadrupole, described by an ellipticity ϵ .

We perform a stack-slide type of search using the GCT (Global Correlation Transform) method [17,18]. In a stack-slide search the data is partitioned in segments and each segment is searched with a matched-filter method [19]. The results from these coherent searches are combined by summing (stacking) the detection statistic values from the segments (sliding), one per segment (\mathcal{F}_i), and this determines the value of the core detection statistic:

$$\bar{\mathcal{F}} := \frac{1}{N_{\text{seg}}} \sum_{i=1}^{N_{\text{seg}}} \mathcal{F}_i. \quad (1)$$

There are different ways to combine the single-segment \mathcal{F}_i values, but independently of the way that this is done, this type of search is usually referred to as a “semicoherent

*Full author list given at end of the article.

Published by the American Physical Society under the terms of the Creative Commons Attribution 3.0 License. Further distribution of this work must maintain attribution to the author(s) and the published article's title, journal citation, and DOI.

B. P. ABBOTT *et al.*

search”. So stack-slide searches are a type of semicoherent search. Important variables for this type of search are the coherent time baseline of the segments T_{coh} , the number of segments used N_{seg} , the total time spanned by the data T_{obs} , the grids in parameter space and the detection statistic used to rank the parameter space cells. For a stack-slide search in Gaussian noise, $N_{\text{seg}} \times 2\mathcal{F}$ follows a $\chi^2_{4N_{\text{seg}}}$ chi-squared distribution with $4N_{\text{seg}}$ degrees of freedom. These parameters are summarized in Table I. The grids in frequency and spin-down are each described by a single parameter, the grid spacing, which is constant over the search range. The same frequency grid spacings are used for the coherent searches over the segments and for the incoherent summing. The spin-down spacing for the incoherent summing, $\delta\dot{f}$, is finer than that used for the coherent searches, $\delta\dot{f}_c$, by a factor γ . The notation used here is consistent with that used in previous observational papers [20] and in the GCT methods papers cited above.

The sky grid is the union of two grids: one is uniform over the projection of the celestial sphere onto the equatorial plane, and the tiling (in the equatorial plane) is approximately square with sides of length

$$d(m_{\text{sky}}) = \frac{1}{f} \frac{\sqrt{m_{\text{sky}}}}{\pi\tau_E}, \quad (2)$$

with $m_{\text{sky}} = 0.3$ and $\tau_E \approx 0.021$ s being half of the light travel time across the Earth. As was done in [7], the sky-grids are constant over 10 Hz bands and the spacings are the ones associated through Eq. (2) to the highest frequency f in the range. The other grid is limited to the equatorial region ($0 \leq \alpha \leq 2\pi$ and $-0.5 \leq \delta \leq 0.5$), with constant right ascension α and declination δ spacings equal to $d(0.3)$ —see Fig. 1. The reason for the equatorial “patching” with a denser sky grid is to improve the sensitivity of the search: the sky resolution actually depends on the ecliptic latitude and the uniform equatorial grid under-resolves particularly in the equatorial region. The resulting number of templates used to search 50 mHz bands as a function of frequency is shown in Fig. 2.

The search is split into work-units (WUs) sized to keep the average Einstein@Home volunteer computer busy for about six hours. Each WU searches a 50 mHz band, the

TABLE I. Search parameters rounded to the first decimal figure. T_{ref} is the reference time that defines the frequency and frequency derivative values.

T_{coh}	60 hours
T_{ref}	960499913.5 GPS sec
N_{seg}	90
$\delta\dot{f}$	1.6×10^{-6} Hz
$\delta\dot{f}_c$	5.8×10^{-11} Hz/s
γ	230
m_{sky}	0.3 + equatorial patch

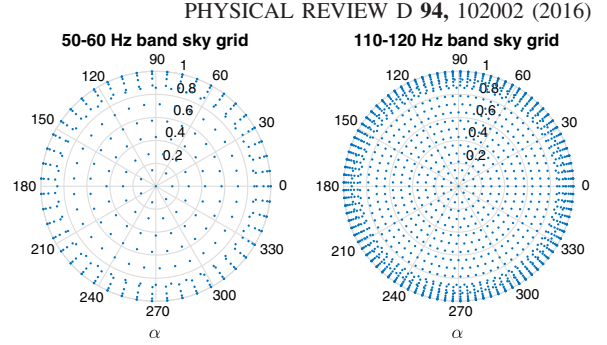


FIG. 1. Polar plots (r, θ plots with $\theta = \alpha$ and $r = \cos \delta$) of the grid points in the northern equatorial hemisphere sky for the band 50–60 Hz (left panel) and for the band 110–120 Hz (right panel). α is the right ascension coordinate and δ the declination coordinate. One can clearly see the higher density in the $-0.5 \leq \delta \leq 0.5$ equatorial region and the higher density ($\propto f^2$) of grid points at higher frequencies. The southern hemispheres looks practically identical to the respective northern ones.

entire spin-down range and 13 points in the sky, corresponding to 4.9×10^9 templates out of which it returns only the top 3000. A total of 12.7 million WUs are necessary to cover the entire parameter space. The total number of templates searched is 6.3×10^{16} .

A. The ranking statistic

The search was actually carried out in separate Einstein@Home runs that used different ranking statistics to define the top-candidate-list, reflecting different stages in the development of a detection statistic robust with respect

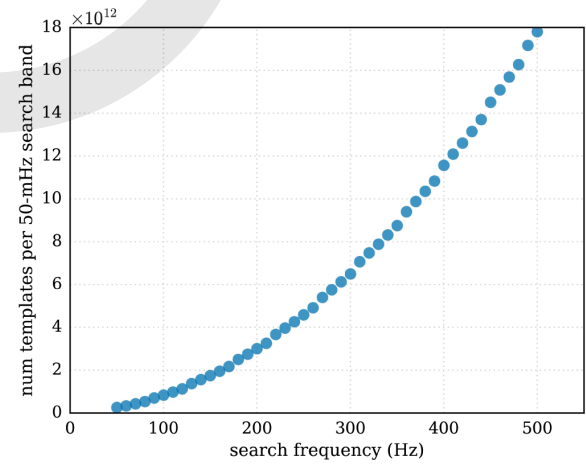


FIG. 2. Number of searched templates in 50 mHz bands. The variation with frequency is due to the increasing sky resolution. $N_f \times N_{\dot{f}} \sim 3.7 \times 10^8$, where N_f and $N_{\dot{f}}$ are the number of f and \dot{f} templates searched in 50 mHz bands. The total number of templates searched between 50 and 510 Hz is 6.3×10^{16} .

RESULTS OF THE DEEPEST ALL-SKY SURVEY FOR ...

to spectral lines in the data [21]. In particular, three ranking statistics were used: the average $2\mathcal{F}$ statistic over the segments, $2\overline{\mathcal{F}}$, which in essence at every template point is the likelihood of having a signal with the shape given by the template versus having Gaussian noise; the line-veto statistic \hat{O}_{SL} which is the odds ratio of having a signal versus having a spectral line; and a general line-robust statistic, \hat{O}_{SGL} , that tests the signal hypothesis against a Gaussian noise + spectral line noise model. Such a statistic can match the performance of both the standard average $2\overline{\mathcal{F}}$ statistic in Gaussian noise and the line-veto statistic in presence of single-detector spectral disturbances and statistically outperforms them when the noise is a mixture of both [21].

We combine the $2\overline{\mathcal{F}}$ -ranked results with the \hat{O}_{SL} -ranked results to produce a single list of candidates ranked according to the general line-robust statistic \hat{O}_{SGL} . We now explain how this is achieved. Alongside the detection statistic value and the parameter space cell coordinates of each candidate, the Einstein@Home application also returns the single-detector $2\mathcal{F}^X$ values (“X” indicates the detector). These are used to compute, for every candidate of any run, the \hat{O}_{SGL} through Eq. 61 of [21]

$$\ln \hat{O}_{\text{SGL}} = \ln \hat{o}_{\text{SL}} + \hat{\mathcal{F}} - \hat{\mathcal{F}}''_{\text{max}} - \ln (e^{\hat{\mathcal{F}}_* - \hat{\mathcal{F}}''_{\text{max}}} + \langle \hat{\mathcal{F}}^X e^{\hat{\mathcal{F}}^X - \hat{\mathcal{F}}''_{\text{max}}} \rangle), \quad (3)$$

with the angle-brackets indicating the average with respect to detectors (X) and

$$\hat{\mathcal{F}} = N_{\text{seg}} \overline{\mathcal{F}} \quad (4)$$

$$\hat{\mathcal{F}}^X = N_{\text{seg}} \overline{\mathcal{F}}^X \quad (5)$$

$$\hat{\mathcal{F}}''_{\text{max}} \equiv \max(\hat{\mathcal{F}}_*, \hat{\mathcal{F}}^X + \ln \hat{\mathcal{F}}^X) \quad (6)$$

$$\hat{\mathcal{F}}_* \equiv \hat{\mathcal{F}}_*^{(0)} - \ln \hat{o}_{\text{LG}} \quad (7)$$

$$\hat{\mathcal{F}}_*^{(0)} \equiv \ln c_*^{N_{\text{seg}}} \quad \text{with } c_* \text{ set to } 20.64 \quad (8)$$

$$\hat{o}_{\text{LG}} = \sum_X \hat{o}_{\text{LG}}^X \quad (9)$$

$$\hat{\mathcal{F}}^X \equiv \frac{\hat{o}_{\text{LG}}^X}{\hat{o}_{\text{LG}}/N_{\text{det}}} \quad (10)$$

$$\hat{\rho}_{\text{L}} \equiv \frac{\hat{o}_{\text{LG}}}{1 + \hat{o}_{\text{LG}}}, \quad (11)$$

where \hat{o}_{LG}^X is the assumed prior probability of a spectral line occurring in any frequency bin of detector X, $\hat{\rho}_{\text{L}}$ is the line prior estimated from the data, $N_{\text{det}} = 2$ is the number of detectors, and \hat{o}_{SL} is an assumed prior probability of a line

PHYSICAL REVIEW D 94, 102002 (2016)

being a signal (set arbitrarily to 1; its specific value does not affect the ranking statistic). Following the reasoning of Eq. 67 of [21], with $N_{\text{seg}} = 90$ we set $c_* = 20.64$ corresponding to a Gaussian false-alarm probability of 10^{-9} and an average $2\overline{\mathcal{F}}$ transition scale of ~ 6 ($\mathcal{F}_*^{(0)} \sim 3$). The \hat{o}_{LG}^X values are estimated from the data as described in Sec. VI. A of [21] in 50-mHz bands with a normalized-SFT-power threshold $\mathcal{P}_{\text{thr}}^X = \mathcal{P}_{\text{thr}}(P_{\text{FA}} = 10^{-9}, N_{\text{SFT}}^X \sim 6000) \approx 1.08$. For every 50 mHz band the list of candidates from the $2\overline{\mathcal{F}}$ -ranked run is merged with the list from the \hat{O}_{SL} -ranked run and duplicate candidates are considered only once. The resulting list is ranked by the newly computed \hat{O}_{SGL} and the top 3000 candidates are kept. This is our result-set, and it is treated in a manner that is very similar to [3].

B. Identification of undisturbed bands

Even after the removal of disturbed data caused by spectral artifacts of known origin, the statistical properties of the results are not uniform across the search band. In what follows we concentrate on the subset of the signal-frequency bands having reasonably uniform statistical properties. This still leaves us with the majority of the search parameter space while allowing us to use methods that rely on theoretical modeling of the significance in the statistical analysis of the results. Our classification of “clean” vs “disturbed” bands has no pretence of being strictly rigorous, because strict rigor here is neither useful nor practical. The classification serves the practical purpose of discarding from the analysis regions in parameter space with evident disturbances and must not dismiss real signals. The classification is carried out in two steps: a visual inspection and a refinement on the visual inspection.

The visual inspection is performed by three scientists who each look at various distributions of the detection statistics over the entire sky and spin-down parameter space in 50 mHz bands. They rank each band with an integer score 0,1,2,3 ranging from “undisturbed” (0) to “disturbed” (3). A band is considered “undisturbed” if all three rankings are 0. The criteria agreed upon for ranking are that the distribution of detection statistic values should not show a visible trend affecting a large portion of the $f - \dot{f}$ plane and, if outliers exist in a small region, outside this region the detection statistic values should be within the expected ranges. Figure 3 shows the \hat{O}_{SGL} for three bands: two were marked as undisturbed and the other as disturbed. One of the bands contains the $f - \dot{f}$ parameter space that harbors a fake signal injected in the data to verify the detection pipelines. The detection statistic is elevated in a small region around the signal parameters. The visual inspection procedure does not mark as disturbed bands with such features.

Based on this visual inspection 13% of the bands between 50 and 510 Hz are marked as “disturbed”. Of these, 34% were given by all visual inspectors rankings

B. P. ABBOTT *et al.*

PHYSICAL REVIEW D 94, 102002 (2016)

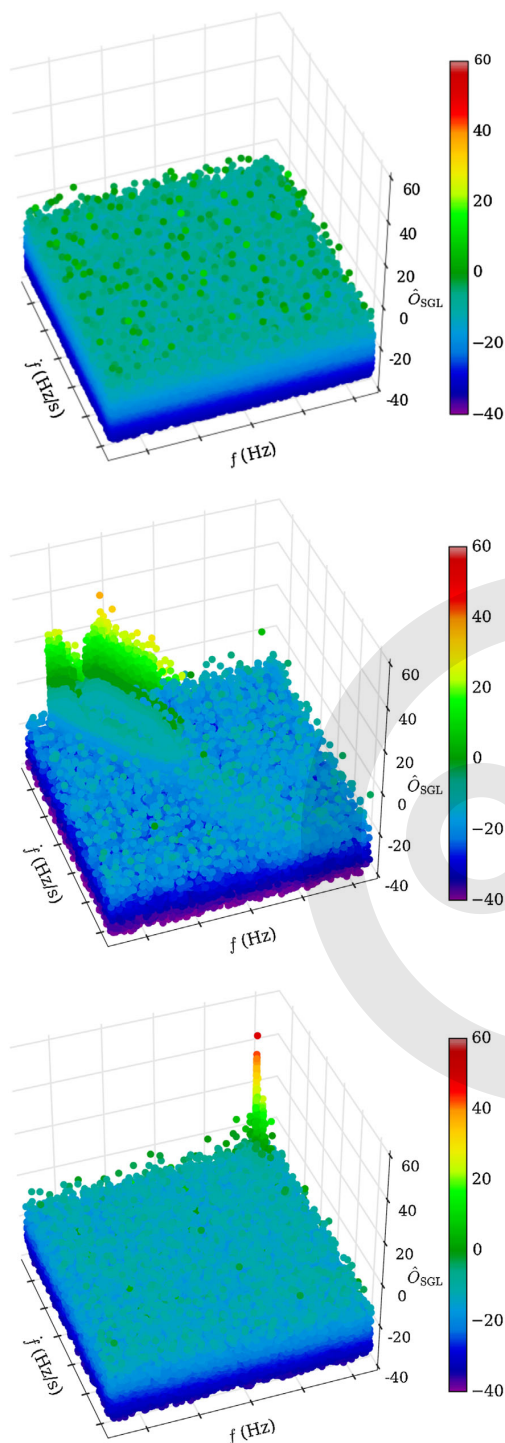


FIG. 3. On the z-axis and color-coded is the \hat{O}_{SGL} in three 50 mHz bands. The top band was marked as “undisturbed”. The middle band is an example of a “disturbed band”. The bottom band is an example of an “undisturbed band” but containing a signal, a fake one, in this case.

smaller than 3, i.e. they were only marginally disturbed. Further inspection “rehabilitated” 42% of these. As a result of this refinement in the selection procedure we exclude from the current analysis 11% of the searched frequencies (Table IV).

Figure 4 shows the highest values of the detection statistic in half-Hz signal-frequency bands compared to the expectations. The set of candidates that the highest detection statistic values are picked from, does not include the 50 mHz signal-frequency bands that stem entirely from fake data, from the cleaning procedure, or that were marked as disturbed. In this paper we refer to the candidates with the highest value of the detection statistic as the *loudest* candidates.

The loudest expected value over N_{trials} independent trials of $2\bar{\mathcal{F}}$ is determined¹ by numerical integration of the probability density function given, for example, by Eq. 7 of [20]. For this search, we estimate that $N_{\text{trials}} \approx 0.87N_{\text{templ}}$, with N_{templ} being the number of templates searched.

As a uniform measure of significance of the highest $2\bar{\mathcal{F}}$ value across bands that were searched with different values of N_{trials} we introduce the critical ratio CR defined as the deviation of the measured highest $2\bar{\mathcal{F}}$ from the expected value, measured in units of the standard deviation

$$\text{CR} := \frac{2\bar{\mathcal{F}}_{\text{meas}} - 2\bar{\mathcal{F}}_{\text{expd}}}{\sigma_{\text{expd}}}. \quad (12)$$

The highest and most significant detection statistic value from our search is $2\bar{\mathcal{F}} = 8.6$ at a frequency of about 52.76 Hz with a $\text{CR} = 29$. This is due to a fake signal. The second highest value of the detection statistic is 7.04 at a frequency of about 329.01 Hz corresponding to a CR of 4.6. The second highest-CR candidate has a $2\bar{\mathcal{F}}$ of 6.99, is

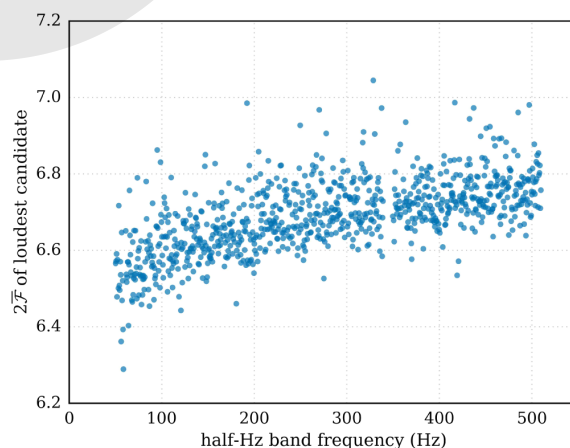


FIG. 4. Highest values of $2\bar{\mathcal{F}}$ in every half-Hz band as a function of band frequency. Since the number of templates increases with frequency so does the loudest $2\bar{\mathcal{F}}$.

RESULTS OF THE DEEPEST ALL-SKY SURVEY FOR ...

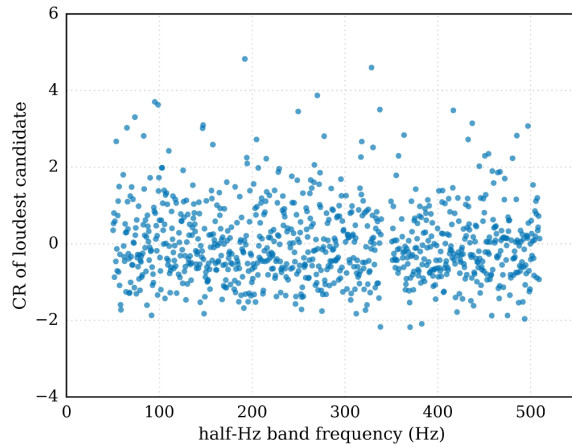


FIG. 5. Highest values of the significance (CR) in every half-Hz band as a function of band frequency. Since the significance folds in the expected value for the loudest $2\mathcal{F}$ and its standard deviation, the significance of the loudest in noise does not increase with frequency. Our results are consistent with this expectation.

at 192.16 Hz and has a CR = 4.8. The CR values are plotted in Fig. 5, and the distribution in Fig. 6.

Sorting loudest candidates from half-Hz bands according to detection statistic values is not the same as sorting them according to CR. The reason for this is that the number of templates is not the same for all half-Hz bands. This is due to the grid spacings decreasing with frequency (Eq. (2)) and to the fact that, as previously explained, some 50 mHz bands have been excluded from the current analysis and hence some half-Hz bands comprise results from fewer than ten 50 mHz bands. Figure 7 gives the fill-level of each half-Hz band, i.e. how many 50 mHz bands have contributed candidates to the analysis out of ten. We use the CR as

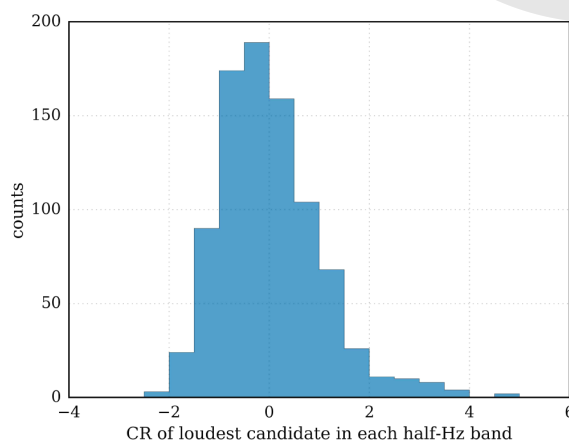


FIG. 6. Histogram of the highest values of the significance CR in every half-Hz band.

PHYSICAL REVIEW D 94, 102002 (2016)

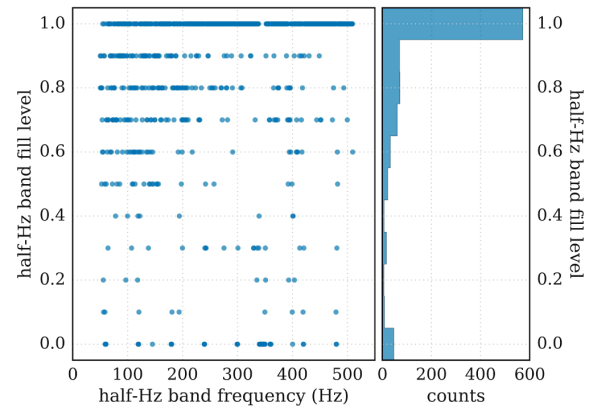


FIG. 7. The fraction of 50 mHz bands (in signal frequency) which contribute to the results in every half-Hz band. As explained in the text, some bands are excluded because they are all from fake data or because they are marked as disturbed by the visual inspection. The list of excluded bands is given in Table IV.

a measure of the significance because it folds in correctly the effect of varying number of templates in the half-Hz bands.

After excluding the candidate due to the fake signal, in this data we see no evidence of a signal: the distribution of p values associated with every measured half-Hz band loudest is consistent with what we expect from noise-only across the measured range (Fig. 8). In particular we note two things: 1) the two candidates at CR = 4.6 and CR = 4.8 are not significant when we consider how many half-Hz bands we have searched, and 2) there is no population of low significance candidates deviating from the expectation of the noise-only case. The p value for the loudest measured in any half-Hz band searched with an

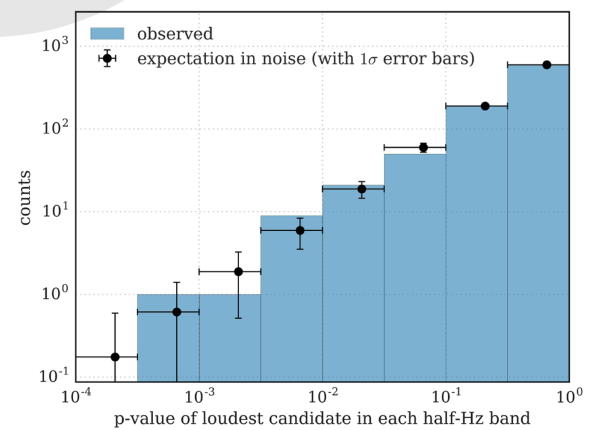


FIG. 8. p values for the loudest in half-Hz bands of our data (histogram bars) and expected distribution of pure noise data for reference (black markers).

B. P. ABBOTT *et al.*

PHYSICAL REVIEW D **94**, 102002 (2016)

effective number of independent trials $N_{\text{trials}} = 0.87N_{\text{trials}}$ is obtained by integrating Eq. 6 of [20] between the observed value and infinity.

IV. UPPER LIMITS

The search did not reveal any continuous gravitational wave signal in the parameter volume that was searched. We hence set frequentist upper limits on the maximum gravitational wave amplitude consistent with this null result in half-Hz bands: $h_0^{90\%}(f)$. $h_0^{90\%}(f)$ is the GW amplitude such that 90% of a population of signals with parameter values in our search range would have produced a candidate louder than what was observed by our search. This is the criterion hereafter referred to as “detection”.

Evaluating these upper limits with injection-and-recovery Monte Carlo simulations in every half-Hz band is too computationally intensive. So we perform them in a subset of 50 bands and infer the upper limit values in the other bands from these. The 50 bands are evenly spaced in the search frequency range. For each band $j = 1 \dots 50$, we measure the 90% upper limit value corresponding to different detection criteria. The different detection criteria are defined by different CR values for the assumed

measured loudest. The first CR bin, CR_0 , is for CR values equal to or smaller than 0, the next bins are for $i < \text{CR}_i \leq (i + 1)$ with $i = 1 \dots 5$. Correspondingly we have $h_{0, \text{CR}_i}^{90\%, j}$ for each band. For every detection criteria and every band we determine the sensitivity depth [22], and by averaging these sensitivity depths over the bands we derive a sensitivity depth for every detection criteria: $\mathcal{D}_{\text{CR}_i}^{90\%} = 1/50 \sum_j \mathcal{D}_{\text{CR}_i}^{90\%, j}$. We use these to set upper limits in the bands k where we have not performed injection-and-recovery simulations as

$$h_0^{90\%}(f_k) = \frac{\sqrt{S_h(f_k)}}{\mathcal{D}_{\text{CR}_i(k)}^{90\%}}, \quad (13)$$

where $\text{CR}_i(k)$ is the significance bin of the loudest candidate of the k th band and $S_h(f_k)$ the power spectral density of the data (measured in $1/\sqrt{\text{Hz}}$). The values of the sensitivity depths range between $\mathcal{D}_{\text{CR}_6}^{90\%} \approx 33(1/\sqrt{\text{Hz}})$ and $\mathcal{D}_{\text{CR}_0}^{90\%} \approx 37(1/\sqrt{\text{Hz}})$. The uncertainties on the upper limit values introduced by this procedure are $\approx 10\%$ of the nominal upper limit value. We represent this uncertainty as a shaded region around the upper limit values in Fig. 9. The upper limit values are also provided in tabular form in the

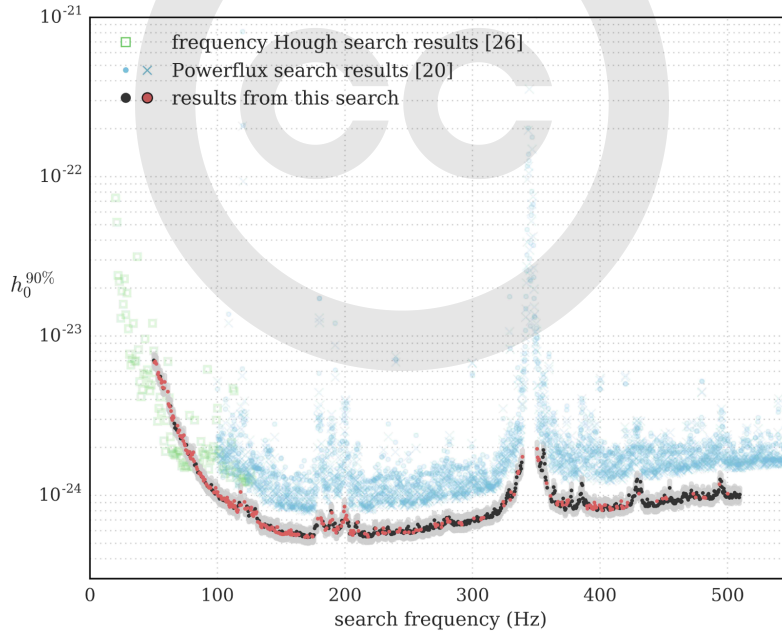


FIG. 9. 90% confidence upper limits on the gravitational wave amplitude of signals with frequency within half-Hz bands, from the entire sky and within the spin-down range of the search. The light red markers denote half-Hz bands where the upper limit value does not hold for all frequencies in that interval. A list of the excluded frequencies is given in the Appendix. Although not obvious from the figure, due to the quality of the data we were not able to analyze the data in some half-Hz bands, so there are some points missing in the plot. For reference we also plot the upper limit results from two searches: one on the same data (Powerflux) [2] and on contemporary data from the Virgo detector (frequency Hough) [4]. The Powerflux points are obtained by rescaling the best (crosses) and worst-case (dots) upper limit values as explained in the text. It should be noted that the Powerflux upper limits are set at 95% rather than 90% but refer to 0.25 Hz bands rather than half-Hz.

RESULTS OF THE DEEPEST ALL-SKY SURVEY FOR ...

Appendix in Table II. We do not set upper limits in half-Hz bands where the results are entirely produced with fake data inserted by the cleaning procedure described in Sec. II. Upper limits for such bands will not appear in Table II nor in Fig. 9. There also exist 50 mHz bands that include contributions from fake data as a result of the cleaning procedure or that have been excluded from the analysis because they were marked as disturbed by the visual inspection procedure described in Sec. III B. We mark the half-Hz bands which host these 50 mHz bands with a different colour (light red) in Fig. 9. In Table IV in the Appendix we provide a complete list of such 50-mHz bands because the upper limit values do not apply to those 50-mHz bands. Finally we note that, due to the cleaning procedure, there exist signal frequency bands where the search results *might* have contributions from fake data. We list these signal-frequency ranges in Table V. For completeness this table also contains the cleaned bands of Table IV, under the column header “all fake data”.

V. CONCLUSIONS

Our upper limits are the tightest ever placed for this set of target signals. The smallest value of the GW amplitude upper limit is 5.5×10^{-25} in the band 170.5–171 Hz. Figure 9 shows the upper limit values as a function of search frequency. We also show the upper limits from [2], another all-sky search on S6 data, rescaled according to [23] to enable a direct comparison with ours. Under the assumption that the sources are uniformly distributed in space, our search probes a volume in space a few times larger than that of [2]. It should however be noted that [2]

PHYSICAL REVIEW D 94, 102002 (2016)

examines a much broader parameter space than the one presented here. The Virgo VSR2 and VSR4 science runs were contemporary to the S6 run and more sensitive at low frequency with respect to LIGO. The Virgo data were analyzed in search of continuous signals from the whole sky in the frequency range 20–128 Hz and a narrower spin-down range than that covered here, with $|\dot{f}| \leq 10^{-10}$ Hz/s [4]. Our sensitivity is comparable to that achieved by that search and improves on it above 80 Hz.

Following [24], we define the fraction x of the spin-down rotational energy emitted in gravitational waves. The star’s ellipticity necessary to sustain such emission is

$$\epsilon(f, x\dot{f}) = \sqrt{\frac{5c^5}{32\pi^4 G I} \frac{x\dot{f}}{f^5}}, \quad (14)$$

where c is the speed of light, G is the gravitational constant, f is the GW frequency and I the principal moment of inertia of the star. Correspondingly, $x\dot{f}$ is the spin-down rate that accounts for the emission of GWs, and this is why we refer to it as the GW spin-down. The gravitational wave amplitude h_0 at the detector coming from a GW source like that of Eq. (14), at a distance D from Earth is

$$h_0(f, x\dot{f}, D) = \frac{1}{D} \sqrt{\frac{5GI}{2c^3} \frac{x\dot{f}}{f}}. \quad (15)$$

Based on this last equation, we can use our GW amplitude upper limits to bound the minimum distance for compact objects emitting continuous gravitational waves under different assumptions on the object’s ellipticity (i.e.

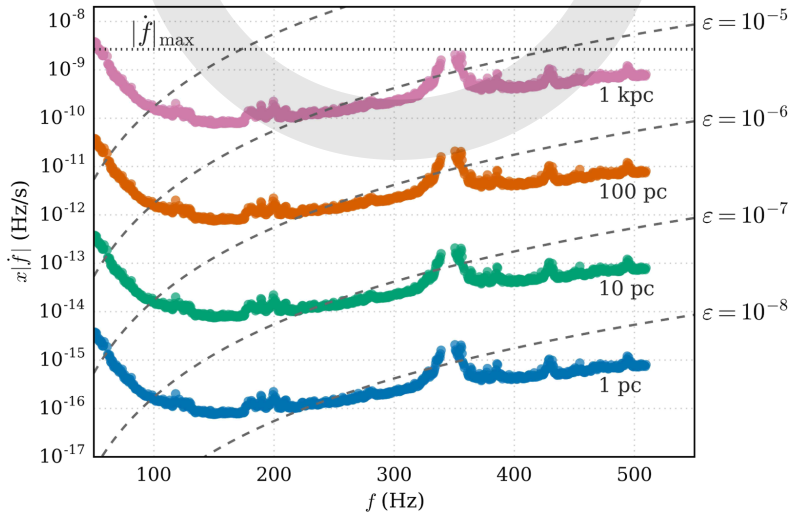


FIG. 10. Gravitational wave amplitude upper limits recast as curves in the $f - x|\dot{f}|$ plane for sources at given distances and having assumed $I = 10^{38}$ kg m². f is the signal frequency and $x|\dot{f}|$ is the gravitational-wave spin-down, i.e. the fraction of the actual spin-down that accounts for the rotational energy loss due to GW emission. Superimposed are curves of constant ellipticity $\epsilon(f, \dot{f}|I = 10^{38}$ kg m²). The dotted line at $|\dot{f}|_{\max}$ indicates the maximum magnitude of searched spin-down.

B. P. ABBOTT *et al.*

PHYSICAL REVIEW D **94**, 102002 (2016)

gravitational wave spin-down). This is shown in Fig. 10. We find that for most frequencies above 230 Hz our upper limits exclude compact objects with ellipticities of $10^{-6} \sqrt{\frac{10^{38} \text{ kg m}^2}{I}}$ (corresponding to GW spin-downs between 10^{-12} Hz/s and 10^{-11} Hz/s) within 100 pc of Earth. Both the ellipticity and the distance ranges span absolutely plausible values and could not have been excluded with other measurements.

We expect the methodology used in this search to serve as a template for the assessment of Einstein@Home run results in the future, for example the next Einstein@Home run, using advanced LIGO data that is being processed as this paper is written. Results of searches for continuous wave signals could also be mined further, probing sub-threshold candidates with a hierarchical series of follow-up searches. This is not the topic of this paper and might be pursued in a forthcoming publication.

ACKNOWLEDGMENTS

The authors gratefully acknowledge the support of the Einstein@Home volunteers, of the United States National Science Foundation for the construction and operation of the LIGO Laboratory, the Science and Technology Facilities Council of the United Kingdom,

the Max-Planck-Society, and the State of Niedersachsen/Germany for support of the construction and operation of the GEO600 detector, and the Italian Istituto Nazionale di Fisica Nucleare and the French Centre National de la Recherche Scientifique for the construction and operation of the Virgo detector. The authors also gratefully acknowledge the support of the research by these agencies and by the Australian Research Council, the International Science Linkages program of the Commonwealth of Australia, the Council of Scientific and Industrial Research of India, the Istituto Nazionale di Fisica Nucleare of Italy, the Spanish Ministerio de Educación y Ciencia, the Conselleria d’Economia Hisenda i Innovació of the Govern de les Illes Balears, the Foundation for Fundamental Research on Matter supported by the Netherlands Organization for Scientific Research, the Polish Ministry of Science and Higher Education, the FOCUS Programme of Foundation for Polish Science, the Royal Society, the Scottish Funding Council, the Scottish Universities Physics Alliance, The National Aeronautics and Space Administration, the Carnegie Trust, the Leverhulme Trust, the David and Lucile Packard Foundation, the Research Corporation, and the Alfred P. Sloan Foundation.

This document has been assigned LIGO Laboratory document No. LIGO-P1600156-v22.

APPENDIX: TABULAR DATA

1. Upper limit values

TABLE II. First frequency of each half Hz signal frequency band in which we set upper limits and upper limit value for that band.

f (in Hz)	$h_0^{90\%} \times 10^{25}$	f (in Hz)	$h_0^{90\%} \times 10^{25}$	f (in Hz)	$h_0^{90\%} \times 10^{25}$	f (in Hz)	$h_0^{90\%} \times 10^{25}$
50.063	70.3 ± 12.8	50.563	68.4 ± 12.5	51.063	69.3 ± 12.6	51.563	67.5 ± 12.4
52.063	66.9 ± 12.2	53.063	57.6 ± 10.5	53.563	58.9 ± 10.9	54.063	55.3 ± 10.1
54.563	54.0 ± 9.9	55.063	55.7 ± 10.2	55.563	53.3 ± 9.8	56.063	50.9 ± 9.3
56.563	51.8 ± 9.5	57.063	47.5 ± 8.7	57.563	46.9 ± 8.6	58.063	47.1 ± 8.6
58.563	51.5 ± 9.4	61.063	44.8 ± 8.2	61.563	37.4 ± 6.9	62.063	36.5 ± 6.7
62.563	36.0 ± 6.6	63.063	36.3 ± 6.6	63.563	33.8 ± 6.2	64.063	30.6 ± 5.6
64.563	29.8 ± 5.4	65.063	31.5 ± 5.9	65.563	30.8 ± 5.7	66.063	28.3 ± 5.2
66.563	26.5 ± 4.8	67.063	26.5 ± 4.9	67.563	27.3 ± 5.0	68.063	25.7 ± 4.7
68.563	27.4 ± 5.0	69.063	24.8 ± 4.5	69.563	25.5 ± 4.7	70.063	25.7 ± 4.7
70.563	23.6 ± 4.3	71.063	22.8 ± 4.2	71.563	23.6 ± 4.3	72.063	23.1 ± 4.2
72.563	23.3 ± 4.2	73.063	22.0 ± 4.0	73.563	23.9 ± 4.5	74.063	21.1 ± 3.8
74.563	20.6 ± 3.8	75.063	19.3 ± 3.5	75.563	20.8 ± 3.8	76.063	19.0 ± 3.5
76.563	18.3 ± 3.4	77.063	18.1 ± 3.3	77.563	18.5 ± 3.4	78.063	18.8 ± 3.4
78.563	17.4 ± 3.2	79.063	17.0 ± 3.1	79.563	18.1 ± 3.3	80.063	18.0 ± 3.3
80.563	16.9 ± 3.1	81.063	18.7 ± 3.4	81.563	16.3 ± 3.0	82.063	15.5 ± 2.8
82.563	15.4 ± 2.8	83.063	15.7 ± 2.9	83.563	15.0 ± 2.8	84.063	14.6 ± 2.7
84.563	13.9 ± 2.5	85.063	14.0 ± 2.6	85.563	13.7 ± 2.5	86.063	13.9 ± 2.5
86.563	13.8 ± 2.5	87.063	13.3 ± 2.4	87.563	13.1 ± 2.4	88.063	12.9 ± 2.4
88.563	13.0 ± 2.4	89.063	12.4 ± 2.3	89.563	12.3 ± 2.3	90.063	12.6 ± 2.3

(Table continued)

RESULTS OF THE DEEPEST ALL-SKY SURVEY FOR ...

PHYSICAL REVIEW D **94**, 102002 (2016)

TABLE II. (Continued)

f (in Hz)	$h_0^{90\%} \times 10^{25}$	f (in Hz)	$h_0^{90\%} \times 10^{25}$	f (in Hz)	$h_0^{90\%} \times 10^{25}$	f (in Hz)	$h_0^{90\%} \times 10^{25}$
90.563	12.0 ± 2.2	91.063	11.8 ± 2.2	91.563	11.6 ± 2.1	92.063	11.4 ± 2.1
92.563	11.3 ± 2.1	93.063	11.2 ± 2.1	93.563	11.1 ± 2.0	94.063	11.3 ± 2.1
94.563	11.1 ± 2.0	95.063	11.6 ± 2.2	95.563	10.8 ± 2.0	96.063	10.8 ± 2.0
96.563	10.6 ± 1.9	97.063	10.4 ± 1.9	97.563	10.5 ± 1.9	98.063	10.2 ± 1.9
98.563	11.1 ± 2.1	99.063	10.5 ± 1.9	99.563	10.3 ± 1.9	100.063	10.5 ± 1.9
100.563	9.9 ± 1.8	101.063	9.8 ± 1.8	101.563	9.5 ± 1.7	102.063	9.9 ± 1.8
102.563	9.9 ± 1.8	103.063	9.6 ± 1.8	103.563	9.5 ± 1.7	104.063	9.4 ± 1.7
104.563	9.3 ± 1.7	105.063	9.6 ± 1.8	105.563	9.3 ± 1.7	106.063	9.3 ± 1.7
106.563	9.4 ± 1.7	107.063	9.1 ± 1.7	107.563	9.7 ± 1.8	108.063	9.3 ± 1.7
108.563	9.0 ± 1.7	109.063	8.7 ± 1.6	109.563	8.5 ± 1.5	110.063	9.0 ± 1.7
110.563	8.6 ± 1.6	111.063	8.6 ± 1.6	111.563	8.8 ± 1.6	112.063	8.5 ± 1.5
112.563	8.3 ± 1.5	113.063	9.2 ± 1.7	113.563	8.6 ± 1.6	114.063	8.4 ± 1.5
114.563	8.4 ± 1.6	115.063	8.0 ± 1.5	115.563	7.9 ± 1.4	116.063	8.1 ± 1.5
116.563	8.6 ± 1.6	117.063	9.0 ± 1.7	117.563	8.7 ± 1.6	118.063	10.5 ± 1.9
118.563	8.7 ± 1.6	121.063	9.1 ± 1.7	121.563	8.2 ± 1.5	122.063	8.3 ± 1.5
122.563	8.2 ± 1.5	123.063	8.5 ± 1.6	123.563	8.3 ± 1.5	124.063	8.0 ± 1.4
124.563	7.4 ± 1.4	125.063	7.5 ± 1.4	125.563	8.3 ± 1.5	126.063	8.1 ± 1.5
126.563	8.4 ± 1.5	127.063	7.6 ± 1.4	127.563	7.7 ± 1.4	128.063	7.4 ± 1.4
128.563	7.8 ± 1.4	129.063	8.0 ± 1.5	129.563	8.2 ± 1.5	130.063	7.7 ± 1.4
130.563	7.9 ± 1.4	131.063	7.2 ± 1.3	131.563	6.8 ± 1.2	132.063	7.0 ± 1.3
132.563	6.9 ± 1.3	133.063	6.7 ± 1.2	133.563	6.6 ± 1.2	134.063	6.4 ± 1.2
134.563	6.3 ± 1.2	135.063	6.5 ± 1.2	135.563	6.5 ± 1.2	136.063	6.6 ± 1.2
136.563	6.3 ± 1.2	137.063	6.6 ± 1.2	137.563	6.5 ± 1.2	138.063	6.4 ± 1.2
138.563	6.4 ± 1.2	139.063	6.5 ± 1.2	139.563	6.2 ± 1.1	140.063	6.3 ± 1.1
140.563	6.2 ± 1.1	141.063	6.1 ± 1.1	141.563	6.5 ± 1.2	142.063	6.2 ± 1.1
142.563	6.3 ± 1.2	143.063	6.3 ± 1.1	143.563	6.0 ± 1.1	144.063	6.2 ± 1.1
144.563	6.0 ± 1.1	145.563	5.9 ± 1.1	146.063	5.9 ± 1.1	146.563	6.3 ± 1.2
147.063	6.3 ± 1.2	147.563	5.8 ± 1.1	148.063	5.8 ± 1.1	148.563	5.9 ± 1.1
149.063	5.8 ± 1.1	149.563	5.7 ± 1.0	150.063	5.7 ± 1.0	150.563	6.0 ± 1.1
151.063	5.7 ± 1.0	151.563	5.7 ± 1.0	152.063	5.7 ± 1.1	152.563	5.7 ± 1.0
153.063	5.8 ± 1.1	153.563	5.8 ± 1.1	154.063	5.7 ± 1.0	154.563	5.7 ± 1.1
155.063	5.9 ± 1.1	155.563	5.9 ± 1.1	156.063	6.0 ± 1.1	156.563	6.0 ± 1.1
157.063	5.7 ± 1.0	157.563	6.0 ± 1.1	158.063	5.8 ± 1.1	158.563	5.7 ± 1.0
159.063	5.8 ± 1.1	159.563	5.6 ± 1.0	160.063	5.8 ± 1.1	160.563	5.7 ± 1.0
161.063	5.7 ± 1.0	161.563	5.6 ± 1.0	162.063	5.9 ± 1.1	162.563	5.7 ± 1.0
163.063	5.7 ± 1.0	163.563	5.7 ± 1.0	164.063	5.6 ± 1.0	164.563	5.8 ± 1.1
165.063	5.7 ± 1.0	165.563	5.7 ± 1.0	166.063	5.7 ± 1.0	166.563	5.5 ± 1.0
167.063	5.7 ± 1.0	167.563	5.6 ± 1.0	168.063	5.6 ± 1.0	168.563	5.5 ± 1.0
169.063	5.5 ± 1.0	169.563	5.5 ± 1.0	170.063	5.6 ± 1.0	170.563	5.5 ± 1.0
171.063	5.5 ± 1.0	171.563	5.5 ± 1.0	172.063	5.5 ± 1.0	172.563	5.7 ± 1.0
173.063	5.6 ± 1.0	173.563	5.7 ± 1.0	174.063	5.5 ± 1.0	174.563	5.5 ± 1.0
175.063	5.5 ± 1.0	175.563	5.6 ± 1.0	176.063	6.2 ± 1.1	176.563	6.4 ± 1.2
177.063	6.4 ± 1.2	177.563	6.5 ± 1.2	178.063	6.5 ± 1.2	178.563	7.2 ± 1.3
181.063	7.2 ± 1.3	181.563	7.0 ± 1.3	182.063	6.7 ± 1.2	182.563	6.9 ± 1.3
183.063	6.6 ± 1.2	183.563	6.4 ± 1.2	184.063	6.4 ± 1.2	184.563	6.1 ± 1.1
185.063	6.3 ± 1.2	185.563	6.2 ± 1.1	186.063	6.2 ± 1.1	186.563	6.3 ± 1.2
187.063	6.2 ± 1.1	187.563	6.5 ± 1.2	188.063	6.8 ± 1.2	188.563	6.9 ± 1.3
189.063	8.0 ± 1.5	189.563	7.8 ± 1.4	190.063	7.0 ± 1.3	190.563	6.5 ± 1.2
191.063	6.1 ± 1.1	191.563	6.2 ± 1.1	192.063	6.7 ± 1.3	192.563	6.1 ± 1.1
193.063	5.8 ± 1.1	193.563	5.8 ± 1.1	194.063	6.3 ± 1.2	194.563	6.1 ± 1.1
195.063	6.1 ± 1.1	195.563	6.2 ± 1.1	196.063	6.5 ± 1.2	196.563	6.3 ± 1.2
197.063	6.4 ± 1.2	197.563	6.9 ± 1.3	198.063	6.8 ± 1.2	198.563	6.8 ± 1.2
199.063	7.9 ± 1.4	199.563	8.5 ± 1.6	200.063	7.1 ± 1.3	200.563	7.3 ± 1.3
201.063	7.5 ± 1.4	201.563	7.0 ± 1.3	202.063	6.7 ± 1.2	202.563	6.8 ± 1.2
203.063	6.4 ± 1.2	203.563	5.7 ± 1.1	204.063	5.8 ± 1.1	204.563	6.0 ± 1.1

(Table continued)

B. P. ABBOTT *et al.*

PHYSICAL REVIEW D **94**, 102002 (2016)

TABLE II. (Continued)

f (in Hz)	$h_0^{90\%} \times 10^{25}$	f (in Hz)	$h_0^{90\%} \times 10^{25}$	f (in Hz)	$h_0^{90\%} \times 10^{25}$	f (in Hz)	$h_0^{90\%} \times 10^{25}$
205.063	5.8 ± 1.1	205.563	5.7 ± 1.0	206.063	5.6 ± 1.0	206.563	6.0 ± 1.1
207.063	5.9 ± 1.1	207.563	5.8 ± 1.1	208.063	6.4 ± 1.2	208.563	6.7 ± 1.2
209.063	6.3 ± 1.2	209.563	6.8 ± 1.2	210.063	6.8 ± 1.2	210.563	6.0 ± 1.1
211.063	5.8 ± 1.1	211.563	5.7 ± 1.0	212.063	5.6 ± 1.0	212.563	5.8 ± 1.1
213.063	5.7 ± 1.0	213.563	5.9 ± 1.1	214.063	5.5 ± 1.0	214.563	5.8 ± 1.1
215.063	5.9 ± 1.1	215.563	5.8 ± 1.1	216.063	5.5 ± 1.0	216.563	5.5 ± 1.0
217.063	5.5 ± 1.0	217.563	5.7 ± 1.0	218.063	5.5 ± 1.0	218.563	5.8 ± 1.1
219.063	5.5 ± 1.0	219.563	5.7 ± 1.0	220.063	5.7 ± 1.0	220.563	5.5 ± 1.0
221.063	5.6 ± 1.0	221.563	5.6 ± 1.0	222.063	5.7 ± 1.0	222.563	5.8 ± 1.1
223.063	6.2 ± 1.1	223.563	6.2 ± 1.1	224.063	6.2 ± 1.1	224.563	5.8 ± 1.1
225.063	5.8 ± 1.1	225.563	5.8 ± 1.1	226.063	5.7 ± 1.0	226.563	5.7 ± 1.0
227.063	6.0 ± 1.1	227.563	5.8 ± 1.1	228.063	5.9 ± 1.1	228.563	5.9 ± 1.1
229.063	6.1 ± 1.1	229.563	5.9 ± 1.1	230.063	6.2 ± 1.1	230.563	5.8 ± 1.1
231.063	5.9 ± 1.1	231.563	5.8 ± 1.1	232.063	5.7 ± 1.1	232.563	5.9 ± 1.1
233.063	6.2 ± 1.1	233.563	6.3 ± 1.1	234.063	6.1 ± 1.1	234.563	5.9 ± 1.1
235.063	5.9 ± 1.1	235.563	5.8 ± 1.1	236.063	5.7 ± 1.0	236.563	5.7 ± 1.0
237.063	5.7 ± 1.0	237.563	5.9 ± 1.1	238.063	5.9 ± 1.1	238.563	5.8 ± 1.1
240.563	6.0 ± 1.1	241.063	5.9 ± 1.1	241.563	5.9 ± 1.1	242.063	5.9 ± 1.1
242.563	6.0 ± 1.1	243.063	6.2 ± 1.1	243.563	6.0 ± 1.1	244.063	5.9 ± 1.1
244.563	5.9 ± 1.1	245.063	6.0 ± 1.1	245.563	5.8 ± 1.1	246.063	5.8 ± 1.1
246.563	5.8 ± 1.1	247.063	5.9 ± 1.1	247.563	6.0 ± 1.1	248.063	5.9 ± 1.1
248.563	6.2 ± 1.1	249.063	6.1 ± 1.1	249.563	6.4 ± 1.2	250.063	5.9 ± 1.1
250.563	6.0 ± 1.1	251.063	5.8 ± 1.1	251.563	5.9 ± 1.1	252.063	5.9 ± 1.1
252.563	5.8 ± 1.1	253.063	5.8 ± 1.1	253.563	5.8 ± 1.1	254.063	5.9 ± 1.1
254.563	6.1 ± 1.1	255.063	5.9 ± 1.1	255.563	6.1 ± 1.1	256.063	6.0 ± 1.1
256.563	6.0 ± 1.1	257.063	6.6 ± 1.2	257.563	6.0 ± 1.1	258.063	6.4 ± 1.2
258.563	6.2 ± 1.1	259.063	6.1 ± 1.1	259.563	6.1 ± 1.1	260.063	6.0 ± 1.1
260.563	6.0 ± 1.1	261.063	6.0 ± 1.1	261.563	6.0 ± 1.1	262.063	6.3 ± 1.1
262.563	6.1 ± 1.1	263.063	6.2 ± 1.1	263.563	6.2 ± 1.1	264.063	6.3 ± 1.2
264.563	6.1 ± 1.1	265.063	6.1 ± 1.1	265.563	6.3 ± 1.1	266.063	6.1 ± 1.1
266.563	6.4 ± 1.2	267.063	6.6 ± 1.2	267.563	6.3 ± 1.2	268.063	6.4 ± 1.2
268.563	6.3 ± 1.2	269.063	6.2 ± 1.1	269.563	6.2 ± 1.1	270.063	7.0 ± 1.3
270.563	6.6 ± 1.2	271.063	6.4 ± 1.2	271.563	6.3 ± 1.2	272.063	6.6 ± 1.2
272.563	6.5 ± 1.2	273.063	6.7 ± 1.2	273.563	6.5 ± 1.2	274.063	6.2 ± 1.1
274.563	6.3 ± 1.1	275.063	6.3 ± 1.1	275.563	6.3 ± 1.2	276.063	6.7 ± 1.2
276.563	6.5 ± 1.2	277.063	6.6 ± 1.2	277.563	7.0 ± 1.3	278.063	6.6 ± 1.2
278.563	6.7 ± 1.2	279.063	6.8 ± 1.3	279.563	7.2 ± 1.3	280.063	7.1 ± 1.3
280.563	6.8 ± 1.2	281.063	6.9 ± 1.3	281.563	7.3 ± 1.3	282.063	6.8 ± 1.3
282.563	6.9 ± 1.3	283.063	6.7 ± 1.2	283.563	6.9 ± 1.3	284.063	6.6 ± 1.2
284.563	6.6 ± 1.2	285.063	6.8 ± 1.3	285.563	6.5 ± 1.2	286.063	6.7 ± 1.2
286.563	6.6 ± 1.2	287.063	6.7 ± 1.2	287.563	6.5 ± 1.2	288.063	6.6 ± 1.2
288.563	6.8 ± 1.2	289.063	6.6 ± 1.2	289.563	6.7 ± 1.2	290.063	6.6 ± 1.2
290.563	6.6 ± 1.2	291.063	6.7 ± 1.2	291.563	6.6 ± 1.2	292.063	6.7 ± 1.2
292.563	6.6 ± 1.2	293.063	6.6 ± 1.2	293.563	6.8 ± 1.2	294.063	6.9 ± 1.3
294.563	6.6 ± 1.2	295.063	6.6 ± 1.2	295.563	6.9 ± 1.3	296.063	6.9 ± 1.3
296.563	6.7 ± 1.2	297.063	6.9 ± 1.3	297.563	6.7 ± 1.2	298.063	6.9 ± 1.3
298.563	6.9 ± 1.3	300.563	7.1 ± 1.3	301.063	7.2 ± 1.3	301.563	6.9 ± 1.3
302.063	6.9 ± 1.3	302.563	7.1 ± 1.3	303.063	7.1 ± 1.3	303.563	7.3 ± 1.3
304.063	7.2 ± 1.3	304.563	6.9 ± 1.3	305.063	7.0 ± 1.3	305.563	7.2 ± 1.3
306.063	7.1 ± 1.3	306.563	7.1 ± 1.3	307.063	7.2 ± 1.3	307.563	7.2 ± 1.3
308.063	7.2 ± 1.3	308.563	7.3 ± 1.3	309.063	7.2 ± 1.3	309.563	7.3 ± 1.3
310.063	7.4 ± 1.4	310.563	7.2 ± 1.3	311.063	7.5 ± 1.4	311.563	7.6 ± 1.4
312.063	7.4 ± 1.4	312.563	7.3 ± 1.3	313.063	7.3 ± 1.3	313.563	7.3 ± 1.3
314.063	7.3 ± 1.3	314.563	7.5 ± 1.4	315.063	7.3 ± 1.3	315.563	7.4 ± 1.4
316.063	7.8 ± 1.4	316.563	7.7 ± 1.4	317.063	8.2 ± 1.5	317.563	7.8 ± 1.4

(Table continued)

RESULTS OF THE DEEPEST ALL-SKY SURVEY FOR ...

PHYSICAL REVIEW D 94, 102002 (2016)

TABLE II. (Continued)

f (in Hz)	$h_0^{90\%} \times 10^{25}$	f (in Hz)	$h_0^{90\%} \times 10^{25}$	f (in Hz)	$h_0^{90\%} \times 10^{25}$	f (in Hz)	$h_0^{90\%} \times 10^{25}$
318.063	8.1 ± 1.5	318.563	7.8 ± 1.4	319.063	7.6 ± 1.4	319.563	8.0 ± 1.5
320.063	7.7 ± 1.4	320.563	7.7 ± 1.4	321.063	8.0 ± 1.5	321.563	8.0 ± 1.5
322.063	8.4 ± 1.5	322.563	8.3 ± 1.5	323.063	8.8 ± 1.6	323.563	8.7 ± 1.6
324.063	9.1 ± 1.7	324.563	8.6 ± 1.6	325.063	9.0 ± 1.6	325.563	8.9 ± 1.6
326.063	9.1 ± 1.7	326.563	9.6 ± 1.8	327.063	10.0 ± 1.8	327.563	10.3 ± 1.9
328.063	10.0 ± 1.8	328.563	10.8 ± 2.0	329.063	9.6 ± 1.8	329.563	9.4 ± 1.7
330.063	10.5 ± 1.9	330.563	10.2 ± 1.9	331.063	9.8 ± 1.8	331.563	10.2 ± 1.9
332.063	10.2 ± 1.9	332.563	10.1 ± 1.9	333.063	10.6 ± 1.9	333.563	11.1 ± 2.0
334.063	11.8 ± 2.2	334.563	13.0 ± 2.4	335.063	14.0 ± 2.6	335.563	13.8 ± 2.5
336.063	14.1 ± 2.6	336.563	13.8 ± 2.5	337.063	14.1 ± 2.6	337.563	15.3 ± 2.9
338.063	14.7 ± 2.7	338.563	16.1 ± 2.9	339.063	17.4 ± 3.2	350.563	19.6 ± 3.6
351.063	17.3 ± 3.2	351.563	16.6 ± 3.0	352.063	16.8 ± 3.1	352.563	15.2 ± 2.8
353.063	15.7 ± 2.9	353.563	16.0 ± 2.9	354.063	14.4 ± 2.6	354.563	14.3 ± 2.6
355.063	17.4 ± 3.2	355.563	19.3 ± 3.5	356.063	18.3 ± 3.3	356.563	15.8 ± 2.9
357.063	13.0 ± 2.4	357.563	12.4 ± 2.3	358.063	11.9 ± 2.2	358.563	11.2 ± 2.0
361.063	9.9 ± 1.8	361.563	9.5 ± 1.7	362.063	9.1 ± 1.7	362.563	9.2 ± 1.7
363.063	10.2 ± 1.9	363.563	11.3 ± 2.1	364.063	10.4 ± 1.9	364.563	10.7 ± 2.0
365.063	9.1 ± 1.7	365.563	8.8 ± 1.6	366.063	8.9 ± 1.6	366.563	8.7 ± 1.6
367.063	9.1 ± 1.7	367.563	9.0 ± 1.6	368.063	8.6 ± 1.6	368.563	9.0 ± 1.6
369.063	8.5 ± 1.6	369.563	8.9 ± 1.6	370.063	9.1 ± 1.7	370.563	8.7 ± 1.6
371.063	9.6 ± 1.8	371.563	9.0 ± 1.6	372.063	8.4 ± 1.5	372.563	8.1 ± 1.5
373.063	8.3 ± 1.5	373.563	8.7 ± 1.6	374.063	9.3 ± 1.7	374.563	9.0 ± 1.6
375.063	9.3 ± 1.7	375.563	8.6 ± 1.6	376.063	8.9 ± 1.6	376.563	8.7 ± 1.6
377.063	9.8 ± 1.8	377.563	10.7 ± 2.0	378.063	9.2 ± 1.7	378.563	8.4 ± 1.5
379.063	8.2 ± 1.5	379.563	8.4 ± 1.5	380.063	8.6 ± 1.6	380.563	8.5 ± 1.5
381.063	8.3 ± 1.5	381.563	8.5 ± 1.6	382.063	8.8 ± 1.6	382.563	8.9 ± 1.6
383.063	9.3 ± 1.7	383.563	9.1 ± 1.7	384.063	9.4 ± 1.7	384.563	10.2 ± 1.9
385.063	10.3 ± 1.9	385.563	11.9 ± 2.2	386.063	11.6 ± 2.1	386.563	9.6 ± 1.7
387.063	9.1 ± 1.7	387.563	8.8 ± 1.6	388.063	8.7 ± 1.6	388.563	9.3 ± 1.7
389.063	9.2 ± 1.7	389.563	8.6 ± 1.6	390.063	8.3 ± 1.5	390.563	8.8 ± 1.6
391.063	8.9 ± 1.6	391.563	8.7 ± 1.6	392.063	8.4 ± 1.5	392.563	8.6 ± 1.6
393.063	8.5 ± 1.6	393.563	8.3 ± 1.5	394.063	8.4 ± 1.5	394.563	8.2 ± 1.5
395.063	8.2 ± 1.5	395.563	9.0 ± 1.7	396.063	8.6 ± 1.6	396.563	8.4 ± 1.5
397.063	8.4 ± 1.5	397.563	8.1 ± 1.5	398.063	8.1 ± 1.5	398.563	8.3 ± 1.5
399.063	8.4 ± 1.5	399.563	8.7 ± 1.6	400.563	8.3 ± 1.5	401.063	8.5 ± 1.6
401.563	8.1 ± 1.5	402.063	8.1 ± 1.5	402.563	8.1 ± 1.5	403.063	8.5 ± 1.6
403.563	8.7 ± 1.6	404.063	8.7 ± 1.6	404.563	8.6 ± 1.6	405.063	8.5 ± 1.6
405.563	8.6 ± 1.6	406.063	8.6 ± 1.6	406.563	8.2 ± 1.5	407.063	8.1 ± 1.5
407.563	8.4 ± 1.5	408.063	8.1 ± 1.5	408.563	8.2 ± 1.5	409.063	8.2 ± 1.5
409.563	8.2 ± 1.5	410.063	8.4 ± 1.5	410.563	8.2 ± 1.5	411.063	8.4 ± 1.5
411.563	8.7 ± 1.6	412.063	8.7 ± 1.6	412.563	8.8 ± 1.6	413.063	8.5 ± 1.6
413.563	8.4 ± 1.5	414.063	8.4 ± 1.5	414.563	8.5 ± 1.5	415.063	8.5 ± 1.5
415.563	8.3 ± 1.5	416.063	8.7 ± 1.6	416.563	9.2 ± 1.7	417.063	8.6 ± 1.6
417.563	8.3 ± 1.5	418.063	8.5 ± 1.6	418.563	8.3 ± 1.5	420.563	8.5 ± 1.6
421.063	8.5 ± 1.6	421.563	9.0 ± 1.7	422.063	8.8 ± 1.6	422.563	10.0 ± 1.8
423.063	8.8 ± 1.6	423.563	8.7 ± 1.6	424.063	8.7 ± 1.6	424.563	8.9 ± 1.6
425.063	9.3 ± 1.7	425.563	9.7 ± 1.8	426.063	9.8 ± 1.8	426.563	9.9 ± 1.8
427.063	9.9 ± 1.8	427.563	10.9 ± 2.0	428.063	11.2 ± 2.1	428.563	12.3 ± 2.2
429.063	12.6 ± 2.3	429.563	10.4 ± 1.9	430.063	10.8 ± 2.0	430.563	10.3 ± 1.9
431.063	10.5 ± 1.9	431.563	12.2 ± 2.2	432.063	10.9 ± 2.0	432.563	10.6 ± 1.9
433.063	9.3 ± 1.7	433.563	9.0 ± 1.6	434.063	9.0 ± 1.6	434.563	9.0 ± 1.6
435.063	8.8 ± 1.6	435.563	8.6 ± 1.6	436.063	8.6 ± 1.6	436.563	8.8 ± 1.6
437.063	9.4 ± 1.8	437.563	8.5 ± 1.6	438.063	9.0 ± 1.6	438.563	8.6 ± 1.6
439.063	8.8 ± 1.6	439.563	8.9 ± 1.6	440.063	9.0 ± 1.6	440.563	8.9 ± 1.6
441.063	9.0 ± 1.6	441.563	8.8 ± 1.6	442.063	8.6 ± 1.6	442.563	8.6 ± 1.6

(Table continued)

B. P. ABBOTT *et al.*

PHYSICAL REVIEW D **94**, 102002 (2016)

TABLE II. (Continued)

f (in Hz)	$h_0^{90\%} \times 10^{25}$	f (in Hz)	$h_0^{90\%} \times 10^{25}$	f (in Hz)	$h_0^{90\%} \times 10^{25}$	f (in Hz)	$h_0^{90\%} \times 10^{25}$
443.063	8.6 ± 1.6	443.563	8.6 ± 1.6	444.063	8.6 ± 1.6	444.563	9.2 ± 1.7
445.063	8.6 ± 1.6	445.563	8.7 ± 1.6	446.063	9.2 ± 1.7	446.563	9.1 ± 1.7
447.063	8.9 ± 1.6	447.563	9.0 ± 1.7	448.063	9.0 ± 1.6	448.563	9.5 ± 1.7
449.063	9.5 ± 1.8	449.563	8.9 ± 1.6	450.063	9.1 ± 1.7	450.563	10.0 ± 1.8
451.063	9.2 ± 1.7	451.563	9.7 ± 1.8	452.063	9.5 ± 1.7	452.563	9.2 ± 1.7
453.063	9.1 ± 1.7	453.563	9.4 ± 1.7	454.063	9.5 ± 1.7	454.563	11.1 ± 2.1
455.063	9.3 ± 1.7	455.563	9.7 ± 1.8	456.063	9.6 ± 1.8	456.563	9.4 ± 1.7
457.063	9.0 ± 1.7	457.563	8.9 ± 1.6	458.063	8.9 ± 1.6	458.563	9.3 ± 1.7
459.063	8.9 ± 1.6	459.563	9.1 ± 1.7	460.063	9.3 ± 1.7	460.563	9.4 ± 1.7
461.063	9.4 ± 1.7	461.563	9.3 ± 1.7	462.063	9.3 ± 1.7	462.563	9.3 ± 1.7
463.063	9.4 ± 1.7	463.563	9.1 ± 1.7	464.063	9.2 ± 1.7	464.563	9.7 ± 1.8
465.063	9.9 ± 1.8	465.563	10.3 ± 1.9	466.063	9.9 ± 1.8	466.563	9.8 ± 1.8
467.063	10.2 ± 1.9	467.563	10.1 ± 1.9	468.063	9.8 ± 1.8	468.563	9.6 ± 1.8
469.063	9.4 ± 1.7	469.563	9.7 ± 1.8	470.063	9.8 ± 1.8	470.563	9.8 ± 1.8
471.063	10.3 ± 1.9	471.563	10.7 ± 2.0	472.063	10.2 ± 1.9	472.563	9.9 ± 1.8
473.063	10.2 ± 1.9	473.563	9.9 ± 1.8	474.063	9.7 ± 1.8	474.563	10.0 ± 1.8
475.063	9.7 ± 1.8	475.563	10.4 ± 1.9	476.063	10.0 ± 1.8	476.563	9.8 ± 1.8
477.063	10.0 ± 1.8	477.563	9.8 ± 1.8	478.063	9.5 ± 1.7	478.563	9.5 ± 1.7
480.563	10.3 ± 1.9	481.063	9.7 ± 1.8	481.563	9.8 ± 1.8	482.063	9.7 ± 1.8
482.563	9.6 ± 1.8	483.063	9.7 ± 1.8	483.563	9.9 ± 1.8	484.063	9.6 ± 1.8
484.563	10.1 ± 1.8	485.063	10.2 ± 1.9	485.563	9.7 ± 1.8	486.063	9.5 ± 1.7
486.563	9.8 ± 1.8	487.063	9.5 ± 1.7	487.563	9.5 ± 1.7	488.063	9.5 ± 1.7
488.563	9.7 ± 1.8	489.063	10.0 ± 1.8	489.563	10.7 ± 1.9	490.063	10.6 ± 1.9
490.563	10.0 ± 1.8	491.063	10.3 ± 1.9	491.563	10.1 ± 1.9	492.063	10.5 ± 1.9
492.563	10.5 ± 1.9	493.063	10.8 ± 2.0	493.563	11.7 ± 2.1	494.063	12.6 ± 2.3
494.563	11.4 ± 2.1	495.063	12.3 ± 2.2	495.563	11.3 ± 2.1	496.063	10.5 ± 1.9
496.563	10.4 ± 1.9	497.063	11.0 ± 2.1	497.563	10.5 ± 1.9	498.063	10.0 ± 1.8
498.563	9.8 ± 1.8	499.063	9.7 ± 1.8	499.563	9.9 ± 1.8	500.063	10.2 ± 1.9
500.563	10.0 ± 1.8	501.063	9.9 ± 1.8	501.563	9.7 ± 1.8	502.063	9.9 ± 1.8
502.563	10.1 ± 1.9	503.063	9.7 ± 1.8	503.563	9.7 ± 1.8	504.063	10.0 ± 1.8
504.563	10.1 ± 1.8	505.063	10.2 ± 1.9	505.563	10.4 ± 1.9	506.063	10.0 ± 1.8
506.563	9.7 ± 1.8	507.063	10.1 ± 1.9	507.563	9.9 ± 1.8	508.063	9.9 ± 1.8

2. Cleaned-out frequency bins

TABLE III. Instrumental lines identified and “cleaned” before the Einstein@Home runs. The different columns represent: (I) the source of the line, (II) the central frequency of the instrumental line, (III) the number of harmonics; (IV) low-frequency-side (LFS) of the knockout band, (V) high-frequency-side (HFS) of the knockout band; (VI) the interferometer where the instrumental lines were identified. Note that when there are higher harmonics, the knockout band width remains constant.

Cause	f_L (Hz)	Harmonics	LFS (Hz)	HFS (Hz)	IFO
Mains	60	8	1	1	L,H
Wire	345	1	5	5	L
Wire	346	1	4	4	H
Electronic	85.8	1	0.01	0.01	H
Electronic	89.9	1	0.06	0.06	H
Electronic	93.29	1	0.015	0.015	L
Electronic	93.05	1	0.01	0.01	H
Electronic	93.25	1	0.01	0.01	H
Electronic	96.71	1	0.015	0.015	L
Electronic	139.94	1	0.02	0.02	L
Electronic	139.95	1	0.01	0.01	H

(Table continued)

RESULTS OF THE DEEPEST ALL-SKY SURVEY FOR ...

PHYSICAL REVIEW D **94**, 102002 (2016)

TABLE III. (Continued)

Cause	f_L (Hz)	Harmonics	LFS (Hz)	HFS (Hz)	IFO
Electronic	145.06	1	0.02	0.02	L
Electronic	164.52	1	0.01	0.01	H
Electronic	186.59	1	0.025	0.025	L
Electronic	193.42	1	0.025	0.025	L
Electronic	233.23	1	0.05	0.05	L
Electronic	241.78	1	0.07	0.07	L
Electronic	329.58	1	0.02	0.01	H
Electronic	329.86	1	0.01	0.02	H
Violin mode	329.32	1	0.11	0.11	L
Violin mode	329.70	1	0.3	0.3	H
Violin mode	335.53	1	0.28	0.28	L
CPU line	54.496	1	0.0006	0.0006	L,H
CPU line	108.992	1	0.0006	0.0006	L,H
Sideband comb	140.4100	1	0.0006	0.0006	H
Sideband comb	166.1205	1	0.0006	0.0006	H
Sideband comb	191.8322	1	0.0006	0.0006	H
Sideband comb	217.5428	1	0.0006	0.0006	H
Sideband comb	243.2539	1	0.0006	0.0006	H
Sideband comb	268.9650	1	0.0006	0.0006	H
Sideband comb	294.6756	1	0.0006	0.0006	H
Sideband comb	320.3867	1	0.0006	0.0006	H
Sideband comb	346.0972	1	0.0006	0.0006	H
Sideband comb	371.8077	1	0.0006	0.0006	H
Sideband comb	383.6639	1	0.0006	0.0006	H
Sideband comb	397.5194	1	0.0006	0.0006	H
Sideband comb	409.3705	1	0.0006	0.0006	H
Sideband comb	423.2306	1	0.0006	0.0006	H
Sideband comb	435.0861	1	0.0006	0.0006	H
Sideband comb	460.7967	1	0.0006	0.0006	H
Sideband comb	486.5078	1	0.0006	0.0006	H
1 Hz comb	1	2000	0.0006	0.0006	L,H
2 Hz comb	52	1	0.0006	0.0006	L,H
2 Hz comb	64	1	0.0006	0.0006	L,H
2 Hz comb	68	1	0.0006	0.0006	L,H
2 Hz comb	76	1	0.0006	0.0006	L,H
2 Hz comb	80	1	0.0006	0.0006	L,H
2 Hz comb	82	1	0.0006	0.0006	L,H
2 Hz comb	90	1	0.0006	0.0006	L,H
2 Hz comb	96	1	0.0006	0.0006	L,H
2 Hz comb	98	1	0.0006	0.0006	L,H
2 Hz comb	102	1	0.0006	0.0006	L,H
2 Hz comb	109	1	0.0006	0.0006	L,H
2 Hz comb	110	1	0.0006	0.0006	L,H
2 Hz comb	111	1	0.0006	0.0006	L,H
2 Hz comb	112	1	0.0006	0.0006	L,H
2 Hz comb	116	1	0.0006	0.0006	L,H
2 Hz comb	120	1	0.0006	0.0006	L,H
2 Hz comb	124	1	0.0006	0.0006	L,H
2 Hz comb	128	1	0.0006	0.0006	L,H
2 Hz comb	132	1	0.0006	0.0006	L,H
2 Hz comb	138	1	0.0006	0.0006	L,H
2 Hz comb	140	1	0.0006	0.0006	L,H
2 Hz comb	142	1	0.0006	0.0006	L,H
2 Hz comb	144	1	0.0006	0.0006	L,H
2 Hz comb	150	1	0.0006	0.0006	L,H

(Table continued)

B. P. ABBOTT *et al.*

PHYSICAL REVIEW D **94**, 102002 (2016)

TABLE III. (Continued)

Cause	f_L (Hz)	Harmonics	LFS (Hz)	HFS (Hz)	IFO
2 Hz comb	158	1	0.0006	0.0006	L,H
2 Hz comb	154	1	0.0006	0.0006	L,H
2 Hz comb	162	1	0.0006	0.0006	L,H
2 Hz comb	166	1	0.0006	0.0006	L,H
2 Hz comb	168	1	0.0006	0.0006	L,H
2 Hz comb	170	1	0.0006	0.0006	L,H
2 Hz comb	172	1	0.0006	0.0006	L,H
2 Hz comb	174	1	0.0006	0.0006	L,H
2 Hz comb	176	1	0.0006	0.0006	L,H
2 Hz comb	178	1	0.0006	0.0006	L,H
2 Hz comb	184	1	0.0006	0.0006	L,H
2 Hz comb	188	1	0.0006	0.0006	L,H
2 Hz comb	192	1	0.0006	0.0006	L,H
2 Hz comb	196	1	0.0006	0.0006	L,H
2 Hz comb	204	1	0.0006	0.0006	L,H
2 Hz comb	206	1	0.0006	0.0006	L,H
2 Hz comb	214	1	0.0006	0.0006	L,H
2 Hz comb	216	1	0.0006	0.0006	L,H
2 Hz comb	218	1	0.0006	0.0006	L,H
2 Hz comb	221	1	0.0006	0.0006	L,H
2 Hz comb	222	1	0.0006	0.0006	L,H
2 Hz comb	226	1	0.0006	0.0006	L,H
2 Hz comb	234	1	0.0006	0.0006	L,H
2 Hz comb	236	1	0.0006	0.0006	L,H
2 Hz comb	242	1	0.0006	0.0006	L,H
2 Hz comb	244	1	0.0006	0.0006	L,H
2 Hz comb	248	1	0.0006	0.0006	L,H
2 Hz comb	252	1	0.0006	0.0006	L,H
2 Hz comb	254	1	0.0006	0.0006	L,H
2 Hz comb	256	1	0.0006	0.0006	L,H
2 Hz comb	260	1	0.0006	0.0006	L,H
2 Hz comb	262	1	0.0006	0.0006	L,H
2 Hz comb	264	1	0.0006	0.0006	L,H
2 Hz comb	266	1	0.0006	0.0006	L,H
2 Hz comb	268	1	0.0006	0.0006	L,H
2 Hz comb	270	1	0.0006	0.0006	L,H
2 Hz comb	274	1	0.0006	0.0006	L,H
2 Hz comb	278	1	0.0006	0.0006	L,H
2 Hz comb	280	1	0.0006	0.0006	L,H
2 Hz comb	282	1	0.0006	0.0006	L,H
2 Hz comb	286	1	0.0006	0.0006	L,H
2 Hz comb	290	1	0.0006	0.0006	L,H
2 Hz comb	298	1	0.0006	0.0006	L,H
2 Hz comb	308	1	0.0006	0.0006	L,H
2 Hz comb	312	1	0.0006	0.0006	L,H
2 Hz comb	316	1	0.0006	0.0006	L,H
2 Hz comb	320	1	0.0006	0.0006	L,H
2 Hz comb	334	1	0.0006	0.0006	L,H
2 Hz comb	372	1	0.0006	0.0006	L,H
2 Hz comb	376	1	0.0006	0.0006	L,H
2 Hz comb	380	1	0.0006	0.0006	L,H
2 Hz comb	384	1	0.0006	0.0006	L,H
2 Hz comb	394	1	0.0006	0.0006	L,H
2 Hz comb	402	1	0.0006	0.0006	L,H
2 Hz comb	410	1	0.0006	0.0006	L,H

(Table continued)

RESULTS OF THE DEEPEST ALL-SKY SURVEY FOR ...

PHYSICAL REVIEW D **94**, 102002 (2016)

TABLE III. (Continued)

Cause	f_L (Hz)	Harmonics	LFS (Hz)	HFS (Hz)	IFO
2 Hz comb	414	1	0.0006	0.0006	L,H
2 Hz comb	418	1	0.0006	0.0006	L,H
2 Hz comb	422	1	0.0006	0.0006	L,H
2 Hz comb	430	1	0.0006	0.0006	L,H
2 Hz comb	432	1	0.0006	0.0006	L,H
2 Hz comb	435	1	0.0006	0.0006	L,H
2 Hz comb	440	1	0.0006	0.0006	L,H
2 Hz comb	448	1	0.0006	0.0006	L,H
2 Hz comb	462	1	0.0006	0.0006	L,H
2 Hz comb	466	1	0.0006	0.0006	L,H
2 Hz comb	468	1	0.0006	0.0006	L,H
2 Hz comb	470	1	0.0006	0.0006	L,H
2 Hz comb	474	1	0.0006	0.0006	L,H
2 Hz comb	482	1	0.0006	0.0006	L,H
2 Hz comb	488	1	0.0006	0.0006	L,H
2 Hz comb	496	1	0.0006	0.0006	L,H
2 Hz comb	500	1	0.0006	0.0006	L,H
2 Hz comb	504	1	0.0006	0.0006	L,H
2 Hz comb	508	1	0.0006	0.0006	L,H
Digital	55.8	1	0.05	0.05	H
Digital	56.875	1	0.005	0.005	H
Digital	58.625	1	0.005	0.005	H
Digital	69.	1	0.05	0.05	H
Digital	85.375	1	0.005	0.005	H
Digital	113.75	1	0.01	0.01	H
Digital	140.24	1	0.01	0.01	H
Digital	153.75	1	0.05	0.05	H
Digital	158.0	1	0.05	0.05	H
Digital	199.57	1	0.01	0.01	H
Digital	210.36	1	0.01	0.01	H
Digital	373.5	1	0.05	0.05	H
Digital	392.2	1	0.0006	0.0006	L,H
Digital	399.3	1	0.0006	0.0006	L
Digital	401.5	1	0.05	0.05	H

3. 50 mHz signal-frequency bands that did not contribute to results

TABLE IV. Signal frequency ranges where the results might have contributions from fake data. When the results are entirely due to artificial data, the band is listed in the “all fake data” column; bands where the results comprise contributions from both fake and real data are listed in the other three columns. The “mixed, left” and “mixed, right” columns are populated only when there is a matching “all fake data” entry, which highlights the same physical cause for the fake data, i.e., the cleaning. The “mixed, isolated” column lists isolated ranges of mixed data. The list of input data frequencies where the data was substituted with artificial noise are given in Table I.

Line type	Mixed, isolated		Mixed, left		All fake data		Mixed, right		Detector
1 Hz	50.9648	51.0352							L,H
1 Hz, 2 Hz	51.9647	52.0353							L,H
1 Hz	52.9646	53.0354							L,H
1 Hz	53.9645	54.0355							L,H
CPU	54.4605	54.5315							L,H
1 Hz	54.9644	55.0356							L,H
D			55.715	55.785	55.785	55.815	55.815	55.885	H
1 Hz	55.9643	56.0357							L,H

(Table continued)

B. P. ABBOTT *et al.*

PHYSICAL REVIEW D **94**, 102002 (2016)

TABLE IV. (Continued)

Line type	Mixed, isolated		Mixed, left		All fake data		Mixed, right		Detector
D	56.8348	56.9152							H
1 Hz	56.9642	57.0358							L,H
1 Hz	57.9641	58.0359							L,H
D	58.5847	58.6653							H
1 Hz, M			58.964	59.0348	59.0348	60.965	60.965	61.0362	L,H
1 Hz	61.9637	62.0363							L,H
1 Hz	62.9636	63.0364							L,H
1 Hz, 2 Hz	63.9635	64.0365							L,H
1 Hz	64.9634	65.0366							L,H
1 Hz	65.9633	66.0367							L,H
1 Hz	66.9632	67.0368							L,H
1 Hz, 2 Hz	67.9631	68.0369							L,H
1 Hz, D			68.9136	68.9864	68.9864	69.0136	69.0136	69.0864	H
1 Hz	68.963	69.037							L
1 Hz	69.9629	70.0371							L,H
1 Hz	70.9628	71.0372							L,H
1 Hz	71.9627	72.0373							L,H
1 Hz	72.9626	73.0374							L,H
1 Hz	73.9625	74.0375							L,H
1 Hz	74.9624	75.0376							L,H
1 Hz, 2 Hz	75.9623	76.0377							L,H
1 Hz	76.9622	77.0378							L,H
1 Hz	77.9621	78.0379							L,H
1 Hz	78.962	79.038							L,H
1 Hz, 2 Hz	79.9619	80.0381							L,H
1 Hz	80.9618	81.0382							L,H
1 Hz, 2 Hz	81.9617	82.0383							L,H
1 Hz	82.9616	83.0384							L,H
1 Hz	83.9615	84.0385							L,H
1 Hz	84.9614	85.0386							L,H
D	85.332	85.418							H
E	85.752	85.848							H
1 Hz	85.9613	86.0387							L,H
1 Hz	86.9612	87.0388							L,H
1 Hz	87.9611	88.0389							L,H
1 Hz	88.961	89.039							L,H
E			89.8016	89.8784	89.8784	89.9215	89.9215	89.9985	H
1 Hz, 2 Hz	89.9609	90.0391							L,H
1 Hz	90.9608	91.0392							L,H
1 Hz	91.9607	92.0393							L,H
1 Hz	92.9606	93.0394							L,H
E	93.0012	93.0988							H
E	93.2012	93.2988							H
E	93.2362	93.3438							L
1 Hz	93.9605	94.0395							L,H
1 Hz	94.9604	95.0396							L,H
1 Hz, 2 Hz	95.9603	96.0397							L,H
E	96.6559	96.7641							L
1 Hz	96.9602	97.0398							L,H
1 Hz, 2 Hz	97.9601	98.0399							L,H
1 Hz	98.96	99.04							L,H
1 Hz	99.9599	100.0401							L,H
1 Hz	100.9598	101.0402							L,H
1 Hz, 2 Hz	101.9597	102.0403							L,H
1 Hz	102.9596	103.0404							L,H

(Table continued)

RESULTS OF THE DEEPEST ALL-SKY SURVEY FOR ...

PHYSICAL REVIEW D **94**, 102002 (2016)

TABLE IV. (Continued)

Line type	Mixed, isolated		Mixed, left		All fake data		Mixed, right		Detector
1 Hz	103.9595	104.0405							L,H
1 Hz	104.9594	105.0406							L,H
1 Hz	105.9593	106.0407							L,H
1 Hz	106.9592	107.0408							L,H
1 Hz	107.9591	108.0409							L,H
CPU	108.951	109.033							L,H
1 Hz, 2 Hz	108.959	109.041							L,H
1 Hz, 2 Hz	109.9589	110.0411							L,H
1 Hz, 2 Hz	110.9588	111.0412							L,H
1 Hz, 2 Hz	111.9587	112.0413							L,H
1 Hz	112.9586	113.0414							L,H
D	113.6992	113.8008							H
1 Hz	113.9585	114.0415							L,H
1 Hz	114.9584	115.0416							L,H
1 Hz, 2 Hz	115.9583	116.0417							L,H
1 Hz	116.9582	117.0418							L,H
1 Hz	117.9581	118.0419							L,H
1 Hz, 2 Hz, M			118.958	119.0408	119.0408	120.959	120.959	121.0422	L,H
1 Hz	121.9577	122.0423							L,H
1 Hz	122.9576	123.0424							L,H
1 Hz, 2 Hz	123.9575	124.0425							L,H
1 Hz	124.9574	125.0426							L,H
1 Hz	125.9573	126.0427							L,H
1 Hz	126.9572	127.0428							L,H
1 Hz, 2 Hz	127.9571	128.0429							L,H
1 Hz	128.957	129.043							L,H
1 Hz	129.9569	130.0431							L,H
1 Hz	130.9568	131.0432							L,H
1 Hz, 2 Hz	131.9567	132.0433							L,H
1 Hz	132.9566	133.0434							L,H
1 Hz	133.9565	134.0435							L,H
1 Hz	134.9564	135.0436							L,H
1 Hz	135.9563	136.0437							L,H
1 Hz	136.9562	137.0438							L,H
1 Hz, 2 Hz	137.9561	138.0439							L,H
1 Hz	138.956	139.044							L,H
E	139.8765	140.0035							L
E	139.8965	140.0035							H
1 Hz, 2 Hz	139.9559	140.0441							L,H
D	140.1865	140.2935							H
SB	140.3659	140.4541							H
1 Hz	140.9558	141.0442							L,H
1 Hz, 2 Hz	141.9557	142.0443							L,H
1 Hz	142.9556	143.0444							L,H
1 Hz, 2 Hz	143.9555	144.0445							L,H
1 Hz	144.9554	145.0446							L,H
E	144.996	145.124							L
1 Hz	145.9553	146.0447							L,H
1 Hz	146.9552	147.0448							L,H
1 Hz	147.9551	148.0449							L,H
1 Hz	148.955	149.045							L,H
1 Hz, 2 Hz	149.9549	150.0451							L,H
1 Hz	150.9548	151.0452							L,H
1 Hz	151.9547	152.0453							L,H
1 Hz	152.9546	153.0454							L,H

(Table continued)

B. P. ABBOTT *et al.*

PHYSICAL REVIEW D **94**, 102002 (2016)

TABLE IV. (Continued)

Line type	Mixed, isolated		Mixed, left		All fake data		Mixed, right		Detector
D			153.6552	153.7448	153.7448	153.7552	153.7552	153.8448	H
1 Hz, 2 Hz	153.9545	154.0455							L,H
1 Hz	154.9544	155.0456							L,H
1 Hz	155.9543	156.0457							L,H
1 Hz	156.9542	157.0458							L,H
1 Hz, 2 Hz, D			157.9047	157.9953	157.9953	158.0047	158.0047	158.0953	H
1 Hz, 2 Hz	157.9541	158.0459							L
1 Hz	158.954	159.046							L,H
1 Hz	159.9539	160.0461							L,H
1 Hz	160.9538	161.0462							L,H
1 Hz, 2 Hz	161.9537	162.0463							L,H
1 Hz	162.9536	163.0464							L,H
1 Hz	163.9535	164.0465							L,H
E	164.4641	164.5759							H
1 Hz	164.9534	165.0466							L,H
1 Hz, 2 Hz	165.9533	166.0467							L,H
SB	166.0738	166.1672							H
1 Hz	166.9532	167.0468							L,H
1 Hz, 2 Hz	167.9531	168.0469							L,H
1 Hz	168.953	169.047							L,H
1 Hz, 2 Hz	169.9529	170.0471							L,H
1 Hz	170.9528	171.0472							L,H
1 Hz, 2 Hz	171.9527	172.0473							L,H
1 Hz	172.9526	173.0474							L,H
1 Hz, 2 Hz	173.9525	174.0475							L,H
1 Hz	174.9524	175.0476							L,H
1 Hz, 2 Hz	175.9523	176.0477							L,H
1 Hz	176.9522	177.0478							L,H
1 Hz, 2 Hz	177.9521	178.0479							L,H
1 Hz, M			178.952	179.0468	179.0468	180.953	180.953	181.0482	L,H
1 Hz	181.9517	182.0483							L,H
1 Hz	182.9516	183.0484							L,H
1 Hz, 2 Hz	183.9515	184.0485							L,H
1 Hz	184.9514	185.0486							L,H
1 Hz	185.9513	186.0487							L,H
E	186.5169	186.6631							L
1 Hz	186.9512	187.0488							L,H
1 Hz, 2 Hz	187.9511	188.0489							L,H
1 Hz	188.951	189.049							L,H
1 Hz	189.9509	190.0491							L,H
1 Hz	190.9508	191.0492							L,H
SB	191.783	191.8814							H
1 Hz, 2 Hz	191.9507	192.0493							L,H
1 Hz	192.9506	193.0494							L,H
E	193.3462	193.4938							L
1 Hz	193.9505	194.0495							L,H
1 Hz	194.9504	195.0496							L,H
1 Hz, 2 Hz	195.9503	196.0497							L,H
1 Hz	196.9502	197.0498							L,H
1 Hz	197.9501	198.0499							L,H
1 Hz	198.95	199.05							L,H
D	199.5106	199.6294							H
1 Hz	199.9499	200.0501							L,H
1 Hz	200.9498	201.0502							L,H
1 Hz	201.9497	202.0503							L,H

(Table continued)

RESULTS OF THE DEEPEST ALL-SKY SURVEY FOR ...

PHYSICAL REVIEW D **94**, 102002 (2016)

TABLE IV. (Continued)

Line type	Mixed, isolated		Mixed, left		All fake data		Mixed, right		Detector
1 Hz	202.9496	203.0504							L,H
1 Hz, 2 Hz	203.9495	204.0505							L,H
1 Hz	204.9494	205.0506							L,H
1 Hz, 2 Hz	205.9493	206.0507							L,H
1 Hz	206.9492	207.0508							L,H
1 Hz	207.9491	208.0509							L,H
1 Hz	208.949	209.051							L,H
1 Hz	209.9489	210.0511							L,H
D	210.2995	210.4205							H
1 Hz	210.9488	211.0512							L,H
1 Hz	211.9487	212.0513							L,H
1 Hz	212.9486	213.0514							L,H
1 Hz, 2 Hz	213.9485	214.0515							L,H
1 Hz	214.9484	215.0516							L,H
1 Hz, 2 Hz	215.9483	216.0517							L,H
1 Hz	216.9482	217.0518							L,H
SB	217.491	217.5946							H
1 Hz, 2 Hz	217.9481	218.0519							L,H
1 Hz	218.948	219.052							L,H
1 Hz	219.9479	220.0521							L,H
1 Hz, 2 Hz	220.9478	221.0522							L,H
1 Hz, 2 Hz	221.9477	222.0523							L,H
1 Hz	222.9476	223.0524							L,H
1 Hz	223.9475	224.0525							L,H
1 Hz	224.9474	225.0526							L,H
1 Hz, 2 Hz	225.9473	226.0527							L,H
1 Hz	226.9472	227.0528							L,H
1 Hz	227.9471	228.0529							L,H
1 Hz	228.947	229.053							L,H
1 Hz	229.9469	230.0531							L,H
1 Hz	230.9468	231.0532							L,H
1 Hz	231.9467	232.0533							L,H
1 Hz	232.9466	233.0534							L,H
E	233.1272	233.3328							L
1 Hz, 2 Hz	233.9465	234.0535							L,H
1 Hz	234.9464	235.0536							L,H
1 Hz, 2 Hz	235.9463	236.0537							L,H
1 Hz	236.9462	237.0538							L,H
1 Hz	237.9461	238.0539							L,H
1 Hz, M			238.946	239.0528	239.0528	240.947	240.947	241.0542	L,H
E			241.6564	241.7636	241.7636	241.7964	241.7964	241.9036	L
1 Hz, 2 Hz	241.9457	242.0543							L,H
1 Hz	242.9456	243.0544							L,H
SB	243.1995	243.3083							H
1 Hz, 2 Hz	243.9455	244.0545							L,H
1 Hz	244.9454	245.0546							L,H
1 Hz	245.9453	246.0547							L,H
1 Hz	246.9452	247.0548							L,H
1 Hz, 2 Hz	247.9451	248.0549							L,H
1 Hz	248.945	249.055							L,H
1 Hz	249.9449	250.0551							L,H
1 Hz	250.9448	251.0552							L,H
1 Hz, 2 Hz	251.9447	252.0553							L,H
1 Hz	252.9446	253.0554							L,H
1 Hz, 2 Hz	253.9445	254.0555							L,H

(Table continued)

B. P. ABBOTT *et al.*

PHYSICAL REVIEW D **94**, 102002 (2016)

TABLE IV. (Continued)

Line type	Mixed, isolated		Mixed, left		All fake data		Mixed, right		Detector
1 Hz	254.9444	255.0556							L,H
1 Hz, 2 Hz	255.9443	256.0557							L,H
1 Hz	256.9442	257.0558							L,H
1 Hz	257.9441	258.0559							L,H
1 Hz	258.944	259.056							L,H
1 Hz, 2 Hz	259.9439	260.0561							L,H
1 Hz	260.9438	261.0562							L,H
1 Hz, 2 Hz	261.9437	262.0563							L,H
1 Hz	262.9436	263.0564							L,H
1 Hz, 2 Hz	263.9435	264.0565							L,H
1 Hz	264.9434	265.0566							L,H
1 Hz, 2 Hz	265.9433	266.0567							L,H
1 Hz	266.9432	267.0568							L,H
1 Hz, 2 Hz	267.9431	268.0569							L,H
SB	268.908	269.022							H
1 Hz	268.943	269.057							L,H
1 Hz, 2 Hz	269.9429	270.0571							L,H
1 Hz	270.9428	271.0572							L,H
1 Hz	271.9427	272.0573							L,H
1 Hz	272.9426	273.0574							L,H
1 Hz, 2 Hz	273.9425	274.0575							L,H
1 Hz	274.9424	275.0576							L,H
1 Hz	275.9423	276.0577							L,H
1 Hz	276.9422	277.0578							L,H
1 Hz, 2 Hz	277.9421	278.0579							L,H
1 Hz	278.942	279.058							L,H
1 Hz, 2 Hz	279.9419	280.0581							L,H
1 Hz	280.9418	281.0582							L,H
1 Hz, 2 Hz	281.9417	282.0583							L,H
1 Hz	282.9416	283.0584							L,H
1 Hz	283.9415	284.0585							L,H
1 Hz	284.9414	285.0586							L,H
1 Hz, 2 Hz	285.9413	286.0587							L,H
1 Hz	286.9412	287.0588							L,H
1 Hz	287.9411	288.0589							L,H
1 Hz	288.941	289.059							L,H
1 Hz, 2 Hz	289.9409	290.0591							L,H
1 Hz	290.9408	291.0592							L,H
1 Hz	291.9407	292.0593							L,H
1 Hz	292.9406	293.0594							L,H
1 Hz	293.9405	294.0595							L,H
SB	294.6161	294.7351							H
1 Hz	294.9404	295.0596							L,H
1 Hz	295.9403	296.0597							L,H
1 Hz	296.9402	297.0598							L,H
1 Hz, 2 Hz	297.9401	298.0599							L,H
1 Hz, M			298.94	299.0588	299.0588	300.941	300.941	301.0602	L,H
1 Hz	301.9397	302.0603							L,H
1 Hz	302.9396	303.0604							L,H
1 Hz	303.9395	304.0605							L,H
1 Hz	304.9394	305.0606							L,H
1 Hz	305.9393	306.0607							L,H
1 Hz	306.9392	307.0608							L,H
1 Hz, 2 Hz	307.9391	308.0609							L,H
1 Hz	308.939	309.061							L,H

(Table continued)

RESULTS OF THE DEEPEST ALL-SKY SURVEY FOR ...

PHYSICAL REVIEW D **94**, 102002 (2016)

TABLE IV. (Continued)

Line type	Mixed, isolated		Mixed, left		All fake data		Mixed, right		Detector
1 Hz	309.9389	310.0611							L,H
1 Hz	310.9388	311.0612							L,H
1 Hz, 2 Hz	311.9387	312.0613							L,H
1 Hz	312.9386	313.0614							L,H
1 Hz	313.9385	314.0615							L,H
1 Hz	314.9384	315.0616							L,H
1 Hz, 2 Hz	315.9383	316.0617							L,H
1 Hz	316.9382	317.0618							L,H
1 Hz	317.9381	318.0619							L,H
1 Hz	318.938	319.062							L,H
1 Hz, 2 Hz	319.9379	320.0621							L,H
SB	320.3246	320.4488							H
1 Hz	320.9378	321.0622							L,H
1 Hz	321.9377	322.0623							L,H
1 Hz	322.9376	323.0624							L,H
1 Hz	323.9375	324.0625							L,H
1 Hz	324.9374	325.0626							L,H
1 Hz	325.9373	326.0627							L,H
1 Hz	326.9372	327.0628							L,H
1 Hz	327.9371	328.0629							L,H
1 Hz	328.937	329.063							L,H
VM			329.1476	329.2724	329.2724	329.3676	329.3676	329.4924	L
1 Hz, E, VM			329.3376	329.4624	329.4624	329.9381	329.9381	330.0631	H
1 Hz	329.9369	330.0631							L
1 Hz	330.9368	331.0632							L,H
1 Hz	331.9367	332.0633							L,H
1 Hz	332.9366	333.0634							L,H
1 Hz, 2 Hz	333.9365	334.0635							L,H
1 Hz	334.9364	335.0636							L,H
VM			335.187	335.313	335.313	335.747	335.747	335.873	L
1 Hz, VM			335.437	335.563	335.563	335.9375	335.9375	336.0637	H
1 Hz	335.9363	336.0637							L
1 Hz	336.9362	337.0638							L,H
1 Hz	337.9361	338.0639							L,H
1 Hz	338.936	339.064							L,H
1 Hz, VM			339.9359	340.0629	340.0629	349.9361	349.9361	350.0651	L
1 Hz	339.9359	340.0641							H
1 Hz	340.9358	341.0642							H
1 Hz, SB, VM			341.9357	342.0631	342.0631	349.9361	349.9361	350.0651	H
1 Hz	350.9348	351.0652							L,H
1 Hz	351.9347	352.0653							L,H
1 Hz	352.9346	353.0654							L,H
1 Hz	353.9345	354.0655							L,H
1 Hz	354.9344	355.0656							L,H
1 Hz	355.9343	356.0657							L,H
1 Hz	356.9342	357.0658							L,H
1 Hz	357.9341	358.0659							L,H
1 Hz, M			358.934	359.0648	359.0648	360.935	360.935	361.0662	L,H
1 Hz	361.9337	362.0663							L,H
1 Hz	362.9336	363.0664							L,H
1 Hz	363.9335	364.0665							L,H
1 Hz	364.9334	365.0666							L,H
1 Hz	365.9333	366.0667							L,H
1 Hz	366.9332	367.0668							L,H
1 Hz	367.9331	368.0669							L,H

(Table continued)

B. P. ABBOTT *et al.*

PHYSICAL REVIEW D **94**, 102002 (2016)

TABLE IV. (Continued)

Line type	Mixed, isolated	Mixed, left	All fake data	Mixed, right	Detector
1 Hz	368.933	369.067			L,H
1 Hz	369.9329	370.0671			L,H
1 Hz	370.9328	371.0672			L,H
SB	371.7405	371.8749			H
1 Hz, 2 Hz	371.9327	372.0673			L,H
1 Hz	372.9326	373.0674			L,H
D	373.3832	373.6168			H
1 Hz	373.9325	374.0675			L,H
1 Hz	374.9324	375.0676			L,H
1 Hz, 2 Hz	375.9323	376.0677			L,H
1 Hz	376.9322	377.0678			L,H
1 Hz	377.9321	378.0679			L,H
1 Hz	378.932	379.068			L,H
1 Hz, 2 Hz	379.9319	380.0681			L,H
1 Hz	380.9318	381.0682			L,H
1 Hz	381.9317	382.0683			L,H
1 Hz	382.9316	383.0684			L,H
SB	383.5955	383.7323			H
1 Hz, 2 Hz	383.9315	384.0685			L,H
1 Hz	384.9314	385.0686			L,H
1 Hz	385.9313	386.0687			L,H
1 Hz	386.9312	387.0688			L,H
1 Hz	387.9311	388.0689			L,H
1 Hz	388.931	389.069			L,H
1 Hz	389.9309	390.0691			L,H
1 Hz	390.9308	391.0692			L,H
1 Hz	391.9307	392.0693			L,H
D	392.1307	392.2693			L,H
1 Hz	392.9306	393.0694			L,H
1 Hz, 2 Hz	393.9305	394.0695			L,H
1 Hz	394.9304	395.0696			L,H
1 Hz	395.9303	396.0697			L,H
1 Hz	396.9302	397.0698			L,H
SB	397.4496	397.5892			H
1 Hz	397.9301	398.0699			L,H
1 Hz	398.93	399.07			L,H
D	399.23	399.37			L
1 Hz	399.9299	400.0701			L,H
1 Hz	400.9298	401.0702			L,H
D	401.3804	401.6196			H
1 Hz, 2 Hz	401.9297	402.0703			L,H
1 Hz	402.9296	403.0704			L,H
1 Hz	403.9295	404.0705			L,H
1 Hz	404.9294	405.0706			L,H
1 Hz	405.9293	406.0707			L,H
1 Hz	406.9292	407.0708			L,H
1 Hz	407.9291	408.0709			L,H
1 Hz	408.929	409.071			L,H
SB	409.2995	409.4415			H
1 Hz, 2 Hz	409.9289	410.0711			L,H
1 Hz	410.9288	411.0712			L,H
1 Hz	411.9287	412.0713			L,H
1 Hz	412.9286	413.0714			L,H
1 Hz, 2 Hz	413.9285	414.0715			L,H
1 Hz	414.9284	415.0716			L,H

(Table continued)

RESULTS OF THE DEEPEST ALL-SKY SURVEY FOR ...

PHYSICAL REVIEW D **94**, 102002 (2016)

TABLE IV. (Continued)

Line type	Mixed, isolated		Mixed, left		All fake data		Mixed, right		Detector
1 Hz	415.9283	416.0717							L,H
1 Hz	416.9282	417.0718							L,H
1 Hz, 2 Hz	417.9281	418.0719							L,H
1 Hz, M			418.928	419.0708	419.0708	420.929	420.929	421.0722	L,H
1 Hz, 2 Hz	421.9277	422.0723							L,H
1 Hz	422.9276	423.0724							L,H
SB	423.1582	423.303							H
1 Hz	423.9275	424.0725							L,H
1 Hz	424.9274	425.0726							L,H
1 Hz	425.9273	426.0727							L,H
1 Hz	426.9272	427.0728							L,H
1 Hz	427.9271	428.0729							L,H
1 Hz	428.927	429.073							L,H
1 Hz, 2 Hz	429.9269	430.0731							L,H
1 Hz	430.9268	431.0732							L,H
1 Hz, 2 Hz	431.9267	432.0733							L,H
1 Hz	432.9266	433.0734							L,H
1 Hz	433.9265	434.0735							L,H
1 Hz, 2 Hz	434.9264	435.0736							L,H
SB	435.0125	435.1597							H
1 Hz	435.9263	436.0737							L,H
1 Hz	436.9262	437.0738							L,H
1 Hz	437.9261	438.0739							L,H
1 Hz	438.926	439.074							L,H
1 Hz, 2 Hz	439.9259	440.0741							L,H
1 Hz	440.9258	441.0742							L,H
1 Hz	441.9257	442.0743							L,H
1 Hz	442.9256	443.0744							L,H
1 Hz	443.9255	444.0745							L,H
1 Hz	444.9254	445.0746							L,H
1 Hz	445.9253	446.0747							L,H
1 Hz	446.9252	447.0748							L,H
1 Hz, 2 Hz	447.9251	448.0749							L,H
1 Hz	448.925	449.075							L,H
1 Hz	449.9249	450.0751							L,H
1 Hz	450.9248	451.0752							L,H
1 Hz	451.9247	452.0753							L,H
1 Hz	452.9246	453.0754							L,H
1 Hz	453.9245	454.0755							L,H
1 Hz	454.9244	455.0756							L,H
1 Hz	455.9243	456.0757							L,H
1 Hz	456.9242	457.0758							L,H
1 Hz	457.9241	458.0759							L,H
1 Hz	458.924	459.076							L,H
1 Hz	459.9239	460.0761							L,H
SB	460.7206	460.8728							H
1 Hz	460.9238	461.0762							L,H
1 Hz, 2 Hz	461.9237	462.0763							L,H
1 Hz	462.9236	463.0764							L,H
1 Hz	463.9235	464.0765							L,H
1 Hz	464.9234	465.0766							L,H
1 Hz, 2 Hz	465.9233	466.0767							L,H
1 Hz	466.9232	467.0768							L,H
1 Hz, 2 Hz	467.9231	468.0769							L,H
1 Hz	468.923	469.077							L,H

(Table continued)

B. P. ABBOTT *et al.*

PHYSICAL REVIEW D **94**, 102002 (2016)

TABLE IV. (Continued)

Line type	Mixed, isolated		Mixed, left		All fake data		Mixed, right		Detector
1 Hz, 2 Hz	469.9229	470.0771							L,H
1 Hz	470.9228	471.0772							L,H
1 Hz	471.9227	472.0773							L,H
1 Hz	472.9226	473.0774							L,H
1 Hz, 2 Hz	473.9225	474.0775							L,H
1 Hz	474.9224	475.0776							L,H
1 Hz	475.9223	476.0777							L,H
1 Hz	476.9222	477.0778							L,H
1 Hz	477.9221	478.0779							L,H
1 Hz, M			478.922	479.0768	479.0768	480.923	480.923	481.0782	L,H
1 Hz, 2 Hz	481.9217	482.0783							L,H
1 Hz	482.9216	483.0784							L,H
1 Hz	483.9215	484.0785							L,H
1 Hz	484.9214	485.0786							L,H
1 Hz	485.9213	486.0787							L,H
SB	486.4291	486.5865							H
1 Hz	486.9212	487.0788							L,H
1 Hz, 2 Hz	487.9211	488.0789							L,H
1 Hz	488.921	489.079							L,H
1 Hz	489.9209	490.0791							L,H
1 Hz	490.9208	491.0792							L,H
1 Hz	491.9207	492.0793							L,H
1 Hz	492.9206	493.0794							L,H
1 Hz	493.9205	494.0795							L,H
1 Hz	494.9204	495.0796							L,H
1 Hz, 2 Hz	495.9203	496.0797							L,H
1 Hz	496.9202	497.0798							L,H
1 Hz	497.9201	498.0799							L,H
1 Hz	498.92	499.08							L,H
1 Hz, 2 Hz	499.9199	500.0801							L,H
1 Hz	500.9198	501.0802							L,H
1 Hz	501.9197	502.0803							L,H
1 Hz	502.9196	503.0804							L,H
1 Hz, 2 Hz	503.9195	504.0805							L,H
1 Hz	504.9194	505.0806							L,H
1 Hz	505.9193	506.0807							L,H
1 Hz	506.9192	507.0808							L,H
1 Hz, 2 Hz	507.9191	508.0809							L,H
1 Hz	508.919	509.081							L,H

RESULTS OF THE DEEPEST ALL-SKY SURVEY FOR ...

PHYSICAL REVIEW D **94**, 102002 (2016)

4. Signal-frequency ranges where the results might have contributions from fake data

TABLE V. 50-mHz search-frequency bands that were identified as disturbed based on visual inspection (D) or where the results were produced from entirely fake data as detailed in Table I (C). Both sets of bands (D and C) were excluded from the analysis. The first two columns list the first frequency of the first and last 50-mHz band in a contiguous range of excluded bands.

Start band	Stop band	Disturbance type
50.113		D
50.563		D
51.013		D
51.113	51.163	D
51.963		D
52.413	52.463	D
52.613		D
52.863	53.113	D
53.663		D
53.863	53.913	D
54.363	54.513	D
55.063	55.113	D
55.463	55.613	D
55.713	55.963	D
56.113	56.513	D
56.613		D
57.563		D
58.163		D
58.363	58.613	D
58.713	59.013	D
59.063		C
59.113		C D
59.163	60.863	C
60.913		C D
60.963	61.013	D
61.313	61.613	D
61.963		D
62.213	62.263	D
62.363		D
63.163	63.213	D
63.463	63.513	D
63.713		D
64.013	64.113	D
64.313	64.513	D
64.713	64.813	D
65.313	65.413	D
68.513		D
68.763	68.913	D
69.263		D
69.713	69.763	D
70.063	70.113	D
70.463	70.513	D
71.063		D
71.513		D
72.013	72.113	D
72.313	72.413	D
72.913	73.013	D

(Table continued)

TABLE V. (Continued)

Start band	Stop band	Disturbance type
73.313	73.413	D
73.763	73.863	D
74.463	74.513	D
74.713		D
75.763		D
76.013	76.113	D
77.563	77.663	D
78.213	78.313	D
78.413	78.563	D
78.963	79.013	D
79.263		D
79.913	80.063	D
80.413	80.463	D
80.563	80.663	D
80.913		D
81.013	81.213	D
83.463		D
83.863		D
85.413		D
85.563		D
85.713	85.813	D
85.963		D
86.513		D
86.713	86.813	D
87.763		D
88.513		D
88.963		D
89.963	90.013	D
90.563	90.713	D
91.513		D
92.113		D
93.063	93.113	D
93.913	94.013	D
94.213		D
96.663	97.163	D
98.263		D
98.863	99.063	D
99.713	99.763	D
99.863	100.013	D
100.213	100.263	D
100.463		D
102.163	102.263	D
102.663		D
103.013	103.113	D
103.413	103.463	D
104.863		D
105.663	105.713	D
106.413	106.663	D
107.013	107.213	D
107.313	107.413	D
107.663		D
108.013	108.063	D
108.813	109.113	D
109.413	109.513	D
109.963		D

(Table continued)

B. P. ABBOTT *et al.*

PHYSICAL REVIEW D **94**, 102002 (2016)

TABLE V. (Continued)

Start band	Stop band	Disturbance type
110.613		D
110.863	110.913	D
111.013	111.113	D
111.713	111.863	D
112.663	112.713	D
113.063		D
113.213	113.313	D
113.713	113.913	D
114.663	114.713	D
115.313	115.413	D
115.763		D
117.463	117.713	D
118.063		D
118.213	118.563	D
118.813	119.013	D
119.063	120.863	C
120.963	121.013	D
121.163	121.313	D
121.613	121.763	D
122.063	122.313	D
123.113		D
125.613	125.663	D
126.213	126.313	D
126.413		D
126.713	126.813	D
127.063		D
127.963	128.013	D
128.363		D
129.713	129.763	D
129.863	129.963	D
130.513		D
131.263		D
132.713	132.763	D
133.413		D
134.013	134.063	D
134.413	134.513	D
135.063	135.163	D
135.613	135.713	D
137.063	137.113	D
137.463	137.513	D
137.613	137.913	D
138.163		D
139.463	139.513	D
139.613	139.813	D
140.113	140.213	D
140.363	140.413	D
140.963		D
141.613	141.663	D
141.813	141.863	D
142.213	142.313	D
142.613	142.713	D
144.313	144.363	D
144.613	144.763	D
145.013	145.713	D
146.313	146.363	D

(Table continued)

TABLE V. (Continued)

Start band	Stop band	Disturbance type
146.663	146.813	D
146.913		D
147.113	147.163	D
147.713		D
148.763		D
149.113	149.213	D
149.563		D
149.963	150.013	D
150.863		D
151.263		D
152.063		D
153.163	153.313	D
153.413		D
153.613	153.713	D
153.863	153.913	D
154.213	154.263	D
155.263		D
155.763		D
156.113		D
156.213	156.263	D
156.363		D
156.513		D
156.813	156.863	D
157.363	157.413	D
157.763		D
158.163		D
158.363		D
160.213	160.313	D
161.413	161.513	D
162.313	162.363	D
162.913	162.963	D
163.463	163.513	D
168.063	168.113	D
169.613	169.713	D
170.813		D
173.713	173.813	D
174.163		D
178.513		D
178.963		D
179.063	180.863	C
180.963	181.013	D
181.363		D
181.813	181.863	D
182.763	182.813	D
184.363	184.463	D
185.363	185.413	D
187.963		D
188.463		D
189.363	189.413	D
189.813	189.863	D
190.763	190.813	D
192.363	192.613	D
193.613	194.313	D
196.963	197.013	D
197.713	197.763	D

(Table continued)

RESULTS OF THE DEEPEST ALL-SKY SURVEY FOR ...

PHYSICAL REVIEW D **94**, 102002 (2016)

TABLE V. (Continued)

Start band	Stop band	Disturbance type
197.863	197.963	D
198.113	198.163	D
198.563	198.663	D
199.213	199.313	D
199.513	199.613	D
199.813	200.013	D
200.413	200.513	D
200.913	201.013	D
201.313	201.363	D
203.663		D
204.113	204.213	D
204.863	204.913	D
205.663		D
205.863		D
206.413	206.663	D
209.213	209.263	D
210.213	210.313	D
215.513		D
217.463	217.563	D
217.913	218.013	D
223.563	223.613	D
225.513	225.563	D
229.363		D
229.813	229.913	D
230.213	230.313	D
231.313	231.413	D
234.113	234.163	D
239.063	240.863	C
241.613	241.713	D
241.813	241.863	D
242.113	242.163	D
242.313	242.863	D
246.513	246.563	D
249.963	250.013	D
253.063	253.113	D
255.063	255.113	D
257.063	257.113	D
257.263	257.363	D
259.063	259.113	D
270.163	270.213	D
270.613	270.663	D
272.413	272.513	D
275.213	275.563	D
279.763	279.813	D
280.313	280.363	D
280.813		D
281.913	282.013	D
289.363		D
290.963	291.013	D
291.213		D
291.313	291.413	D
299.063	300.863	C
306.463	306.563	D
308.463	308.513	D
324.013	324.063	D

(Table continued)

TABLE V. (Continued)

Start band	Stop band	Disturbance type
329.113	329.263	D
329.313		C
329.463	329.863	C
332.163	332.263	D
335.163	335.263	D
335.313	335.663	C
335.713		C D
335.763		C D
335.813		C D
335.863		C
338.613	338.863	D
339.013	339.213	D
339.463	340.013	D
340.063		C D
340.113	349.863	C
349.963	350.563	D
350.663	350.763	D
350.913	351.213	D
351.363	351.563	D
357.863	357.963	D
358.913	359.063	D
359.113	360.863	C
360.913	361.013	D
365.563	365.613	D
366.513	366.613	D
366.863		D
369.763	369.813	D
370.013	370.163	D
373.263	373.313	D
373.513	373.613	D
374.163		D
374.513	374.613	D
389.513	389.613	D
391.213	391.313	D
392.063	392.213	D
392.513	392.613	D
393.013	393.263	D
393.413	393.513	D
393.913		D
394.013	394.213	D
394.813	394.913	D
395.463	395.513	D
395.863		D
395.963	396.063	D
396.513	396.713	D
399.063	399.113	D
399.213	399.313	D
399.613	400.613	D
400.713	400.813	D
401.013	401.313	D
403.513	403.913	D
407.213	407.363	D
407.813	407.913	D
408.213	408.363	D
409.263	409.413	D

(Table continued)

B. P. ABBOTT *et al.*PHYSICAL REVIEW D **94**, 102002 (2016)

TABLE V. (Continued)

Start band	Stop band	Disturbance type
413.013	413.363	D
416.113	416.213	D
417.013	417.213	D
418.163	418.213	D
419.113	420.863	C
421.213		D

(Table continued)

TABLE V. (Continued)

Start band	Stop band	Disturbance type
430.313		D
444.413	444.513	D
448.913		D
451.413	451.663	D
472.563	472.663	D
474.563	474.613	D
479.113	480.863	C

- [1] <https://www.einsteinathome.org/>.
- [2] B. P. Abbott *et al.* (LIGO Scientific and Virgo Collaborations), Comprehensive all-sky search for periodic gravitational waves in the sixth science run LIGO data, *Phys. Rev. D* **94**, 042002 (2016).
- [3] A. Singh, M. A. Papa, H.-B. Eggenstein, S. Zhu, H. Pletsch, B. Allen, O. Bock, B. Maschenchalk, R. Prix, and X. Siemens, Results of an all-sky high-frequency Einstein@Home search for continuous gravitational waves in LIGO fifth science run, *Phys. Rev. D* **94**, 064061 (2016).
- [4] J. Aasi *et al.* (LIGO Scientific and Virgo Collaborations), First low frequency all-sky search for continuous gravitational wave signals, *Phys. Rev. D* **93**, 042007 (2016).
- [5] B. P. Abbott *et al.* (LIGO Scientific Collaboration), Einstein@Home all-sky search for periodic gravitational waves in LIGO S5 data, *Phys. Rev. D* **87**, 042001 (2013).
- [6] J. Abadie *et al.* (LIGO Scientific and Virgo Collaborations), All-sky search for periodic gravitational waves in the full S5 data, *Phys. Rev. D* **85**, 022001 (2012).
- [7] B. P. Abbott *et al.* (LIGO Scientific Collaboration), Einstein@Home search for periodic gravitational waves in early S5 LIGO data, *Phys. Rev. D* **80**, 042003 (2009).
- [8] B. P. Abbott *et al.* (LIGO Scientific Collaboration), All-sky LIGO search for periodic gravitational waves in the early S5 data, *Phys. Rev. Lett.* **102**, 111102 (2009).
- [9] B. Abbott *et al.* (LIGO Scientific Collaboration), All-sky search for periodic gravitational waves in LIGO S4 data, *Phys. Rev. D* **77**, 022001 (2008).
- [10] B. Abbott *et al.* (LIGO Scientific Collaboration), Einstein@Home search for periodic gravitational waves in LIGO S4 data, *Phys. Rev. D* **79**, 022001 (2009).
- [11] B. Abbott *et al.* (LIGO Scientific Collaboration), Searches for periodic gravitational waves from unknown isolated sources and Scorpius X-1: Results from the second LIGO science run, *Phys. Rev. D* **76**, 082001 (2007).
- [12] B. P. Abbott *et al.* (LIGO Scientific Collaboration), LIGO: The laser interferometer gravitational-wave observatory, *Rep. Prog. Phys.* **72**, 076901 (2009).
- [13] J. Abadie *et al.* (LIGO Scientific and Virgo Collaborations), Sensitivity achieved by the LIGO and Virgo gravitational wave detectors during LIGO's sixth and Virgo's second and third science runs, [arXiv:1203.2674](https://arxiv.org/abs/1203.2674).
- [14] J. Aasi *et al.* (LIGO Scientific Collaboration), Advanced LIGO, *Classical Quantum Gravity* **32**, 074001 (2015).
- [15] M. Shaltev, Optimizing the StackSlide setup and data selection for continuous-gravitational-wave searches in realistic detector data, *Phys. Rev. D* **93**, 044058, 2016.
- [16] J. Aasi *et al.* (LIGO Scientific and Virgo Collaborations), Characterization of the LIGO detectors during their sixth science run, *Classical Quantum Gravity* **32**, 115012 (2015).
- [17] H. J. Pletsch, Parameter-space correlations of the optimal statistic for continuous gravitational-wave detection, *Phys. Rev. D* **78**, 102005 (2008).
- [18] H. J. Pletsch, Parameter-space metric of semicoherent searches for continuous gravitational waves, *Phys. Rev. D* **82**, 042002 (2010).
- [19] C. Cutler and B. F. Schutz, The generalized \mathcal{F} -statistic: multiple detectors and multiple gravitational wave pulsars, *Phys. Rev. D* **72**, 063006 (2005).
- [20] J. Aasi *et al.* (LIGO Scientific and Virgo Collaborations), Directed search for continuous gravitational waves from the Galactic Center, *Phys. Rev. D* **88**, 102002 (2013).
- [21] D. Keitel, R. Prix, M. A. Papa, P. Leaci, and M. Siddiqi, Search for continuous gravitational waves: Improving robustness versus instrumental artifacts, *Phys. Rev. D* **89**, 064023 (2014).
- [22] B. Behnke, M. A. Papa, and R. Prix, Postprocessing methods used in the search for continuous gravitational-wave signals from the Galactic Center, *Phys. Rev. D* **91**, 064007 (2015).
- [23] Karl Wette, Estimating the sensitivity of wide-parameter-space searches for gravitational-wave pulsars, *Phys. Rev. D* **85**, 042003 (2012).
- [24] J. Ming, B. Krishnan, M. A. Papa, C. Aulbert, and H. Fehrmann, Optimal directed searches for continuous gravitational waves, *Phys. Rev. D* **93**, 064011 (2016).

RESULTS OF THE DEEPEST ALL-SKY SURVEY FOR ...

PHYSICAL REVIEW D **94**, 102002 (2016)

B. P. Abbott,¹ R. Abbott,¹ T. D. Abbott,² M. R. Abernathy,³ F. Acernese,^{4,5} K. Ackley,⁶ C. Adams,⁷ T. Adams,⁸ P. Addesso,⁹ R. X. Adhikari,¹ V. B. Adya,¹⁰ C. Affeldt,¹⁰ M. Agathos,¹¹ K. Agatsuma,¹¹ N. Aggarwal,¹² O. D. Aguiar,¹³ L. Aiello,^{14,15} A. Ain,¹⁶ B. Allen,^{10,18,19} A. Allocca,^{20,21} P. A. Altin,²² S. B. Anderson,¹ W. G. Anderson,¹⁸ K. Arai,¹ M. C. Araya,¹ C. C. Arceneaux,²³ J. S. Areeda,²⁴ N. Arnaud,²⁵ K. G. Arun,²⁶ S. Ascenzi,^{27,15} G. Ashton,²⁸ M. Ast,²⁹ S. M. Aston,⁷ P. Astone,³⁰ P. Aufmuth,¹⁹ C. Aulbert,¹⁰ S. Babak,³¹ P. Bacon,³² M. K. M. Bader,¹¹ P. T. Baker,³³ F. Baldaccini,^{34,35} G. Ballardin,³⁶ S. W. Ballmer,³⁷ J. C. Barayoga,¹ S. E. Barclay,³⁸ B. C. Barish,¹ D. Barker,³⁹ F. Barone,^{4,5} B. Barr,³⁸ L. Barsotti,¹² M. Barsuglia,³² D. Barta,⁴⁰ J. Bartlett,³⁹ I. Bartos,⁴¹ R. Bassiri,⁴² A. Basti,^{20,21} J. C. Batch,³⁹ C. Baune,¹⁰ V. Bavigadda,³⁶ M. Bazzan,^{43,44} M. Bejger,⁴⁵ A. S. Bell,³⁸ B. K. Berger,¹ G. Bergmann,¹⁰ C. P. L. Berry,⁴⁶ D. Bersanetti,^{47,48} A. Bertolini,¹¹ J. Betzwieser,⁷ S. Bhagwat,³⁷ R. Bhandare,⁴⁹ I. A. Bilenko,⁵⁰ G. Billingsley,¹ J. Birch,⁷ R. Birney,⁵¹ S. Biscans,¹² A. Bisht,^{10,19} M. Bitossi,³⁶ C. Biwer,³⁷ M. A. Bizouard,²⁵ J. K. Blackburn,¹ C. D. Blair,⁵² D. G. Blair,⁵² R. M. Blair,³⁹ S. Bloemen,⁵³ O. Bock,¹⁰ M. Boer,⁵⁴ G. Bogaert,⁵⁴ C. Bogan,¹⁰ A. Bohe,³¹ C. Bond,⁴⁶ F. Bondu,⁵⁵ R. Bonnand,⁸ B. A. Boom,¹¹ R. Bork,¹ V. Boschi,^{20,21} S. Bose,^{56,16} Y. Bouffanais,³² A. Bozzi,³⁶ C. Bradaschia,²¹ P. R. Brady,¹⁸ V. B. Braginsky,^{50,f} M. Branchesi,^{57,58} J. E. Brau,⁵⁹ T. Briant,⁶⁰ A. Brillet,⁶⁰ M. Brinkmann,¹⁰ V. Brisson,²⁵ P. Brockill,¹⁸ J. E. Broida,⁶¹ A. F. Brooks,¹ D. A. Brown,³⁷ D. D. Brown,⁴⁶ N. M. Brown,¹² S. Brunett,¹ C. C. Buchanan,² A. Buikema,¹² T. Bulik,⁶² H. J. Bulten,^{63,11} A. Buonanno,^{31,64} D. Buskulic,⁸ C. Buy,³² R. L. Byer,⁴² M. Cabero,¹⁰ L. Cadonati,⁶⁵ G. Cagnoli,^{66,67} C. Cahillane,¹ J. Calderón Bustillo,⁶⁵ T. Callister,¹ E. Calloni,^{68,5} J. B. Camp,⁶⁹ K. C. Cannon,⁷⁰ J. Cao,⁷¹ C. D. Capano,¹⁰ E. Capocasa,³² F. Carbognani,³⁶ S. Caride,⁷² J. Casanueva Diaz,²⁵ C. Casentini,^{27,15} S. Caudill,¹⁸ M. Cavaglia,²³ F. Cavalier,²⁵ R. Cavalieri,³⁶ G. Cella,²¹ C. B. Cepeda,¹ L. Cerboni Baiardi,^{57,58} G. Cerretani,^{20,21} E. Cesarini,^{27,15} S. J. Chamberlin,⁷³ M. Chan,³⁸ S. Chao,⁷⁴ P. Charlton,⁷⁵ E. Chassande-Mottin,³² B. D. Cheeseboro,⁷⁶ H. Y. Chen,⁷⁷ Y. Chen,⁷⁸ C. Cheng,⁷⁴ A. Chincarini,⁴⁸ A. Chiummo,³⁶ H. S. Cho,⁷⁹ M. Cho,⁶⁴ J. H. Chow,²² N. Christensen,⁶¹ Q. Chu,⁵² S. Chua,⁶⁰ S. Chung,⁵² G. Ciani,⁶ F. Clara,³⁹ J. A. Clark,⁶⁵ F. Cleva,⁵⁴ E. Coccia,^{27,14} P.-F. Cohadon,⁶⁰ A. Colla,^{80,30} C. G. Collette,⁸¹ L. Cominsky,⁸² M. Constancio Jr.,¹³ A. Conte,^{80,30} L. Conti,⁴⁴ D. Cook,³⁹ T. R. Corbitt,² N. Cornish,³³ A. Corsi,⁷² S. Cortese,³⁶ C. A. Costa,¹³ M. W. Coughlin,⁶¹ S. B. Coughlin,⁸³ J.-P. Coulon,⁵⁴ S. T. Countryman,⁴¹ P. Couvares,¹ E. E. Cowan,⁶⁵ D. M. Coward,⁵² M. J. Cowart,⁷ D. C. Coyne,¹ R. Coyne,⁷² K. Craig,³⁸ J. D. E. Creighton,¹⁸ T. D. Creighton,⁸⁸ J. Cripe,² S. G. Crowder,⁸⁴ A. Cumming,³⁸ L. Cunningham,³⁸ E. Cuoco,³⁶ T. Dal Canton,¹⁰ S. L. Danilishin,³⁸ S. D'Antonio,¹⁵ K. Danzmann,^{19,10} N. S. Darman,⁸⁵ A. Dasgupta,⁸⁶ C. F. Da Silva Costa,⁶ V. Dattilo,³⁶ I. Dave,⁴⁹ M. Davies,²⁵ G. S. Davies,³⁸ E. J. Daw,⁸⁷ R. Day,³⁶ S. De,³⁷ D. DeBra,⁴² G. Debreczeni,⁴⁰ J. Degallaix,⁶⁶ M. De Laurentis,^{68,5} S. Deléglise,⁶⁰ W. Del Pozzo,⁴⁶ T. Denker,¹⁰ T. Dent,¹⁰ V. Dergachev,¹ R. De Rosa,^{68,5} R. T. DeRosa,⁷ R. DeSalvo,⁹ R. C. Devine,⁷⁶ S. Dhurandhar,¹⁶ M. C. Díaz,⁸⁸ L. Di Fiore,⁵ M. Di Giovanni,^{89,90} T. Di Girolamo,^{68,5} A. Di Lieto,^{20,21} S. Di Pace,^{80,30} I. Di Palma,^{31,80,30} A. Di Virgilio,²¹ V. Dolique,⁶⁶ F. Donovan,¹² K. L. Dooley,²³ S. Doravari,¹⁰ R. Douglas,³⁸ T. P. Downes,¹⁸ M. Drago,¹⁰ R. W. P. Drever,¹ J. C. Driggers,³⁹ M. Ducrot,⁸ S. E. Dwyer,³⁹ T. B. Edo,⁸⁷ M. C. Edwards,⁶¹ A. Effler,⁷ H.-B. Eggenstein,¹⁰ P. Ehrens,¹ J. Eichholz,⁶¹ S. S. Eikenberry,⁶ W. Engels,⁷⁸ R. C. Essick,¹² T. Etzel,¹ M. Evans,¹² T. M. Evans,⁷ R. Everett,⁷³ M. Factourovich,⁴¹ V. Fafone,^{27,15} H. Fair,³⁷ S. Fairhurst,⁹¹ X. Fan,⁷¹ Q. Fang,⁵² S. Farinon,⁴⁸ B. Farr,⁷⁷ W. M. Farr,⁴⁶ M. Favata,⁹² M. Fays,⁹¹ H. Fehrmann,¹⁰ M. M. Fejer,⁴² E. Fenyvesi,⁹³ I. Ferrante,^{20,21} E. C. Ferreira,¹³ F. Ferrini,³⁶ F. Fidecaro,^{20,21} I. Fiori,³⁶ D. Fiorucci,³² R. P. Fisher,³⁷ R. Flaminio,^{66,94} M. Fletcher,³⁸ J.-D. Fournier,⁵⁴ S. Frasca,^{80,30} F. Frasconi,²¹ Z. Frei,⁹³ A. Freise,⁴⁶ R. Frey,⁵⁹ V. Frey,²⁵ P. Fritschel,¹² V. V. Frolov,⁷ P. Fulda,⁶ M. Fyffe,⁷ H. A. G. Gabbard,²³ J. R. Gair,⁹⁵ L. Gammaitoni,³⁴ S. G. Gaonkar,¹⁶ F. Garufi,^{68,5} G. Gaur,^{96,86} N. Gehrels,⁶⁹ G. Gemme,⁴⁸ P. Geng,⁸⁸ E. Genin,³⁶ A. Gennai,²¹ J. George,⁴⁹ L. Gergely,⁹⁷ V. Germain,⁸ Abhirup Ghosh,¹⁷ Archisman Ghosh,¹⁷ S. Ghosh,^{53,11} J. A. Giaime,^{2,7} K. D. Giardino,⁷ A. Giazotto,²¹ K. Gill,⁹⁸ A. Glaefke,³⁸ E. Goetz,³⁹ R. Goetz,⁶ L. Gondan,⁹³ G. González,² J. M. Gonzalez Castro,^{20,21} A. Gopakumar,⁹⁹ N. A. Gordon,³⁸ M. L. Gorodetsky,⁵⁰ S. E. Gossan,¹ M. Gosselin,³⁶ R. Gouaty,⁸ A. Grado,^{100,5} C. Graef,³⁸ P. B. Graff,⁶⁴ M. Granata,⁶⁶ A. Grant,³⁸ S. Gras,¹² C. Gray,³⁹ G. Greco,^{57,58} A. C. Green,⁴⁶ P. Groot,⁵³ H. Grote,¹⁰ S. Grunewald,³¹ G. M. Guidi,^{57,58} X. Guo,⁷¹ A. Gupta,¹⁶ M. K. Gupta,⁸⁶ K. E. Gushwa,¹ E. K. Gustafson,¹ R. Gustafson,¹⁰¹ J. J. Hacker,²⁴ B. R. Hall,⁵⁶ E. D. Hall,¹ G. Hammond,³⁸ M. Haney,⁹⁹ M. M. Hanke,¹⁰ J. Hanks,³⁹ C. Hanna,⁷³ J. Hanson,⁷ T. Hardwick,² J. Harms,^{57,58} G. M. Harry,³ I. W. Harry,³¹ M. J. Hart,³⁸ M. T. Hartman,⁶ C.-J. Haster,⁴⁶ K. Haughian,³⁸ A. Heidmann,⁶⁰ M. C. Heintze,⁷ H. Heitmann,⁵⁴ P. Hello,²⁵ G. Hemming,³⁶ M. Hendry,³⁸ I. S. Heng,³⁸ J. Hennig,³⁸ J. Henry,¹⁰² A. W. Heptonstall,¹ M. Heurs,^{10,19} S. Hild,³⁸ D. Hoak,³⁶ D. Hofman,⁶⁶ K. Holt,⁷ D. E. Holz,⁷⁷ P. Hopkins,⁹¹ J. Hough,³⁸ E. A. Houston,³⁸ E. J. Howell,⁵² Y. M. Hu,¹⁰ S. Huang,⁷⁴ E. A. Huerta,¹⁰³ D. Huet,²⁵ B. Hughey,⁹⁸ S. Husa,¹⁰⁴ S. H. Huttner,³⁸ T. Huynh-Dinh,⁷ N. Indik,¹⁰ D. R. Ingram,³⁹ R. Inta,⁷² H. N. Isa,³⁸ J.-M. Isac,⁶⁰

102002-29

B. P. ABBOTT *et al.*PHYSICAL REVIEW D **94**, 102002 (2016)

M. Isi,¹ T. Isogai,¹² B. R. Iyer,¹⁷ K. Izumi,³⁹ T. Jacqmin,⁶⁰ H. Jang,⁷⁹ K. Jani,⁶⁵ P. Jaranowski,¹⁰⁵ S. Jawahar,¹⁰⁶ L. Jian,⁵² F. Jiménez-Forteza,¹⁰⁴ W. W. Johnson,² D. I. Jones,²⁸ R. Jones,³⁸ R. J. G. Jonker,¹¹ L. Ju,⁵² Haris K,¹⁰⁷ C. V. Kalaghatgi,⁹¹ V. Kalogera,⁸³ S. Kandhasamy,²³ G. Kang,⁷⁹ J. B. Kanner,¹ S. J. Kapadia,¹⁰ S. Karki,⁵⁹ K. S. Karvinen,¹⁰ M. Kasprzack,^{36,2} E. Katsavounidis,¹² W. Katzman,⁷ S. Kaufer,¹⁹ T. Kaur,⁵² K. Kawabe,³⁹ F. Kéfélian,⁵⁴ M. S. Kehl,¹⁰⁸ D. Keitel,¹⁰⁴ D. B. Kelley,³⁷ W. Kells,¹ R. Kennedy,⁸⁷ J. S. Key,⁸⁸ F. Y. Khalili,⁵⁰ I. Khan,¹⁴ S. Khan,⁹¹ Z. Khan,⁸⁶ E. A. Khazanov,¹⁰⁹ N. Kijbunchoo,³⁹ Chi-Woong Kim,⁷⁹ Chunglee Kim,⁷⁹ J. Kim,¹¹⁰ K. Kim,¹¹¹ N. Kim,⁴² W. Kim,¹¹² Y.-M. Kim,¹¹⁰ S. J. Kimbrell,⁶⁵ E. J. King,¹¹² P. J. King,³⁹ J. S. Kissel,³⁹ B. Klein,⁸³ L. Kleybolte,²⁹ S. Klimenko,⁶ S. M. Koehlenbeck,¹⁰ S. Koley,¹¹ V. Kondrashov,¹ A. Kontos,¹² M. Korobko,²⁹ W. Z. Korth,¹ I. Kowalska,⁶² D. B. Kozak,¹ V. Kringel,¹⁰ B. Krishnan,¹⁰ A. Królak,^{113,114} C. Krueger,¹⁹ G. Kuehn,¹⁰ P. Kumar,¹⁰⁸ R. Kumar,⁸⁶ L. Kuo,⁷⁴ A. Kutynia,¹¹³ B. D. Lackey,³⁷ M. Landry,³⁹ J. Lange,¹⁰² B. Lantz,⁴² P. D. Lasky,¹¹⁵ M. Laxen,⁷ C. Lazzaro,⁴⁴ P. Leaci,^{80,30} S. Leavey,³⁸ E. O. Lebigot,^{32,71} C. H. Lee,¹¹⁰ H. K. Lee,¹¹¹ H. M. Lee,¹¹⁶ K. Lee,³⁸ A. Lenon,³⁷ M. Leonardi,^{89,90} J. R. Leong,¹⁰ N. Leroy,²⁵ N. Letendre,⁸ Y. Levin,¹¹⁵ J. B. Lewis,¹ T. G. F. Li,¹¹⁷ A. Libson,¹² T. B. Littenberg,¹¹⁸ N. A. Lockerbie,¹⁰⁶ A. L. Lombardi,¹¹⁹ L. T. London,⁹¹ J. E. Lord,³⁷ M. Lorenzini,^{14,15} V. Lorette,¹²⁰ M. Lormand,⁷ G. Losurdo,⁵⁸ J. D. Lough,^{10,19} H. Lück,^{19,10} A. P. Lundgren,¹⁰ R. Lynch,¹² Y. Ma,⁵² B. Machenschalk,¹⁰ M. MacInnis,¹² D. M. Macleod,² F. Magaña-Sandoval,³⁷ L. Magaña Zertuche,³⁷ R. M. Magee,⁵⁶ E. Majorana,³⁰ I. Maksimovic,¹²⁰ V. Malvezzi,^{27,15} N. Man,⁵⁴ V. Mandic,⁸⁴ V. Mangano,³⁸ G. L. Mansell,²² M. Manske,¹⁸ M. Mantovani,³⁶ F. Marchesoni,^{121,35} F. Marion,⁸ S. Márka,⁴¹ Z. Márka,⁴¹ A. S. Markosyan,⁴² E. Maros,¹ F. Martelli,^{57,58} L. Martellini,⁵⁴ I. W. Martin,³⁸ D. V. Martynov,¹² J. N. Marx,¹ K. Mason,¹² A. Masserot,⁸ T. J. Massinger,³⁷ M. Masso-Reid,³⁸ S. Mastrogiovanni,^{80,30} F. Matichard,¹² L. Matone,⁴¹ N. Mavalvala,¹² N. Mazumder,⁵⁶ R. McCarthy,³⁹ D. E. McClelland,²² S. McCormick,⁷ S. C. McGuire,¹²² G. McIntyre,¹ J. McIver,¹ D. J. McManus,²² T. McRae,²² S. T. McWilliams,⁷⁶ D. Meacher,⁷³ G. D. Meadors,^{31,10} J. Meidam,¹¹ A. Melatos,⁸⁵ G. Mendell,³⁹ R. A. Mercer,¹⁸ E. L. Merilh,³⁹ M. Merzougui,⁵⁴ S. Meshkov,¹ C. Messenger,³⁸ C. Messick,⁷³ R. Metzdrorf,⁶⁰ P. M. Meyers,⁸⁴ F. Mezzani,^{30,80} H. Miao,⁴⁶ C. Michel,⁶⁶ H. Middleton,⁴⁶ E. E. Mikhailov,¹²³ L. Milano,^{68,5} A. L. Miller,^{6,80,30} A. Miller,⁸³ B. B. Miller,⁸³ J. Miller,¹² M. Millhouse,³³ Y. Minenkov,¹⁵ J. Ming,³¹ S. Mirshekari,¹²⁴ C. Mishra,¹⁷ S. Mitra,¹⁶ V. P. Mitrofanov,⁵⁰ G. Mitselmakher,⁶ R. Mittleman,¹² A. Moggi,²¹ M. Mohan,³⁶ S. R. P. Mohapatra,¹² M. Montani,^{57,58} B. C. Moore,⁹² C. J. Moore,¹²⁵ D. Moraru,³⁹ G. Moreno,³⁹ S. R. Morris,⁸⁸ K. Mossavi,¹⁰ B. Mours,⁸ C. M. Mow-Lowry,⁴⁶ G. Mueller,⁶ A. W. Muir,⁹¹ Arunava Mukherjee,¹⁷ D. Mukherjee,¹⁸ S. Mukherjee,⁸⁸ N. Mukund,¹⁶ A. Mullavey,⁷ J. Munch,¹¹² D. J. Murphy,⁴¹ P. G. Murray,³⁸ A. Mytidis,⁶ I. Nardecchia,^{27,15} L. Naticchioni,^{80,30} R. K. Nayak,¹²⁶ K. Nedkova,¹¹⁹ G. Nelemans,^{53,11} T. J. N. Nelson,⁷ M. Neri,^{47,48} A. Neunzert,¹⁰¹ G. Newton,³⁸ T. T. Nguyen,²² A. B. Nielsen,¹⁰ S. Nissanke,^{53,11} A. Nitz,¹⁰ F. Nocera,³⁶ D. Nolting,⁷ M. E. N. Normandin,⁸⁸ L. K. Nuttall,³⁷ J. Oberling,³⁹ E. Ochsner,¹⁸ J. O'Dell,¹²⁷ E. Oelker,¹² G. H. Ogin,¹²⁸ J. J. Oh,¹²⁹ S. H. Oh,¹²⁹ F. Ohme,⁷ M. Oliver,¹⁰⁴ P. Oppermann,¹⁰ Richard J. Oram,⁷ B. O'Reilly,⁷ R. O'Shaughnessy,¹⁰² D. J. Ottaway,¹¹² H. Overmier,⁷ B. J. Owen,⁷² A. Pai,¹⁰⁷ S. A. Pai,⁴⁹ J. R. Palamos,⁵⁹ O. Palashov,¹⁰⁹ C. Palomba,³⁰ A. Pal-Singh,²⁹ H. Pan,⁷⁴ C. Pankow,⁸³ F. Pannarale,⁹¹ B. C. Pant,⁴⁹ F. Paoletti,^{36,21} A. Paoli,³⁶ M. A. Papa,^{31,18,10} H. R. Paris,⁴² W. Parker,⁷ D. Pascucci,³⁸ A. Pasqualetti,³⁶ R. Passaquietti,^{20,21} D. Passuello,²¹ B. Patricelli,^{20,21} Z. Patrick,⁴² B. L. Pearlstone,³⁸ M. Pedraza,¹ R. Pedurand,^{66,130} L. Pekowsky,³⁷ A. Pele,⁷ S. Penn,¹³¹ A. Perreca,¹ L. M. Perri,⁸³ M. Phelps,³⁸ O. J. Piccinni,^{80,30} M. Pichot,⁵⁴ F. Piergiovanni,^{57,58} V. Pierro,⁹ G. Pillant,³⁶ L. Pinard,⁶⁶ I. M. Pinto,⁹ M. Pitkin,³⁸ M. Poe,¹⁸ R. Poggiani,^{20,21} P. Popolizio,³⁶ A. Post,¹⁰ J. Powell,³⁸ J. Prasad,¹⁶ V. Predoi,⁹¹ T. Prestegard,⁸⁴ L. R. Price,¹ M. Prijatelj,^{10,36} M. Principe,⁹ S. Privitera,³¹ R. Prix,¹⁰ G. A. Prodi,^{89,90} L. Prokhorov,⁵⁰ O. Puncken,¹⁰ M. Punturo,³⁵ P. Puppo,³⁰ M. Pürner,³¹ H. Qi,¹⁸ J. Qin,⁵² S. Qiu,¹¹⁵ V. Quetschke,⁸⁸ E. A. Quintero,¹ R. Quitzow-James,⁵⁹ F. J. Raab,³⁹ D. S. Rabeling,²² H. Radkins,³⁹ P. Raffai,⁹³ S. Raja,⁴⁹ C. Rajan,⁴⁹ M. Rakhmanov,⁸⁸ P. Rapagnani,^{80,30} V. Raymond,³¹ M. Razzano,^{20,21} V. Re,²⁷ J. Read,²⁴ C. M. Reed,³⁹ T. Regimbau,⁵⁴ L. Rei,⁴⁸ S. Reid,⁵¹ D. H. Reitze,^{1,6} H. Rew,¹²³ S. D. Reyes,³⁷ F. Ricci,^{80,30} K. Riles,¹⁰¹ M. Rizzo,¹⁰² N. A. Robertson,^{1,38} R. Robie,³⁸ F. Robinet,²⁵ A. Rocchi,¹⁵ L. Rolland,⁸ J. G. Rollins,¹ V. J. Roma,⁵⁹ R. Romano,^{4,5} G. Romanov,¹²³ J. H. Romie,⁷ D. Rosińska,^{132,45} S. Rowan,³⁸ A. Rüdiger,¹⁰ P. Ruggi,³⁶ K. Ryan,³⁹ S. Sachdev,¹ T. Sadecki,³⁹ L. Sadeghian,¹⁸ M. Sakellariadou,¹³³ L. Salconi,³⁶ M. Saleem,¹⁰⁷ F. Salemi,¹⁰ A. Samajdar,¹²⁶ L. Sammut,¹¹⁵ E. J. Sanchez,¹ V. Sandberg,³⁹ B. Sandeen,⁸³ J. R. Sanders,³⁷ B. Sassolas,⁶⁶ P. R. Saulson,³⁷ O. E. S. Sauter,¹⁰¹ R. L. Savage,³⁹ A. Sawadsky,¹⁹ P. Schale,⁵⁹ R. Schilling,^{10,†} J. Schmidt,¹⁰ P. Schmidt,^{1,78} R. Schnabel,²⁹ R. M. S. Schofield,⁵⁹ A. Schönbeck,²⁹ E. Schreiber,¹⁰ D. Schuette,^{10,19} B. F. Schutz,^{91,31} J. Scott,³⁸ S. M. Scott,²² D. Sellers,⁷ A. S. Sengupta,⁹⁶ D. Sentenac,³⁶ V. Sequino,^{27,15} A. Sergeev,¹⁰⁹ Y. Setyawati,^{53,11} D. A. Shaddock,²² T. Shaffer,³⁹ M. S. Shahriar,⁸³ M. Shaltev,¹⁰ B. Shapiro,⁴² P. Shawhan,⁶⁴ A. Sheperd,¹⁸ D. H. Shoemaker,¹² D. M. Shoemaker,⁶⁵

RESULTS OF THE DEEPEST ALL-SKY SURVEY FOR ...

PHYSICAL REVIEW D **94**, 102002 (2016)

K. Siellez,⁶⁵ X. Siemens,¹⁸ M. Sieniawska,⁴⁵ D. Sigg,³⁹ A. D. Silva,¹³ A. Singer,¹ L. P. Singer,⁶⁹ A. Singh,^{31,10,19} R. Singh,² A. Singhal,¹⁴ A. M. Sintes,¹⁰⁴ B. J. J. Slagmolen,²² J. R. Smith,²⁴ N. D. Smith,¹ R. J. E. Smith,¹ E. J. Son,¹²⁹ B. Sorazu,³⁸ F. Sorrentino,⁴⁸ T. Souradeep,¹⁶ A. K. Srivastava,⁸⁶ A. Staley,⁴¹ M. Steinke,¹⁰ J. Steinlechner,³⁸ S. Steinlechner,³⁸ D. Steinmeyer,^{10,19} B. C. Stephens,¹⁸ R. Stone,⁸⁸ K. A. Strain,³⁸ N. Straniero,⁶⁶ G. Stratta,^{57,58} N. A. Strauss,⁶¹ S. Strigin,⁵⁰ R. Sturani,¹²⁴ A. L. Stuver,⁷ T. Z. Summerscales,¹³⁴ L. Sun,⁸⁵ S. Sunil,⁸⁶ P. J. Sutton,⁹¹ B. L. Swinkels,³⁶ M. J. Szczepańczyk,⁹⁸ M. Tacca,³² D. Talukder,⁵⁹ D. B. Tanner,⁶ M. Tápai,⁹⁷ S. P. Tarabrin,¹⁰ A. Taracchini,³¹ R. Taylor,¹ T. Theeg,¹⁰ M. P. Thirugnanasambandam,¹ E. G. Thomas,⁴⁶ M. Thomas,⁴⁶ P. Thomas,³⁹ K. A. Thorne,⁷ E. Thrane,¹¹⁵ S. Tiwari,^{14,90} V. Tiwari,⁹¹ K. V. Tokmakov,¹⁰⁶ K. Toland,³⁸ C. Tomlinson,⁸⁷ M. Tonelli,^{20,21} Z. Tornasi,³⁸ C. V. Torres,^{88,†} C. I. Torrie,¹ D. Töyrä,⁴⁶ F. Traverso,^{34,35} G. Traylor,⁷ D. Trifirò,²³ M. C. Tringali,^{89,90} L. Trozzo,^{135,21} M. Tse,¹² M. Turconi,⁵⁴ D. Tuyenbayev,⁸⁸ D. Ugolini,¹³⁶ C. S. Unnikrishnan,⁹⁹ A. L. Urban,¹⁸ S. A. Usman,³⁷ H. Vahlbruch,¹⁹ G. Vajente,¹ G. Valdes,⁸⁸ N. van Bakel,¹¹ M. van Beuzekom,¹¹ J. F. J. van den Brand,^{63,11} C. Van Den Broeck,¹¹ D. C. VanderHyde,³⁷ L. van der Schaaf,¹¹ J. V. van Heijningen,¹¹ A. A. van Veggel,³⁸ M. Vardaro,^{43,44} S. Vass,¹ M. Vasúth,⁴⁰ R. Vaulin,¹² A. Vecchio,⁴⁶ G. Vedovato,⁴⁴ J. Veitch,⁴⁶ P. J. Veitch,¹¹² K. Venkateswara,¹³⁷ D. Verkint,⁸ F. Vetrano,^{57,58} A. Viceré,^{57,58} S. Vinciguerra,⁴⁶ D. J. Vine,⁵¹ J.-Y. Vinet,⁵⁴ S. Vitale,¹² T. Vo,³⁷ H. Vocca,^{34,35} C. Vorvick,³⁹ D. V. Voss,⁶ W. D. Voudsen,⁴⁶ S. P. Vyatchanin,⁵⁰ A. R. Wade,²² L. E. Wade,¹³⁸ M. Wade,¹³⁸ M. Walker,² L. Wallace,¹ S. Walsh,^{31,10} G. Wang,^{14,58} H. Wang,⁴⁶ M. Wang,⁴⁶ X. Wang,⁷¹ Y. Wang,⁵² R. L. Ward,²² J. Warner,³⁹ M. Was,⁸ B. Weaver,³⁹ L.-W. Wei,⁵⁴ M. Weinert,¹⁰ A. J. Weinstein,¹ R. Weiss,¹² L. Wen,⁵² P. Weßels,¹⁰ T. Westphal,¹⁰ K. Wette,¹⁰ J. T. Whelan,¹⁰² B. F. Whiting,⁶ R. D. Williams,¹ A. R. Williamson,⁹¹ J. L. Willis,¹³⁹ B. Willke,^{19,10} M. H. Wimmer,^{10,19} W. Winkler,¹⁰ C. C. Wipf,¹ H. Wittel,^{10,19} G. Woan,³⁸ J. Woehler,¹⁰ J. Worden,³⁹ J. L. Wright,³⁸ D. S. Wu,¹⁰ G. Wu,⁷ J. Yablon,⁸³ W. Yam,¹² H. Yamamoto,¹ C. C. Yancey,⁶⁴ H. Yu,¹² M. Yvert,⁸ A. Zadrożny,¹¹³ L. Zangrando,⁴⁴ M. Zanolin,⁹⁸ J.-P. Zendri,⁴⁴ M. Zevin,⁸³ L. Zhang,¹²³ M. Zhang,¹⁰² Y. Zhang,¹⁰² C. Zhao,⁵² M. Zhou,⁸³ Z. Zhou,⁸³ S. J. Zhu,^{31,10} X. Zhu,⁵² M. E. Zucker,^{1,12} S. E. Zuraw,¹¹⁹ and J. Zweizig¹

(LIGO Scientific Collaboration and Virgo Collaboration)

¹LIGO, California Institute of Technology, Pasadena, California 91125, USA²Louisiana State University, Baton Rouge, Louisiana 70803, USA³American University, Washington, D.C. 20016, USA⁴Università di Salerno, Fisciano, I-84084 Salerno, Italy⁵INFN, Sezione di Napoli, Complesso Universitario di Monte S. Angelo, I-80126 Napoli, Italy⁶University of Florida, Gainesville, Florida 32611, USA⁷LIGO Livingston Observatory, Livingston, Louisiana 70754, USA⁸Laboratoire d'Annecy-le-Vieux de Physique des Particules (LAPP), Université Savoie Mont Blanc, CNRS/IN2P3, F-74941 Annecy-le-Vieux, France⁹University of Sannio at Benevento, I-82100 Benevento, Italy and INFN, Sezione di Napoli, I-80100 Napoli, Italy¹⁰Albert-Einstein-Institut, Max-Planck-Institut für Gravitationsphysik, D-30167 Hannover, Germany¹¹Nikhef, Science Park, 1098 XG Amsterdam, The Netherlands¹²LIGO, Massachusetts Institute of Technology, Cambridge, Massachusetts 02139, USA¹³Instituto Nacional de Pesquisas Espaciais, 12227-010 São José dos Campos, Sao Paulo, Brazil¹⁴INFN, Gran Sasso Science Institute, I-67100 L'Aquila, Italy¹⁵INFN, Sezione di Roma Tor Vergata, I-00133 Roma, Italy¹⁶Inter-University Centre for Astronomy and Astrophysics, Pune 411007, India¹⁷International Centre for Theoretical Sciences, Tata Institute of Fundamental Research, Bangalore 560012, India¹⁸University of Wisconsin-Milwaukee, Milwaukee, Wisconsin 53201, USA¹⁹Leibniz Universität Hannover, D-30167 Hannover, Germany²⁰Università di Pisa, I-56127 Pisa, Italy²¹INFN, Sezione di Pisa, I-56127 Pisa, Italy²²Australian National University, Canberra, Australian Capital Territory 0200, Australia²³The University of Mississippi, University, Mississippi 38677, USA²⁴California State University Fullerton, Fullerton, California 92831, USA

B. P. ABBOTT *et al.*PHYSICAL REVIEW D **94**, 102002 (2016)

- ²⁵LAL, Univ. Paris-Sud, CNRS/IN2P3, Université Paris-Saclay, F-91898 Orsay, France
- ²⁶Chennai Mathematical Institute, Chennai 603103, India
- ²⁷Università di Roma Tor Vergata, I-00133 Roma, Italy
- ²⁸University of Southampton, Southampton SO17 1BJ, United Kingdom
- ²⁹Universität Hamburg, D-22761 Hamburg, Germany
- ³⁰INFN, Sezione di Roma, I-00185 Roma, Italy
- ³¹Albert-Einstein-Institut, Max-Planck-Institut für Gravitationsphysik, D-14476 Potsdam-Golm, Germany
- ³²APC, AstroParticule et Cosmologie, Université Paris Diderot, CNRS/IN2P3, CEA/Irfu, Observatoire de Paris, Sorbonne Paris Cité, F-75205 Paris Cedex 13, France
- ³³Montana State University, Bozeman, Montana 59717, USA
- ³⁴Università di Perugia, I-06123 Perugia, Italy
- ³⁵INFN, Sezione di Perugia, I-06123 Perugia, Italy
- ³⁶European Gravitational Observatory (EGO), I-56021 Cascina, Pisa, Italy
- ³⁷Syracuse University, Syracuse, New York 13244, USA
- ³⁸SUPA, University of Glasgow, Glasgow G12 8QQ, United Kingdom
- ³⁹LIGO Hanford Observatory, Richland, Washington 99352, USA
- ⁴⁰Wigner RCP, RMKI, H-1121 Budapest, Konkoly Thege Miklós út 29-33, Hungary
- ⁴¹Columbia University, New York, New York 10027, USA
- ⁴²Stanford University, Stanford, California 94305, USA
- ⁴³Università di Padova, Dipartimento di Fisica e Astronomia, I-35131 Padova, Italy
- ⁴⁴INFN, Sezione di Padova, I-35131 Padova, Italy
- ⁴⁵CAMK-PAN, 00-716 Warsaw, Poland
- ⁴⁶University of Birmingham, Birmingham B15 2TT, United Kingdom
- ⁴⁷Università degli Studi di Genova, I-16146 Genova, Italy
- ⁴⁸INFN, Sezione di Genova, I-16146 Genova, Italy
- ⁴⁹RRCAT, Indore Madhya Pradesh 452013, India
- ⁵⁰Faculty of Physics, Lomonosov Moscow State University, Moscow 119991, Russia
- ⁵¹SUPA, University of the West of Scotland, Paisley PA1 2BE, United Kingdom
- ⁵²University of Western Australia, Crawley, Western Australia 6009, Australia
- ⁵³Department of Astrophysics/IMAPP, Radboud University Nijmegen, P.O. Box 9010, 6500 GL Nijmegen, The Netherlands
- ⁵⁴Artemis, Université Côte d'Azur, CNRS, Observatoire Côte d'Azur, CS 34229 Nice cedex 4, France
- ⁵⁵Institut de Physique de Rennes, CNRS, Université de Rennes 1, F-35042 Rennes, France
- ⁵⁶Washington State University, Pullman, Washington 99164, USA
- ⁵⁷Università degli Studi di Urbino "Carlo Bo," I-61029 Urbino, Italy
- ⁵⁸INFN, Sezione di Firenze, I-50019 Sesto Fiorentino, Firenze, Italy
- ⁵⁹University of Oregon, Eugene, Oregon 97403, USA
- ⁶⁰Laboratoire Kastler Brossel, UPMC-Sorbonne Universités, CNRS, ENS-PSL Research University, Collège de France, F-75005 Paris, France
- ⁶¹Carleton College, Northfield, Minnesota 55057, USA
- ⁶²Astronomical Observatory Warsaw University, 00-478 Warsaw, Poland
- ⁶³VU University Amsterdam, 1081 HV Amsterdam, The Netherlands
- ⁶⁴University of Maryland, College Park, Maryland 20742, USA
- ⁶⁵Center for Relativistic Astrophysics and School of Physics, Georgia Institute of Technology, Atlanta, Georgia 30332, USA
- ⁶⁶Laboratoire des Matériaux Avancés (LMA), CNRS/IN2P3, F-69622 Villeurbanne, France
- ⁶⁷Université Claude Bernard Lyon 1, F-69622 Villeurbanne, France
- ⁶⁸Università di Napoli "Federico II," Complesso Universitario di Monte S. Angelo, I-80126 Napoli, Italy
- ⁶⁹NASA/Goddard Space Flight Center, Greenbelt, Maryland 20771, USA
- ⁷⁰RESCEU, University of Tokyo, Tokyo 113-0033, Japan
- ⁷¹Tsinghua University, Beijing 100084, China
- ⁷²Texas Tech University, Lubbock, Texas 79409, USA
- ⁷³Pennsylvania State University, University Park, Pennsylvania 16802, USA
- ⁷⁴National Tsing Hua University, Hsinchu City, 30013 Taiwan, Republic of China
- ⁷⁵Charles Sturt University, Wagga Wagga, New South Wales 2678, Australia
- ⁷⁶West Virginia University, Morgantown, West Virginia 26506, USA
- ⁷⁷University of Chicago, Chicago, Illinois 60637, USA
- ⁷⁸Caltech CaRT, Pasadena, California 91125, USA

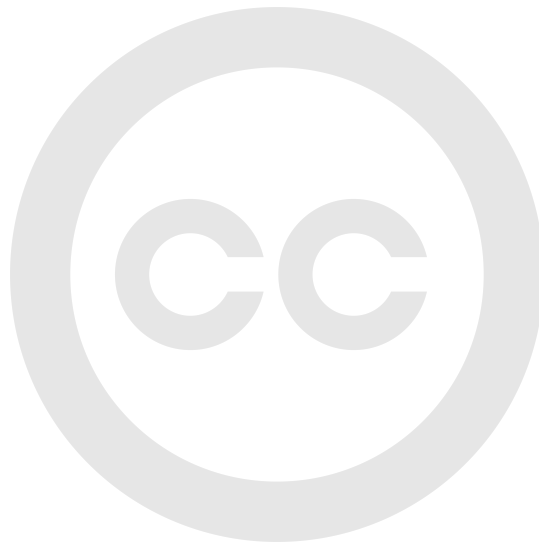
- ⁷⁹Korea Institute of Science and Technology Information, Daejeon 305-806, Korea
⁸⁰Università di Roma “La Sapienza,” I-00185 Roma, Italy
⁸¹University of Brussels, Brussels 1050 Belgium
⁸²Sonoma State University, Rohnert Park, California 94928, USA
⁸³Center for Interdisciplinary Exploration and Research in Astrophysics (CIERA), Northwestern University, Evanston, Illinois 60208, USA
⁸⁴University of Minnesota, Minneapolis, Minnesota 55455, USA
⁸⁵The University of Melbourne, Parkville, Victoria 3010, Australia
⁸⁶Institute for Plasma Research, Bhat, Gandhinagar 382428, India
⁸⁷The University of Sheffield, Sheffield S10 2TN, United Kingdom
⁸⁸The University of Texas Rio Grande Valley, Brownsville, Texas 78520, USA
⁸⁹Università di Trento, Dipartimento di Fisica, I-38123 Povo, Trento, Italy
⁹⁰INFN, Trento Institute for Fundamental Physics and Applications, I-38123 Povo, Trento, Italy
⁹¹Cardiff University, Cardiff CF24 3AA, United Kingdom
⁹²Montclair State University, Montclair, New Jersey 07043, USA
⁹³MTA Eötvös University, “Lendulet” Astrophysics Research Group, Budapest 1117, Hungary
⁹⁴National Astronomical Observatory of Japan, 2-21-1 Osawa, Mitaka, Tokyo 181-8588, Japan
⁹⁵School of Mathematics, University of Edinburgh, Edinburgh EH9 3FD, United Kingdom
⁹⁶Indian Institute of Technology, Gandhinagar Ahmedabad Gujarat 382424, India
⁹⁷University of Szeged, Dóm tér 9, Szeged 6720, Hungary
⁹⁸Embry-Riddle Aeronautical University, Prescott, Arizona 86301, USA
⁹⁹Tata Institute of Fundamental Research, Mumbai 400005, India
¹⁰⁰INAF, Osservatorio Astronomico di Capodimonte, I-80131 Napoli, Italy
¹⁰¹University of Michigan, Ann Arbor, Michigan 48109, USA
¹⁰²Rochester Institute of Technology, Rochester, New York 14623, USA
¹⁰³NCSA, University of Illinois at Urbana-Champaign, Urbana, Illinois 61801, USA
¹⁰⁴Universitat de les Illes Balears, IAC3—IEEC, E-07122 Palma de Mallorca, Spain
¹⁰⁵University of Białystok, 15-424 Białystok, Poland
¹⁰⁶SUPA, University of Strathclyde, Glasgow G1 1XQ, United Kingdom
¹⁰⁷IISER-TVM, CET Campus, Trivandrum Kerala 695016, India
¹⁰⁸Canadian Institute for Theoretical Astrophysics, University of Toronto, Toronto, Ontario M5S 3H8, Canada
¹⁰⁹Institute of Applied Physics, Nizhny Novgorod 603950, Russia
¹¹⁰Pusan National University, Busan 609-735, Korea
¹¹¹Hanyang University, Seoul 133-791, Korea
¹¹²University of Adelaide, Adelaide, South Australia 5005, Australia
¹¹³NCBJ, 05-400 Świerk-Otwock, Poland
¹¹⁴IM-PAN, 00-956 Warsaw, Poland
¹¹⁵Monash University, Victoria 3800, Australia
¹¹⁶Seoul National University, Seoul 151-742, Korea
¹¹⁷The Chinese University of Hong Kong, Shatin, New Territories, Hong Kong SAR, China
¹¹⁸University of Alabama in Huntsville, Huntsville, Alabama 35899, USA
¹¹⁹University of Massachusetts-Amherst, Amherst, Massachusetts 01003, USA
¹²⁰ESPCI, CNRS, F-75005 Paris, France
¹²¹Università di Camerino, Dipartimento di Fisica, I-62032 Camerino, Italy
¹²²Southern University and A&M College, Baton Rouge, Louisiana 70813, USA
¹²³College of William and Mary, Williamsburg, Virginia 23187, USA
¹²⁴Instituto de Física Teórica, University Estadual Paulista/ICTP South American Institute for Fundamental Research, São Paulo São Paulo 01140-070, Brazil
¹²⁵University of Cambridge, Cambridge CB2 1TN, United Kingdom
¹²⁶IISER-Kolkata, Mohanpur, West Bengal 741252, India
¹²⁷Rutherford Appleton Laboratory, HSIC, Chilton, Didcot, Oxon OX11 0QX, United Kingdom
¹²⁸Whitman College, 345 Boyer Avenue, Walla Walla, Washington 99362 USA
¹²⁹National Institute for Mathematical Sciences, Daejeon 305-390, Korea
¹³⁰Université de Lyon, F-69361 Lyon, France
¹³¹Hobart and William Smith Colleges, Geneva, New York 14456, USA
¹³²Janusz Gil Institute of Astronomy, University of Zielona Góra, 65-265 Zielona Góra, Poland
¹³³King’s College London, University of London, London WC2R 2LS, United Kingdom
¹³⁴Andrews University, Berrien Springs, Michigan 49104, USA
¹³⁵Università di Siena, I-53100 Siena, Italy

B. P. ABBOTT *et al.*

PHYSICAL REVIEW D **94**, 102002 (2016)

- ¹³⁶*Trinity University, San Antonio, Texas 78212, USA*
¹³⁷*University of Washington, Seattle, Washington 98195, USA*
¹³⁸*Kenyon College, Gambier, Ohio 43022, USA*
¹³⁹*Abilene Christian University, Abilene, Texas 79699, USA*

†Deceased.



PHYSICAL REVIEW D 94, 122006 (2016)

3 Hierarchical follow-up of subthreshold candidates of an all-sky Einstein@Home search for continuous gravitational waves on LIGO sixth science run data

Maria Alessandra Papa,^{1,2,4,*} Heinz-Bernd Eggenstein,^{2,3} Sinéad Walsh,^{1,2} Irene Di Palma,^{1,2,5}
 Bruce Allen,^{2,4,3} Pia Astone,⁵ Oliver Bock,^{2,3} Teviet D. Creighton,⁷ David Keitel,^{2,3,6}
 Bernd Machenschalk,^{2,3} Reinhard Prix,^{2,3} Xavier Siemens,⁴ Avneet Singh,^{1,2,3}
 Sylvia J. Zhu,^{1,2} and Bernard F. Schutz^{8,1}

¹Max-Planck-Institut für Gravitationsphysik, am Mühlenberg 1, 14476 Potsdam, Germany

²Max-Planck-Institut für Gravitationsphysik, Callinstraße 38, 30167 Hannover, Germany

³Leibniz Universität Hannover, Welfengarten 1, 30167 Hannover, Germany

⁴University of Wisconsin-Milwaukee, Milwaukee, Wisconsin 53201, USA

⁵Università di Roma “La Sapienza,” P.zze A. Moro 2, 00185 Roma, Italy

⁶Universitat de les Illes Balears, IAC3—IEEC, E-07122 Palma de Mallorca, Spain

⁷The University of Texas Rio Grande Valley, Brownsville, Texas 78520, USA

⁸Cardiff University, Cardiff CF24 3AA, United Kingdom

(Received 1 September 2016; published 28 December 2016)

We report results of an all-sky search for periodic gravitational waves with frequency between 50 and 510 Hz from isolated compact objects, e.g., neutron stars. A new hierarchical multistage approach is taken, supported by the computing power of the Einstein@Home project, allowing us to probe more deeply than ever before. 16 million subthreshold candidates from the initial search [LIGO Scientific and Virgo Collaborations, *Phys. Rev. D* **94**, 102002 (2016)] are followed up in four stages. None of those candidates is consistent with an isolated gravitational wave emitter, and 90% confidence level upper limits are placed on the amplitudes of continuous waves from the target population. Between 170.5 and 171 Hz, we set the most constraining 90% confidence upper limit on the strain amplitude h_0 at 4.3×10^{-25} , while at the high end of our frequency range, we achieve an upper limit of 7.6×10^{-25} . These are the most constraining all-sky upper limits to date and constrain the ellipticity of rotating compact objects emitting at 300 Hz at a distance D to less than $6 \times 10^{-7} \left[\frac{D}{100 \text{ pc}} \right]$.

DOI: 10.1103/PhysRevD.94.122006

I. INTRODUCTION

The beauty of continuous signals is that, even if a candidate is not significant enough to be recognized as a real signal after a first semicoherent search, it is still possible to improve its significance to the level necessary to claim a detection after a series of follow-up searches. Hierarchical approaches were first proposed in the late 1990s and developed over a number of searches on LIGO data: Refs. [1] and [2] detail a semicoherent search plus a three-stage follow-up of order 100 candidates; Refs. [3] and [4] detail a semicoherent search plus a series of vetoes and a final coherent follow-up of over 1000 candidates. The search detailed here follows up 16 million candidates and is the first large-scale hierarchical search ever done.

We use a hierarchical approach consisting of four stages applied to the processed results (“Stage 0”) of an initial

search [5]. At each stage, a semicoherent search is performed, and the top ranking cells in parameter space (also referred to as “candidates”) are marked and are searched in the next stage. At each stage, the significance of a cell harboring a real signal would increase with respect to the significance it had in the previous stage. The significance of a cell that did not contain a signal, on the other hand, is not expected to increase consistently over the different stages. In the first three stages, the thresholds that define the top ranking cells are low enough that many false alarms are expected over the large parameter space that was searched. And indeed at the end of the first stage, we have 16 million candidates. At the end of the second stage, we have five million. At the end of the third stage, we have one million. At the end of the fourth stage we are left with only 10 candidates.

The paper is organized very simply. Section II introduces the quantities that characterize each stage of the follow-up. Section III illustrates how the different stages were set up and the results for the S6 LIGO Einstein@Home candidates follow-ups. Section IV present the gravitational wave amplitude and ellipticity upper limit results. In the last section, Sec. V, we summarize the main findings and discuss prospects for this type of search.

*maria.alessandra.papa@aei.mpg.de

Published by the American Physical Society under the terms of the Creative Commons Attribution 3.0 License. Further distribution of this work must maintain attribution to the author(s) and the published article’s title, journal citation, and DOI.

MARIA ALESSANDRA PAPA *et al.*PHYSICAL REVIEW D **94**, 122006 (2016)

II. QUANTITIES DEFINING EACH STAGE

From one stage to the next in this hierarchical scheme, the number of surviving candidates is reduced, the uncertainty over the signal parameters for each candidate is also reduced, and the significance of a real signal is increased. This latter effect is due both to the search being intrinsically more sensitive and to the trials' factor decreasing for every search from one stage to the next.

Each stage performs a stack-slide type of search using the Global Correlations Transform (GCT) method and implementation of Refs. [6,7]. Important variables are the coherent time baseline of the segments, the number of segments used (N_{seg}), the total time spanned by the data, the grids in parameter space, and the detection statistic used to rank the parameter space cells. All stages use the same data set. The first three follow-up searches are performed on the Einstein@Home volunteer computing platform [8], and the last is performed on the Atlas computing cluster [9].

The parameters for the various stages are summarized in Table I. The grids in frequency and spindown are each described by a single parameter, the grid spacing, which is constant over the search range. The same frequency grid spacings (δf) are used for the coherent searches over the segments and for the incoherent summing. The spindown spacing for the incoherent summing step is finer than that ($\delta \dot{f}_c$) used for the coherent searches by a factor γ . The notation used here is consistent with that used in previous observational papers [3,5,10] and in the GCT methods papers [6,7].

The sky grids for stages 1 to 4 are approximately uniform on the celestial sphere projected on the ecliptic plane. The tiling is a hexagonal covering of the unit circle with hexagons' edge length d ,

$$d(m_{\text{sky}}) = \frac{1}{f} \frac{\sqrt{m_{\text{sky}}}}{\pi \tau_E}, \quad (1)$$

with $\tau_E \approx 0.021$ s being half of the light travel time across the Earth and m_{sky} the so-called mismatch parameter. As was done in previous searches [1,5], the sky grids are constant over 10 Hz bands, and the spacings are the ones associated through Eq. (1) to the highest frequency in the range. The sky grid of stage 0 is the union of two grids: one is uniform on the celestial sphere after projection onto the equatorial plane, and the tiling (in the equatorial plane) is

approximately square with edge $d(0.3)$ from Eq. (1); the other grid is limited to the equatorial region ($0 \leq \alpha \leq 2\pi$ and $-0.5 \leq \delta \leq 0.5$), with constant actual α and δ spacings equal to $d(0.3)$ (see Fig. 1 of Ref. [5]). The reason for the equatorial "patching" with a denser sky grid is to improve the sensitivity of the search.

After each stage, a threshold is set on the detection statistic to determine what candidates will be searched by the next stage. We set this detection threshold to be the highest such that the weakest signal that survived the first stage of the pipeline would, with high confidence, not be lost.

The setup for each stage is determined at fixed computational cost. The computational cost is mostly set by practical considerations such as the time frame on which we would like to have a result, the number of stages that we envision in the hierarchy, and the availability of Einstein@Home.

Since an analytical model that predicts the sensitivity of a search with the current implementation of the GCT method does not exist, we consider different search setups, and for every setup we perform fake-signal injection and recovery Monte Carlos. From these, we determine the detection efficiency and the signal parameter uncertainty for signals at the detection threshold. We pick the search setup based on these. Typically, the search setup with the lowest parameter uncertainty volume also has the highest detection efficiency, and we pick that. As a further cross-check, we also determine the mismatch distributions for the detection statistic. We define the mismatch μ as

$$\mu = \frac{2\bar{\mathcal{F}}_{\text{signal}} - 2\bar{\mathcal{F}}_{\text{candidate}}}{2\bar{\mathcal{F}}_{\text{signal}} - 4}, \quad (2)$$

where $\bar{\mathcal{F}}_{\text{signal}}$ is the value of the detection statistic that we measure when we search the data with a template that is perfectly matched to the signal and $\bar{\mathcal{F}}_{\text{candidate}}$ is the value of the detection statistic that we obtain when running a search on a set of templates, none of which, in general, will perfectly coincide with the signal waveform. The mismatch is hence a measure of how fine the grid that we are using is. As expected, Fig. 1 shows that the grids of subsequent stages get finer and finer.

At each stage, we determine the signal parameter uncertainty for signals at least at the detection threshold, in each search dimension: the distance in parameter space

TABLE I. Search parameters for each of the semicoherent stages.

	T_{coh} (hr)	N_{seg}	δf (Hz)	$\delta \dot{f}_c$ (Hz/s)	γ	m_{sky}
Stage 0	60	90	1.6×10^{-6}	5.8×10^{-11}	230	0.3 + equatorial patch
Stage 1	60	90	3.6×10^{-6}	1×10^{-10}	230	0.0042
Stage 2	140	44	2.0×10^{-6}	2.4×10^{-11}	100	0.0004
Stage 3	140	44	1.8×10^{-6}	2.1×10^{-11}	100	1×10^{-5}
Stage 4	280	22	1.9×10^{-7}	7.0×10^{-12}	50	4×10^{-7}

HIERARCHICAL FOLLOW-UP OF SUBTHRESHOLD ...

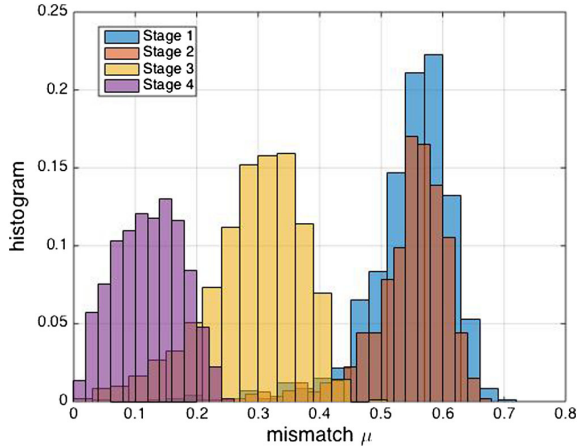


FIG. 1. These are the mismatch histograms of the four follow-up searches, so the y axis represents normalized counts. For a given search and search setup, the mismatch distribution depends on the template grid. The injection-and-recovery Monte Carlo studies to determine these distributions were performed without noise.

around a candidate that with high confidence (at least 90%) includes the signal parameter values. The uncertainty region around each candidate associated with stage i is searched in stage $i + 1$. The uncertainty volume at stage i is smaller than the uncertainty volume of stage $i - 1$.

III. S6 SEARCH FOLLOW-UP

A series of all-sky Einstein@Home searches looked for signals with frequencies from 50 through 510 Hz and frequency derivatives from 3.1×10^{-10} through -2.6×10^{-9} Hz/s. Results from these were combined and analyzed as described in Ref. [5]: no significant candidate was found, and upper limits were set on the gravitational wave signal amplitude in the target signal parameter space. The data set that we begin with is that described in Secs. III. 1 and III. 2 of Ref. [5]: a ranked list of 3.8×10^{10} candidates, each with an associated detection statistic value $2\bar{\mathcal{F}}$. We now take the 16 million most promising regions in parameter space from that search and inspect them more closely. This is done in four stages, which we describe in the next subsections.

We remind the reader that some of the input data to this search were treated by substituting the original frequency-domain data with fake Gaussian noise at the same level as that of the neighboring frequencies. This is done in frequency regions affected by well-known artifacts, as described in Ref. [5]. Results stemming entirely from these fake data are not considered in any further stage. Moreover, after the initial Einstein@Home search, the results in 50 mHz bands were visually inspected, and those 50 mHz bands that presented obvious noise disturbances were also removed

PHYSICAL REVIEW D 94, 122006 (2016)

from the analysis. A complete list of the excluded bands is given in the Appendixes of Ref. [5]. We will come back to this point as we present the results of this search.

A. Stage 0

This is the most complex stage of the hierarchy and determines the sensitivity of the search; if a signal does not pass this initial stage, it will be lost. So, we try here to keep the threshold that candidates have to exceed to be considered further as low as possible, compatibly with the feasibility of the next stage with the available computing resources. Such a threshold was set at $2\bar{\mathcal{F}} = 6.109$.

The identification of correlated candidates saves compute cycles in the next steps of the search. As was done in Ref. [3], the clustering procedure aims to bundle together candidates that could be ascribed to the same cause. In fact, a loud signal as well as a loud disturbance would produce high values of the detection statistic at a number of different template grid points, and it would be a waste to follow up each of these independently. As described in Refs., [3,4], we begin with the loudest candidate, i.e., the candidate with the highest value of $2\bar{\mathcal{F}}$. This is the seed for the first cluster. We associate with it close-by candidates in parameter space. Together, the seed and the nearby candidates constitute the first cluster. We remove the candidates from the first cluster from the candidate list. The loudest candidate on the resulting list is the seed of the second cluster. We proceed in the same way as for the first cluster and reiterate the procedure until no more seeds with $2\bar{\mathcal{F}}$ values equal to or larger than 6.109 remain.

Monte Carlo studies are conducted to determine the cluster box size, i.e., the neighborhood of the seed that determines the cluster occupants. We inject signals in Gaussian noise data at the level of our detectors' noise, search a small parameter space region around the signal parameters, and use the resulting candidates as a representative of what we would find in an actual search. For signals at the detection threshold, the 90% confidence cluster box is

$$\begin{cases} \Delta f^{\text{Stage-0}} &= \pm 1.2 \times 10^{-3} \text{ Hz} \\ \Delta \dot{f}^{\text{Stage-0}} &= \pm 2.6 \times 10^{-10} \text{ Hz/s} \\ \Delta \text{sky}^{\text{Stage-0}} &\approx 25 \text{ points around seed.} \end{cases} \quad (3)$$

If we consider as cluster occupants only those with $2\bar{\mathcal{F}}$ values greater than or equal to 5.9, we observe that signals tend to produce slight overdensities in the clusters with respect to noise. This feature is exploited with an *occupancy veto* that discards all clusters with less than two occupants. We find that the false dismissal for signals at threshold is hardly affected ($\sim 0.02\%$ of signal clusters), whereas the noise rejection is quite significant: we exclude 45% of noise clusters.

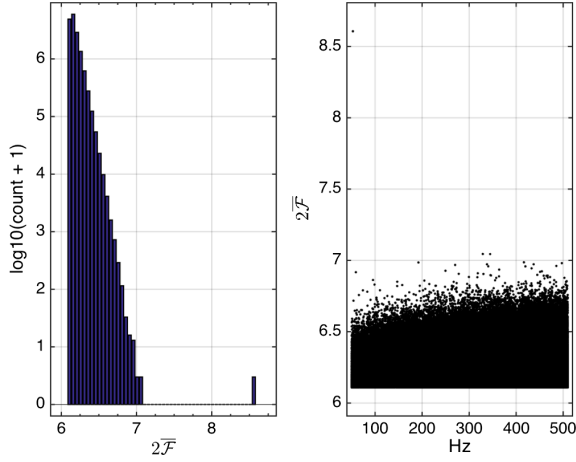
MARIA ALESSANDRA PAPA *et al.*PHYSICAL REVIEW D **94**, 122006 (2016)

FIG. 2. Candidates that are followed up in Stage-1: the distribution of their detection statistic values $2\bar{\mathcal{F}}$ (left plot) and their distribution as a function of frequency (right plot). Most notable are two outliers around ≈ 53 Hz close enough in frequency that they are not resolvable in the left plot.

This same data set containing fake signals is utilized to characterize the false dismissals and the parameter uncertainty regions for all the stages of the hierarchy.

To summarize, the total number of candidates returned by the Einstein@Home searches is 3.8×10^{10} . Of these, we consider the ones with $2\bar{\mathcal{F}}$ above 6.109, excluding frequency bands with obvious noise disturbances. There are 21.6 million such candidates. After clustering and occupancy veto, we reduced this number to 16.23×10^6 . The distribution of the detection statistic values $2\bar{\mathcal{F}}$ for these candidates is shown in Fig. 2 as is their distribution in frequency. The maximum value is 8.6 and occurs at ≈ 53 Hz. All remaining values are smaller than 7.1.

B. Stage 1

In this stage we search a volume of parameter space around each candidate (around each seed) equal to the cluster box defined by Eq. (3). We fix the total run time to be 4 months on Einstein@Home, and this yields an optimal search set-up having the same coherent time baseline as stage 0, 60 h, with the same number of segments $N_{\text{seg}} = 90$ and the grid spacings shown in Table I. We use the same ranking statistic as in the original search [5], the \hat{O}_{SGL} [11], with the same tunings (c_* and normalized short Fourier transform power threshold). The 90% uncertainty regions for this search setup for signals just above the detection threshold are

$$\begin{cases} \Delta f^{\text{Stage-1}} & = \pm 6.7 \times 10^{-4} \text{ Hz} \\ \Delta \dot{f}^{\text{Stage-1}} & = \pm 1.8 \times 10^{-10} \text{ Hz/s} \\ \Delta \text{sky}^{\text{Stage-1}} & \approx 0.55 \Delta \text{sky}^{\text{Stage-0}}. \end{cases} \quad (4)$$

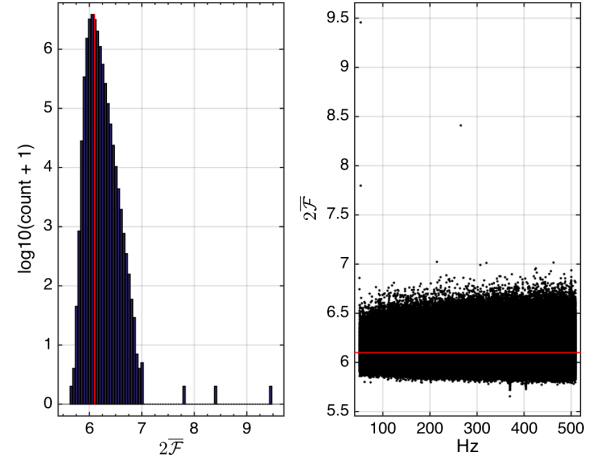


FIG. 3. Loudest from each of the Stage-1 searches: the distribution of their detection statistic values $2\bar{\mathcal{F}}$ (left plot) and their distribution as a function of frequency (right plot). The red line marks $2\bar{\mathcal{F}} = 6.109$, which is the threshold at and above which candidates are passed on to stage 2. The two outliers at ≈ 53 Hz also visible in the previous stage remain notable, and another one becomes visible, at ≈ 266 Hz.

The search is divided among 16.23×10^6 work units (WUs), each lasting about 2 h and performed by one of the Einstein@Home volunteer computers. From each follow-up search, we record the most significant candidate. The distribution of these is shown in Fig. 3. A threshold at $2\bar{\mathcal{F}} = 6.109$ has a $\sim 9\%$ false dismissal for signals at threshold (Fig. 4) and a 70% noise rejection. Using this threshold to determine what candidates to consider in the next stage yields 5.3×10^6 candidates.

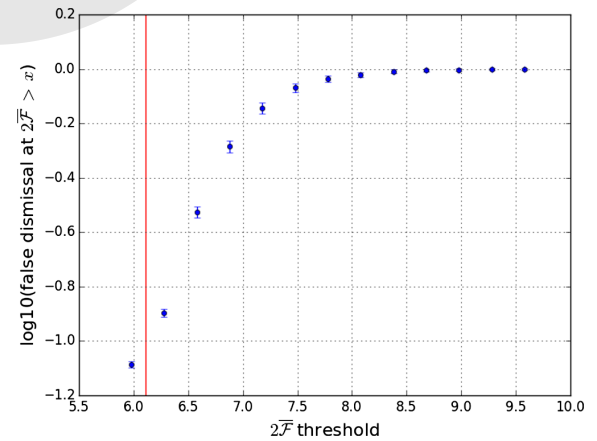


FIG. 4. Fraction of signals that are recovered with a detection statistic value larger than or equal to the threshold value after the Stage-1 follow-up.

HIERARCHICAL FOLLOW-UP OF SUBTHRESHOLD ...

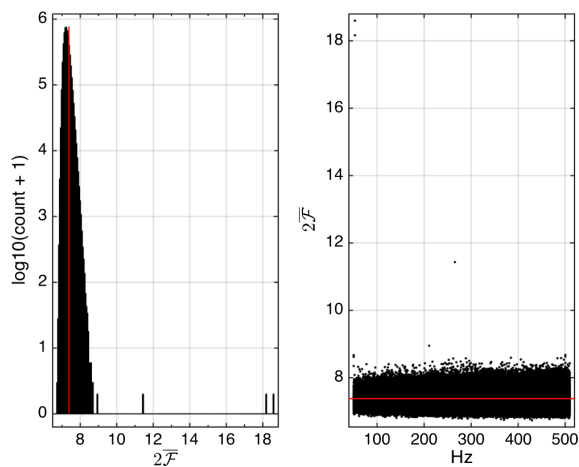


FIG. 5. Loudest from each of the Stage-2 searches: the distribution of their detection statistic values $2\bar{\mathcal{F}}$ (left plot) and their distribution as a function of frequency (right plot). The red line marks $2\bar{\mathcal{F}} = 7.38$, which is the threshold at and above which candidates are passed on to stage 3. The two outliers at ≈ 53 Hz and the one at ≈ 266 Hz from the previous stage remain significant. A new candidate stands out of the bulk of the distribution at ≈ 220 Hz, and two new candidates begin to appear at ≈ 50 Hz.

C. Stage 2

In this stage, we search a volume of parameter space around each candidate defined by Eq. (4). As shown in Table I, we use a coherent time baseline which is about twice as long as that used in the previous stages and the grid spacings are finer. The ranking statistic is \hat{O}_{SGL} with the same tunings (c_* and normalized short Fourier transform power threshold) as in the previous stages. The

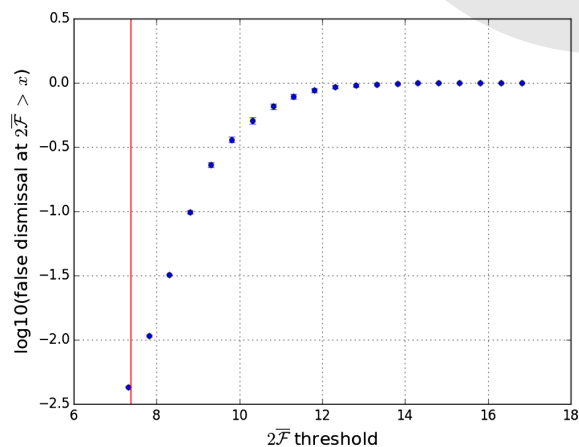


FIG. 6. Fraction of signals that are recovered with a detection statistic value larger than or equal to the threshold value after the Stage-2 follow-up.

PHYSICAL REVIEW D 94, 122006 (2016)

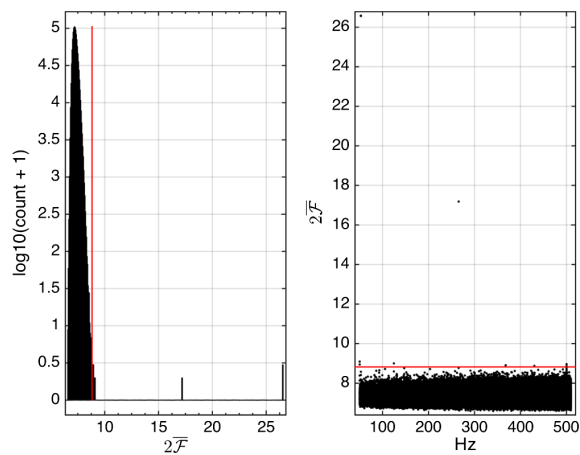


FIG. 7. Loudest from each of the Stage-3 searches: the distribution of their detection statistic values $2\bar{\mathcal{F}}$ (left plot) and their distribution as a function of frequency (right plot). The red line marks $2\bar{\mathcal{F}} = 8.82$, which is the threshold at and above which candidates are passed on to stage 4. The two outliers at ≈ 53 Hz and the one at ≈ 266 Hz well visible in all the previous stages remain significant; these are the ones that are clearly outside of the bulk of the distribution. The candidate that at Stage-2 was at ≈ 220 Hz has now fallen below threshold, whereas the two at ≈ 50 Hz have risen above threshold. Five new candidates have emerged just above threshold.

computational load is divided among 5.3×10^6 WUs, each lasting about 12 h.

The $> 99\%$ uncertainty regions for this search setup for signals close to the detection threshold are

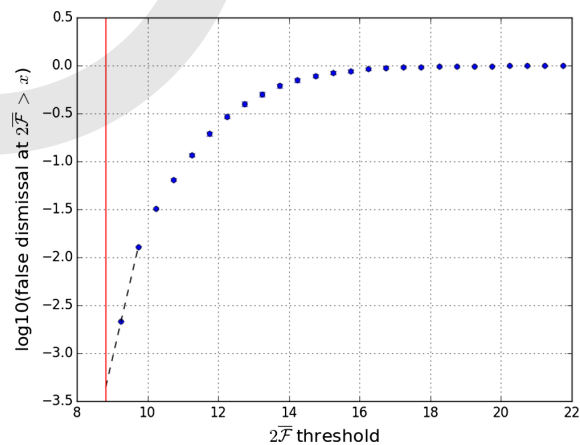


FIG. 8. Fraction of signals that are recovered with a detection statistic value larger than or equal to the threshold value (vertical line) after the Stage-3 follow-up. The dashed line is a linear extrapolation based on the last two data points to guide the eye to the false dismissal value for signals at threshold. This line is a conservative estimate in the sense that it overestimates the false dismissal.

MARIA ALESSANDRA PAPA *et al.*

PHYSICAL REVIEW D **94**, 122006 (2016)

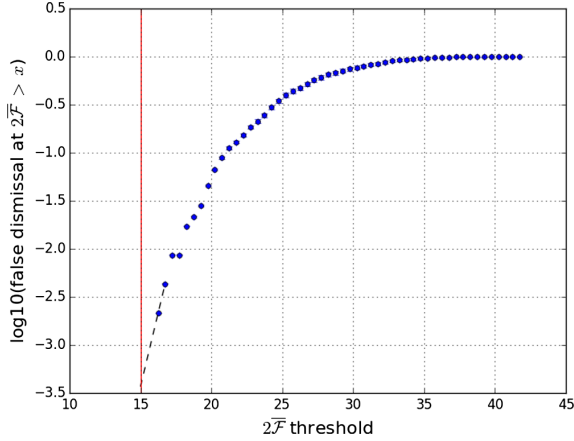


FIG. 9. Fraction of signals that are recovered with a detection statistic value larger than or equal to the threshold value (vertical line) after the Stage-4 follow-up. The dashed line is a linear extrapolation based on the last two data points to guide the eye to the false dismissal value for signals at threshold. This line is a conservative estimate in the sense that it overestimates the false dismissal.

$$\begin{cases} \Delta f^{\text{Stage-2}} & = \pm 1.9 \times 10^{-4} \text{ Hz} \\ \Delta \dot{f}^{\text{Stage-2}} & = \pm 3.5 \times 10^{-11} \text{ Hz/s} \\ \Delta \text{sky}^{\text{Stage-2}} & \approx 0.19 \Delta \text{sky}^{\text{Stage-1}}. \end{cases} \quad (5)$$

As was done in stage 1, we record the most significant candidate from each search. The distribution is shown in Fig. 5. In the next stage, we follow up the top 1.1 million candidates, corresponding to a threshold on $2\bar{\mathcal{F}}$ at 7.38. This threshold has a $\sim 0.6\%$ false dismissal for signals at threshold (Fig. 6) and a 79% noise rejection.

D. Stage 3

In this stage, we search a volume of parameter space around each candidate defined by Eq. (5). As shown in Table I, the coherent time baseline is as long as that used in the previous stage, but the grid spacings are finer. The search is divided among 1.1 million WUs, each lasting about 2 h.

The $>99\%$ uncertainty regions for this search setup for signals close to the detection threshold are

$$\begin{cases} \Delta f^{\text{Stage-3}} & = \pm 5 \times 10^{-5} \text{ Hz} \\ \Delta \dot{f}^{\text{Stage-3}} & = \pm 7 \times 10^{-12} \text{ Hz/s} \\ \Delta \text{sky}^{\text{Stage-3}} & \approx 0.4 \Delta \text{sky}^{\text{Stage-2}}. \end{cases} \quad (6)$$

As was done in previous stages, we record the most significant candidate from each search. The distribution is shown in Fig. 7. In the next stage, we follow up the top ten candidates, corresponding to a threshold on $2\bar{\mathcal{F}}$ at 8.82.

TABLE II. Stage-4 results from each of the ten follow-ups from the candidates surviving Stage-3. For illustration purposes, in the last two columns, we show the values of the average single-detector detection statistics. Typically, for signals, the single-detector values do not exceed the multidetector $2\bar{\mathcal{F}}$.

ID	f (Hz)	α (rad)	δ (rad)	\dot{f} (Hz/s)	$2\bar{\mathcal{F}}$	$2\bar{\mathcal{F}}_{\text{HI}}$	$2\bar{\mathcal{F}}_{\text{L1}}$
1	50.19985463	4.7716026	1.1412922	3.013×10^{-11}	11.6	6.9	9.5
2	50.20001612	4.7124554	1.1683832	-5.674×10^{-12}	12.3	5.5	11.2
3	52.80832455	5.2805366	-1.4631895	7.311×10^{-14}	52.0	16.9	39.7
4	52.80832422	5.2819543	-1.4632398	2.968×10^{-14}	55.9	18.1	44.0
5	124.60002077	4.7067880	1.1648704	-4.164×10^{-12}	11.8	11.2	6.1
6	265.57623841	1.2487972	-0.9812202	-4.015×10^{-12}	37.3	25.1	17.0
7	367.83543941	1.4807437	0.7112582	-9.236×10^{-10}	10.4	9.5	4.9
8	430.28626637	6.1499768	0.9203753	-2.056×10^{-9}	10.0	7.3	5.5
9	500.36312713	4.7121294	1.1617860	9.878×10^{-13}	12.2	11.9	5.4
10	500.36594568	4.5662765	1.4276343	-2.507×10^{-9}	10.6	10.0	4.6

TABLE III. Columns 2–6 show the parameters of the fake injected signal closest to the candidate whose ID identifies it in Table II. The reference time (GPS s) is 960541454.5. We note that the h_0 upper limit values for the 0.5 Hz bands corresponding to the frequencies of these recovered fake signals are consistent with the fake signals’ amplitudes. Columns 7–9 display the distance between the candidates’ and the signals’ parameters (candidate parameter minus signal parameter).

ID	f_s (Hz)	α_s (rad)	δ_s (rad)	\dot{f}_s (Hz/s)	h_0	Δf (Hz)	$\Delta \alpha$ (rad)	$\Delta \delta$ (rad)	$\Delta \dot{f}$ (Hz/s)
3	52.8083244	5.281831296	-1.463269033	-4.03×10^{-18}	4.85×10^{-24}	1.5×10^{-7}	-1.29×10^{-3}	7.95×10^{-5}	7.3×10^{-14}
4	52.8083244	5.281831296	-1.463269033	-4.03×10^{-18}	4.85×10^{-24}	-1.8×10^{-7}	1.23×10^{-4}	2.92×10^{-5}	3.0×10^{-14}
6	265.5762386	1.248816734	-0.981180225	-4.15×10^{-12}	2.47×10^{-25}	-1.9×10^{-7}	-1.95×10^{-5}	-4.00×10^{-5}	1.4×10^{-13}

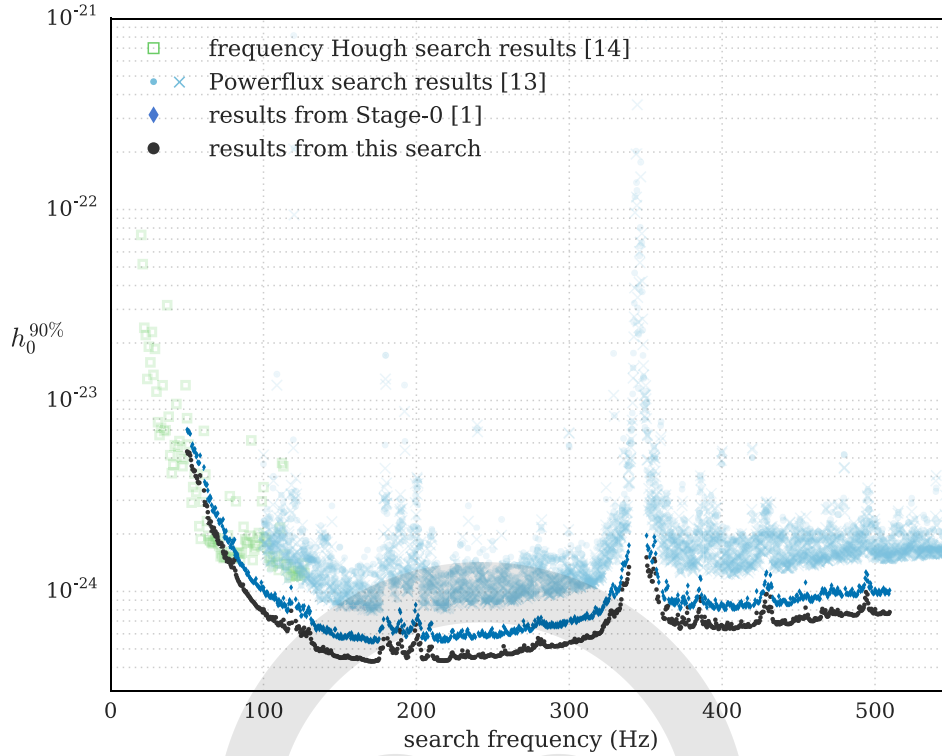


FIG. 10. 90% confidence upper limits on the gravitational wave amplitude of continuous gravitational wave signals with frequency in 0.5 Hz bands and with spindown values within the searched range. The lowest set of points (black circles) is the result of this search. For comparison, we show the upper limits from only the stage-0 results [5]. These lie on the curve above the lowest one and are marked by dark blue diamonds. The results from a previous broad all-sky survey [13] are the top curve (lighter circles and crosses) above 100 Hz. In the lower frequency range, we compare with a search on Virgo data contemporary to the LIGO S6 data [14].

This threshold has a $\sim 4 \times 10^{-4}$ false dismissal for signals at threshold (Fig. 8) and a 99.9991% noise rejection.

E. Stage 4

In this stage, we search a volume of parameter space around each candidate defined by Eq. (6). The setup of choice has a coherent time baseline of 280 h, twice as long as that used in stage 3, and the grid spacings shown in Table I. The search has a relatively modest cost and is performed on the Atlas cluster: each follow-up lasts about 14 h. The ranking statistic is \hat{O}_{SGL} with a retuned $c_* = 96.1$. We consider the loudest candidate from each of the ten follow-ups. In our Monte Carlo studies, no signal candidate (out of 464 injections at threshold) was found more distant than

$$\begin{cases} \Delta f^{\text{Stage-4}} &= \pm 4 \times 10^{-7} \text{ Hz} \\ \Delta \dot{f}^{\text{Stage-4}} &= \pm 4.0 \times 10^{-13} \text{ Hz/s} \\ \Delta \text{sky}^{\text{Stage-4}} &\approx 0.03 \Delta \text{sky}^{\text{Stage-3}}. \end{cases} \quad (7)$$

None of those injections has a $2\bar{\mathcal{F}}$ below 16.2 (Fig. 9), so conservatively, we pick a threshold at 15.0. The Gaussian

false alarm at $2\bar{\mathcal{F}} = 15.0$ for a search over the volume of Eq. (6) is very low ($\approx 2 \times 10^{-20}$), and hence we do not expect any candidate from random Gaussian noise fluctuations.

Since we only follow up ten candidates, we report our findings explicitly for each follow-up. As was done in the previous stages, we consider the most significant candidate from each follow-up. Table II details each of these candidates. Only candidates 3, 4, and 6 have a detection statistic value above the detection threshold $2\bar{\mathcal{F}} = 15.0$, but unfortunately they are ascribable to fake signals hardware injected in the detector to test the detection pipelines. The search recovers all fake signals in the data with parameters within its search range and not absurdly loud.¹ We note that

¹A fake signal was injected at about 108 Hz at such a high amplitude that it saturates the Einstein@Home toplist across the entire sky. Upon visual inspection, it is immediately obvious that the $f - \dot{f}$ morphology is that of a signal, albeit an unrealistically loud one. We categorized the associated band as disturbed because the data are corrupted by this loud injection and it is impossible to detect any real signal in its frequency neighborhood.

MARIA ALESSANDRA PAPA *et al.*

candidates 3 and 4 come from the same fake signal. For a complete list of the fake signals present in the data, see Table 6 of Ref. [12]. In Table III, we show the signal parameters and report the distance with respect to the candidate parameter values. These distances are all within the stage-4 uncertainties of Eq. (7). We do not follow up these candidates any further because we know that they are associated with the hardware injections.

The remaining candidates are below the threshold of 15.0, which is the minimum value of $2\bar{\mathcal{F}}$ that we demand candidates to pass before we inspect them further. However, since these are the most significant ten candidates out of 16 million, we have all the same considered each of them, and it is worth spending a few words on them. Candidates 1 and 2 are close in frequency and are very likely due to the same root cause. The frequencies are also very close to being exact multiples of 0.1 Hz, which is a known comb of spectral artifacts, and the positions are close to the ecliptic poles, which is where stationary lines in the detector frame aggregate in the search results. The same considerations also apply to candidate 5. Candidates 9 and 10 are similar to candidates 1 and 2, apart from the fact that the frequencies are not close to multiples of 0.1 Hz. However, these candidates come from a spectral region where we see an excess of noise candidates. Candidates 7 and 8 cannot be ruled out based on the arguments made previously, so we dug deeper. In particular, we looked at the per-segment contributions to the average detection statistic. We did not find that all segments contribute consistently, as would be expected for a signal. Furthermore, the per-segment detection statistic does not grow as expected between the third- and fourth-stage follow-up. This makes it very unlikely that these candidates come from a continuous gravitational wave signal, phase coherent during the observational period.

IV. RESULTS

The search did not reveal any continuous gravitational wave signal in the parameter volume that was searched. We hence set frequentist upper limits on the maximum gravitational wave amplitude consistent with this null result in 0.5 Hz bands: $h_0^{90\%}(f)$. $h_0^{90\%}(f)$ is the GW amplitude such that 90% of a population of signals with parameter values in our search range would have been detected by our search, i.e., would have survived the last $2\bar{\mathcal{F}}$ threshold at 15.0 at stage 4. Since an actual full-scale injection-and-recovery Monte Carlo for the entire set of follow-ups in every 0.5 Hz band is prohibitive, in the same spirit as Refs. [5,10], we perform such a study in a limited set of trial bands. We pick 100. For each of these, we determine the sensitivity depth of the search corresponding to the detection criterion stated above. As representative of the sensitivity depth $\mathcal{D}^{90\%}$ of this hierarchical search, we take the average of these depths, 46.9 [1/√Hz]. Given the noise level of the data

PHYSICAL REVIEW D 94, 122006 (2016)

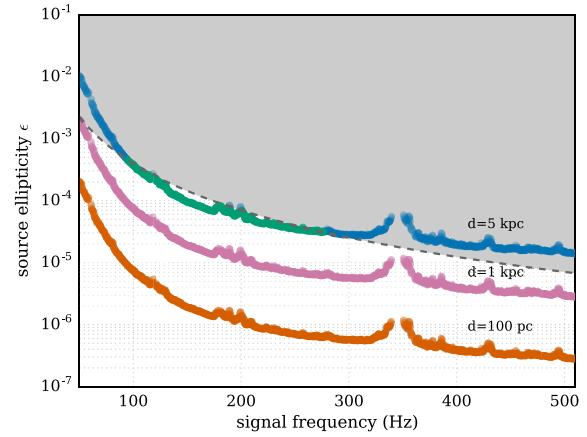


FIG. 11. Ellipticity ϵ of a source at a distance d emitting continuous gravitational waves that would have been detected by this search. The dashed line shows the spindown ellipticity for the highest magnitude spindown parameter value searched: 2.6×10^{-9} Hz/s. The spindown ellipticity is the ellipticity necessary for all the lost rotational kinetic energy to be emitted in gravitational waves. If we assume that the observed spindown is all actual spindown of the object, then no ellipticities could be possible above the dashed curve. In reality, the observed and actual spindowns could differ due to radial motion of the source. In this case, the actual spindown of the object may even be larger than the apparent one. In this case, our search would be sensitive to objects with ellipticities above the dashed line.

as a function of frequency, $S_h(f)$, we then determine the 90% upper limits as

$$h_0^{90\%}(f) = \frac{\sqrt{S_h(f)}}{\mathcal{D}^{90\%}}. \quad (8)$$

Figure 10 shows these upper limits as a function of frequency. They are also presented in tabular form in Table IV in the Appendix with the associated uncertainties, which amount to 20%, including calibration uncertainties. The most constraining upper limit is in the band between 170.5 and 171 Hz, and it is 4.3×10^{-25} . At the upper end of the frequency range, around 510 Hz, the upper limit rises to 7.6×10^{-25} .

The upper limits can be recast as exclusion regions in the signal frequency-ellipticity plane parametrized by the distance, for an isolated source emitting continuous gravitational waves due to its shape presenting an ellipticity ϵ ,

$$\epsilon = \frac{|I_{xx} - I_{yy}|}{I_{zz}}, \quad (9)$$

where I are the principal moments of inertia and the coordinate system is taken so that the z axis is aligned with the spin axis of the star. Figure 11 shows these upper

HIERARCHICAL FOLLOW-UP OF SUBTHRESHOLD ...

limits. Above 200 Hz, we can exclude sources with ellipticities larger than 10^{-6} within 100 pc of Earth and above 400 Hz ellipticities above 4×10^{-7} , values that are much lower than the highest ones that compact objects could sustain [15].

V. CONCLUSIONS

With a hierarchy of five semicoherent searches at increasing coherent time baselines and resolutions in parameter space, we searched over 16 million regions over a few hundred Hz around the most sensitive frequencies of the LIGO detectors during the S6 science run. All stages but the very last ran on the Einstein@Home distributed computing project, lasting a few to several weeks. This is the first large-scale hierarchical search for gravitational wave signals ever performed.

Having carried out this search proves that one can successfully perform deep follow-ups of marginal candidates and elevate their significance to the level necessary to be able to claim a detection. This paper proves that searches with thresholds at the level of the Einstein@Home search described in Ref. [16] are possible; Ref. [16] demonstrates that they are the most sensitive, and these observational results confirm this.

The sensitivity of broad surveys for continuous gravitational wave signals is computationally limited. For this reason, we employ Einstein@Home to deploy our searches. However, following up tens of millions of candidates is not just a matter of having the computational power. This paper illustrates how to perform and optimize the different stages, factoring in all the practical aspects of a real analysis.

None of the investigated candidates survived the five stages, apart from those arising from the two fake signals injected in the detector for control purposes. These fake signals were recovered with the correct signal parameters. Candidate 6 comes from a hardware injection weak enough that no other search on this data set was ever able to detect it. This search recovers it well above the detection threshold.

The gravitational wave amplitude upper limits that we set improve on existing ones [5] by about 30%. This corresponds to an increase in accessible space volume of ≈ 2 .

We excluded 10% of the original data from this analysis where the Stage-0 results had different statistical properties than the bulk of the results and the automated methods employed here, which are necessary in order to deal with a large number of candidates, would not have yielded meaningful statistical results. We might go back to these

PHYSICAL REVIEW D **94**, 122006 (2016)

excluded parameter space regions and attempt to extract information. This is a time-consuming process, and the odds of finding a signal vs the odds of missing one by not analyzing more sensitive data might well indicate that we should not pursue this.

The optimal setup for the various stages and the upper limits were determined at the expense of signal injection-and-recovery Monte Carlo studies. This is due to the fact that the implementation of a stack-slide search that we are using does not allow an analytical prediction of the sensitivity of a search with a given setup (coherent segments and grid spacings). This major drawback will soon be overcome by a new implementation of stack-slide searches based on Refs. [17–20]. Such a search is being characterized and tuned at the time of writing, and we hope to employ it in the context of our contributions to the LIGO Scientific Collaboration for searches on data from the O2 LIGO run.

In principle, we would like to carry out the entire hierarchy of stages on Einstein@Home. For this to happen, two aspects of the search presented here need to be automated: the visual inspection and the follow-up stages. The first is underway [21]. The second will be significantly eased by the new stack-slide search to which we alluded, above.

ACKNOWLEDGMENTS

Our sincere gratitude first goes to the Einstein@Home volunteers who have made these searches possible. Maria Alessandra Papa, Sinéad Walsh, Bruce Allen, and Xavier Siemens gratefully acknowledge the support from NSF PHY Grant No. 1104902. The work for this paper was funded by the Max-Planck-Institut für Gravitationsphysik and the Leibniz Universität Hannover (Germany), the Italian Istituto Nazionale di Fisica Nucleare and the Università di Roma La Sapienza, Rome (Italy), The University of Texas, Rio Grande Valley, Brownsville, Texas (USA) and Cardiff University, Cardiff (UK). All the tuning and preparatory computational work for this search was carried out on the ATLAS supercomputing cluster at the Max-Planck-Institut für Gravitationsphysik/Leibniz Universität Hannover. We also acknowledge the Continuous Wave Group of the LIGO Scientific Collaboration for useful discussions and Graham Woan for reviewing the manuscript on behalf of the collaboration. This document has been assigned LIGO Laboratory document number LIGO-P1600213.

MARIA ALESSANDRA PAPA *et al.*

PHYSICAL REVIEW D 94, 122006 (2016)

APPENDIX: TABULAR DATA

1. Upper limit values

TABLE IV. First frequency of each half Hz signal frequency band in which we set upper limits and the upper limit value for that band.

f (Hz)	$h_0^{90\%} \times 10^{25}$	f (Hz)	$h_0^{90\%} \times 10^{25}$	f (Hz)	$h_0^{90\%} \times 10^{25}$	f (Hz)	$h_0^{90\%} \times 10^{25}$
50.063	54.1 ± 10.8	50.563	52.6 ± 10.5	51.063	53.3 ± 10.7	51.563	53.2 ± 10.6
52.063	51.5 ± 10.3	52.563	48.7 ± 9.7	53.063	45.4 ± 9.1	53.563	43.5 ± 8.7
54.063	43.5 ± 8.7	54.563	42.5 ± 8.5	55.063	42.9 ± 8.6	55.563	40.2 ± 8.0
56.063	40.1 ± 8.0	56.563	39.1 ± 7.8	57.063	37.4 ± 7.5	57.563	36.9 ± 7.4
58.063	37.1 ± 7.4	58.563	40.6 ± 8.1	61.063	33.8 ± 6.8	61.563	29.5 ± 5.9
62.063	28.8 ± 5.8	62.563	28.4 ± 5.7	63.063	27.9 ± 5.6	63.563	26.0 ± 5.2
64.063	24.1 ± 4.8	64.563	22.9 ± 4.6	65.063	22.8 ± 4.6	65.563	23.2 ± 4.6
66.063	21.8 ± 4.4	66.563	20.9 ± 4.2	67.063	20.9 ± 4.2	67.563	21.5 ± 4.3
68.063	20.3 ± 4.1	68.563	20.6 ± 4.1	69.063	19.6 ± 3.9	69.563	20.1 ± 4.0
70.063	19.4 ± 3.9	70.563	18.6 ± 3.7	71.063	17.9 ± 3.6	71.563	17.8 ± 3.6
72.063	17.8 ± 3.6	72.563	17.9 ± 3.6	73.063	17.3 ± 3.5	73.563	17.3 ± 3.5
74.063	16.2 ± 3.2	74.563	15.9 ± 3.2	75.063	15.2 ± 3.0	75.563	16.0 ± 3.2
76.063	15.0 ± 3.0	76.563	14.4 ± 2.9	77.063	14.3 ± 2.9	77.563	14.2 ± 2.8
78.063	14.8 ± 3.0	78.563	13.7 ± 2.7	79.063	13.4 ± 2.7	79.563	14.3 ± 2.9
80.063	14.2 ± 2.8	80.563	13.3 ± 2.7	81.063	14.7 ± 2.9	81.563	12.9 ± 2.6
82.063	12.2 ± 2.4	82.563	11.9 ± 2.4	83.063	11.6 ± 2.3	83.563	11.3 ± 2.3
84.063	11.2 ± 2.2	84.563	11.0 ± 2.2	85.063	10.8 ± 2.2	85.563	10.8 ± 2.2
86.063	10.7 ± 2.1	86.563	10.9 ± 2.2	87.063	10.2 ± 2.0	87.563	10.1 ± 2.0
88.063	9.9 ± 2.0	88.563	10.0 ± 2.0	89.063	9.7 ± 1.9	89.563	9.7 ± 1.9
90.063	9.5 ± 1.9	90.563	9.4 ± 1.9	91.063	9.3 ± 1.9	91.563	9.2 ± 1.8
92.063	9.0 ± 1.8	92.563	8.9 ± 1.8	93.063	8.8 ± 1.8	93.563	8.8 ± 1.8
94.063	8.7 ± 1.7	94.563	8.6 ± 1.7	95.063	8.5 ± 1.7	95.563	8.3 ± 1.7
96.063	8.3 ± 1.7	96.563	8.2 ± 1.6	97.063	8.2 ± 1.6	97.563	8.1 ± 1.6
98.063	8.1 ± 1.6	98.563	8.1 ± 1.6	99.063	7.9 ± 1.6	99.563	7.8 ± 1.6
100.063	8.1 ± 1.6	100.563	7.8 ± 1.6	101.063	7.7 ± 1.5	101.563	7.5 ± 1.5
102.063	7.6 ± 1.5	102.563	7.4 ± 1.5	103.063	7.2 ± 1.4	103.563	7.1 ± 1.4
104.063	7.2 ± 1.4	104.563	7.3 ± 1.5	105.063	7.2 ± 1.4	105.563	7.1 ± 1.4
106.063	7.3 ± 1.5	106.563	7.1 ± 1.4	107.063	7.0 ± 1.4	107.563	7.3 ± 1.5
108.063	7.3 ± 1.5	108.563	6.8 ± 1.4	109.063	6.8 ± 1.4	109.563	6.7 ± 1.3
110.063	6.7 ± 1.3	110.563	6.7 ± 1.3	111.063	6.8 ± 1.4	111.563	6.9 ± 1.4
112.063	6.7 ± 1.3	112.563	6.6 ± 1.3	113.063	7.1 ± 1.4	113.563	6.6 ± 1.3
114.063	6.4 ± 1.3	114.563	6.4 ± 1.3	115.063	6.3 ± 1.3	115.563	6.2 ± 1.2
116.063	6.4 ± 1.3	116.563	6.8 ± 1.4	117.063	6.8 ± 1.4	117.563	6.8 ± 1.4
118.063	7.9 ± 1.6	118.563	6.9 ± 1.4	121.063	7.0 ± 1.4	121.563	6.3 ± 1.3
122.063	6.5 ± 1.3	122.563	6.5 ± 1.3	123.063	6.6 ± 1.3	123.563	6.4 ± 1.3
124.063	6.1 ± 1.2	124.563	5.9 ± 1.2	125.063	5.9 ± 1.2	125.563	6.3 ± 1.3
126.063	6.1 ± 1.2	126.563	6.5 ± 1.3	127.063	6.0 ± 1.2	127.563	6.0 ± 1.2
128.063	5.8 ± 1.2	128.563	6.2 ± 1.2	129.063	6.1 ± 1.2	129.563	6.3 ± 1.3
130.063	6.0 ± 1.2	130.563	6.1 ± 1.2	131.063	5.6 ± 1.1	131.563	5.4 ± 1.1
132.063	5.4 ± 1.1	132.563	5.3 ± 1.1	133.063	5.3 ± 1.1	133.563	5.2 ± 1.0
134.063	5.0 ± 1.0	134.563	5.0 ± 1.0	135.063	5.0 ± 1.0	135.563	5.0 ± 1.0
136.063	5.0 ± 1.0	136.563	4.9 ± 1.0	137.063	5.0 ± 1.0	137.563	5.0 ± 1.0
138.063	4.9 ± 1.0	138.563	4.9 ± 1.0	139.063	5.1 ± 1.0	139.563	4.9 ± 1.0
140.063	4.9 ± 1.0	140.563	4.9 ± 1.0	141.063	4.8 ± 1.0	141.563	5.0 ± 1.0
142.063	4.8 ± 1.0	142.563	4.8 ± 1.0	143.063	4.8 ± 1.0	143.563	4.8 ± 1.0
144.063	4.9 ± 1.0	144.563	4.8 ± 1.0	145.563	4.6 ± 0.9	146.063	4.6 ± 0.9
146.563	4.6 ± 0.9	147.063	4.6 ± 0.9	147.563	4.6 ± 0.9	148.063	4.6 ± 0.9
148.563	4.6 ± 0.9	149.063	4.5 ± 0.9	149.563	4.5 ± 0.9	150.063	4.5 ± 0.9

(Table continued)

HIERARCHICAL FOLLOW-UP OF SUBTHRESHOLD ...

PHYSICAL REVIEW D **94**, 122006 (2016)

TABLE IV. (Continued)

f (Hz)	$h_0^{90\%} \times 10^{25}$	f (Hz)	$h_0^{90\%} \times 10^{25}$	f (Hz)	$h_0^{90\%} \times 10^{25}$	f (Hz)	$h_0^{90\%} \times 10^{25}$
150.563	4.5 ± 0.9	151.063	4.5 ± 0.9	151.563	4.5 ± 0.9	152.063	4.5 ± 0.9
152.563	4.5 ± 0.9	153.063	4.6 ± 0.9	153.563	4.5 ± 0.9	154.063	4.5 ± 0.9
154.563	4.5 ± 0.9	155.063	4.6 ± 0.9	155.563	4.5 ± 0.9	156.063	4.5 ± 0.9
156.563	4.5 ± 0.9	157.063	4.5 ± 0.9	157.563	4.5 ± 0.9	158.063	4.5 ± 0.9
158.563	4.5 ± 0.9	159.063	4.5 ± 0.9	159.563	4.4 ± 0.9	160.063	4.4 ± 0.9
160.563	4.5 ± 0.9	161.063	4.5 ± 0.9	161.563	4.4 ± 0.9	162.063	4.5 ± 0.9
162.563	4.5 ± 0.9	163.063	4.5 ± 0.9	163.563	4.5 ± 0.9	164.063	4.4 ± 0.9
164.563	4.4 ± 0.9	165.063	4.4 ± 0.9	165.563	4.4 ± 0.9	166.063	4.4 ± 0.9
166.563	4.4 ± 0.9	167.063	4.4 ± 0.9	167.563	4.4 ± 0.9	168.063	4.3 ± 0.9
168.563	4.3 ± 0.9	169.063	4.3 ± 0.9	169.563	4.3 ± 0.9	170.063	4.3 ± 0.9
170.563	4.3 ± 0.9	171.063	4.3 ± 0.9	171.563	4.3 ± 0.9	172.063	4.3 ± 0.9
172.563	4.3 ± 0.9	173.063	4.3 ± 0.9	173.563	4.3 ± 0.9	174.063	4.4 ± 0.9
174.563	4.3 ± 0.9	175.063	4.4 ± 0.9	175.563	4.4 ± 0.9	176.063	4.8 ± 1.0
176.563	5.0 ± 1.0	177.063	5.0 ± 1.0	177.563	5.0 ± 1.0	178.063	5.1 ± 1.0
178.563	5.6 ± 1.1	181.063	5.7 ± 1.1	181.563	5.3 ± 1.1	182.063	5.3 ± 1.1
182.563	5.4 ± 1.1	183.063	5.2 ± 1.0	183.563	4.9 ± 1.0	184.063	5.1 ± 1.0
184.563	4.8 ± 1.0	185.063	5.0 ± 1.0	185.563	4.9 ± 1.0	186.063	4.9 ± 1.0
186.563	4.8 ± 1.0	187.063	4.8 ± 1.0	187.563	5.0 ± 1.0	188.063	5.3 ± 1.1
188.563	5.3 ± 1.1	189.063	6.3 ± 1.3	189.563	6.1 ± 1.2	190.063	5.5 ± 1.1
190.563	5.1 ± 1.0	191.063	4.8 ± 1.0	191.563	4.8 ± 1.0	192.063	4.8 ± 1.0
192.563	4.8 ± 1.0	193.063	4.6 ± 0.9	193.563	4.5 ± 0.9	194.063	4.7 ± 0.9
194.563	4.5 ± 0.9	195.063	4.8 ± 1.0	195.563	4.9 ± 1.0	196.063	5.1 ± 1.0
196.563	5.0 ± 1.0	197.063	4.9 ± 1.0	197.563	5.2 ± 1.0	198.063	5.3 ± 1.1
198.563	5.3 ± 1.1	199.063	6.2 ± 1.2	199.563	6.7 ± 1.3	200.063	5.6 ± 1.1
200.563	5.7 ± 1.1	201.063	5.9 ± 1.2	201.563	5.3 ± 1.1	202.063	5.3 ± 1.1
202.563	5.4 ± 1.1	203.063	4.9 ± 1.0	203.563	4.5 ± 0.9	204.063	4.4 ± 0.9
204.563	4.4 ± 0.9	205.063	4.4 ± 0.9	205.563	4.5 ± 0.9	206.063	4.4 ± 0.9
206.563	4.5 ± 0.9	207.063	4.6 ± 0.9	207.563	4.6 ± 0.9	208.063	4.9 ± 1.0
208.563	5.1 ± 1.0	209.063	5.0 ± 1.0	209.563	5.1 ± 1.0	210.063	5.1 ± 1.0
210.563	4.6 ± 0.9	211.063	4.6 ± 0.9	211.563	4.5 ± 0.9	212.063	4.4 ± 0.9
212.563	4.4 ± 0.9	213.063	4.5 ± 0.9	213.563	4.5 ± 0.9	214.063	4.3 ± 0.9
214.563	4.4 ± 0.9	215.063	4.4 ± 0.9	215.563	4.3 ± 0.9	216.063	4.3 ± 0.9
216.563	4.3 ± 0.9	217.063	4.3 ± 0.9	217.563	4.3 ± 0.9	218.063	4.3 ± 0.9
218.563	4.3 ± 0.9	219.063	4.4 ± 0.9	219.563	4.3 ± 0.9	220.063	4.4 ± 0.9
220.563	4.4 ± 0.9	221.063	4.4 ± 0.9	221.563	4.4 ± 0.9	222.063	4.5 ± 0.9
222.563	4.6 ± 0.9	223.063	4.7 ± 0.9	223.563	4.8 ± 1.0	224.063	4.7 ± 0.9
224.563	4.6 ± 0.9	225.063	4.6 ± 0.9	225.563	4.6 ± 0.9	226.063	4.5 ± 0.9
226.563	4.5 ± 0.9	227.063	4.5 ± 0.9	227.563	4.5 ± 0.9	228.063	4.5 ± 0.9
228.563	4.6 ± 0.9	229.063	4.6 ± 0.9	229.563	4.6 ± 0.9	230.063	4.9 ± 1.0
230.563	4.6 ± 0.9	231.063	4.6 ± 0.9	231.563	4.6 ± 0.9	232.063	4.5 ± 0.9
232.563	4.6 ± 0.9	233.063	4.7 ± 0.9	233.563	4.8 ± 1.0	234.063	4.7 ± 0.9
234.563	4.6 ± 0.9	235.063	4.6 ± 0.9	235.563	4.6 ± 0.9	236.063	4.5 ± 0.9
236.563	4.5 ± 0.9	237.063	4.5 ± 0.9	237.563	4.5 ± 0.9	238.063	4.5 ± 0.9
238.563	4.5 ± 0.9	240.563	4.6 ± 0.9	241.063	4.6 ± 0.9	241.563	4.7 ± 0.9
242.063	4.6 ± 0.9	242.563	4.5 ± 0.9	243.063	4.7 ± 0.9	243.563	4.7 ± 0.9
244.063	4.5 ± 0.9	244.563	4.5 ± 0.9	245.063	4.5 ± 0.9	245.563	4.6 ± 0.9
246.063	4.6 ± 0.9	246.563	4.6 ± 0.9	247.063	4.6 ± 0.9	247.563	4.6 ± 0.9
248.063	4.6 ± 0.9	248.563	4.7 ± 0.9	249.063	4.7 ± 0.9	249.563	4.6 ± 0.9
250.063	4.6 ± 0.9	250.563	4.6 ± 0.9	251.063	4.6 ± 0.9	251.563	4.6 ± 0.9
252.063	4.6 ± 0.9	252.563	4.6 ± 0.9	253.063	4.6 ± 0.9	253.563	4.6 ± 0.9
254.063	4.6 ± 0.9	254.563	4.6 ± 0.9	255.063	4.6 ± 0.9	255.563	4.8 ± 1.0
256.063	4.7 ± 0.9	256.563	4.7 ± 0.9	257.063	5.2 ± 1.0	257.563	4.8 ± 1.0
258.063	4.9 ± 1.0	258.563	4.8 ± 1.0	259.063	4.7 ± 0.9	259.563	4.7 ± 0.9
260.063	4.7 ± 0.9	260.563	4.7 ± 0.9	261.063	4.7 ± 0.9	261.563	4.7 ± 0.9
262.063	4.7 ± 0.9	262.563	4.7 ± 0.9	263.063	4.7 ± 0.9	263.563	4.7 ± 0.9

(Table continued)

MARIA ALESSANDRA PAPA *et al.*PHYSICAL REVIEW D **94**, 122006 (2016)

TABLE IV. (Continued)

f (Hz)	$h_0^{90\%} \times 10^{25}$	f (Hz)	$h_0^{90\%} \times 10^{25}$	f (Hz)	$h_0^{90\%} \times 10^{25}$	f (Hz)	$h_0^{90\%} \times 10^{25}$
264.063	4.8 ± 1.0	264.563	4.8 ± 1.0	265.063	4.8 ± 1.0	265.563	4.8 ± 1.0
266.063	4.8 ± 1.0	266.563	4.8 ± 1.0	267.063	4.8 ± 1.0	267.563	5.0 ± 1.0
268.063	5.0 ± 1.0	268.563	4.9 ± 1.0	269.063	4.9 ± 1.0	269.563	4.9 ± 1.0
270.063	5.1 ± 1.0	270.563	5.2 ± 1.0	271.063	5.0 ± 1.0	271.563	5.0 ± 1.0
272.063	4.9 ± 1.0	272.563	4.9 ± 1.0	273.063	5.0 ± 1.0	273.563	5.0 ± 1.0
274.063	4.9 ± 1.0	274.563	4.9 ± 1.0	275.063	4.9 ± 1.0	275.563	5.0 ± 1.0
276.063	5.3 ± 1.1	276.563	5.1 ± 1.0	277.063	5.1 ± 1.0	277.563	5.2 ± 1.0
278.063	5.2 ± 1.0	278.563	5.2 ± 1.0	279.063	5.4 ± 1.1	279.563	5.7 ± 1.1
280.063	5.5 ± 1.1	280.563	5.4 ± 1.1	281.063	5.3 ± 1.1	281.563	5.6 ± 1.1
282.063	5.4 ± 1.1	282.563	5.3 ± 1.1	283.063	5.3 ± 1.1	283.563	5.5 ± 1.1
284.063	5.2 ± 1.0	284.563	5.2 ± 1.0	285.063	5.2 ± 1.0	285.563	5.1 ± 1.0
286.063	5.1 ± 1.0	286.563	5.2 ± 1.0	287.063	5.2 ± 1.0	287.563	5.2 ± 1.0
288.063	5.2 ± 1.0	288.563	5.3 ± 1.1	289.063	5.2 ± 1.0	289.563	5.2 ± 1.0
290.063	5.2 ± 1.0	290.563	5.2 ± 1.0	291.063	5.2 ± 1.0	291.563	5.2 ± 1.0
292.063	5.2 ± 1.0	292.563	5.2 ± 1.0	293.063	5.2 ± 1.0	293.563	5.2 ± 1.0
294.063	5.3 ± 1.1	294.563	5.2 ± 1.0	295.063	5.2 ± 1.0	295.563	5.2 ± 1.0
296.063	5.2 ± 1.0	296.563	5.3 ± 1.1	297.063	5.3 ± 1.1	297.563	5.3 ± 1.1
298.063	5.3 ± 1.1	298.563	5.3 ± 1.1	300.563	5.4 ± 1.1	301.063	5.4 ± 1.1
301.563	5.4 ± 1.1	302.063	5.5 ± 1.1	302.563	5.4 ± 1.1	303.063	5.5 ± 1.1
303.563	5.6 ± 1.1	304.063	5.5 ± 1.1	304.563	5.4 ± 1.1	305.063	5.5 ± 1.1
305.563	5.5 ± 1.1	306.063	5.6 ± 1.1	306.563	5.6 ± 1.1	307.063	5.5 ± 1.1
307.563	5.5 ± 1.1	308.063	5.5 ± 1.1	308.563	5.6 ± 1.1	309.063	5.7 ± 1.1
309.563	5.8 ± 1.2	310.063	5.7 ± 1.1	310.563	5.7 ± 1.1	311.063	5.7 ± 1.1
311.563	5.9 ± 1.2	312.063	5.8 ± 1.2	312.563	5.7 ± 1.1	313.063	5.7 ± 1.1
313.563	5.8 ± 1.2	314.063	5.8 ± 1.2	314.563	5.7 ± 1.1	315.063	5.8 ± 1.2
315.563	5.8 ± 1.2	316.063	5.9 ± 1.2	316.563	6.1 ± 1.2	317.063	6.0 ± 1.2
317.563	5.9 ± 1.2	318.063	6.0 ± 1.2	318.563	6.0 ± 1.2	319.063	6.0 ± 1.2
319.563	6.0 ± 1.2	320.063	6.0 ± 1.2	320.563	6.1 ± 1.2	321.063	6.2 ± 1.2
321.563	6.3 ± 1.3	322.063	6.6 ± 1.3	322.563	6.5 ± 1.3	323.063	6.8 ± 1.4
323.563	6.9 ± 1.4	324.063	7.0 ± 1.4	324.563	6.8 ± 1.4	325.063	6.9 ± 1.4
325.563	7.0 ± 1.4	326.063	7.2 ± 1.4	326.563	7.6 ± 1.5	327.063	7.9 ± 1.6
327.563	7.9 ± 1.6	328.063	7.8 ± 1.6	328.563	7.7 ± 1.5	329.063	7.5 ± 1.5
329.563	7.4 ± 1.5	330.063	7.7 ± 1.5	330.563	7.9 ± 1.6	331.063	7.7 ± 1.5
331.563	8.0 ± 1.6	332.063	8.0 ± 1.6	332.563	8.0 ± 1.6	333.063	8.1 ± 1.6
333.563	8.5 ± 1.7	334.063	9.1 ± 1.8	334.563	10.2 ± 2.0	335.063	11.0 ± 2.2
335.563	10.8 ± 2.2	336.063	10.8 ± 2.2	336.563	10.8 ± 2.2	337.063	10.9 ± 2.2
337.563	11.1 ± 2.2	338.063	11.6 ± 2.3	338.563	12.4 ± 2.5	339.063	13.4 ± 2.7
350.563	15.1 ± 3.0	351.063	13.6 ± 2.7	351.563	12.7 ± 2.5	352.063	12.9 ± 2.6
352.563	12.0 ± 2.4	353.063	12.1 ± 2.4	353.563	12.6 ± 2.5	354.063	11.3 ± 2.3
354.563	11.3 ± 2.3	355.063	13.1 ± 2.6	355.563	14.8 ± 3.0	356.063	14.4 ± 2.9
356.563	12.4 ± 2.5	357.063	10.2 ± 2.0	357.563	9.1 ± 1.8	358.063	9.4 ± 1.9
358.563	8.8 ± 1.8	361.063	7.6 ± 1.5	361.563	7.3 ± 1.5	362.063	7.2 ± 1.4
362.563	7.2 ± 1.4	363.063	8.1 ± 1.6	363.563	8.3 ± 1.7	364.063	8.2 ± 1.6
364.563	8.4 ± 1.7	365.063	7.1 ± 1.4	365.563	6.9 ± 1.4	366.063	7.0 ± 1.4
366.563	6.9 ± 1.4	367.063	7.2 ± 1.4	367.563	7.1 ± 1.4	368.063	6.8 ± 1.4
368.563	6.9 ± 1.4	369.063	6.7 ± 1.3	369.563	7.0 ± 1.4	370.063	7.1 ± 1.4
370.563	6.9 ± 1.4	371.063	7.5 ± 1.5	371.563	6.8 ± 1.4	372.063	6.4 ± 1.3
372.563	6.4 ± 1.3	373.063	6.5 ± 1.3	373.563	6.9 ± 1.4	374.063	7.3 ± 1.5
374.563	6.9 ± 1.4	375.063	7.2 ± 1.4	375.563	6.8 ± 1.4	376.063	6.7 ± 1.3
376.563	6.8 ± 1.4	377.063	7.7 ± 1.5	377.563	8.3 ± 1.7	378.063	7.1 ± 1.4
378.563	6.6 ± 1.3	379.063	6.5 ± 1.3	379.563	6.6 ± 1.3	380.063	6.6 ± 1.3
380.563	6.5 ± 1.3	381.063	6.6 ± 1.3	381.563	6.7 ± 1.3	382.063	6.8 ± 1.4
382.563	7.0 ± 1.4	383.063	7.3 ± 1.5	383.563	7.2 ± 1.4	384.063	7.4 ± 1.5
384.563	7.8 ± 1.6	385.063	8.1 ± 1.6	385.563	9.3 ± 1.9	386.063	8.9 ± 1.8
386.563	7.4 ± 1.5	387.063	7.0 ± 1.4	387.563	6.8 ± 1.4	388.063	6.9 ± 1.4

(Table continued)

HIERARCHICAL FOLLOW-UP OF SUBTHRESHOLD ...

PHYSICAL REVIEW D **94**, 122006 (2016)

TABLE IV. (Continued)

f (Hz)	$h_0^{90\%} \times 10^{25}$	f (Hz)	$h_0^{90\%} \times 10^{25}$	f (Hz)	$h_0^{90\%} \times 10^{25}$	f (Hz)	$h_0^{90\%} \times 10^{25}$
388.563	7.4 ± 1.5	389.063	6.9 ± 1.4	389.563	6.6 ± 1.3	390.063	6.5 ± 1.3
390.563	6.8 ± 1.4	391.063	7.0 ± 1.4	391.563	6.8 ± 1.4	392.063	6.6 ± 1.3
392.563	6.6 ± 1.3	393.063	6.6 ± 1.3	393.563	6.5 ± 1.3	394.063	6.5 ± 1.3
394.563	6.4 ± 1.3	395.063	6.5 ± 1.3	395.563	7.1 ± 1.4	396.063	6.8 ± 1.4
396.563	6.6 ± 1.3	397.063	6.6 ± 1.3	397.563	6.4 ± 1.3	398.063	6.4 ± 1.3
398.563	6.6 ± 1.3	399.063	6.6 ± 1.3	399.563	6.7 ± 1.3	400.563	6.6 ± 1.3
401.063	6.4 ± 1.3	401.563	6.4 ± 1.3	402.063	6.4 ± 1.3	402.563	6.4 ± 1.3
403.063	6.7 ± 1.3	403.563	6.8 ± 1.4	404.063	6.7 ± 1.3	404.563	6.5 ± 1.3
405.063	6.4 ± 1.3	405.563	6.6 ± 1.3	406.063	6.7 ± 1.3	406.563	6.5 ± 1.3
407.063	6.4 ± 1.3	407.563	6.4 ± 1.3	408.063	6.4 ± 1.3	408.563	6.5 ± 1.3
409.063	6.5 ± 1.3	409.563	6.4 ± 1.3	410.063	6.4 ± 1.3	410.563	6.5 ± 1.3
411.063	6.6 ± 1.3	411.563	6.6 ± 1.3	412.063	6.7 ± 1.3	412.563	7.0 ± 1.4
413.063	6.6 ± 1.3	413.563	6.6 ± 1.3	414.063	6.6 ± 1.3	414.563	6.7 ± 1.3
415.063	6.5 ± 1.3	415.563	6.5 ± 1.3	416.063	6.5 ± 1.3	416.563	6.7 ± 1.3
417.063	6.7 ± 1.3	417.563	6.6 ± 1.3	418.063	6.5 ± 1.3	418.563	6.6 ± 1.3
420.563	6.7 ± 1.3	421.063	6.7 ± 1.3	421.563	6.8 ± 1.4	422.063	7.0 ± 1.4
422.563	7.7 ± 1.5	423.063	7.0 ± 1.4	423.563	6.9 ± 1.4	424.063	6.9 ± 1.4
424.563	7.0 ± 1.4	425.063	7.3 ± 1.5	425.563	7.7 ± 1.5	426.063	7.8 ± 1.6
426.563	7.8 ± 1.6	427.063	7.8 ± 1.6	427.563	8.3 ± 1.7	428.063	8.8 ± 1.8
428.563	9.7 ± 1.9	429.063	9.7 ± 1.9	429.563	8.2 ± 1.6	430.063	8.2 ± 1.6
430.563	7.9 ± 1.6	431.063	8.3 ± 1.7	431.563	9.4 ± 1.9	432.063	8.3 ± 1.7
432.563	7.8 ± 1.6	433.063	7.2 ± 1.4	433.563	6.9 ± 1.4	434.063	6.9 ± 1.4
434.563	6.9 ± 1.4	435.063	6.9 ± 1.4	435.563	6.7 ± 1.3	436.063	6.7 ± 1.3
436.563	6.9 ± 1.4	437.063	6.9 ± 1.4	437.563	6.7 ± 1.3	438.063	6.9 ± 1.4
438.563	6.8 ± 1.4	439.063	7.0 ± 1.4	439.563	7.0 ± 1.4	440.063	6.9 ± 1.4
440.563	6.9 ± 1.4	441.063	7.1 ± 1.4	441.563	6.8 ± 1.4	442.063	6.8 ± 1.4
442.563	6.8 ± 1.4	443.063	6.8 ± 1.4	443.563	6.8 ± 1.4	444.063	6.8 ± 1.4
444.563	6.8 ± 1.4	445.063	6.8 ± 1.4	445.563	6.9 ± 1.4	446.063	6.9 ± 1.4
446.563	7.2 ± 1.4	447.063	7.0 ± 1.4	447.563	7.1 ± 1.4	448.063	7.1 ± 1.4
448.563	7.3 ± 1.5	449.063	7.2 ± 1.4	449.563	7.0 ± 1.4	450.063	7.0 ± 1.4
450.563	7.4 ± 1.5	451.063	7.2 ± 1.4	451.563	7.3 ± 1.5	452.063	7.3 ± 1.5
452.563	7.2 ± 1.4	453.063	7.2 ± 1.4	453.563	7.2 ± 1.4	454.063	7.4 ± 1.5
454.563	8.2 ± 1.6	455.063	7.3 ± 1.5	455.563	7.4 ± 1.5	456.063	7.5 ± 1.5
456.563	7.2 ± 1.4	457.063	7.1 ± 1.4	457.563	7.0 ± 1.4	458.063	7.0 ± 1.4
458.563	7.0 ± 1.4	459.063	7.0 ± 1.4	459.563	7.0 ± 1.4	460.063	7.0 ± 1.4
460.563	7.2 ± 1.4	461.063	7.2 ± 1.4	461.563	7.1 ± 1.4	462.063	7.1 ± 1.4
462.563	7.2 ± 1.4	463.063	7.2 ± 1.4	463.563	7.2 ± 1.4	464.063	7.2 ± 1.4
464.563	7.3 ± 1.5	465.063	7.8 ± 1.6	465.563	8.1 ± 1.6	466.063	7.8 ± 1.6
466.563	7.8 ± 1.6	467.063	7.7 ± 1.5	467.563	8.0 ± 1.6	468.063	7.5 ± 1.5
468.563	7.4 ± 1.5	469.063	7.4 ± 1.5	469.563	7.4 ± 1.5	470.063	7.7 ± 1.5
470.563	7.7 ± 1.5	471.063	7.9 ± 1.6	471.563	8.1 ± 1.6	472.063	7.7 ± 1.5
472.563	7.6 ± 1.5	473.063	7.9 ± 1.6	473.563	7.8 ± 1.6	474.063	7.6 ± 1.5
474.563	7.7 ± 1.5	475.063	7.7 ± 1.5	475.563	8.0 ± 1.6	476.063	7.7 ± 1.5
476.563	7.5 ± 1.5	477.063	7.7 ± 1.5	477.563	7.7 ± 1.5	478.063	7.5 ± 1.5
478.563	7.5 ± 1.5	480.563	7.6 ± 1.5	481.063	7.6 ± 1.5	481.563	7.7 ± 1.5
482.063	7.6 ± 1.5	482.563	7.6 ± 1.5	483.063	7.7 ± 1.5	483.563	7.6 ± 1.5
484.063	7.6 ± 1.5	484.563	7.6 ± 1.5	485.063	7.6 ± 1.5	485.563	7.5 ± 1.5
486.063	7.5 ± 1.5	486.563	7.5 ± 1.5	487.063	7.5 ± 1.5	487.563	7.5 ± 1.5
488.063	7.5 ± 1.5	488.563	7.6 ± 1.5	489.063	7.7 ± 1.5	489.563	8.2 ± 1.6
490.063	8.3 ± 1.7	490.563	7.9 ± 1.6	491.063	7.9 ± 1.6	491.563	8.0 ± 1.6
492.063	8.1 ± 1.6	492.563	8.2 ± 1.6	493.063	8.5 ± 1.7	493.563	9.2 ± 1.8
494.063	9.9 ± 2.0	494.563	9.0 ± 1.8	495.063	9.6 ± 1.9	495.563	8.7 ± 1.7
496.063	8.1 ± 1.6	496.563	8.0 ± 1.6	497.063	8.0 ± 1.6	497.563	8.1 ± 1.6
498.063	7.8 ± 1.6	498.563	7.7 ± 1.5	499.063	7.7 ± 1.5	499.563	7.8 ± 1.6
500.063	8.1 ± 1.6	500.563	7.7 ± 1.5	501.063	7.6 ± 1.5	501.563	7.6 ± 1.5

(Table continued)

MARIA ALESSANDRA PAPA *et al.*PHYSICAL REVIEW D **94**, 122006 (2016)TABLE IV. (*Continued*)

f (Hz)	$h_0^{90\%} \times 10^{25}$	f (Hz)	$h_0^{90\%} \times 10^{25}$	f (Hz)	$h_0^{90\%} \times 10^{25}$	f (Hz)	$h_0^{90\%} \times 10^{25}$
502.063	7.6 ± 1.5	502.563	7.6 ± 1.5	503.063	7.7 ± 1.5	503.563	7.6 ± 1.5
504.063	7.7 ± 1.5	504.563	7.8 ± 1.6	505.063	7.8 ± 1.6	505.563	7.8 ± 1.6
506.063	7.7 ± 1.5	506.563	7.7 ± 1.5	507.063	7.6 ± 1.5	507.563	7.6 ± 1.5
508.063	7.6 ± 1.5	508.563	7.6 ± 1.5	509.063	7.7 ± 1.5	509.563	7.8 ± 1.6

- [1] B. P. Abbott *et al.* (LIGO Scientific Collaboration), Einstein@Home all-sky search for periodic gravitational waves in LIGO S5 data, *Phys. Rev. D* **87**, 042001 (2013).
- [2] M. Shaltev, P. Leaci, M. A. Papa, and R. Prix, Fully coherent follow-up of continuous gravitational-wave candidates: an application to Einstein@Home results, *Phys. Rev. D* **89**, 124030 (2014).
- [3] J. Aasi *et al.* (LIGO Scientific and VIRGO Collaborations), Directed search for continuous gravitational waves from the Galactic center, *Phys. Rev. D* **88**, 102002 (2013).
- [4] B. Behnke, M. A. Papa, and R. Prix, Postprocessing methods used in the search for continuous gravitational-wave signals from the Galactic Center, *Phys. Rev. D* **91**, 064007 (2015).
- [5] B. P. Abbott *et al.* (LIGO Scientific and Virgo Collaborations), Results of the deepest all-sky survey for continuous gravitational waves on LIGO S6 data running on the Einstein@Home volunteer distributed computing project, *Phys. Rev. D* **94**, 102002 (2016)..
- [6] H. J. Pletsch, Parameter-space correlations of the optimal statistic for continuous gravitational-wave detection, *Phys. Rev. D* **78**, 102005 (2008).
- [7] H. J. Pletsch, Parameter-space metric of semicoherent searches for continuous gravitational waves, *Phys. Rev. D* **82**, 042002 (2010).
- [8] <https://www.einsteinathome.org/>.
- [9] http://www.aei.mpg.de/24838/02_Computing_and_ATLAS.
- [10] A. Singh, M. A. Papa, H.-B. Eggenstein, S. Zhu, H. Pletsch, B. Allen, O. Bock, B. Maschenchalk, R. Prix, and X. Siemens, Results of an all-sky high-frequency Einstein@Home search for continuous gravitational waves in LIGO 5th Science Run, *Phys. Rev. D* **94**, 064061 (2016).
- [11] D. Keitel, R. Prix, M. A. Papa, P. Leaci, and M. Siddiqi, Search for continuous gravitational waves: Improving robustness versus instrumental artifacts, *Phys. Rev. D* **89**, 064023 (2014).
- [12] J. Aasi *et al.* (LIGO Collaboration), Searches for continuous gravitational waves from nine young supernova remnants, *Astrophys. J.* **813**, 39 (2015).
- [13] B. P. Abbott *et al.* (LIGO Scientific and Virgo Collaborations), Comprehensive all-sky search for periodic gravitational waves in the sixth science run LIGO data, *Phys. Rev. D* **94**, 042002 (2016).
- [14] J. Aasi *et al.* (LIGO Scientific and VIRGO Collaborations), First low frequency all-sky search for continuous gravitational wave signals, *Phys. Rev. D* **93**, 042007 (2016).
- [15] N. K. Johnson-McDaniel and B. J. Owen, Maximum elastic deformations of relativistic stars, *Phys. Rev. D* **88**, 044004 (2013).
- [16] S. Walsh *et al.*, Comparison of methods for the detection of gravitational waves from unknown neutron stars, *Phys. Rev. D* **94**, 124010 (2016).
- [17] K. Wette, Empirically extending the range of validity of parameter-space metrics for all-sky searches for gravitational-wave pulsars, [arXiv:1607.00241](https://arxiv.org/abs/1607.00241).
- [18] K. Wette, Parameter-space metric for all-sky semicoherent searches for gravitational-wave pulsars, *Phys. Rev. D* **92**, 082003 (2015).
- [19] K. Wette, Lattice template placement for coherent all-sky searches for gravitational-wave pulsars, *Phys. Rev. D* **90**, 122010 (2014).
- [20] K. Wette and R. Prix, Flat parameter-space metric for all-sky searches for gravitational-wave pulsars, *Phys. Rev. D* **88**, 123005 (2013).
- [21] S. J. Zhu *et al.*, An Einstein@home search for continuous gravitational waves from Cassiopeia A, *Phys. Rev. D* **94**, 082008 (2016).

Conclusions

The neutron stars' structural dynamics have long remained an elusive mystery, while at the same time, several analytical, numerical and observational efforts are ongoing to fill this void. In particular, the field of gravitational wave astronomy with isolated neutron stars is a book missing many chapters (see [24] for a detailed review). For instance, neutron stars are expected to emit nearly monochromatic gravitational wave radiation on varying time-scales depending on the magnitude and the nature of the deformation in their structure. This deformation could be in the form of a rigid non-axisymmetry (i.e. *ellipticity*) or dynamic non-axisymmetric motions of the internal fluid(s). In both cases, the uncertainty on the deformation is large and typically hard to predict. This is simply because the modeling of neutron star dynamics involves a very complex interplay between fluid dynamics of the exotic matter in the bulk, solid crust dynamics, effect of the magnetic field, crust-core interactions, nature of superfluidity and superconductivity in the bulk, equation(s) of state of the internal matter, and many other such factors [43, 24, 37, 23, 48, 33, 22]. In recent years, many attempts have been made to numerically and analytically constrain the possible forms of the equation of state (refer to [69, 59] and the references therein), and the testing of predictions made in these models depends on fitting them against complementary observational data sets. In this quest, several missions targeting the electromagnetic spectrum have attempted to discern the classes of models to some extent (e.g. GAIA, NICER, LOFAR, FERMI, Arecibo etc). Yet, there still remains a large amount of unresolved degeneracy among the plethora of models simply because the scope of the electromagnetic observations is limited. The field of (continuous) gravitational wave astronomy will help in bridging this gap and broaden the scope of observations by probing the gravitational spectrum.

In this work, we have explored a mechanism that adds to the list of possible gravitational wave signal morphologies from a neutron star. In chapter II, we expand upon a mechanism that relates the tCW emission triggered by a glitch to purely hydrodynamic motions in the bulk of the star, previously analysed by Melatos *et al* [73, 26]. The scale of emission of tCW from the resulting asymmetries is found to be large enough to be targeted by advanced LIGO and next generation gravitational wave detectors. The detection of tCW attributable to such a mechanism presents with a possibility to constrain certain regimes of the elusive equation of state. In addition, since tCW may be emitted by other mecha-

nisms (e.g. *r*-modes, two-fluid instabilities, star-quakes etc), the unique power spectrum of the emission and association of tCW in time with a glitch could provide us with more means to discern between different models.

Yet, the source modeling is only half of the story. The expected strain of the CW or tCW signals emitted from a wide class of models are estimated to be very low. This can be directly inferred from the approximate scale-based analytic and numerical models¹ as well as from the upper limits derived on CW amplitudes from the most sensitive searches on the latest LIGO data [45, 15]. The onus then lies on the search methods to be able to dig for smaller needles in larger and larger haystacks. In chapters III and VI, we present three such deep searches in the LIGO S5, S6 and O1 data using the Einstein@Home framework. Each of these searches target different frequency bandwidths in data from different LIGO science runs. For instance, the only high-frequency all-sky CW search in S5 data (chapter III) rules out CW amplitudes $\gtrsim O(10^{-24} - 10^{-23})$ and ellipticities $\gtrsim O(10^{-7})$ within 100 pc of earth in the 1.25–1.5 kHz range. The most sensitive all-sky CW search in S6 data in the mid-frequency region (chapters VI.2–3) excludes CW amplitudes $\gtrsim O(10^{-25} - 10^{-24})$ and ellipticities $\gtrsim O(10^{-6})$ within 100 pc of earth in the 230–500 Hz range. The deepest all-sky CW search in the low-frequency region in the advanced LIGO O1 data (chapter VI.1) excludes CW amplitudes $\gtrsim O(10^{-25} - 10^{-24})$ and ellipticities $\gtrsim O(10^{-5})$ within 100 pc of earth in the 55–100 Hz range. These searches typically use a similar methodology, as detailed in chapter IV. In addition, all these searches use the upper-limit procedure described in chapter V.

The searches quoted above report no detection of CW. While this may simply be due to the lack of a detectable source in our effective search radius, it nonetheless inspires us to improve our methods and achieve greater sensitivities. In chapter IV, we present a new topology-sensitive clustering algorithm that helps in greatly reducing the number of candidates to be followed up and allows to use the limited amount of computational resources for sub-threshold searches. Such methods are especially useful in relatively noisier data (such as O1 data) where they can discard more than 99.8% of the noise candidates, leaving only a few important ones to follow up in the hierarchical stages of post-processing. This new procedure was employed in [45], reducing the number of significant candidates from nearly 15,000,000 to approximately 35,000 before the hierarchical follow-up stages.

In conclusion, my work in the past three years at AEI is aimed at developing methods that compliment

¹Referring to the colloquium by Prof. Dr. Nils Andersson at the Albert Einstein Institute, Hannover in May 2017.

and improve the chances of detecting CW/tCW from isolated neutron stars. It is hoped that the ideas proposed herein will prove beneficial in making CW/tCW searches more sensitive in the current day and in the future, and in allowing us to explore and decipher the last known state of matter in form of neutron stars or other compact objects.

References

- [1] J Aasi *et al.* *Directed search for continuous gravitational waves from the Galactic center.* **Phys. Rev. Lett.** [↗](#), 88(10):102002, 2013.
- [2] J Aasi *et al.* *Implementation of an F-statistic all-sky search for continuous gravitational waves in Virgo VSR1 data.* **Class. Quant. Grav.** [↗](#), 31(16):165014, 2014.
- [3] J Aasi *et al* (LIGO Scientific Collaboration). *Directed search for continuous gravitational waves from the Galactic center.* **Phys. Rev. D** [↗](#), 88(10):102002, 2013.
- [4] J Aasi *et al* (LIGO Scientific Collaboration). *Einstein@Home all-sky search for periodic gravitational waves in LIGO S5 data.* **Phys. Rev. D** [↗](#), 87(8):042001, 2013.
- [5] B Abadie *et al* (LIGO Scientific Collaboration). *All-sky search for periodic gravitational waves in the full S5 LIGO data.* **Phys. Rev. D** [↗](#), 85(2):022001, 2012.
- [6] J Abadie *et al* (LIGO Scientific Collaboration). *Calibration of the LIGO gravitational wave detectors in the fifth science run.* **Nucl. Instrum. Meth. A** [↗](#), 624(1):223–240, 2010.
- [7] B Abbot *et al* (LIGO Scientific Collaboration). *Searches for periodic gravitational waves from unknown isolated sources and Scorpius X-1: Results from the second LIGO science run.* **Phys. Rev. D** [↗](#), 76(8):082001, 2007.
- [8] B Abbot *et al* (LIGO Scientific Collaboration). *All-sky search for periodic gravitational waves in LIGO S4 data.* **Phys. Rev. D** [↗](#), 77(2):022001, 2008.
- [9] B Abbot *et al* (LIGO Scientific Collaboration). *LIGO: the Laser Interferometer Gravitational-Wave Observatory.* **Rep. Prog. Phys.** [↗](#), 72(7):076901, 2009.
- [10] B Abbot *et al* (LIGO Scientific Collaboration). *All-Sky LIGO Search for Periodic Gravitational Waves in the Early Fifth-Science-Run Data.* **Phys. Rev. Lett.** [↗](#), 102(11):111102, 2009.
- [11] B Abbot *et al* (LIGO Scientific Collaboration). *Results of the deepest all-sky survey for continuous gravitational waves on LIGO S6 data running on the Einstein@Home volunteer distributed computing project.* **Phys. Rev. D** [↗](#), 94(10):102002, 2016.
- [12] B Abbot *et al* (LIGO Scientific Collaboration). *Comprehensive All-sky Search for Periodic Gravitational Waves in the Sixth Science Run LIGO Data.* **Phys. Rev. D** [↗](#), 94(4):042002, 2016.
- [13] B Abbot *et al* (LIGO Scientific Collaboration), A G Lyne, and M Kramer. *Upper limits on gravitational wave emission from 78 radio pulsars.* **Phys. Rev. D** [↗](#), 76(4):042001, 2007.
- [14] B Abbott *et al* (LIGO Scientific Collaboration). *Einstein@Home search for periodic gravitational waves in LIGO S4 data.* **Phys. Rev. D** [↗](#), 79(2):022001, 2009.
- [15] B Abbott *et al* (LIGO Scientific Collaboration). *All-sky Search for Periodic Gravitational Waves in the O1 LIGO Data.* **arXiv** [↗](#), 1707.02667(–):33, 2017.
- [16] B P Abbott *et al* (LIGO Scientific Collaboration). *Einstein@Home search for periodic gravitational waves in early S5 LIGO data.* **Phys. Rev. D** [↗](#), 80(4):042003, 2009.
- [17] M Abney and R I Epstein. *Ekman pumping in compact astrophysical bodies.* **J. Fluid Mech.** [↗](#), 312(1):327–340, 1996.
- [18] M Abney, R I Epstein, and A V Olinto. *Observational Constraints on the Internal Structure and Dynamics of the Vela Pulsar.* **ApJ** [↗](#), 466(1):91–94, 1996.
- [19] A Adare *et al.* *J/ψ Production versus Centrality, Transverse Momentum, and Rapidity in Au + Au Collisions at $\sqrt{s_{NN}} = 200$ GeV.* **PRL** [↗](#), 98(17):172301, 2007.
- [20] S S Adler *et al.* *Elliptic Flow of Identified Hadrons in Au + Au Collisions at $\sqrt{s_{NN}} = 200$ GeV.* **PRL** [↗](#), 91(18):182301, 2003.
- [21] N Andersson, G L Comer, and R Prix. *Are Pulsar Glitches Triggered by a Superfluid Two-Stream Instability.* **Phys. Rev. Lett.** [↗](#), 90(09):091101, 2003.
- [22] N Andersson, G L Comer, and K Glampedakis. *How viscous is a superfluid neutron star core.* **Nuclear Phys. A** [↗](#), 763(1):212–229, 2005.
- [23] N Andersson, T Sidery, and G L Comer. *Mutual friction in superfluid neutron stars.* **MNRAS** [↗](#), 368(1):162–170, 2006.
- [24] N Andersson, V Ferrari, D I Jones, K D Kokkotas, B Krishnan, J Read, L Rezzolla, and B Zink. *Gravitational waves from neutron stars: Promises and challenges.* **Gen. Rel. Grav.** [↗](#), 43(2):409–436, 2011.
- [25] B Behnke, M A Papa, and R Prix. *Postprocessing methods used in the search for continuous gravitational-wave signals from the Galactic Center.* **Phys. Rev. D** [↗](#), 91(6):064007, 2015.

- [26] M F Bennett, C A van Eysden, and A Melatos. *Continuous-wave gravitational radiation from pulsar glitch recovery*. **MNRAS** [↗](#), 409(4):1705–1718, 2010.
- [27] LIGO Scientific Collaboration and Virgo Collaboration. *Observation of Gravitational Waves from a Binary Black Hole Merger*. **Phys. Rev. Lett.** [↗](#), 116(6):061102, 2016.
- [28] LIGO Scientific Collaboration and Virgo Collaboration. *Astrophysical Implications of the Binary Black-Hole Merger GW150914*. **ApJ Letters** [↗](#), 818(2):22, 2016.
- [29] LIGO Scientific Collaboration and Virgo Collaboration. *Properties of the binary black hole merger GW150914*. **Phys. Rev. Lett.** [↗](#), 116(24):241102, 2016.
- [30] LIGO Scientific Collaboration and Virgo Collaboration. *The Rate of Binary Black Hole Mergers Inferred from Advanced LIGO Observations Surrounding GW150914*. **ApJ Letters** [↗](#), 833(1):1, 2016.
- [31] LIGO Scientific Collaboration and Virgo Collaboration. *GW151226: Observation of Gravitational Waves from a 22-Solar-Mass Binary Black Hole Coalescence*. **Phys. Rev. Lett.** [↗](#), 116(24):241103, 2016.
- [32] LIGO Scientific Collaboration and Virgo Collaboration. *GW170104: Observation of a 50-Solar-Mass Binary Black Hole Coalescence at Redshift 0.2*. **Phys. Rev. Lett.** [↗](#), 118(22):221101, 2017.
- [33] C Cutler and L Lindblom. *The effect of viscosity on neutron star oscillations*. **ApJ** [↗](#), 314(1):234–241, 1987.
- [34] C Cutler and B F Schutz. *Generalized \mathcal{F} -statistic: Multiple detectors and multiple gravitational wave pulsars*. **Phys. Rev. D** [↗](#), 72(6):063006, 2005.
- [35] S Dall’Osso, G L Israel, L Stella, A Possenti, and E Perozzi. *The Glitches of the Anomalous X-Ray Pulsar 1RXS J170849.0-400910*. **ApJ** [↗](#), 599(1):485–497, 2003.
- [36] I Easson. *Postglitch behavior of the plasma inside neutron stars*. **ApJ** [↗](#), 228(1):257–267, 1979.
- [37] J L Friedman and Stergioulas N. *Rotating Relativistic Stars*. **Cambridge University Press** [↗](#), 2013. ISBN 9780521872546.
- [38] A Helman. *The Finest Peaks: Prominence and other Mountain Measures*. (**E-Book**) [↗](#), 2012. ISBN 978-1-41223-664-5.
- [39] N K Johnson-McDaniel and B J Owen. *Maximum elastic deformations of relativistic stars*. **Phys. Rev. D** [↗](#), 84(4):044004, 2013.
- [40] D I Jones and N Andersson. *Gravitational waves from freely precessing neutron stars*. **MNRAS** [↗](#), 331(3):203–220, 2002.
- [41] D Keitel. *Robust semicoherent searches for continuous gravitational waves with noise and signal models including hours to days long transients*. **Phys. Rev. D** [↗](#), 93(8):084024, 2016.
- [42] P K Kovtun, D T Son, and A O Starinets. *Viscosity in Strongly Interacting Quantum Field Theories from Black Hole Physics*. **PRL** [↗](#), 94(11):111601, 2005.
- [43] J M Lattimer. *The Nuclear Equation of State and Neutron Star Masses*. **Annu. Rev. Nucl. Part. Sci.** [↗](#), 62(-):485–515, 2012.
- [44] F Leclercq. *Bayesian large-scale structure inference and cosmic web analysis*. **arXiv** [↗](#), 1605.08420(-):237, 2015.
- [45] LIGO Scientific Collaboration and Virgo Collaboration. *First low-frequency all-sky search for continuous gravitational waves in advanced LIGO data*. **Phys. Rev. D** [↗](#), 96(12):122004, 2017.
- [46] A G Lyne, S L Shemar, and F Graham Smith. *Statistical studies of pulsar glitches*. **MNRAS** [↗](#), 315(3):534–542, 2000.
- [47] A Mastrano and A Melatos. *Kelvin–Helmholtz instability and circulation transfer at an isotropic–anisotropic superfluid interface in a neutron star*. **MNRAS** [↗](#), 361(3):927–941, 2005.
- [48] D Mateos, R C Myers, and R M Thomson. *Holographic viscosity of fundamental matter*. **PRL** [↗](#), 98(10):101601, 2007.
- [49] P M McCulloch, P A Hamilton, D McConnell, and E A King. *The Vela glitch of Christmas 1988*. **Nature** [↗](#), 346(1):822–824, 1990.
- [50] A Melatos and C Peralta. *Superfluid Turbulence and Pulsar Glitch Statistics*. **ApJ** [↗](#), 662(2):99–102, 2007.
- [51] A Melatos and C Peralta. *Gravitational Radiation from Hydrodynamic Turbulence in a Differentially Rotating Neutron Star*. **ApJ** [↗](#), 709(1):77, 2010.
- [52] A Melatos, C Peralta, and J S B Wyithe. *Avalanche Dynamics of Radio Pulsar Glitches*. **ApJ** [↗](#), 672(2):1103–1118, 2008.
- [53] J Ming *et al.* *Optimal directed searches for continuous gravitational waves*. **Phys. Rev. D** [↗](#), 93(6):064011, 2016.

- [54] J Mound and B Buffett. *Viscosity of the Earth's fluid core and torsional oscillations*. **J. Geophys. Res. (Solid Earth)** [↗](#), 112(B5):5402, 2007.
- [55] M A Papa *et al.* *Hierarchical follow-up of sub-threshold candidates of an all-sky Einstein@Home search for continuous gravitational waves on LIGO sixth science run data*. **Phys. Rev. D** [↗](#), 94(12):122006, 2016.
- [56] C Peralta, A Melatos, M Giacobello, and A Ooi. *Global Three-dimensional Flow of a Neutron Superfluid in a Spherical Shell in a Neutron Star*. **ApJ** [↗](#), 635(2):1224–1232, 2005.
- [57] H J Pletsch. *Parameter-space correlations of the optimal statistic for continuous gravitational-wave detection*. **Phys. Rev. D** [↗](#), 78(10):102005, 2008.
- [58] H J Pletsch. *Parameter-space metric of semicoherent searches for continuous gravitational waves*. **Phys. Rev. D** [↗](#), 82(4):042002, 2010.
- [59] R Prix, J Novak, and G L Comer. *Relativistic numerical models for stationary superfluid Neutron Stars*. **Phys. Rev. D** [↗](#), 71(4):043005, 2005.
- [60] R Prix, S Giampanis, and C Messenger. *Search method for long-duration gravitational-wave transients from neutron stars*. **Phys. Rev. D** [↗](#), 84(2):023007, 2011.
- [61] R Prix, S Giampanis, and C Messenger. *Search method for long-duration gravitational-wave transients from neutron stars*. **Phys. Rev. D** [↗](#), 84(2):023007, 2011.
- [62] V Rezanian and M Jahan-Miri. *The possible role of r -modes in post-glitch relaxation of the Crab pulsar*. **MNRAS** [↗](#), 315(2):263–268, 2000.
- [63] D M Sedrakian, M Benacquista, K M Shahabassian, A A Sadoyan, and M Hairapetyan. *Gravitational Radiation from Fluctuations in Rotating Neutron Stars*. **Astrophysics** [↗](#), 46(4):445–454, 2003.
- [64] D M Sedrakian, M Benacquista, and K M Shahabassian. *Gravitational radiation of slowly rotating neutron stars*. **Astrophysics** [↗](#), 49(2):194–200, 2006.
- [65] A Singh. *Gravitational Wave transient signal emission via Ekman Pumping in Neutron Stars during post-glitch relaxation phase*. **Phys. Rev. D** [↗](#), 95(2):024022, 2016.
- [66] A Singh, M A Papa, H B Eggenstein, and S Walsh. *Adaptive clustering procedure for continuous gravitational wave searches*. **Phys. Rev. D** [↗](#), 96(8):082003, 2017.
- [67] A Singh, M A Papa, H B Eggenstein, S Walsh, and S J Zhu. *The upper-limit procedure for the most recent Einstein@Home searches. in preparation* [↗](#), –(–):–, 2017.
- [68] A Singh *et al.* *Results of an all-sky high-frequency Einstein@Home search for continuous gravitational waves in LIGO's fifth Science Run*. **Phys. Rev. D** [↗](#), 94(6):064061, 2016.
- [69] A Sourie, M Oertel, and J Novak. *Numerical models for stationary superfluid neutron stars in general relativity with realistic equations of state*. **Phys. Rev. D** [↗](#), 93(8):083004, 2016.
- [70] Kip S Thorne. *Multipole expansions of gravitational radiation*. **Reviews of Modern Physics** [↗](#), 52(2):299, 1980.
- [71] M Tristram and K Ganga. *Data analysis methods for the cosmic microwave background*. **Rept. Prog. Phys.** [↗](#), 70(6):899, 2007.
- [72] C A van Eysden. *Short-period pulsar oscillations following a glitch*. **ApJ** [↗](#), 789(2):142–155, 2014.
- [73] C A van Eysden and A Melatos. *Gravitational radiation from pulsar glitches*. **Class. Quantum Grav.** [↗](#), 25(22):225020, 2008.
- [74] C A van Eysden and A Melatos. *Spin-up of a two-component superfluid: analytic theory in arbitrary geometry*. **J. Fluid Mech.** [↗](#), 729(1):180–213, 2013.
- [75] M van Hoven and Y Levin. *On the excitation of f -modes and torsional modes by magnetar giant flares*. **MNRAS** [↗](#), 410(2):1036–1051, 2011.
- [76] G Walin. *Some aspects of time-dependent motion of a stratified rotating fluid*. **J. Fluid Mech.** [↗](#), 36(2):289–307, 1969.
- [77] S Walsh *et al.* *A comparison of methods for the detection of gravitational waves from unknown neutron stars*. **Phys. Rev. D** [↗](#), 94(12):124010, 2016.
- [78] K Wette. *Estimating the sensitivity of wide-parameter-space searches for gravitational-wave pulsars*. **Phys. Rev. D** [↗](#), 85(4):042003, 2012.
- [79] M Yu, R N Manchester, G Hobbs, S Johnston, V M Kaspi, M Keith, A G Lyne, G J Qiao, V Ravi, J M Sarkissian, R Shannon, and R X Xu. *Detection of 107 glitches in 36 southern pulsars*. **MNRAS** [↗](#), 429(1):688–724, 2013.
- [80] S J Zhu, M A Papa, and S Walsh. *A new veto for continuous gravitational wave searches*. **arXiv** [↗](#), 1707.05268(–):10, 2017.
- [81] S Zhu *et al.* *An Einstein@Home search for continuous gravitational waves from Cassiopeia A*. **Phys. Rev. D** [↗](#), 94(8):082008, 2016.

Acknowledgments

I acknowledge all contributions toward thought and knowledge, and I anticipate those even more who are yet to come.

Curriculum Vitae

Personal Information

Full name: Avneet Singh
Date of birth: 12 January 1991
Place of Birth: Ambala Cantt, India

Education and scientific career

1994-2001 Kindergarten and Primary School, Ambala Public School, Ambala
2001-2006 Secondary School, Ambala Public School, Ambala
2006-2008 High School, Shivalik Public School, Chandigarh
Non-medical sciences
2008-2012 Bachelors degree, Indian Institute of Technology (IIT), Guwahati
Bachelor of Technology in Applied Physics
Thesis *Constraints on Hybrid Inflation*, Prof. Arunansu Sil
2010 Research Associate, University of Texas, Brownsville
2011 Research Associate, Max-Planck-Institut für Gravitationsphysik, Hannover
2010-2011 Lecturer in Physics and Organic Chemistry, Concept Educations, Guwahati
2012-2014 Masters degree, Erasmus Mundus Joint Masters Program
Master of Science in Astronomy and Astrophysics
S.I Leopold-Franzens-Universität Innsbruck, Austria
S.II, IV Università degli Studi di Padova, Italy
Thesis *Non-Gaussianity in Horndeski-type models of Inflation*, Prof. Sabino Matarrese and Prof. Nicola Bartolo
S.III Università degli Studi di Roma ‘Tor Vergata’, Italy
2014-2017 Doctor rerum naturalium (Dr. rer. nat.), Max-Planck-Institut für Gravitationsphysik, Potsdam-Golm and Hannover
Ph.D at the International Max Planck Research School (IMPRS)
Leibniz Universität Hannover
Thesis *Improved post-processing in searches for continuous gravitational waves*, Dr. Maria Alessandra Papa
2014– Member of the LIGO Scientific Collaboration (LSG).
2016-2017 Instructor, G9-137 – Data Analysis and Cluster Computing Laboratory.
2017– Post-doctoral researcher, Max-Planck-Institut für Gravitationsphysik, Potsdam-Golm and Hannover

List of Publications [[Google Scholar](#)

- Avneet Singh
Gravitational wave transient signal emission via Ekman pumping in neutron stars during post-glitch relaxation phase in Physical Review D **95(2):024022** (2017), [arXiv:\[gr-qc\] 1605.08420](#)
- Avneet Singh, Maria Alessandra Papa, Heinz-Bernd Eggenstein, Sylvia Zhu, Holger Pletsch, Bruce Allen, Oliver Bock, Bernd Maschenschalk, Reinhard Prix, Xavier Siemens
Results of an all-sky high-frequency Einstein@Home search for continuous gravitational waves in LIGO's fifth science run in Physical Review D **94(6):064061** (2016), [arXiv:\[gr-qc\]\[astro-ph\] 1607.00745](#)
- Avneet Singh, Maria Alessandra Papa, Heinz-Bernd Eggenstein, Sinéad Walsh
An adaptive clustering algorithm for continuous gravitational wave searches in Physical Review D **96(8):082003** (2017), [arXiv:\[gr-qc\]\[astro-ph\]\[math\] 1707.02676](#)
- Avneet Singh, Maria Alessandra Papa, Sinéad Walsh, Sylvia Zhu, Heinz-Bernd Eggenstein
The upper-limit procedure for the most recent Einstein@Home searches review in progress (2017), [LIGO DCC:T1700389](#)
- LIGO Scientific Collaboration and Virgo Collaboration
First low-frequency Einstein@Home all-sky search for continuous gravitational waves in Advanced LIGO data accepted by Physical Review D **96(12):122004** (2017), [arXiv:\[gr-qc\] 1707.02669](#)
- LIGO Scientific Collaboration and Virgo Collaboration
Results of the deepest all-sky survey for continuous gravitational waves on LIGO S6 data running on the Einstein@Home volunteer distributed computing project in Physical Review D **94(10):102002** (2016), [arXiv:\[gr-qc\]\[astro-ph\] 1606.09619](#)
- Maria Alessandra Papa, Heinz-Bernd Eggenstein, Sinéad Walsh, Irene Di Palma, Bruce Allen, Pia Astone, Oliver Bock, Teviet D. Creighton, David Keitel, Bernd Machenschalk, Reinhard Prix, Xavier Siemens, Avneet Singh, Sylvia J. Zhu, Bernard F. Schutz
Hierarchical follow-up of subthreshold candidates of an all-sky Einstein@Home search for continuous gravitational waves on LIGO sixth science run data in Physical Review D **94(12):122006** (2016), [arXiv:\[gr-qc\]\[astro-ph\] 1608.08928](#)
- Avneet Singh
Primordial non-Gaussianity in Horndeski-type Model for Inflation in arXiv:[gr-qc][hep-th] 1708.02911 (2014)